Fischer-Tropsch catalysis: osmium and platinum promoted cobalt supported in/on hollow carbon spheres

By

Tshepo Molefe

Student number: 604157

A thesis submitted to the Faculty of Science, University of the Witwatersrand, Johannesburg, in fulfilment of the requirements for the Degree of Doctor of Philosophy.

Supervisor: Prof Neil J. Coville

Co-Supervisor: Dr Roy Forbes

DECLARATION

I Tshepo Molefe declare that this thesis is my own, unaided work, under the supervision of Doctor Roy Forbes and Professor Neil. J. Coville. This work is submitted to obtain the degree of Doctor of Philosophy at the University of the Witwatersrand, Johannesburg. It has not been submitted before for any degree or examination at any other University.

WITS
UNIVERSITY

_____Signature_____

Tshepo Molefe

On this 6th day of February 2023

Abstract

The Fischer-Tropsch synthesis (FTS) is a process is used to convert traditional energy carriers such as coal, biomass, and natural gas into hydrocarbon products. The process involves a catalyst assistance in the conversion of syngas to hydrocarbons, which is usually composed of cobalt or iron supported on high surface area materials such as carbon-based materials, metal oxides, silica or alumina. In this thesis, the studies are focused on the fundamental processes involved in FT catalysts by using a hollow carbon sphere support. The study uses hollow carbon sphere (HCS) nanoreactors as the catalyst support and evaluates the effect of the nanoreactor's on the FT process, using Os and Pt nanoparticles as the reduction promoter for a Co catalyst encapsulated inside the HCSs. The synthesis and utilization of Os and Pt nanoparticles loaded on/in Co@HCS FT catalysts to give promoter-Co@HCS (e.g., OsCo@HCS & PtCo@HCS) and promoter/(Co@HCS) (e.g., Os/(Co@HCS) & Pt/(Co@HCS)) catalysts are reported.

The use of Os as a promoter for FTS has received very little attention. In previous studies, Os has been shown to be a poor FT catalyst, but its use as a catalyst promoter has not been studied. The hollow morphology of the HCSs nanoreactor was used to investigate the effect of Os and Pt promoter nanoparticle location relative to the Co_3O_4 (Co 10 wt %) nanoparticles (d_{Co} = 3.5 – 12.5) and on the effect of Os and Pt on the reduction behaviour and activity of the Co FT catalyst. Electron microscopy, in situ PXRD, TGA, PDF, TPR and BET studies revealed that the prepared catalysts were successfully synthesized with Co nanoparticles well dispersed. The Co nanoparticles had a high degree of stability as catalysts because they were encased in a carbon nanoreactor shell with a large surface area which showed good stability against sintering. The use of PXRD, PDF and TPR studies provided information on the Co phases and reduction pathways of the Co_3O_4 metal catalyst and the spillover effect from the Os and Pt promoters. Co_3O_4, CoO and Co (fcc) phases were observed for the promoter-Co@HCS and promoter/(Co@HCS) catalysts. More interesting was the observation of the Co hcp phase in the promoter-Co@HCS catalysts, indicating the importance of the promoter-Co interaction. The Co (hcp/fcc) phase ratio increased with the increase in promoter percentage loading and intimacy.

The synthesis of Co nanoparticles with varying thickness of a carbon shell was conducted with Os promotion on the outside of the shell to investigate the secondary hydrogen spillover effect.

The information obtained from the PXRD and TPR data revealed that the intimacy of the Os promoter with the Co catalyst in a thin and medium carbon shell (Os/(Co@HCS16) and (Os/(Co@HCS28)) promoted the reduction of CoOx to give metallic Co hcp and fcc phase due to secondary spillover effect. Whereas, when the Os promoter and Co were separated by a thicker carbon shell (Os/(Co@HCS51)) no metallic Co phase was observed. The study highlights the importance of Os-Co interaction and the ease of H_2 diffusion through the carbon shell in determining the reduction of Co oxides. More interesting was the observation of the Co hcp phase in the Os/(Co@HCS16)) catalyst, indicating the importance of the promoter-Co intimate interaction.

Nitrogen doping of HCS support was investigated in this thesis. The XPS, BET, and TPR studies showed that N-HCSs can offer a special unique material that is suitable for use as a catalyst support. Nitrogen doping increased the number of catalyst anchoring sites on the support, improved the thermal stability of the material, and assisted in immobilizing the catalyst nanoparticles during the reaction. These properties can improve the efficiency and stability of the catalyst, making nitrogen-doped HCS an attractive material for use as a support in catalytic reactions.

In order to explain the synergism during the FT reaction, hydrogen spillover was invoked once more. The primary spillover process (Co and promoter inside a HCS) produced a catalyst that gave a higher Fischer-Tropsch activity (e.g. OsCo@HCS, 38.5 – 46.4 $x10^{-6}$ $mol_{CO}/g_{Co}.s$) and outperformed unpromoted catalyst (e.g. Co@HCS, 27.8 $x10^{-6}$ $mol_{CO}/g_{Co}.s$) and catalysts where the promoter and Co were separated (e.g. Os/(Co@HCS), 25.1 – 36.4 $x10^{-6}$ $mol_{CO}/g_{Co}.s$) by a mesoporous carbon shell (secondary spillover effect) in regards to the FTS activity and C_{5+} production. In short, secondary hydrogen spillover effect on FTS performance was studied as a function of shell thickness. A shorter distance between the Os promoter and Co catalyst improved CO conversion and enhanced the reduction of CoO to Co^0. Thicker shell (Co@HCS_51nm) reduced reactant flow and led to lower CO conversion and greater selectivity to C_{5+} hydrocarbon production. The Os promoter and nitrogen doping increased the FTS catalytic performance. Nitrogen doping improved the hydrocarbon selectivity of the Co FTS reaction towards the production of long-chain hydrocarbons. In the spent catalysts, nitrogen doped catalysts revealed less particle sintering.

Dedication

Dedicated to my first love – mom (Lizzie Molefe).

And my family who supported me throughout

Thank you!

Acknowledgements

I would like to express my sincere gratitude to the following people and institutions for their various roles in making this project a success:

My supervisor, Professor N. J. Coville for his invaluable support, guidance, sharing of knowledge and helpful suggestions and criticisms during this project.

My co-supervisor, Dr R. Forbes for his input and support regarding the thesis write up, especially with XRD. Dr D Barrett for his input regarding the PDF work.

The staff members of the Microscopy and Microanalysis Unit at the University of the Witwatersrand for assistance with electron microscopy work.

The glassblower, Mr T. Dzara for assistance with the quartz tubes and glassware modifications used for this work.

Dr T. Phaahlamohlaka and Dr W. Dlamini for assistance with Fischer-Tropsch analysis.

Tshepo for helping to set-up the Fischer- Trospch rig and assistance with other technical work.

All my colleagues in chemistry department and the CATMAT group for their support and assistance in helping with the research project.

The DST-NRF Scarce Skills scholarship, DST-NRF Centre of Excellence in Catalysis “Cchange”, and the University of the Witwatersrand.

NRF Freestanding, Innovation and Scarce Skills Development Fund for Doctoral Scholarship.

Lastly, my partner and family for their love and patience in seeing me through this work and to the Almighty God.

Publications and Presentations

Publications

Molefe T, Barrett D, Moreno BD, Forbes RP, Coville NJ (2023) Fischer-Tropsch synthesis: osmium promoted Co@HCS catalysts. Journal of Catalysis

Presentations

Tshepo Molefe, Nomthandazo Mbita, Arthur Moya, and Dr S Durbach. *Carbon Nano-fibres formation on a fly ash catalyst with hydrogen and nitrogen gas as carrier gases*. (**2nd Best oral presentation**). RAP, November 2013.

Tshepo Molefe, and Dr Carren Billing. *Investigation and parameter optimization for DPASV used to study complex formation.* (**Oral presentation**). RAP, November 2014.

Tshepo Molefe, Tumelo Phaahlamohlaka, Dr Roy Forbes, and Prof Neil Coville. *Osmium as a potential Fischer-Tropsch catalyst using hollow carbon spheres as support*. (**Oral presentation**). DST center of excellence in catalysis (cchange) meeting, Wits and UCT-Johannesburg, July 2016.

Tshepo Molefe, Tumelo Phaahlamohlaka, Dr Roy Forbes, and Prof Neil Coville. *Osmium as a potential Fischer-Tropsch catalyst using hollow carbon spheres as support*. (**Poster presentation**). Catalysis South Africa (CATSA) conference - Drakensburg, November 2016.

Tshepo Molefe, Dr William Dlamini, Dr Roy Forbes, and Prof Neil Coville. *Osmium as a potential Fischer-Tropsch catalyst using hollow carbon spheres as support*. (**2nd Best poster presentation**). 7th SANi 2017 symposium – Technology University of Tshwane, November 2017.

Tshepo Molefe, Dr William Dlamini, Dr Roy Forbes, and Prof Neil Coville. *Osmium as a potential Fischer-Tropsch catalyst using hollow carbon spheres as support*. (**Oral presentation**). DST center of excellence in catalysis, Cchange symposium - Wits and UCT - Johannesburg, November 2017.

Tshepo Molefe, Tumelo Phaahlamohlaka, Dr Roy Forbes, and Prof Neil Coville. *Osmium as a potential Fischer-Tropsch catalyst using hollow carbon spheres as support*. (**Poster presentation**). Catalysis South Africa (CATSA) conference – Limpopo, November 2018.

Tshepo Molefe, Tumelo Phaahlamohlaka, Dr Roy Forbes, and Prof Neil Coville. *Osmium as a potential Fischer-Tropsch catalyst using hollow carbon spheres as support*. (**Oral presentation**). Catalysis South Africa (CATSA) conference – Cape Town, November 2019.

Contents

Chapter 1

1. Introduction

1.1. Overview

The growing demand for renewable energy due to climate change (global warming), the impending depletion of fossil fuel sources, the increase in human population and the growth of the world's economy have all led to a revised view of energy production/storage and use. This has meant new approaches to the production of liquid fuels from renewable sources. One of the main causes of the current environmental problems, such as global warming, is due to the centuries-long use of fossil fuels. The consumption of fossil fuels by modern motor vehicles and power plants has also led to the high levels of local air pollution [1, 2]. More recently, novel technologies have enabled the production of energy from renewable sources at lower production costs, compared to a decade or more ago [3].

Researchers have extensively worked on the development of X to liquid (XTL) (X a carbon source) technologies involving the conversion of various carbon-containing feedstocks such as coal (CTL), biomass (BTL), natural gas (GTL), and waste oil residues (WTL), to liquid fuels [4]. The X, importantly, can also be a renewable carbon source. The technology involves the gasification of carbon-containing sources to produce syngas (H_2 and CO) which is then further processed to produce a variety of hydrocarbons. The final products like liquefied petroleum gas (LPG), jet fuel, gasoline, distillate, diesel, and fine chemicals can be made by further refining the hydrocarbons. [5].

The FTS is a catalytic conversion reaction that converts syngas into hydrocarbons and oxygenates [6, 7]. The process occurs through a surface catalytic-polymerisation reaction which results in the production of paraffins, olefins, alcohols, and aldehydes. The FTS is an

exothermic catalytic gas liquefaction process and it is one of the most promising alternative processes for generating energy and chemicals from renewable resources [8].

In FTS, the most commonly used catalysts are the group 8-10 metals of the Periodic Table [9, 10]. In particular, cobalt, iron, nickel and ruthenium all catalyse the FTS reaction. However, due to their high activity, selectivity, affordability, and longer lifespan, Fe- and Co-based catalysts are the most prevalent and industrially viable catalysts [11]. Generally, Fe-based catalysts have a high water-gas-shift (WGS) activity, hence, they are utilized in the conversion of hydrogen lean syngas ($H_2/CO < 1.8$), typically derived from coal and biomass carbon sources [12]. Fe-based catalysts are more selective towards the production of olefins (gasoline, hydrocarbons and linear alpha-olefins) and oxygenates (alcohols, aldehydes and ketones) compared to paraffins. Nevertheless, the selectivity towards the Fe-catalyst can be varied by physical parameters such as temperature [13]. On the other hand, Co-based catalysts show low activity for the WGS reaction and they are utilized for the synthesis of long-chain linear paraffin's. Co-based catalysts are more selective towards the production of paraffin's and C_5+ hydrocarbons or heavy molecular weight waxes compared to Fe-based catalysts and they typically exhibit higher hydrocarbon production per unit mass of the catalyst [12, 13].

Although both Co and Fe are abundant in nature relative to other FTS catalysing metals, these metals are finite natural resources. Thus, one approach in maximizing their catalytic properties is by applying the use of a suitable support material and depositing small metal crystallites on it. Support materials enhance the catalyst performance by reducing/retarding metal sintering, enhancing the catalysts reducibility, increasing resistance towards poisoning, producing a large surface area for the active metal, and creating an easy flow of reactants into the catalyst pores [14]. The conventional support materials utilized in the FTS are metal oxides such as Al_2O_3, TiO_2, SiO_2 and MgO, and various shaped carbon materials [15–17]. The use of metal oxide support materials presents a challenge because they form a strong metal-support interaction with the FT catalyst. The costly metal catalyst activity is lost as a result of this interaction, which creates irreducible mixed compounds that are inactive in the FTS reaction. In contrast, carbon-based materials are a promising alternative as a support material for studying the FT catalysts as they reduce interaction with the support. Furthermore, doping carbon materials with heteroatoms such as nitrogen has been reported to produce a favourable metal-support interaction, enhancing the performance of the catalyst [18].

The backbone of the FTS process is the catalyst performance. Thus, development of catalysts to give high yields of specified hydrocarbons is one of the main objectives in the research field of FTS. This objective can be achieved by improving the support material or incorporating appropriate catalyst promoters into the overall catalyst material.

Promoters are substances that are added in small quantities to a catalyst (active metal) to improve its catalytic properties such as activity, selectivity, or stability. [19]. Promoters have a large variety of uses which can be broken down into their electronic and structural effects and their influence as a textural modifier, in catalyst-poison resistance, and as stabilizer, all of which can improve the catalytic performance/selectivity of a FT catalyst [20]. Structural promoters affect the metal-support interaction by improving the number of active metal sites and the dispersion of the metal on the surface of the support, thus modifying the surface properties of the catalyst. Electronic promoters donate or withdraw electrons from a catalyst to improve the reducibility and catalytic activity of the active metal [21, 22]. Electronic promoters can improve the reduction of MOx species to M species and improve the number of active sites by changing the metal-support interaction by mainly lowering the reduction temperature. Those promoters used when M = Co include Ag, Pt, Re and Ru [21, 23–25]. Well-known structural promoters are TiO_2, Al_2O, SiO_2, and CeO_2 [26–31]. Noble metal promoters can exhibit both structural and electronic promoter effects, which makes it challenging to define the function of noble metal promoters due to their effects overlapping with one another [31].

Hydrogen spillover is the term used to describe the mechanism that enhances the reduction of one CoO species by another species. The hydrogen spillover effect is a phenomenon which involves the relocation or migration of hydrogen atoms from an activating species, usually a noble metal such as Ru, to an accepting species which could be the support material or the metal oxide [32]. The migration of the hydrogen atom to the metal oxide results in the reduction of the metal oxide, and the promoter/noble metal is said to catalyse the reduction of metal oxide to metal (e.g. CoO to Co^0) [33–35]. In this study the hydrogen spillover effect will be studied with the use of Os and Pt as promoters, Co as the catalyst, and hollow carbon spheres (HCS) as the support material.

The HCS will be used to encapsulate the Co nanoparticles and provide a physical barrier, while the Os promoter will be loaded inside (OsCo@HCS catalyst) and outside (Os/(Co@HCS catalyst) the HCS to enable the examination of both primary and secondary spillover effects, respectively. Doping the HCS with nitrogen will also be investigated due to the enhanced effect

of metal-support interaction and the modification of the catalyst nanoparticles' electronic structure, which may improve the intrinsic catalytic activity of the catalyst.

1.2. Aim

The aim of this study is to promote Co@HCS with Os and Pt in the FTS. Hollow carbon spheres (HCSs) and N-doped HCSs (N-HCSs) will be used as the catalyst support to study the promoter-Co interaction. Various techniques will be used (e.g. XRD; TEM; TPR; etc.) to study the hydrogen spillover effect.

1.3. Objectives

The aim of this project will be achieved through the following objectives:

I. Synthesis - (polystyrene; PSS).
II. Synthesis - 10% Co/PSS.
III. Synthesis - 10% Co@HCS.
IV. Synthesis – Os or Pt promoted 10% Co@HCS with 1%, 0,5% and 0,1% promoter levels.
V. Synthesis - HCSs with varied shell thickness and N-doped HCSs (e.g. Os/(Co@HCS)).
VI. Study - promoter-Co interaction, spillover effect.
VII. Evaluation - the catalyst performance in Fischer-Tropsch synthesis.

1.4. Thesis outline

Chapter 1 briefly introduces the aims, objectives, and thesis outline as well as the fundamental ideas of Fischer-Tropsch synthesis.

Chapter 2 provides a detailed literature review of the Fischer-Tropsch synthesis, the different types of support materials used, and the different types of noble metals used as promoters and how the hydrogen spillover effect occurs.

Chapter 3 describes the experimental procedures used to synthesise the Co encapsulated inside the HCSs and how the addition of the promoter is achieved. The different characterization techniques used in the research are described, as well as the FT rig used in this work.

Chapter 4 reports the study of Fischer-Tropsch Synthesis: Osmium promoted Co@HCS catalyst.

Chapter 5 reports the study of Fischer-Tropsch synthesis: platinum promoted Co@HCS catalysts.

Chapter 6 presents the study of the effect of shell thickness on hydrogen spillover in Os promoted Co@HCS.

Chapter 7 presents the study of osmium promoter effects on the hydrogen spillover and performance of nitrogen functionalized hollow carbon spheres supported cobalt Fischer-Tropsch synthesis catalysts.

Chapter 8 provides the study's overall conclusion in its entirety, along with recommendations for future research.

1.5. Reference

1. Klass DL (1998) Biomass for renewable energy, fuels, and chemicals. Elsevier

2. Gholami Z, Zabidi NAM, Gholami F, Ayodele OB, Vakili M (2017) The influence of catalyst factors for sustainable production of hydrocarbons via Fischer-Tropsch synthesis. Rev Chem Eng 33:337–358

3. Ail SS, Dasappa S (2016) Investigations into enhanced wax production with combustion synthesized Fischer–Tropsch catalysts. Energy Convers Manag 116:80–90

4. Vosoughi V, Badoga S, Dalai AK, Abatzoglou N (2017) Modification of mesoporous alumina as a support for cobalt-based catalyst in Fischer-Tropsch synthesis. Fuel Process Technol 162:55–65

5. Pratt JW (2012) A Fischer-Tropsch synthesis reactor model framework for liquid biofuels production. SANDIA Rep SAND2012-7848

6. Okoye-Chine CG, Moyo M, Liu X, Hildebrandt D (2019) A critical review of the impact of water on cobalt-based catalysts in Fischer-Tropsch synthesis. Fuel Process Technol

192:105–129

7. Vosoughi V, Badoga S, Dalai AK, Abatzoglou N (2016) Effect of pretreatment on physicochemical properties and performance of multiwalled carbon nanotube supported cobalt catalyst for Fischer–Tropsch Synthesis. Ind Eng Chem Res 55:6049–6059

8. Odunsi AO, O'Donovan TS, Reay DA (2016) Dynamic Modeling of Fixed-Bed Fischer-Tropsch Reactors with Phase Change Material Diluents. Chem Eng Technol 39:2066–2076

9. Flandrois S, Simon B (1999) Carbon materials for lithium-ion rechargeable batteries. Carbon N Y 37:165–180

10. Liu R, Qu F, Guo Y, Yao N, Priestley RD (2014) Au@carbon yolk-shell nanostructures via one-step core-shell-shell template. Chem Commun 50:478–480. https://doi.org/10.1039/c3cc47050d

11. Everett DH (1972) Manual of symbols and terminology for physicochemical quantities and units, appendix II: Definitions, terminology and symbols in colloid and surface chemistry. Pure Appl Chem 31:577–638

12. Ge J, Zhang Q, Zhang T, Yin Y (2008) Core-satellite nanocomposite catalysts protected by a porous silica shell: Controllable reactivity, high stability, and magnetic recyclability. Angew Chemie - Int Ed 47:8924–8928. https://doi.org/10.1002/anie.200803968

13. Yue Q, Li J, Luo W, Zhang Y, Elzatahry AA, Wang X, Wang C, Li W, Cheng X, Alghamdi A (2015) An interface coassembly in biliquid phase: Toward core–shell magnetic mesoporous silica microspheres with tunable pore size. J Am Chem Soc 137:13282–13289

14. Zsoldos Z, Hoffer T, Guczi L (1991) Structure and catalytic activity of alumina-supported platinum-cobalt bimetallic catalysts. 1. Characterization by x-ray photoelectron spectroscopy. J Phys Chem 95:798–801

15. Joo SH, Park JY, Tsung CK, Yamada Y, Yang P, Somorjai GA (2009) Thermally stable Pt/mesoporous silica core-shell nanocatalysts for high-temperature reactions. Nat Mater

8:126–131. https://doi.org/10.1038/nmat2329

16. Ikeda S, Ishino S, Harada T, Okamoto N, Sakata T, Mori H, Kuwabata S, Torimoto T, Matsumura M (2006) Ligand-free platinum nanoparticles encapsulated in a hollow porous carbon shell as a highly active heterogeneous hydrogenation catalyst. Angew Chemie - Int Ed 45:7063–7066. https://doi.org/10.1002/anie.200602700

17. Harada T, Ikeda S, Ng YH, Sakata T, Mori H, Torimoto T, Matsumura M (2008) Rhodium nanoparticle encapsulated in a porous carbon shell as an active heterogeneous catalyst for aromatic hydrogenation. Adv Funct Mater 18:2190–2196

18. Galeano C, Meier JC, Soorholtz M, Bongard H, Baldizzone C, Mayrhofer KJJ, Schüth F (2014) Nitrogen-doped hollow carbon spheres as a support for platinum-based electrocatalysts. Acs Catal 4:3856–3868

19. Burwell RL (1976) Manual of Symbols and Terminology for Physicochemical Quantities and Units-Appendix II. Definitions, Terminology and Symbols in Colloid and Surface Chemistry. Part II: Heterogeneous Catalysis. Pure Appl Chem 46:71–90

20. Bahadoran F, Moradian A, Shirazi L, Zamani Y (2018) Fischer–Tropsch synthesis: evaluation of Gd and Ru promoters effect on Co/γ-Al 2 O 3 catalyst at different conditions. Chem Pap 72:309–325

21. Xu R, Hou C, Xia G, Sun X, Li M, Nie H, Li D (2020) Effects of Ag promotion for Co / Al 2 O 3 catalyst in Fischer-Tropsch synthesis. Catal Today 342:111–114. https://doi.org/10.1016/j.cattod.2019.04.004

22. Morales F, Weckhuysen BM, Spivey JJ, Dooley KM (2006) Promotion effects in Co-based Fischer-Tropsch catalysis. Catalysis 19:1–40

23. Mehrbod M, Martinelli M, Martino AG, Cronauer DC, Kropf AJ, Marshall CL, Jacobs G (2019) Fischer-Tropsch synthesis: Direct cobalt nitrate reduction of promoted Co/TiO2 catalysts. Fuel 245:488–504

24. Nabaho D, Niemantsverdriet JWH, Claeys M, van Steen E (2016) Hydrogen spillover in the Fischer–Tropsch synthesis: An analysis of platinum as a promoter for cobalt–alumina catalysts. Catal Today 261:17–27

25. Mandal S, Maity S, Gupta PK, Mahato A, Bhanja P, Sahu G (2018) Synthesis of middle distillate through low temperature Fischer-Tropsch (LTFT) reaction over mesoporous SDA supported cobalt catalysts using syngas equivalent to coal gasification. Appl Catal A Gen 557:55–63

26. Liu C, He Y, Wei L, Zhao Y, Zhang Y, Zhao F, Lyu S, Chen S, Hong J, Li J (2018) Effect of TiO2 Surface Engineering on the Performance of Cobalt-Based Catalysts for Fischer–Tropsch Synthesis. Ind Eng Chem Res 58:1095–1104

27. Munnik P, Krans NA, De Jongh PE, De Jong KP (2014) Effects of drying conditions on the synthesis of Co/SiO2 and Co/Al2O3 Fischer–Tropsch catalysts. ACS Catal 4:3219–3226

28. Yu S-Y, Huang W-L, Ma Y, Cao Z, Su H-Q (2012) Characterization of cobalt-based catalyst supported on CeO2 nanocubes for Fischer-Tropsch synthesis. Integr Ferroelectr 138:32–37

29. Pan Z, Parvari M, Bukur DB (2014) Fischer–Tropsch Synthesis on Co/Al 2 O 3 Catalyst: Effect of Pretreatment Procedure. Top Catal 57:470–478

30. Garcilaso V, Barrientos J, Bobadilla LF, Laguna OH, Boutonnet M, Centeno MA, Odriozola JA (2019) Promoting effect of CeO2, ZrO2 and Ce/Zr mixed oxides on Co/γ-Al2O3 catalyst for Fischer-Tropsch synthesis. Renew energy 132:1141–1150

31. Shimura K, Miyazawa T, Hanaoka T, Hirata S (2013) Fischer–Tropsch synthesis over TiO2 supported cobalt catalyst: Effect of TiO2 crystal phase and metal ion loading. Appl Catal A Gen 460:8–14

32. Mitchell PCH, Ramirez-Cuesta AJ, Parker SF, Tomkinson J, Thompsett D (2003) Hydrogen spillover on carbon-supported metal catalysts studied by inelastic neutron scattering. Surface vibrational states and hydrogen riding modes. J Phys Chem B 107:6838–6845

33. Psofogiannakis GM, Froudakis GE (2011) Fundamental studies and perceptions on the spillover mechanism for hydrogen storage. Chem Commun 47:7933–7943

34. Chung T-Y, Tsao C-S, Tseng H-P, Chen C-H, Yu M-S (2015) Effects of oxygen

functional groups on the enhancement of the hydrogen spillover of Pd-doped activated carbon. J Colloid Interface Sci 441:98–105

35. Psofogiannakis GM, Froudakis GE (2009) DFT study of hydrogen storage by spillover on graphite with oxygen surface groups. J Am Chem Soc 131:15133–15135

Chapter 2

2. Literature Review

2.1. Fischer Tropsch Synthesis

2.1.1 Background

The catalytic hydrogenation reaction was discovered by Dorbereiner in 1823 when finely divided platinum particles triggered hydrogen to spontaneously ignite in air [1]. Five decades later, the investigation of a variety of metals' catalytic properties, such as iron, copper, palladium, nickel, etc. was delved into by scientists. In 1902, Sabatier and Senderens reported the first catalytic methanation reaction between hydrogen and CO or CO2 over transition metal (Ni or Co) catalysts at temperatures of 180–200 °C and at atmospheric pressure [2]. Their discovery led to the foundation of XTL technology (X = coal, gas, biomass; T = to; L = liquid) [3–5]. Friedrich Bergius in Rheinau-Mannheim, Germany, invented and developed the high-pressure coal hydrogenation process during the period 1910-1925 [6]. In 1913, a German company BASF (Badishe Anilin und Soda Fabrik) patented the process for the hydrogenation of CO over a Co catalyst to produce hydrocarbons other than methane, ketones, alcohols, and acids [5, 7–10]. However, due to World War I the company discontinued their work on CO hydrogenation and focused on the synthesis of ammonia and methanol [2]. Later on, the development of the CO hydrogenation process was conducted by Franz Fischer and Hans Tropsch at the Kaiser Wihelm Institute in 1923. They did this by synthesising aliphatic oxygenated compounds over alkalised iron chips at 325-425 ℃ and 100-150 atm. The process of converting coal to petroleum was named the Fischer–Tropsch Synthesis (FTS) which applied to the synthesis of a broad range of hydrocarbon products [11]. Through their studies they later discovered that at low pressures of approximately 7 atm that only a small percentage of oxygenated organic compounds were present in the products produced, which were almost entirely paraffinic [12]. An important breakthrough was made in 1925 by Fischer and Tropsch when they discovered that a Co-Fe catalyst, at 250-300 ℃ and 1 atm, eliminated the production of oxygenates and only resulted in the production of hydrocarbon gases and heavy hydrocarbons.

A few years later, a chemist Otto Roelen who worked with both Fischer and Tropsch developed a standard FT industrial Co-based catalyst (100Co-5ThO2-8MgO-200 Kieselguhr) that had low

reaction temperature (180-200 ℃), high activity and low/medium pressure (1-15 atm). Due to Co being a costly catalyst at the time it was recovered from a spent catalyst by treating with nitric acid and hydrogen gas, and reused in the preparation of a fresh catalyst [13]. Otto Roelen also developed a Co-based industrial catalyst that converted CO and alkenes into aldehydes, and the process is now known as the homogeneously catalysed hydroformylation reaction [5]. In 1927, scientists began to solve chemical engineering problems associated with the FT reaction and the development of fixed bed reactors for the FT process under the supervision of Roelen. In 1936, Ruhrchemie granted the Steinkohlen-Bergwerk Rheinpreussen plant a license and it was finished as the first industrial-scale plant in Germany's Ruhr. The FT plant had an annual capacity of 25,000-30,000 metric tons of gasoline, diesel and paraffin wax. In a space of two years later, Germany had built a total of 9 commissioned coal-based FT plants (using Co and Fe catalysts) that operated with an annual combined total capacity of 660,000 tons [14, 15]. Table 1 shows data from the earliest FT plants in Germany [16].

Table 1: Earliest Fischer-Tropsch plants in Germany [16].

Year	Plant/ Location	Catalyst	Pressure	Annual Capacity (metric tons)	Products
1936	Steinkohlen Bergwerk Rheinpreussen/Ruhr	*standard FT catalyst	Atmospheric (1atm)	25,000-30,000	Gasoline, diesel oil, paraffin wax
1936	Wintershall AG/Ruhr	standard FT catalyst	Atmospheric (1atm)	30,000-40,000	Gasoline, diesel oil
1937	Ruhrbenzin AG/Ruhr	standard FT catalyst	Atmospheric and medium (5-15atm)	62,000	Gasoline, diesel oil, lubrication oil
1937	Brabag II, Ruhland-Schwarzheide	standard FT catalyst	Atmospheric (1atm)	200,000	Gasoline, diesel oil
1938	Mitteldeustche Treibstoff Lutzkendorf	standard FT catalyst	Atmospheric (1atm)	30,000	Gasoline, diesel oil
1938	Krupp Treibstoffwerk GmbH/Wanne-Eickel	standard FT catalyst	Atmospheric and medium (5-15atm)	130,000	Gasoline, diesel oil

1939	Essener Steinkohl/ Dortmund	standard FT catalyst	Atmospheric (1atm)	86,000	Gasoline, diesel oil
1939	1939 Hoesch-Benzin GmbH/ Dortmund	standard FT catalyst	Medium (5-15 atm)	51,000	Gasoline, diesel oil
1939	Schaffgotsch Benzin/	standard FT catalyst	Medium (5-15 atm)	80,000	Gasoline, diesel oil

*standard FT catalyst: 100Co-5ThO2-8MgO- 200 Kieselguhr

The occurrence of World War II in 1939-1945, led to the construction of German plants being halted. Despite the occurrence of World War II, research on the FTS continued and led to the development of low-cost catalysts such as Fe-based catalysts, due to the high prices of the Co metal during the time of war. In 1944, Germany had a high demand for FT fuels and this also contributed to new technologies and improved catalysts and reactors being established. Germany had the synthetic fuel capacity of 14, 675 tons per day. After World War II, different teams from the British Intelligence Objectives Subcommittee (BIOS) and the United States Technical Oil Mission (TOM), visited Germany to examine reports and interview personnel regarding the German synthetic fuel process Afterwards, the Combined Intelligence Office Subcommittee (CIOS), TOM, BIOS, and Field Intelligence Agency Technical (FIAT) published more than 1400 printed reports on the German synthetic fuel industry [6, 16]. From the reports released, countries began to adopt, build and run their own FT plants. One of the comprehensive reports was 'The Fischer-Tropsch and Related Synthesis' source by Henry et al. [17].

Table 2.1 below shows a summary of commercial FT plants established outside Germany in other countries [18–24]. After World War II, Arbeit-Gemeinschaft Lurgi and Ruhrchemie (ARGE) developed a large-scale fixed bed reactor, and Carthage Hydrocol Inc. focused on the development of a circulating catalyst bed FT technology [25]. As South Africa was in an apartheid era and was internationally isolated to trade and purchase fuel products, the government of the day via Sasol adopted and implemented both the processes of Arbeit-Gemeinschaft Lurgi and Ruhrchemie, and Carthage Hydrocol Inc. FT processes. Since South Africa is a coal abundant country, the abundant coal reserves enabled the generation of cheap syngas. In 1955 Sasol built its first coal to synthetic fuels FT plant (Sasol I) using circulating fluidized bed (CFB) reactors over a fused Fe/K catalyst at Sasolburg [3, 15]. This plant today

is fed with natural gas imported from Mozambique into a slurry phase reactor to produce liquid fuels. A low-temperature FT (LTFT, 200-250 °C) multi-tubulur fixed-bed reactor was used to produce wax products in 1955 and later a slurry reactor was used for this purpose (1993). In 1980 and 1982, Sasol expanded by building two new plants known as Sasol II and III, respectively, at Secunda. The plants specialised in coal to synthetic fuel production using a fused Fe/Ke catalyst in CFB reactors and a high-temperature FT (HTFT) process [21, 22]. Shell first developed their Shell middle distilled Synthesis (SMDS) process in 1993 in Bintulu, Malaysia. This FT technology used natural gas as feedstock and a Co-based catalyst was used to produce heavy parafins, which were further processed or converted into middle distillates by hydroprocessing [21]. In 1987 Mossgas was established in Mossel Bay, South Africa and was the first FT plant to use South Africa's gas producing fields. The discovery led to PetroSA being commissioned and in 1993, an iron-based (fused Fe/K) FT plant based on HTFT synthol technology, using a CFB reactor with a capacity of 20,000 barrels per day (bbl/day) and was operated to produce synthetic fuels from natural gas [21, 22, 26].

In 2006, Sasol and Qatar Petroleum collaborated to build the $900 million Sasol Oryx GTL (Sasol-QP (Oryx)) plant in Ras Laffan, Qatar. Based on the LTFT Sasol slurry phase distillate (SPD) technology, the plant used a Co-based (Co/Al_2O_3) catalyst. The plant used natural gas feedstock and its initial capacity was 34 000 bbl/day of hydrocarbons (24000 barrels of diesel, 9000 barrels of naphtha and 1000 barrels of liquefied petroleum gas) [27]. In 2009, China built the high-temperature slurry FT process (HTSFTP) for iron-based coal feedstock. The plant used a slurry-bed reactor that operated at medium-temperature (MTFT, 270-300 °C) [23]. More recently, Shell built the Qatar Petroleum, Pearl GTL plant based on the SMDS process in 2011, Qatar. The Pearl GTL plant uses natural gas feedstock, and is Co-based (Co/TiO_2) and used a LTFT multitubular fixed-bed reactor with a total capacity of 140,000 bbl/day [21–24, 27, 28]. Another GTL plant, owned by Chevron-Sasol-Nigerian National Petroleum Company, was constructed in Escravos, Nigeria, in 2013. The plant is based on LTFT SPD and Chevron Isocracking technologies and uses a Co-based (Co/Al_2O_3) catalyst [22, 29, 30]. China, Indonesia, Iran, Syntroleum, ConocoPhillips, BP, ExxonMobile, Eni/IFP, and Rentech are just a few of the nations and businesses that have looked into the use of FT technologies. A most recent development, in 2016, of a medium-temperature slurry-bed FT process (MTSFTP) technology was developed by Synfuels Company in China. The plant uses a Fe-based FT synthesis catalyst and a slurry-bed reactor to produce clean high-quality liquid fuels, such as diesel and gasoline [18, 24].

Table 2.1: Current commercial Fischer-Tropsch plants in the world [18–24].

Start year	Company/location	Feedstock	Reactor	Catalyst
1955	Sasol/Sasolburg, South Africa	Coal (initially), natural gas (current)	HTFT circulating fluidized bed	Fused Fe/K
1955	Sasol/Sasolburg, South Africa		LTFT multitubular fixed-bed (Sasol I)	Precipitated Fe/K
1980	Sasol/Secunda, South Africa	Coal, natural gas	HTFT circulating fluidized bed (Sasol II)	Fused Fe/K
1982	Sasol/Secunda, South Africa	Coal, natural gas	HTFT circulating fluidized bed (Sasol III)	Fused Fe/K
1993	Sasol/Sasolburg, South Africa	Coal (initially), natural gas (current)	LTFT slurry phase	Precipitated Fe/K
1993	Shell/Bintulu, Malaysia	Natural gas	LTFT multitubular fixed-bed	Co/TiO2, Co/SiO2
1993	PetroSA/Mosselbay, South Africa	Natural gas	HTFT circulating fluidized bed	Fused Fe/K
1995	Sasol/Secunda, South Africa	Coal, natural gas	HTFT SAS reactor	Fused Fe/K
2006	Sasol-QP (Oryx)/Ras Laffan, Qatar	Natural gas	LTFT slurry phase	Co/Al_2O_3
2006	Synfuels China, Taiyuan, Shanxi, China	Coal	HTFT slurry-bed	Fe
2008	NiQUAN GTL/Trinidad (Pointe-à-Pierre)	Natural gas	LTFT multitubular fixed bed	Co

			(Compression two fixed-bed reactors with catalyst filled tubes)	
2009	Yitai CTL Plant/Inner Mongolia, China	Coal	MTFT slurry-bed	Fe
2009	Shenhua ICL/China		HTFT slurry-bed	Fe
2010	Shanxi Lu'an/Shanxi, China		HTFT fixed-bed	Fe, Co
2011	Shell (Pearl)/Ras Laffan, Qatar	Natural gas	LTFT multitubular fixed-bed	Co/TiO_2
2013	Sasol-Chevron/Escravos, Nigeria		LTFT slurry-bed	Co/Al_2O_3
2016	Synfuels China, Ningdong Energy, Ningxia, China	Coal	MTFT slurry-bed	Fe

2.2.2. Fischer-Tropsch Synthesis

The FTS is the fundamental process entailing coal-to-liquid and gas-to-liquid technologies. The process involves syngas transformed into hydrocarbons and alcohols through a catalytic process. The industrial application of FTS is broken down into three stages: (i) syngas gasification from a carbon source such as coal, natural gas or biomass, (ii) FTS, and (iii) product upgrading such as hydrocracking. The overall process is summarised in Fig 2.1 below [31].

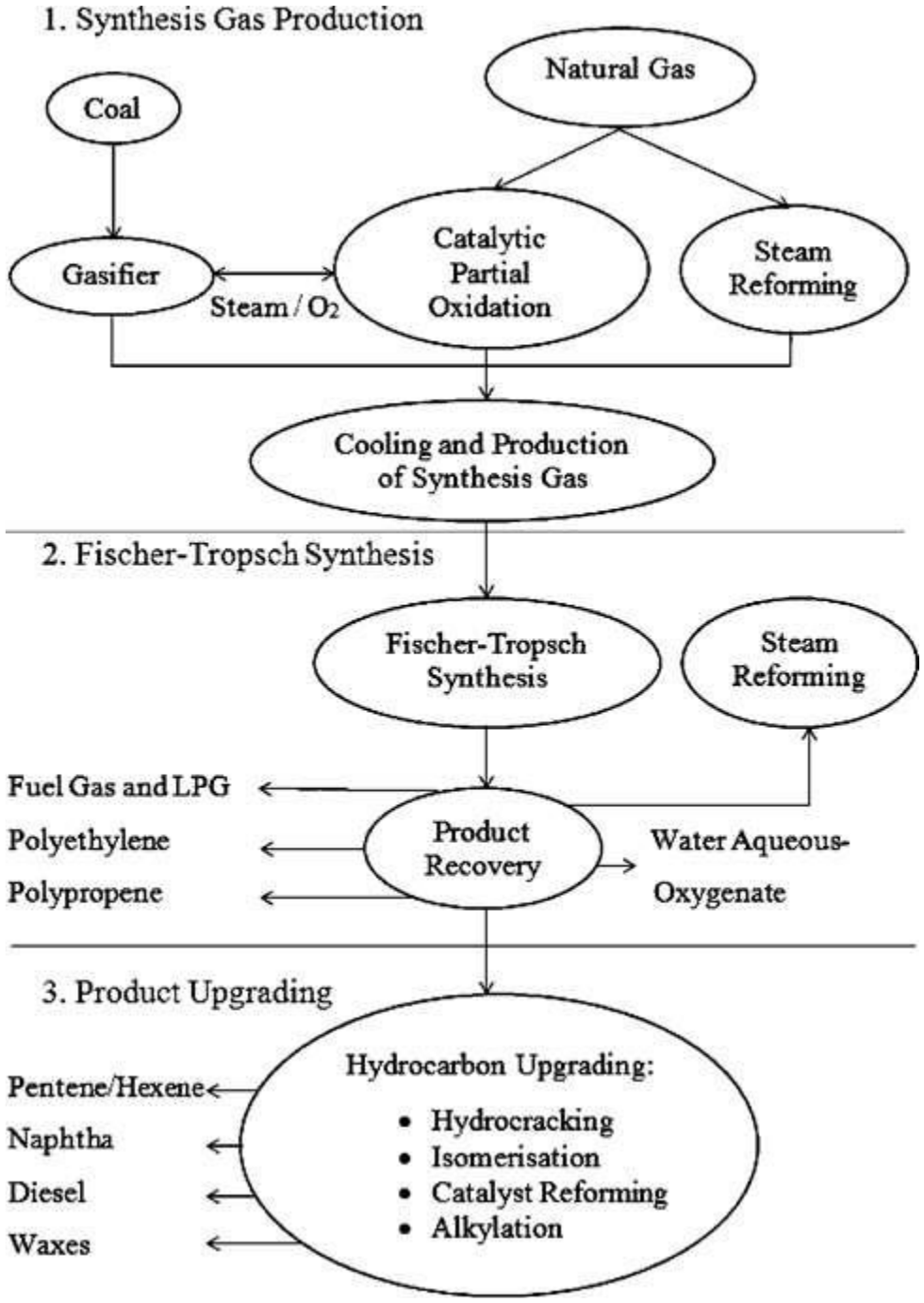

Fig 2.1: Three stage industrial application of the Fischer-Tropsch process [32].

Steam reformation is the process applied for the gasification of carbon sources into syngas. The steam reformation reaction results in the production of clean syngas by removing sulphur and impurities which is then utilized in FTS to produce clean petroleum goods such as fuel gas, ethylene, propene, liquefied petroleum gas, etc. The process is based on the production of cleaner fuels or higher quality hydrocarbons with very low sulphur content, low CO and NO_x emissions, and high cetane number. Further studies over the years have revealed that the FT process can provide an alternative to the production of fuels from crude oil [33]. The FTS

produced fuels are more attractive than crude oil produced fuels due to their properties of having a low sulphur content that contributes to less sulphur oxide emissions.

2.2.3. Fischer-Tropsch chemistry

The following equations describe the FTS chemistry reactions with n being the carbon number [34]:

Production of paraffinic (alkanes) hydrocarbons

$$(2n + 1)\ H_2 + nCO \rightarrow C_nH_{2n+2} + H_2O \quad (2.1)$$

$$(n + 1)\ H_2 + 2nCO \rightarrow C_nH_{2n+2} + nCO2 \quad (2.2)$$

Production of olefinic (alkenes) hydrocarbons

$$2nH_2 + nCO \rightarrow C_nH_{2n} + H2O \quad (2.3)$$

Production of alcohols (oxygenates)

$$2nH_2 + nCO \rightarrow C_nH_{2n+2}O + (n - 1)\ H_2O \quad (2.4)$$

Side reactions may also occur depending on the type of catalyst used, in addition to the above equations, such as the following:

Water Gas Shift (WGS) reaction that contributes as the main source of carbon dioxide production

$$H_2O + CO \rightarrow CO_2 + H_2 \quad (2.5)$$

Boudouard reaction (carbon deposition)

$$2CO \rightarrow C + CO_2 \quad (2.6)$$

Bulk carbide formation

$$yC + xM \rightarrow MxCy \quad (2.7)$$

Catalyst Oxidation-Reduction

$$yH_2O + xM \rightarrow MxOy + yH_2 \quad (2.8)$$

$$yCO_2 + xM \rightarrow MxOy + yCO \quad (2.9)$$

The FTS is a kinetically controlled step-by-step chain growth process that produces a variety of hydrocarbons by polymerizing CHx (x = 1, 2, or 3) groups on the surface of a catalyst.

There are two proposals for the chain growth of the FTS process: (i) the carbide mechanism which was originally proposed by Fischer and Tropsch in 1926 and later modified by Pettit and Biloen [35]. The mechanism postulates a C-O cleavage on the surface of the active metal followed by partial hydrogenation to form $CH_{x,\ ads}$ groups, which then polymerizes to produce heavy hydrocarbons and (ii) the Pichler-Schulz mechanism which postulates that chain growth involves the insertion of CO into a metal–methyl or metal–methylene carbon bond that then hydrogenates into an alkene or alcohol [36]. The catalyst utilized in the FTS influences the selectivity of the product in that the catalyst can either promote chain propagation resulting in heavy hydrocarbons (long chain) or terminate the reaction to produce light hydrocarbons such as methane. The FTS is both a hydrogenation and polymerisation reaction with a product distribution described statistically by the Anderson, Shultz and Flory (ASF) kinetic model [37, 38], expressed as:

$$W_n/n = (1-\alpha)^2\ \alpha^{n-1}$$

with n being carbon atom number, W_n being the weight fraction of hydrocarbon molecules, and α being the probability of chain growth. The α value is generally governed by the properties of the catalyst utilized and the reaction conditions of the FTS process.

Generally, FT reactions are highly exothermic, heterogeneous catalysed polymerisation reactions with the following stoichiometric equation:

Formation of paraffins: $(2n+1)H_2 + nCO \rightarrow C_nH_{2n+2} + nH_2O$ $-\Delta_{rxn}H$ (230 ℃) =210 -160kJ/molCO

Formation of olefins: $2nH_2 + nCO \rightarrow C_nH_{2n} + nH_2O$ $-\Delta_{rxn}H$ (230 ℃) =110-150kJ/molCO

The heat required to convert each mole of CO varies as the hydrocarbons' thermodynamic stability declines with product chain length. The heat involved to form low molecular mass olefins is less than the heat required to the form paraffins. FTS products are known to vary with the temperature utilized in the reaction. For example low temperature Fischer-Tropsch (LTFT) operational conditions operate around 230 ℃ and result in the formation of long chain hydrocarbons, whereas, high temperature Fischer-Tropsch (HTFT) operational conditions are used at around 340 ℃ and result in the production of short chain hydrocarbons [15, 39, 40]. Generally, Fe-based catalysts are applied in HTFT processes to produce gasoline and low

molecular mass olefins ranging from $C_2 – C_{15}$ [15, 39, 40]. In contrast, both Co-based and Fe-based catalysts are applied in LTFT processes to produce long chain linear waxes or hydrocarbons that can be converted into high quality diesel oil [9].

2.2.4. Fischer-Tropsch catalysts

In FTS a catalyst has to have adequate physical and chemical properties for the catalyst to achieve high catalytic activity in FTS. High porosity and high surface area are important physical properties that lead to high catalytic activity. In terms of chemical properties the catalyst must be able to chemically adsorb and dissociate the C-O bond while also having a strong H_2 adsorption capacity. In the process, water and carbon dioxide are produced due to O atoms being detached on the surface of the catalyst. The ability of the catalyst to be easily reducible is an essential parameter in FTS catalysis in that enhanced reducibility leads to an increase in CO and H_2 chemisorption, as well as a greater number of active sites. As a result, CO conversion increases, and there is good product selectivity. [41–43]. In the periodic table, most group 8-10 metals have been shown to be active in the FT reaction due to their chemical ability for adsorption and dissociation of CO and H_2 [39, 44, 45]. Literature work has reported that the specific activity for methane produced over a catalyst supported on silica decreased as follows: Ru > Fe > Ni > Co > Rh > Os > Pt > Pd > Ir [46, 47]. From these metals only Ru , Co, Fe and Ni catalysts have satisfactory activity for industrial FT usage. The FT activity of the metals decreases as follows: Ru > Co > Fe > Ni and in terms of cost the Fe: Ni: Co: Ru ratio is 1:250:1000:50000, respectively. The overall selectivity of an active metal used in the FTS depends on the syngas composition (H_2/CO ratio), the metal's cost and availability, and the final product that is desired. Despite nickel being cheap it is known to be a non-desirable catalyst in FT due to its high selectivity towards methane production [39, 48]. In addition, Ni forms highly toxic and volatile Ni carbonyls at low temperature [48]. The catalyst with best activity and selectivity for producing heavy hydrocarbons at low temperature (140 °C) is Ru, however, due to its low availability and high cost its use is not economically viable for large scale FT product production. Therefore, Fe and Co are the most practical catalysts in FTS for industrial-scale commercial application.

Fe catalysts are flexible, low cost, highly abundant, and have a low selectivity towards methane production in FTS. The use of a Fe catalyst in FTS produces alpha olefins and a mixture of oxygenated products such as alcohols, ketones and aldehydes. Iron-based catalysts have a tendency to produce undesirable large amounts of CO_2 due to their capacity for the water-gas

shift reaction, despite the Fe catalyst's high activity in the FT reaction. The water-gas shift is more pronounced when natural syngas is used as compared to syngas derived from biomass or coal, due to its low H_2 to CO ratios (H_2/Co ~1) [49, 50]. In FTS, Fe is known to exist in a mixture of different Fe phases such as metallic Fe (α-Fe), Fe oxides, and iron carbides [51]. The formation of Fe carbides takes place when carbon dissolves in the interstitial vacancies of metallic Fe. All three phases of the Fe catalyst are active in the FT reaction [52]. However, studies have shown that Fe carbides are the phases with highest FTS activity, whereas, magnetite (Fe_3O_4) is the most active phase for the water-gas shift reaction [53–55]. Generally, Fe catalysts contain promoters that enhance reducibility such as copper, that improve CO dissociation such as potassium, and can be used as structural promoters that improve the catalyst dispersion, such as zinc oxide or silica [56]. The challenge that one faces when utilizing Fe catalyst in FTS is that the catalyst has a high rate of deactivation and a relatively short catalyst life-time.

On the other hand, Co catalysts in FTS possess high activity, low water-gas shift reaction ability with a selectivity towards heavy hydrocarbons such as diesel fuel and wax [44, 56]. The Co catalyst is more expensive than the iron catalyst, therefore, to improve their dispersion, Co-based catalysts are typically supported on a material with a high surface area. This gives a cost–effective and efficient FT catalyst. The more dispersed the Co metal on the support the higher the selectivity to liquid hydrocarbons; however, an excessive increase in Co loading on the support materials leads to a decreased selectivity of the liquid hydrocarbons. Generally, metallic Co (Co^0) is accepted as the active phase of cobalt catalysts in FTS. The hexagonal closed packed (hcp) structure and the face-centered cubic (fcc) structure are two different crystalline phases in which the metallic Co can be found. The FT reaction conditions and the support material are typically what determine the phase that forms. The support material that results in fcc Co is silica, whereas the Al_2O_3 support material forms hcp Co catalysts after reduction [57]. In FTS, Co hcp catalysts have been shown to have higher CO conversions and C_5^+ selectivity relative to Co fcc catalysts (Table 2.2) [58]. Studies attribute such behaviour of Co hcp to a large number of surface defects (edges and corners) on the Co hcp structure compared to Co fcc. Iglesias et al. reported that decreasing the crystallite size of a Co catalyst ($d < 10$ nm) decreased the FTS reaction rate and that the rate of the FTS reaction was linearly correlated with metal dispersion [59–61]. Co catalysts are sensitive to the operational FT conditions such as pressure, temperature and H_2/CO ratios. In contrast to Fe which shows WSG activity, CO derived from natural gas with a H_2/CO ratio of ~2 is used when Co catalysts are

applied in FTS. The Co-based catalyst has a high hydrogenation capacity, thus it produces paraffinic waxes when natural syngas is fed into the catalyst. These waxes are then hydrocracked to produce lubricants and diesel fuel with excellent cetane ratings. Another advantage of a Co catalyst is its long catalytic life-time and this can be observed ferom the data obtained from the large-scale Qatar (Oryx GTL) and Malaysia (Shell) plants.

Table 2.2: Data for hcp and fcc phases of Co/SiO_2 catalysts in FTS. Reaction conditions: T = 220 °C, P = 20 bar, H_2/CO = 2/1 and syngas flow rate: 3.0 $sl.h^{-1}$ g_{cat}^{-1} [58].

Catalyst	TOS(h)	CO conv. [%]	Selectivty		TOF (s^{-1})
			CH_4	C_5^+	
Co hcp	16	63.1	3.5	88.2	0.095
	450	55.5	4.2	90.2	0.068
Co fcc	13	45.1	6.4	86.1	0.092
	492	32.1	7.2	82.9	0.049

2.2.5. Fischer-Tropsch catalyst support materials

Support materials in FTS facilitate metal particle crystallization and stabilization, as well as affect metal-support interactions, metal dispersion, mechanical strength, thermal stability, crystallite size, and mass transfer of the reactants/products of the active metal catalyst through its physicochemical and textural properties [62, 63]. The type of support material used influences a catalyst's performance in FTS, it is preferable that the support material have a high surface area and pore volume in order to improve the active metal's dispersion and remove mass transfer constraints. Co-based catalytic performance is highly influenced by the support material properties [64]. In FTS, a balanced chemical interaction between the metal and support material is important to produce a highly functional catalyst. The formation of a Co-support mixed compound could occur as a result of the metal-support interaction, which also affects the electron density and the structure of the metal particles. When the chemical interaction is imbalanced the following could occur: 1) a strong metal-support interaction (SMSI) may form

which results in formation of an irreducible catalyst or 2) a weaker metal-support interaction may form resulting in poor dispersion of the active metal [65].

Generally, FT catalysts are dispersed on metal oxides such as SiO_2, TiO_2, Al_2O_3 and MgO. The use of both TiO_2 and Al_2O_3 as support materials for Co introduces the concept of SMSI [48]. SMSI support materials contribute towards a good Co metal dispersion, however, they hinder the reducibility of the Co metal thus resulting in less active sites. A study by Reuel and Bartholemew investigated the turnover frequency (TOF) of metal oxides as Co support materials in FTS and they found that the TOF declined in the following order $TiO_2 > SiO_2 > Al_2O_3 >$ MgO [66, 67]. The SMSI of Co with the metal oxides resulted in the following mixed compounds $CoTiO_4$ [68], Co_2SiO_2 [69, 70], and Co_2AlO_4 [71, 72] all of which required elevated temperatures to be reduced. A weaker support material on the other hand contributes towards greater Co reducibility but with poor dispersion. A balanced support material is generally an inert material resulting in the optimal performance of the catalyst in FTS. Carbon support materials are relatively chemically inert and they can withstand both acidic and basic media. Their 'inertness' enables the reducibility of Co_3O_4 to Co to easily occur at lower temperatures compared to when metal oxide materials are used as supports. They are thermally stable at elevated temperatures, exhibit high mechanical strength and are cheap to produce compared to conventional support materials such as silica, titania and alumina.

2.2.5.1. Carbonaceous support material with a focus on hollow carbon spheres

Carbon materials are widely used as support materials and are relatively cheap compared with other support materials. Their porous structure can be easily modified to suit a reaction; in the e.g. for FTS use its surface area and pore size can be functionalized or modified to enhance metal dispersion and adsorption [73, 74] to achieve optimal FTS performance. Another advantage of a carbon support is the ease with which the active metal phase can be recovered from a used catalyst by burning off the carbon in the air, resulting in the easy reclamation of the active metal phase. The spent catalyst can easily be recovered due to the superb stability of carbon which (under inert conditions) and can be stable at high temperatures > 700 °C. However, carbon supported catalysts cannot be utilized in the presence of oxygen at temperatures exceeding 230 ^oC and in hydrogenation reactions at temperatures exceeding above 430 ^0C due to the production of carbon dioxide and methane, respectively [75, 76].

Generally, in supporting noble metal catalysts, particularly Pt-based catalysts, carbonaceous support materials are used [77]. Carbon materials with oxygen groups on their surface are thought to enhance the interaction between metals and carbon, and facilitate better active metal dispersion. As a catalyst support, carbon materials are known to sometimes facilitate a catalytic reaction known as hydrogen spillover. The presence of oxygen groups on the surface of the carbonaceous and metal oxide materials typically increases the spillover effect [78].

One way to conceptualize spherically shaped carbon materials is as layers of randomly twisted graphitic flakes deposited in a manner that follows the curvature of the sphere. Different carbon ring sizes that coexist cause the spherical curvature layer. Three different kinds of carbon materials with spherical shapes exist: solid carbon spheres (SCSs), core-shell carbon spheres (CSCSs), and hollow carbon spheres (HCSs) [79].

Nanospheres made of graphitic flakes that have a completely dense structure are known as solid carbon spheres (SCSs). Due to the fact that the layers of graphitic flakes within a SCS are not closed, they can be used for a variety of purposes, including catalyst support, lubricating materials, and rubber reinforcement [7].

Core-shell and hollow carbon spheres (HCS) structures are closely related, in that the core-shell structure encloses a core in a "shell" that has a different chemical composition, therefore enabling the creation of materials with multiple functions. The multiple functionality of these materials makes them excellent candidates in applications of photonic crystals, drug delivery, bio-diagnostics, catalysis and energy and energy storage [80]. They also have high surface area, excellent electronic conductivity, low weight properties and are chemically inert. The spherical hollow structure can be used as a nanoreactor by encapsulating an active metal phase by a carbon shell to form a heterogeneous catalyst. These structures have application in different catalysed chemical reactions such as oxidation, nitroarene reduction, hydrogenation reaction, Fischer-Tropsch synthesis, and the integration of multiple catalytic reactions. Mesoporous core-shell carbon spheres have been reported to comprise of an active metal precursor as the core encapsulated by a mesoporous carbon shell which is a suitable candidate for immobilizing nanoparticles in catalysis [81]. The porous shell prevents particle aggregation and can ensure a short diffusion distant of reagent molecules [82]. Particularly a carbon-based shell encapsulating metal nanoparticles is interesting because of carbon’s tuneable pore structure and relative chemical inertness. One such example of a core-shell composite is of a hollow, porous carbon shell encapsulating platinum nanoparticles (Pt@hmC) [83]. The Pt@hmC was

synthesised using a hard template method where Pt nanoparticles were coated with a silica layer, and subsequently coated again with a carbon layer to form Pt@SiO_2@C. Afterwards, silica was etched out resulting in the formation of a Pt@hmC structure. The Pt@hmC structure proved to prevent Pt particle aggregation during olefin hydrogenation reactions [84]. This structure was further tested by replacing platinum with rhodium, and similar findings were observed whereby metals were stabilized against aggregation while still maintaining their catalytic activity [84].

2.2.6. Fischer-Tropsch promoters

In order to enhance the catalytic activity of the cobalt active sites, platinum, ruthenium, and rhenium are typically promoted with cobalt FT catalysts [85, 86]. According to literature, the catalyst's physicochemical properties are significantly influenced by the active metal, the amount of loading, the support's textural characteristics, the properties of the additives, and the methods used in its preparation. The cobalt catalyst's physicochemical characteristics include its particle size, degree of reduction, dispersion, electronic structure, number of active sites, and cobalt-support interaction. The FT catalytic performance is directly affected by cobalt support materials and promoters. Promoters are substances added to a catalyst (active metal) in small amounts in order to improve the catalysts properties such as activity, selectivity or stability [82]. By incorporating a promoter, a catalyst's properties can be greatly enhanced compared to the promoter's sole action; however, the promoter may not always have catalytic activity on its own. Promoters are usually added through co-impregnation or subsequent impregnation methods to the supported catalyst. In general, promoters can be divided into two groups based on their intended use: 1) facilitating the desired reaction, for example by increasing the activity of the catalyst; and 2) suppressing the unwanted processes, for example by increasing the selectivity of the catalyst [87]. Promoters of the first group are distinguished into structure forming and activating materials. Structure-forming promoters are inert substances that are present in the catalyst as tiny particles. They work to prevent the sintering of the particles of the active catalytic phase, which either stops or encourages the reduction of the active surface during catalysis. Well known structural promoters are TiO_2, Al_2O_3, SiO_2, ZrO_2, La_2O_3 and CeO_2 [88–92]. Activating or electronic promoters can increase the number of active sites and have an impact on the electronic structure of the active phase by modifying the electron density on the surface of the active metal by removing or adding electron density near the Fermi level in the metal's valence band [33, 93]. For example, the iron catalyst for ammonia synthesis, contain aluminium oxide (structure-forming additive) and potassium oxide

(activator) as promoters [94]. Well known activating or electronic promoters are noble and transition metals such as Ag, Pt, Re, Ru, etc. which contribute in increasing the number of active sites and in enhancing the reduction of Co_3O_4 species by lowering the reduction temperature of the CoO to Co^0 reduction step [93, 95–97]. Furthermore, electronic promoters also alter how chemical bonds in reactants dissociate, which affects the catalyst's performance.

2.2.6.1. Platinum as a promoter

Studies on Pt as a promoter have been well documented e.g. in its ability to catalyse the reduction of Co oxide. Its role as a structural promoter is to enhance the dispersion of supported Co catalysts and the Co reducibility [33]. The promotion effect of Pt on Co catalyst is linked to Pt location relative to Co crystallites: Pt coordinated directly to Co induces an electronic promotion effect. When exposed to H_2 molecules the Pt activates the H_2 that subsequently shows spillover to Co for reduction to occur. Literature has shown that Pt – Co coordination occurs readily and that significant effects are observed on the activity, deactivation and the reducibility of Co oxide phase [71, 96, 98, 99]. Pt in its metallic state is the active phase for promotion effect on metal catalysts. A study on hardly reducible Co aluminates was conducted in the presence of small amounts of Pt and it was observed that Pt was able to reduce Co as a result of its promotional effect due to the Pt in the Pt – Co/Al_2O_3 [100].

Studies have shown that promoter effects are not limited to hydrogen spillover (reduction of a Co catalyst), but that Pt can also have an effect on the activity and selectivity of the Co catalyst in the FT reaction [101–104]. A study by Chu et al. revealed that even though improvements in Co reducibility were observed due to Pt promotion, the reaction rate of Co increased 8 times more and that a decrease in C_{5+} selectivity was also observed [105]. The decrease in C_{5+} selectivity resulted in a higher methane selectivity and this observation can be attributed to the high Pt hydrogenation activity therefore resulting in a smaller chain growth. Another study by Nabaho demonstrated that the Pt-promoted the Co/Al_2O_3 catalyst had a higher TOF and improved selectivity towards methane and paraffins as a result of hydrogen spillover caused by Pt. Additionally, electronic promoters affect the dissociation of chemical bonds in reactants, which has an impact on catalytic performance [106].

2.2.6.2. Osmium as a catalyst promoter

Among the noble metals, osmium is the densest known natural metal and the rarest stable element in the earth's crust with an abundance of 0.05 parts per billion [107]. Generally, Os is

alloyed with noble metals for use in electrical contacts, instrument pivots and phonograph needles. Osmium tetroxide is a powerful oxidizing agent applied in organic chemistry and is quite toxic, [108].

Little literature has been reported on Os as a CO hydrogenation catalyst in FTS and no promoter application of Os has been investigated. As an FT catalyst, the first work done in investigating its catalytic properties was reported on an Os/SiO_2 catalyst and it was reported to be catalytically active with $C_1 – C_5$ hydrocarbons being produced [109]. However, Os was shown to be a poor FT catalyst with 70% methane as the dominant product. Another study performed on a triosmium carbonyl cluster supported on Al_3O_4 was reported to be catalytic active [110–114]. Ntombovuyo and associates, conducted research on a Os/SiO_2 catalyst under FTS and the catalyst produced C_1-C_3 hydrocarbons as result of some catalytic activity [115]. A recent study on Os@HCS was reported and it showed to correlate with other studies on osmium being a poor catalyst with methane as a dominant product [116].

Even though osmium has been investigated on conventional oxide supports, to date, there has been no reports on the use of of Os nanoparticles as a Co or Fe catalyst promoter for gas phase CO hydrogenation reaction in FTS. Since osmium and ruthenium resemble one another in their low oxidation state, similar promoter effects are expected to be observed in a study on Co promotion. On the hand, the reduction of Co oxide nanoparticles via a hydrogen spillover mechanism has been suggested for noble metal promoters [117–121].

2.2. Hydrogen spillover effects

2.2.1. Overview and background

The term "spillover effect" in heterogeneous catalysis refers to the migration of formed active species (hydrogen atom) that move from one surface to another surface accompanied by a phase change which would not otherwise generate or sorb these species under the given conditions [122–127]. In 1957, Kuriacose made the observation that GeH_4 decomposed to give H_2 that was generated in the presence of Pt wire. Taylor attributed the reaction to the recombination of H atoms to give H_2 molecules in the presence of a Pt surface [128]. The term “spillover” was coined by Boudart et al. to elaborate the migration of H atoms or H atoms that spilt over from a hydrogen-rich metal phase to a hydrogen poor support surface [124]. In the spillover effect, the phase providing sites for the active species to adsorb is known as the

acceptor, whereas the phase where generation of active species occurred was known as the initiator (or activator). When both the initiator and acceptor phase are in direct contact then the reaction is known as a primary spillover effect, whereas, when the phases are separated by an additional inert carrier, the reaction is said to be a secondary spillover effect.

A solid-state reaction provided the first concrete evidence of the spillover effect and it was discovered by Khoobiar in 1964 [123]. The experiment was conducted on yellow WO_3 which is known to be reduced by hydrogen at temperatures above 200 °C resulting in the formation of W_4O_{11} which is blue in colour. When the experiment was conducted on WO_3/Al_2O_3 in the presence of platinum (Pt), while passing pure H_2 over the mixture, reduction of WO_3 to W_4O_{11} occurred in room temperature, with a colour change from yellow to blue. The effect was not observed on an $Al_2O_3 + WO_3$ mechanical mixture at room temperature. The mechanism is explained by the dissociation of hydrogen molecules on the platinum surface and the migration of H atoms via the Al_2O_3 onto the WO_3 surface (in the form of H^+ ions) that reduced the WO_3 to W_4O_{11} at room temperature. See equations below:

$$H_2 \xrightarrow{Pt} 2H$$

$$2H \underset{}{\overset{Al_3O_4}{\rightleftharpoons}} 2H^+ + 2e^-$$

$$2H + 4WO_3 \longrightarrow W_4O_{11} + H_2O$$

Further experiments showed that the measurement of hydrogen adsorbed on the $Pt/SiO_2 + WO_3$ was several times more than on the Pt/SiO_2 without WO_3 [124]. This led to the formation of tungsten bronze under the influence of hydrogen that was transferred from Pt onto WO_3 via SiO_2 (or Al_2O_3), tungsten oxide acquired its blue colour as a result.

2.2.2. Characterization techniques to study the hydrogen spillover effect.

In hydrogen spillover, it is important to be able to detect the occurrence of the spillover effect and to evaluate how the hydrogen interacts with the acceptor. The spillover effect has been identified and studied using a variety of techniques. The commonly used techniques are listed as follows.

2.2.2.1. Chemisorption

Chemisorption is generally used to determine the surface area of a metal in supported catalysts and this enables method allows for the study of the hydrogen spillover phenomenon [124]. Extensive chemisorption experiments have been reported (they usually take place between 200-300 °C) and the data demonstrated a correlation between the number of metal atoms on the surface (N_M) and the number of hydrogen atoms adsorbed on the metal surface (N_H). The ratio of N_H/N_M varies in range 0.5-2.0 for different supported metals and the ratio decreases with decrease in metal particle size [126]. Diverse elements, including a change in the crystal system in small particles, a change in the metal's oxidation number, hydrogen's dissolution in the metal's bulk, and the spillover effect, all caused deviations from unity.

The deviation of the ratio N_H/N_M from unity is due to hydrogen adsorption and the possible explanation for such is the flow of hydrogen onto the support material or carrier. The N_H/N_M ratios of Pt/Al_2O_3 and Pd/Al_2O_3 catalyst from the hydrogen adsorption data equals 5-10 [129] and on a Pt/C catalyst equals 75 [122]; this can be explained by the hydrogen spillover phenomenon. The increase in hydrogen chemisorbed on Pt/C at hydrogen atmosphere is related to the hydrogen spillover from the platinum to the charcoal (activated C) support material [130]. The spillover effect has been shown to promote an increase in the hydrogen adsorption rate on a mixture of Co/C with activated charcoal [44]. As well as being unaffected by the concentration of the initiator (Co) or other initiators like Cu, Ni, or Fe, the acceptor's capacity also determined the rate at which hydrogen adsorption occurred. Conditions that are typically favourable for the adsorption method's ability to observe spillover involve a high H_2 pressure and a high temperature [126].

2.2.2.2. Infrared spectroscopy

The most common method for observing the hydrogen spillover is the isotope H-D exchange between D_2 and hydroxyl groups (OH-) on the support material of the metal catalyst. The process of H-D exchange is generally monitored by infrared spectroscopy [131, 132]. A study by Carter et al. showed the rate of isotope exchange between OD and OH groups increased on the Pt/Al_2O_3 compared to that of Al_2O_3 thus suggesting that the isotopic exchange rate was accelerated by the presence of Pt [133]. Furthermore, a similar study was conducted on Pt/SiO_2 in the presence of D_2 via FTIR (Fourier-transform infrared) spectroscopy by Conner et al. due to hydrogen spillover [127]. The experiment was conducted by measuring the concentration

gradient during the spillover by placing Pt at the centre of pressed $Pt/Al_2O_3/SiO_2$ and Pt/SiO_2 discs.

In contrast, other researchers have argued that the H-D exchange experiments are not sufficient evidence to give direct evidence of the hydrogen spillover. According to the arguments, the H-D experiments may not have been caused by a net migration of H/D 'atoms' over the support material, but rather by H^+-D^- ion-exchange at the metal-support interface. Furthermore, the is low activation energy required for H^+-D^- ion-exchange to occur at the metal-support interface thus readily taking place at room/mild temperatures. From such an argument, the FTIR method has to be supported by other reliable techniques in order to prove the hydrogen spillover effect.

2.2.2.3. In-situ characterization techniques

The improvement of in-situ characterization techniques has made it possible to track the hydrogen spillover in real time.

The in-situ powder X-ray diffraction (PXRD) characterization technique has been utelized to investigate hydrogen spillover effect on a Ru@MHCS@Co catalyst, where Co was encapsulated inside a mesoporous hollow carbon sphere (MHCS) and the Ru was loaded on the outer carbon shell of MHCS [134]. PXRD studies were conducted after the introduction of H_2 to the catalyst and PXRD patterns were collected at 50 °C interval; the Co species were reduced and underwent a phase transformation occurring from Co_3O_4, to a CoO intermediate phase to a Co metallic phase. The transition from Co_3O_4 to Co occurred at a lower temperature in the presence of Ru, Ru@MHCS@Co (150 °C) compared to a catalyst prepared without Ru, MHCS@Co (200 °C). The decrease in temperature for the transition to occur was due to a hydrogen spillover from Ru to Co through the carrier which in this case was the carbon layer of the MHCS.

The X-ray adsorption spectroscopy (XAS) characterization technique has been used on Fe/TiO_2 to study the hydrogen spillover effect by varying the distance of the metal-support interaction. A pair of Fe oxide and Pt nanoparticles supported on reducible TiO_2 with varied distances from 0-45 nm were prepared. The catalysts were monitored with XAS, and the Pt and Fe oxide spectra that were separated by 45 nm were compared with one another. The ex-situ XAS with the introduction of hydrogen at 70 °C showed that the Pt and Fe oxide in both pairs was reduced equally. Karim et al. thus concluded that hydrogen spillover could reduce a distant metal oxide

that was not in close proximity to the Pt catalyst, and can occur over a large metal-metal separation distance [135].

The visualization of the active hydrogen species spillover on the surface of bimetallic catalysts was made possible through the use of low-temperature scanning microscopy (LT-STM) [136–138]. Kyriakou et al. investigated a Pd/Cu (111) surface formation by the deposition of a 0.01 monolayer of Pd on Cu (111) at ca. 10 Langmuirs (L, 10^{-6} Torrs.s) of hydrogen at 80 K. As individual hydrogen atoms spilled over onto the Cu (111) surface from Pd atom sites, hydrogen atoms emerged as depressions in the LT-STM image (Fig 2.2).

Another technique that involves STM is tip enhanced Raman spectroscopy combined with STM (STM-TERS) which has been used effectively used in the investigation of hydrogen spillover on a nanoscale level [139]. A study of the selective hydrogenation of chloronitrobenzenethiol (CNBT) to chloroaminobenzenthiol (CABT) was done by Yin et al. The study was performed on a bimetallic Pd/Au catalyst with CNBT immobilized on its surface. The CNBT@Pd/Au was exposed to hydrogen at room temperature followed by analysis with STM-TERS, Fig 2.2 b. From the TERS, a surface scan of a small Au crater showed the disappearance of the peak at 1336 cm^{-1} while the C=C stretch frequency shifted to 1586 cm^{-1}, revealing the synthesis of CABT due to a hydrogen spillover occurrence from Pd to the small Au crater.

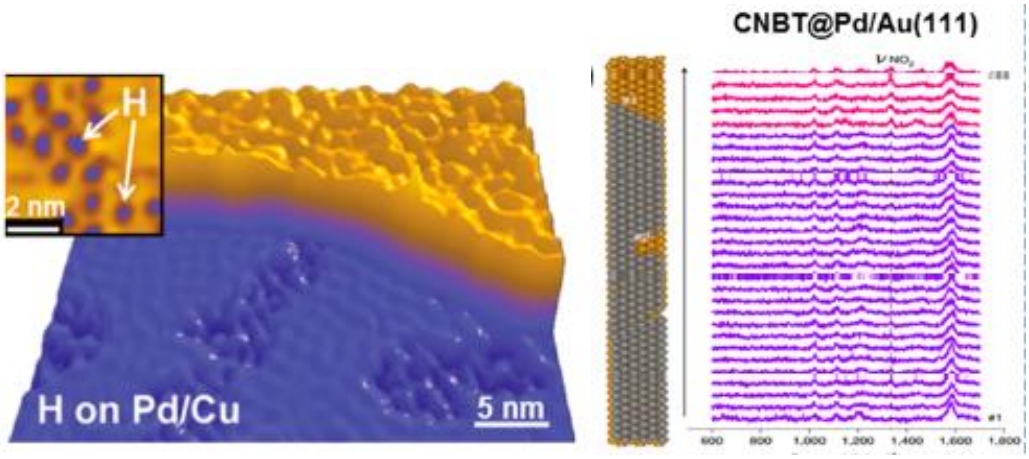

Figure 2.2: a) STM image of hydrogen atoms on 0.01 ML Pd/Cu(111). The high resolution image of individual hydrogen atoms on Cu(111) is shown from the inset [136]. b) STM images and TERS line scan results of CNBT self-assembled monolayers on Pd/Au after exposure to H_2 [139].

2.2.2.4. Temperature programmed reduction/desorption (TPR and TPD)

In general, the addition of noble metals improves the reduction of metal oxides, and this effect is due to hydrogen spillover [140–142]. The temperature-programmed reduction/desorption (TPR/TPD) technique can be utilized to study the spillover of adsorbed species [130]. The change in temperature that is employed in the technique with time on the surface of the catalyst enables the rate to be recorded. In this, the initial substances that were adsorbed in one form or another undergoes desorption and becomes converted via various pathways into their final form or products. The spillover of adsorbed species is a possibility in supported catalysts, whereas, unsupported catalysts do not experience this. The increase of the TPD peak areas is due to substances adsorbed beforehand.

Many studies have shown that TPR data measured in the presence of hydrogen shows how the enhancement or acceleration of metal species reduction occurs when a shift of the reduction peak moves to a lower temperature [85, 96, 98, 101, 143, 144]. Furthermore, hydrogen desorption in TPD measurements has been used to identify the presence of hydrogen that has been spilled [136, 145, 146].

2.2.3. Mechanism of hydrogen spillover

2.2.3.1. Surface and gas-phase pathways to spillover

Scientists have questioned whether the hydrogen spillover effect occurs through the gas phase or along the surface. Dmitriev et al. investigated the isotope exchange between deuterium and the surface OH groups of the HNaY zeolite and found that the activated deuterium was transported along the support's surface rather than through the gas phase, separating the spillover initiator (Pt) and the zeolite[147].

Another study to prove the transfer of hydrogen atoms occurs through the support surface involved in the study of hydrogen atoms adsorbed/produced via the microwave discharge technique on a Pt/TiO_2 catalyst. The F centres (trapped electrons on oxygen vacancies) of Pt/TiO_2 that can affect the hydrogenation of ethene were developed on the TiO_2 support material when the hydrogen atoms adsorbed. When the Pt/zeolite catalyst was employed instead of the Pt/TiO_2 catalyst, poor hydrogen atom adsorption from microwave discharge technique due to the fact that these hydrogen atoms only interact with the catalysts' outer surface [148].

Relatively few investigations have been put forward that hypothesise that spillover for the gas-phase transport of hydrogen atoms [149, 150]. However, one cannot rule out that hydrogen

transfer occurs through a source to the acceptor and not directly in the form of other species such as OH, H_2O, etc. since desorption of hydrogen atoms occurs at low temperatures and is thermodynamically unfavourable.

2.2.3.2. Spillover mechanism for the diffusion of hydrogen atoms on reducible oxide and non-reducible oxide surfaces

The in-situ FTIR spectroscopy was one the first techniques used to study the spillover mechanism. Conner et al. studied the diffusion of adsorbed deuterium on a Pt/SiO_2 surface which occured from Pt to the carrier as a result of an exchange between the OH groups on the SiO2 carrier and deuterium (D) atoms [127]. The process was postulated to proceed as shown in the following scheme, Fig 2.3:

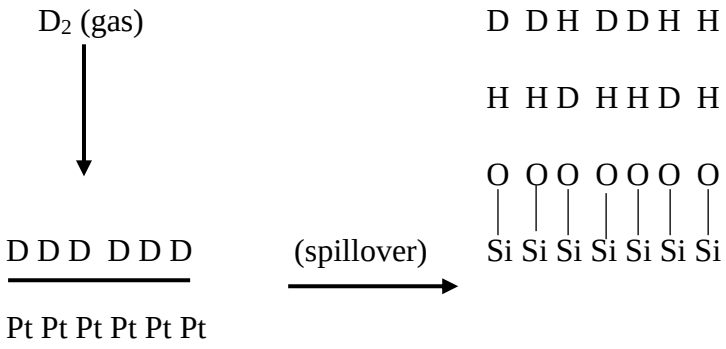

Figure 2.3: Schematic illustration of adsorbed deuterium on a Pt/SiO_2 surface

The spillover of deuterium on SiO_2 has been postulated to occur via the formation of associative complexes with OH groups [151]. Studies conducted using IR spectra of 10% Pt/TiO_2 have shown adsorption of H_2 (D_2) at low temperature which resulted in the formation of a new broad adsorption band at ~ 3000 (2300 for D) cm^{-1} assigned to the OH (OD) groups at the metal-support interface [152]. The OH (OD) adsorption band is thermally unstable at room temperature.

Most researchers in this field suggest that hydrogen atoms are the ones that participate in the spillover, and thus the effect is known as the hydrogen spillover effect [147, 153, 154]. A study by Neikam and Vannice found that in the Pt/CeY system the rate of EPR signal disappearance of perylene correlated with the rate of hydrogen adsorption [153]. The direct detection of H atoms by EPR is only possible at temperatures below -170 °C, however, with thorough analysis of the shift in ^1H NMR spectra, the technique has made it possible to confirm that hydrogen migrates as $H\cdot$ radical species on the SiO_2 surface [154]. Another popular postulation is that

spillover proceeds via a proton mechanism and this is in accordance with the promoting agent's proton affinity and spillover rate [155–157]. The solvation of the diffusion proton occurs in the following order: H_2O >> CH_3OH > C_2H_5OH > n-C_3H_7OH > n-C_4H_9OH. The rate of spillover was not affected by the specific surface of the supported Pt on all these promoting agents, however, in the presence of CH_3COOH, known to have low proton affinity the rate of spillover was affected. Therefore, the rate of reaction for the latter can be determined by the rate of solvation of the proton.

The mechanism of hydrogen spillover is different with different acceptors. Spillover of hydrogen atoms is generally recognized when it occurs from metal particles to reducible metal oxides. Prins et al. concluded that the hydrogen molecule initially adsorbs on the metal surface and dissociates to hydrogen atoms on the surface, followed by the hydrogen atoms migration to the metal-support interface, where they combine with the protons and electrons [158]. The process then becomes the electron reduction of M^{n+} cations to $M^{(n-1)+}$ cations, a location where oxygen anions' surfaces attract protons. Following the first reduction at the metal-support interface, the reduction can be transferred by exchanging electrons between the $M^{(n-1)+}$ cation and the neighbouring M^{n+} cation, complemented by the migration of the proton to an O^{2-} anion attached to the nearby M^{n+} cation. When another spilled hydrogen reduces the reoxidized metal cation at the metal particle's edge, the remaining M^{n+} cations are reduced. This process can continue until all metal cations are reduced.

Hydrogen spillover over non-reducible supports has been controversial and it is not clear if it actually exists or not. Scientists have theoretically predicted that spillover over non-reducible supports is energetically unfavourable and that the occurrence of spillover over such supports may be due to contamination [158, 159]. Recently, more studies have been conducted that show that hydrogen spillover over non-reducible oxides can exist. Karma et al. conducted a study on a non-reducible Al_2O_3 support material that was an uncontaminated well-defined model system to investigate the hydrogen spillover using electron beam lithography (EBL) [135]. On Al_2O_3, Fe oxide–Pt nanoparticles were supported and the distance between the Fe oxide and Pt nanoparticles was varied. The results obtained from Fe XAS spectra showed that when hydrogen was introduced into the system that the Fe nanopartciles supported on Al_2O_3 became reduced by spilled hydrogen atoms from Pt nanoparticles, as shown in Fig 2.4 a. The reduction of the Fe oxide was distant dependent (i.e. Fe oxide – Pt distance). The further the distance between the two nanoparticles the lower degree of reduction of the Fe oxide, shown in Fig 2.4 b. The hydride species formation on the Al_2O_3 was through dissociative adsorption for the

hydrogen migration to occur. The species could bind to three-coordinated aluminium defect sites that could also engage in interactions with water molecules. The transfer of hydride species among neighbouring Al_2O_3 defect sites was shown, Fig 2.4 c, by a first-principle atomistic simulation where the activation energy barrier was found to be between 1.15 to 1.63 eV, depending on the hydration of the surface. The hydrogen desorption rate was observed to be faster resulting in a gradient in the hydrogen coverage of the surface.

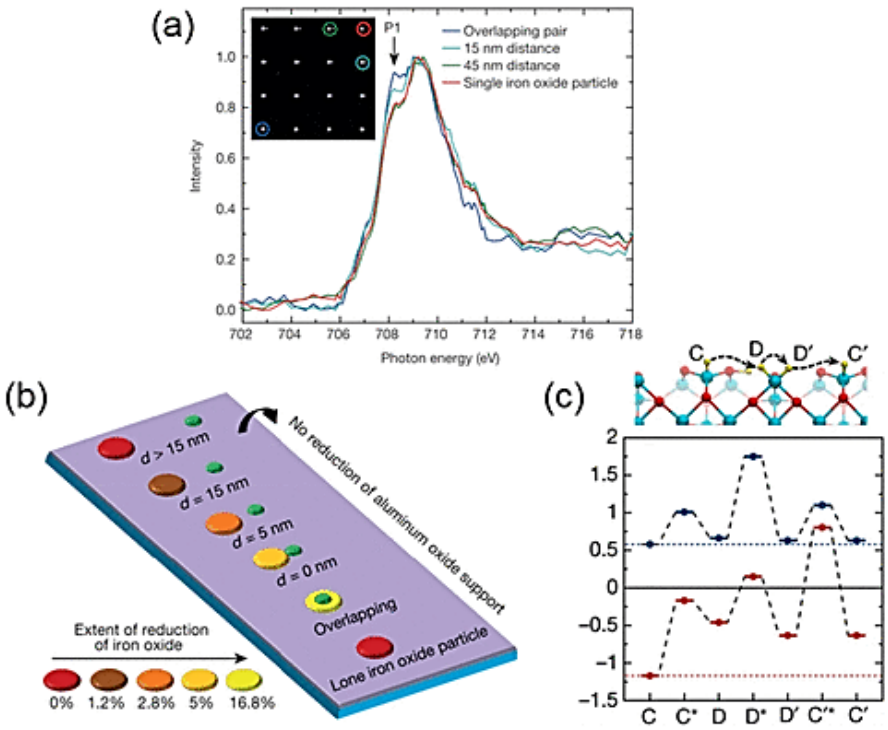

Fig 2.4: (a) XAS spectra at the Fe L3 edge during hydrogen dosage for three selected pairs (an overlapping pair and the pairs with interparticle distances of 15 and 45 nm) and a single iron oxide particle. (b) Schematic illustration of the distance-dependent hydrogen spillover on the Al2O3 support. (c) Hydride mobility on γ-Al2O3: maximum Eact = 1.63 eV (clean surface, red) and Eact = 1.15 eV (hydrated surface, blue) [135].

The hydrogen spillover on non-reducible oxides was also observed to take place on an alumina-silicate support material [160, 161]. Im et al. proposed that an alumina-silicate with an alternative arrangement of the Brønsted acid sites (BASs) could facilitate the hydrogen migration or spillover. The proton (H^+) migrates over the Si atom in the BAS which results in the generation of two defect sites, $[AlO_4]^-$ and $[AlO_4H_2]^+$ as shown in Fig 2.4 [160]. When the H^+ migrates among the two defect sites, the $[AlO_4H_2]^+$ defect site migrates to the trivalent Al site resulting in the spilled hydrogen radical $H^\bullet$ binding to the $[AlO_4]^-$ defect site forming a

$[AlO_4]^-$ $H^•$ species via a three-centered O-H-O bond. With the unpaired electron in the $[AlO_4]^-$ $H^•$ species, the O-H bond can transform into an O-H-O bond when the electron easily moves to the nearest BAS. The unpaired electron then eventually migrates and pairs with the $[AlO_4H_2]^+$ defect site at the external surface result in recombination, thereforeleaving molecules adsorbed at the external Al site to interact with the H• radical. Overall, the migration or hopping of the proton (H^+) occurs over the surface of OH groups (Figure 2.4).

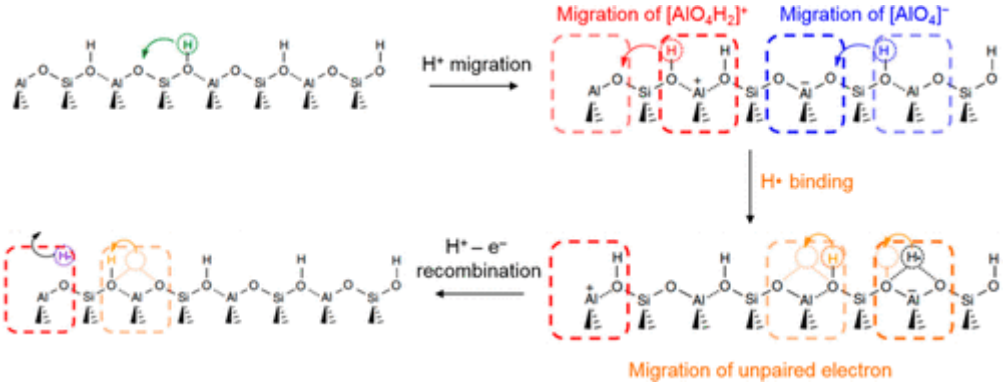

Figure 2.4: Schematic illustration of the hydrogen spillover mechanism on the surface of alumina-silicate [160].

2.2.3.3. Synergism effect in catalysis

Synergism has been often investigated in hydrodesulfurisation processes where non-additives increase the activity in mixtures of catalyst components. The first elaboration of this subject was addressed by Delmon who conducted a study on Co-Mo-S and postulating that this mixture consists of two phases [162, 163]. He proposed that hydrogen is activated on the Co_9S_8 phase of the catalyst and hydrogen spillover occurs between the CoS_2 and CoMoS phases as the sulfur compound is hydrogenated [164].

The proposed role of the Co_9S_8 phase in hydro-treating has not been shown to play any decisive role in the process [164–166]. Utilization of physical techniques such as EXAFS, NMR, and XRD has shown that the formation of Co–Mo–S phase has Co atoms with a coordination number of IV or V situated on the peripheries of MoS_2 microplates [167]. Despite its existence, the Co_9S_8 phase serves as a support phase for the Co-Mo-S phase rather than being involved in hydrogen spillover.

The mechanism of hydrodesulfurisation of thiophene was investigated by Rozanov et al., using TPR, TPD, and H–D methods on Co/Al_2O_3, Mo/Al_2O_3, and $CoMo/Al_2O_3$ catalysts [168]. TPR

spectra of thiophene, butanethiol and tetrahydrothiophene of the three catalysts proved to be very similar, however, the peaks of $CoMo/Al_2O_3$ were displaced towards the regions of low temperature which is attributed to the high rates of the reaction products. On the other hand, the main product peaks were not observed on the Co/Al_2O_3 catalyst. The Mo/Al_2O_3 showed strongly bound hydrogen on its surface, which was weakly bound on the surfaces of Co/Al_2O_3, and $CoMo/Al_2O_3$ catalysts. From the obtained results it can be confirmed that indeed thiophene and its derivatives are adsorbed on the MoS_2 anionic vacancies while cobalt sulphide activates the hydrogen. The hydrogen spillover occurs when Co and Mo centres belong to different phases or when they form a composition of a single phase for migration of hydrogen to occur.

Hydrogenation of CO in the mixture of a Ni/Al_2O_3 and a Pt/SiO_2 composite catalyst, showed that the CO was adsorbed on the Pt, whereas, hydrogen spillover effect took place with migration of hydrogen from Ni to Al_2O_3 [128]. Information attained from the TPD technique showed that the products desorbed from the H_2CO complex. The complex also has proven to exist on the surface of the support because when Pt/SiO_2 was removed the complex was found on the Al_2O_3 support surface.

2.2.3.4. Spillover to carbon or MOFs

The occurrence of hydrogen spillover over a defect-free carbon surface is thermodynamically unfavourable [169, 170]; however, when it occurs over a carbon surface with defects, hydrogen spillover is both theoretically and experimentally proven and realistic [158]. A study by Phaahlamohlaka et al. investigated the hydrogen spilllover on ruthenium loaded on cobalt encapsulated inside mesoporous hollow carbon spheres (Ru@MHCS@Co) and their findings showed that hydrogen spillover from Ru to Co through the carbon layer was possible when the Co oxide encapsulated became reduced [134]. Therefore, the carbon layer acted as the hydrogen spillover carrier between Ru the initiator and Co the acceptor. The mechanism over a carbon support material was reported by Nishihara et al. where the hydrogen molecule adsorbed on the metal surface in a dissociative manner and the dissociated hydrogen atoms moved over the carbon layer by forming C-H chemical bonds [171]. The evidence of spillover existence over the C–H bonds was observed from inelastic neutron scattering of hydrogen atoms where the spilled hydrogen atom caused dangling of the C–H bonds at the edge sites of carbon black surface to react as the hydrogen spillover took place from Pt to Ru metal [172].

Functionalised carbon materials containing oxygen groups also facilitated hydrogen spillover from metal to carbon. It is well known that oxygen functional groups are able to facilitate hydrogen spillover via direct adsorptions sites that form surface diffusion of hydrogen [173]. A study by Chung et al. elaborated the hydrogen spillover on Pd supported on oxygenated activated carbon. In their study, the increase in the content of oxygen functionality resulted in the enhancement of hydrogen spillover [174]. Psofogiannakis and Froudakis investigated Pt supported on a graphitic surface with epoxide hydroxyl groups for hydrogen spillover [170]. From their investigation, they observed that hydrogen atoms on the surface of the functionalized graphite migrated across low energy barriers, and they also noticed that the epoxide hydroxyl functional bridge groups on the carbon surface improved hydrogen spillover.

2.2.4. Application of the hydrogen spillover effect in catalysis

In catalysis, the presence of the spillover effect has been shown to improve the catalytic performance of a catalyst (activity, selectivity, and stability) [128, 147]. The application of hydrogen a spillover effect has been used in single atom catalysts, strong metal-support interfaces catalysts, encapsulated metal catalysts, promoter-metal separated catalysts, and more. The application of hydrogen spillover in some types of catalysts are listed as follows.

2.2.4.1. Single–atom catalysts

Single-atom catalysis is a new concept in catalysis and their use has been shown to improve the hydrogen spillover effect and the catalytic performance of catalysts [175, 176]. The ability of a catalyst to be in the form of a single atom enables higher utilization of the metal, thus resulting in better catalytic performance [177]. The effect of downsizing from metal nanoparticles into single atoms has been shown to enhance both catalytic and hydrogen spillover. An example of this phenomenon was reported from a study by Park et al., where Pt single atoms supported on mesoporous tungsten suboxide (Pt SA/m-WO_{3-x}) resulted in high hydrogen evolution in comparison to when the mesoporous tungsten supported Pt nanoparticles (Pt/m-WO_{3-x}) were used [178]. The reason for the high hydrogen evolution was due to the efficient and maximized interface between Pt and m-WO_{3-x} in a single atom catalyst and the shorter length for hydrogen diffusion to take place on the surface of Pt.

Unique adsorption and desorption properties have been observed on single-atom alloys (SAA) where an alloy containing a Pt group metal and another metal partnered in hydrogen spillover where one metal exhibited the splitting of a hydrogen molecule and the other metal acted as the active site for hydrogenation to take place. This unique adsorption and desorption properties

of SAA has been studied on a Pd_1/Cu (111) catalyst where Cu (111) was the active site for hydrogenation to occur and Pd was the active site for splitting hydrogen molecules. This was used in converting acetylene to ethene through a semi-hydrogenation selective reaction [136].

2.2.4.2. Strong support metal interface catalysts

The rate of hydrogenation reaction is highly dependent on the metal-support interface. Spillover takes place at the interface between the metal and support material [179]. Lachawiec et al. studied the effect of building carbon nanostructured bridges and their impact in hydrogen storage and they found that the carbon bridges served in improving the contact between a spillover source and a secondary receptor therefore increasing the capacity of hydrogen storage [180]. Furthermore, when the Ru nanoparticles and the carbon support material are in sandwich structure they displayed an intimate interfacial contact, for the hydrogenation of benzene [181].

Atomic layer deposition (ALD), a potent technique that creates thin films and highly dispersed nanoparticles, allowed for a controllable approach to precisely tailor the metal-oxide interface [182–186]. The ALD technique was used to show the advantages of increasing the interfacial sites between a metal and the support material. An example was done on using ALD to synthesise Al_2O_3 nanotubes - confined with Ni nanoparticles embedded within the cavities of the Al_2O_3 interior wall [187]. The presence of cavities created more Ni- Al_2O_3 interfacial sites, which had an enhanced hydrogen spillover effect, thus increasing the hydrogenation reaction rate. In addition, Pt nanoparticles also maximized their interfacial sites by atomically accurate Pt nanoparticles by thickness being synthesized and decorated or supported on ultrathin coating of ALD Al_2O_3 (Al-Pt-in-ANTs) [188]. Due to more Pt-Al_2O_3 interfacial sites that formed on the Al-Pt-in-ANTs catalyst, the hydrogenation reaction of 4-nitrophenol showed significantly greater activity than Pt nanoparticles contained in Al_2O_3 nanotubes (Pt-in-ANTs).

2.2.4.3. Metal particles encapsulated catalysts

Literature that has reported on the design of metal nanoparticles encapsulated inside a support material catalyst has provided new possibilities for using hydrogen spillover to improve catalytic efficiency [189–192]. For instance, Zhang et al. synthesised Co nanoparticles encapsulated inside porous carbon, Co@C [193]. The pore size of the porous carbon shell, which was 0.53 nm, allowed H_2 (0.29 nm) to access the Co sites for H_2 activation and then promoted hydrogen spillover to occur on the carbon surface where catalytic hydrogenation of the adsorbed N-heteroarenes could occur. The Co@C catalyst showed significantly higher

selective N-heteroarenes hydrogenation and also high durability of the catalyst to perform in an oxidative and sulphur-containing atmosphere. Phaahlamohlaka et al. incited hydrogen spillover in their CO hydrogenation (Fischer-Tropsch synthesis) study [134]. From their study, they showed that for spillover to occur the promoter does not have to be in intimate contact with the metal oxide. The study involved Ru as the reduction promoter and Co nanoparticles supported on mesoporous hollow carbon spheres (MHCS). The primary spillover effect was observed when both Ru and Co were placed in intimate contact, (Ru-Co/MHCS). For a secondary spillover effect to be observed, they exploited the hollow cavity of HCS, where the Co and Ru were separated by a carbon shell layer resulting in the Ru being encapsulated while the Co was loaded on the outer carbon shell of the MHCS (Co@MHCS@Ru). However, when comparing the two catalysts, more Co reducibility was observed in the primary spillover reaction, owing to the synergistic effects of intimate contact between Ru and Co.

A study conducted by Wang et al. investigated the catatylic performance of a sub-1 nm Pd nano – clusters confined within a solidalite (SOD) zeolite. The Pd@SOD, and Pd nanoparticles were loaded on the surface of SOD zeolite, Pd/SOD [131]. The comparison between the two catalysts was conducted in the acetylene hydrogenation reaction and both catalysts showed above 99% of acetylene conversion, whereas, the Pd@SOD catalyst showed a higher selectivity of ethylene compared to that of Pd/SOD catalyst, Fig 2.5 a. Furthermore, the Pd/SOD catalyst generated more ethane due to the acetylene molecules adsorbing directly on the exposed Pd and reacting with hydrogen. The generated intermediate species on the surface of Pd atoms desorbed with difficulty, thus, resulting in over-hydrogenation which produced ethane, Fig 2.5 b [193]. In contrast, over the Pd@SOD catalysts, the surface OH species of the SOD, which are produced from activated hydrogen formed in the encapsulated Pd atom sites, may react with the acetylene. This resulted in the production of ethylene with a high selectivity, Fig 2.5 b.

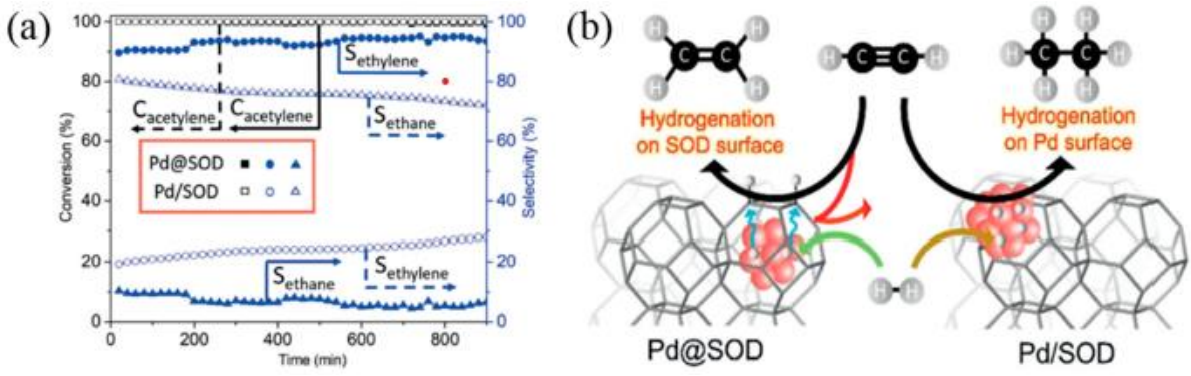

Figure 2.5: a) Catalytic activity and selectivity of Pd@SOD and Pd/SOD convertiion of acetylene to ethylene and ethane, respectively. b) In the hydrogenation of acetylene, metal catalysis and the spatial confinement effect of a small-pore zeolite effect [131].

2.2.4.4. Nanoscale separated bi-component catalysts

The behaviour of the hydrogen spillover and the catalytic performance of the catalysts in bi-component catalysts separated at the nanoscale depend on the distance between the components. Wei et al. studied the impact of nanoscale distance on hydrogen spillover and the catalytic performance of $Au/TiO_2/Pt$ sandwich nanostructures [194]. With the assistance of the in-situ surface-enhanced Raman spectroscopy measurements, the hydrogen spillover was observed. It was noted that the activated hydrogen species on the surface of Pt could be transferred to Au via the intermediate TiO_2 surface. The selectivity of catalytic hydrogenation could be tuned by varying the thickness of the TiO_2 layer, therefore, impacting the hydrogen spillover distance. The impact of increasing the distance of hydrogen spillover, resulted in significant improvement of NO_2 hydrogenation selectivity in the presence of N≡C groups.

The application of an ALD template-assisted strategy was used to synthesise a number of single-component TiO_2/Pt catalysts, in intimate contact with CoO_xPt/TiO_2, spatially separated $CoO_x/TiO_2/Pt$, and $CoO_x/TiO_2/Pt/TiO_2$ and $Al_2O_3/CoO_x/TiO_2/Pt$ for investigating the bi-component catalysts' synergistic spillover-promoting effect, Fig 2.6 a [195]. In $CoO_x/TiO_2/Pt$ catalyst, the proximity of CoO_x-Pt was controlled by varying the thickness layer of TiO_2. In the cinnamaldehyde (CALD) hydrogenation reaction, the CoO_xPt/TiO_2 catalysts exhibited enhanced selectivity towards the production of cinnamyl alcohol (82.1%) compared with TiO_2/Pt (16.2%), and $CoO_x/TiO_2/Pt$ (81.5%). By increasing the TiO_2 thickness to 40.5 nm in the CoO_x/TiO_2 (900)/Pt catalyst the authors showed that the catalyst exhibited similar selectivity to the $CoO_x/TiO_2/Pt$ catalyst. The Pt-TiO_2 interface regions were shown to be responsible for the conversion of CALD because when they were covered the catalytic activity decreased drastically. In this reaction, the Co_xO is the promoter and its coverage with a dense layer of Al_2O_3 did not negatively impact its promoter effect in facilitating the hydrogen spillover, Fig 2.6 b. Therefore, the enhanced selectivity to CALC was due to the Co_xO promoter effect through hydrogen spillover, which was not reliant on the Co_xO-Pt proximity, Fig 2.6 c.

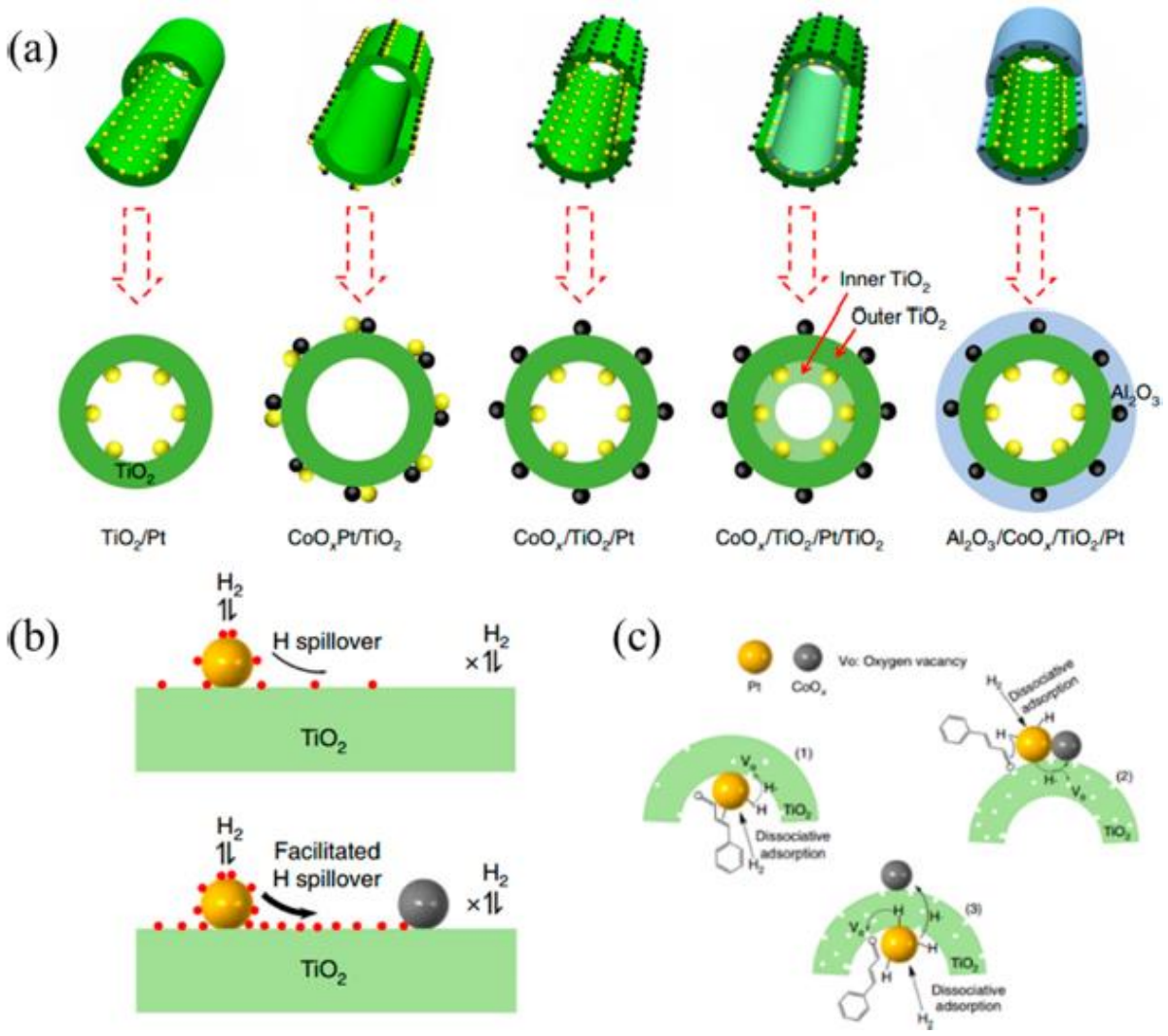

Figure 2.6: a) A schematic series illustration of the catalysts synthesised. b) TiO_2-supported Pt catalyst mechanism effect of Co_xO promoter, through hydrogen spillover. c) The enhanced selectivity mechanism of CALC in CALD hydrogenation reaction [195].

2.3 Reference

1. Kauffman GB (1999) The origins of heterogeneous catalysis by platinum: Johann Wolfgang Döbereiner's contributions. Enantiomer 4:609–619

2. Lesch J (2000) The German chemical industry in the twentieth century. Springer Science & Business Media

3. Madon RJ, Taylor WF (1981) Fischer-Tropsch synthesis on a precipitated iron catalyst. J Catal 69:32–43

4. Huff Jr GA, Satterfield CN (1984) Evidence for two chain growth probabilities on iron catalysts in the Fischer-Tropsch synthesis. J Catal 85:370–379

5. König L, Gaube J (1983) Fischer-Tropsch-Synthese. Neuere Untersuchungen und Entwicklungen. Chemie Ing Tech 55:14–22

6. Stranges AN (2007) A history of the fischer-tropsch synthesis in Germany 1926-45. Stud Surf Sci Catal 1–27

7. Flandrois S, Simon B (1999) Carbon materials for lithium-ion rechargeable batteries. Carbon N Y 37:165–180

8. Iglesia E, Reyes SC, Madon RJ (1991) Transport-enhanced α-olefin readsorption pathways in Ru-catalyzed hydrocarbon synthesis. J Catal 129:238–256

9. Masuku CM, Hildebrandt D, Glasser D (2011) The role of vapour–liquid equilibrium in Fischer–Tropsch product distribution. Chem Eng Sci 66:6254–6263

10. Fischer F, Pichler H (1939) Synthesis of paraffin from carbon monoxide and hydrogen.[Using CoThO/sub 2/--kieselguhr as catalyst]. Ber 72:

11. Sabatier P, Senderens JB (1902) New methane synthesis. CR Acad Sci Paris 134:514–516

12. Storch HH (1948) The Fischer-Tropsch and related processes for synthesis of hydrocarbons by hydrogenation of carbon monoxide. In: Advances in catalysis. Elsevier, pp 115–156

13. Van Der Laan GP, Beenackers AACM (1999) Kinetics and Selectivity of the Fischer-Tropsch Synthesis: A Literature Review. Catal Rev - Sci Eng 41:255–318. https://doi.org/10.1081/CR-100101170

14. Jager B (1997) Developments in Fischer-Tropsch technology. In: Studies in surface science and catalysis. Elsevier, pp 219–224

15. Madon RJ, Reyes SC, Iglesia E (1991) Primary and secondary reaction pathways in ruthenium-catalyzed hydrocarbon synthesis. J Phys Chem 95:7795–7804

16. Davis BH, Occelli ML (2016) Fischer-Tropsch synthesis, catalysts, and catalysis: advances and applications. CRC Press

17. Storch HH, Golumbic N, Anderson RB (1951) The Fischer-Tropsch and related syntheses: including a summary of theoretical and applied contact catalysis. Wiley

18. (2019) Synfuels China

19. Minchener AJ (2011) Coal-to-oil, gas and chemicals in China. IEA Clean Coal Cent

20. Moulijn JA, Makkee M, Van Diepen AE (2013) Chemical process technology. John Wiley & Sons

21. Rauch R, Kiennemann A, Sauciuc A (2013) Fischer-Tropsch synthesis to biofuels (BtL process). In: The Role of Catalysis for the Sustainable Production of Bio-fuels and Bio-chemicals. Elsevier, pp 397–443

22. Van de Loosdrecht J, Botes FG, Ciobica IM, et al (2013) Fischer-Tropsch synthesis: catalysts and chemistry. In: Comprehensive Inorganic Chemistry II: from elements to applications. Elsevier, pp 525–557

23. Maitlis PM, de Klerk A (2013) Greener Fischer-tropsch processes: for fuels and feedstocks. John Wiley & Sons

24. Spivey J, Dooley KM, Han Y-F (2014) Catalysis: Volume 26. Royal Society of Chemistry

25. Liu R, Qu F, Guo Y, et al (2014) Au@carbon yolk-shell nanostructures via one-step core-shell-shell template. Chem Commun 50:478–480. https://doi.org/10.1039/c3cc47050d

26. (2008) PetroSA. www.petrosa.co.za, retrieved 29 July 2008

27. (2016) www.hydrocarbons-technology.com/projects/oryx (Accessed: 20 January 2016). www.hydrocarbons-technology.com/projects/oryx (Accessed: 20 January%0A2016).

28. Leckel D (2009) Diesel production from Fischer− Tropsch: the past, the present, and new concepts. Energy & Fuels 23:2342–2358

29. Perego C, Bortolo R, Zennaro R (2009) Gas to liquids technologies for natural gas reserves valorization: The Eni experience. Catal Today 142:9–16

30. Nwaoha C, Wood DA (2014) A review of the utilization and monetization of Nigeria's natural gas resources: Current realities. J Nat Gas Sci Eng 18:412–432

31. Brady III RC, Pettit R (1980) Reactions of diazomethane on transition-metal surfaces and their relationship to the mechanism of the Fischer-Tropsch reaction. J Am Chem Soc 102:6181–6182

32. Davis BH (2003) Fischer-Tropsch synthesis: relationship between iron catalyst

composition and process variables. Catal Today 84:83–98

33. Morales F, Weckhuysen BM, Spivey JJ, Dooley KM (2006) Promotion effects in Co-based Fischer-Tropsch catalysis. Catalysis 19:1–40

34. Steynberg AP, Dry ME (2004) Studies in surface science and catalysis. In: Fischer-Tropsch technology. Elsevier, pp 1–63

35. Rodríguez-Reinoso F (1998) The role of carbon materials in heterogeneous catalysis. Carbon N Y 36:159–175. https://doi.org/10.1016/S0008-6223(97)00173-5

36. van Santen RA, Markvoort AJ, Ghouri MM, et al (2013) Monomer formation model versus chain growth model of the Fischer–Tropsch reaction. J Phys Chem C 117:4488–4504

37. Choi GN, Kramer SJ, Tam ST, Fox JM (1996) Design/economics of a natural gas based Fischer-Tropsch plant. In: Spring National Meeting. American Institute of Chemical Engineers Houston

38. Schulz H, Ramananda R, Elstner M (1970) Carbon-14 studies for the evaluation of the reaction mechanism of the Fischer--Tropsch synthesis. Erdoel Kohle, Erdgas, Petrochem Brennst-Chem 23:

39. Khodakov AY, Chu W, Fongarland P (2007) Advances in the development of novel cobalt Fischer-Tropsch catalysts for synthesis of long-chain hydrocarbons and clean fuels. Chem Rev 107:1692–1744. https://doi.org/10.1021/cr050972v

40. Espinoza RL, Steynberg AP, Jager B, Vosloo AC (1999) Low temperature Fischer-Tropsch synthesis from a Sasol perspective. Appl Catal A Gen 186:13–26. https://doi.org/10.1016/S0926-860X(99)00161-1

41. Gholami Z, Zabidi NAM, Gholami F, et al (2017) The influence of catalyst factors for sustainable production of hydrocarbons via Fischer-Tropsch synthesis. Rev Chem Eng 33:337–358

42. Ali S, Zabidi NAM, Subbarao D (2011) Correlation between Fischer-Tropsch catalytic activity and composition of catalysts. Chem Cent J 5:1–8

43. Liu Y, Fang K, Chen J, Sun Y (2007) Effect of pore size on the performance of mesoporous zirconia-supported cobalt Fischer–Tropsch catalysts. Green Chem 9:611–

615

44. Dalgleish T, Williams JMG., Golden A-MJ, et al (2007) [No Title]中国农业物种遗产的保护与利用研究. J Exp Psychol Gen 136:23–42. https://doi.org/https://doi.org/10.1007/s00393-018-0552-0

45. Pastuszak AW, Wang R (2015) Scholar (7). Asian J. Androl. 17:659–67

46. Zhao Y-L, Hu L, Grüner G, Stoddart JF (2008) A tunable photosensor. J Am Chem Soc 130:16996–17003

47. Xiong H, Jewell LL, Coville NJ (2015) Shaped carbons as supports for the catalytic conversion of syngas to clean fuels. ACS Catal 5:2640–2658

48. Dry ME (1981) The fischer-tropsch synthesis. Catal Sci Technol 1:159–255

49. Mardkhe MK, Keyvanloo K, Bartholomew CH, et al (2014) Acid site properties of thermally stable, silica-doped alumina as a function of silica/alumina ratio and calcination temperature. Appl Catal A Gen 482:16–23

50. An B, Cheng K, Wang C, et al (2016) Pyrolysis of metal–organic frameworks to Fe3O4@ Fe5C2 core–shell nanoparticles for Fischer–Tropsch synthesis. ACS Catal 6:3610–3618

51. Zhang Q, Kang J, Wang Y (2010) Development of novel catalysts for Fischer–Tropsch synthesis: tuning the product selectivity. ChemCatChem 2:1030–1058

52. de Smit E, Weckhuysen BM (2008) The renaissance of iron-based Fischer–Tropsch synthesis: on the multifaceted catalyst deactivation behaviour. Chem Soc Rev 37:2758–2781

53. Van der Laan GP, Beenackers AACM (2000) Intrinsic kinetics of the gas–solid Fischer–Tropsch and water gas shift reactions over a precipitated iron catalyst. Appl Catal A Gen 193:39–53

54. Wang Y-N, Ma W-P, Lu Y-J, et al (2003) Kinetics modelling of Fischer–Tropsch synthesis over an industrial Fe–Cu–K catalyst. Fuel 82:195–213

55. Van Der Laan GP, Beenackers A (1999) Kinetics and selectivity of the Fischer–Tropsch synthesis: a literature review. Catal Rev 41:255–318

56. Choudhury HA, Moholkar VS (2013) Synthesis of liquid hydrocarbons by Fischer–Tropsch process using industrial iron catalyst. Int J Innov Res Sci Eng Technol 2:3493–3499

57. Elbashir NO, Dutta P, Manivannan A, et al (2005) Impact of cobalt-based catalyst characteristics on the performance of conventional gas-phase and supercritical-phase Fischer-Tropsch synthesis. Appl Catal A Gen 285:169–180. https://doi.org/10.1016/j.apcata.2005.02.023

58. Gnanamani MK, Jacobs G, Shafer WD, Davis BH (2013) Fischer-Tropsch synthesis: Activity of metallic phases of cobalt supported on silica. Catal Today 215:13–17. https://doi.org/10.1016/j.cattod.2013.03.004

59. Iglesia E, Soled SL, Fiato RA, Via GH (1993) Bimetallic synergy in cobalt ruthenium Fischer-Tropsch synthesis catalysts. J Catal 143:345–368

60. Iglesia E (1997) Design, synthesis, and use of cobalt-based Fischer-Tropsch synthesis catalysts. Appl Catal A Gen 161:59–78. https://doi.org/10.1016/S0926-860X(97)00186-5

61. Iglesia E, Soled SL, Fiato RA (1992) Fischer-Tropsch synthesis on cobalt and ruthenium. Metal dispersion and support effects on reaction rate and selectivity. J Catal 137:212–224

62. Bukur DB, Lang X, Mukesh D, et al (1990) Binder/support effects on the activity and selectivity of iron catalysts in the Fischer-Tropsch synthesis. Ind Eng Chem Res 29:1588–1599

63. Regalbuto J (2016) Catalyst preparation: science and engineering. CRC press

64. Borg Ø, Eri S, Blekkan EA, et al (2007) Fischer–Tropsch synthesis over γ-alumina-supported cobalt catalysts: Effect of support variables. J Catal 248:89–100

65. Soled SL, Iglesia E, Fiato RA, et al (2003) Control of metal dispersion and structure by changes in the solid-state chemistry of supported cobalt Fischer–Tropsch catalysts. Top Catal 26:101–109

66. Reuel RC, Bartholomew CH (1984) The stoichiometries of H2 and CO adsorptions on cobalt: Effects of support and preparation. J Catal 85:63–77

67. Reuel RC, Bartholomew CH (1984) Effects of support and dispersion on the CO hydrogenation activity/selectivity properties of cobalt. J Catal 85:78–88

68. Li J, Coville NJ (1999) The effect of boron on the catalyst reducibility and activity of Co/TiO2Fischer-Tropsch catalysts. Appl Catal A Gen 181:201–208. https://doi.org/10.1016/S0926-860X(98)00434-7

69. Carballo JMG, Finocchio E, Garcia S, et al (2011) Support effects on the structure and performance of ruthenium catalysts for the Fischer–Tropsch synthesis. Catal Sci Technol 1:1013–1023

70. Mochizuki T, Hara T, Koizumi N, Yamada M (2007) Surface structure and Fischer–Tropsch synthesis activity of highly active Co/SiO2 catalysts prepared from the impregnating solution modified with some chelating agents. Appl Catal A Gen 317:97–104

71. Jacobs G, Chaney JA, Patterson PM, et al (2004) Fischer-Tropsch synthesis: Study of the promotion of Re on the reduction property of Co/Al2O3 catalysts by in situ EXAFS/XANES of Co K and Re LIII edges and XPS. Appl Catal A Gen 264:203–212. https://doi.org/10.1016/j.apcata.2003.12.049

72. Jongsomjit B, Panpranot J, Goodwin Jr JG (2003) Effect of zirconia-modified alumina on the properties of Co/γ-Al2O3 catalysts. J Catal 215:66–77

73. Fu T, Li Z (2015) Review of recent development in Co-based catalysts supported on carbon materials for Fischer-Tropsch synthesis. Chem Eng Sci 135:3–20. https://doi.org/10.1016/j.ces.2015.03.007

74. Akbarzadeh O, Mohd Zabidi NA, Abdul Wahab Y, et al (2018) Effect of cobalt catalyst confinement in carbon nanotubes support on fischer-tropsch synthesis performance. Symmetry (Basel) 10:572

75. Bahome MC, Jewell LL, Hildebrandt D, et al (2005) Fischer-Tropsch synthesis over iron catalysts supported on carbon nanotubes. Appl Catal A Gen 287:60–67. https://doi.org/10.1016/j.apcata.2005.03.029

76. Titirici M-M, Antonietti M, Baccile N (2008) Hydrothermal carbon from biomass: a comparison of the local structure from poly-to monosaccharides and pentoses/hexoses. Green Chem 10:1204–1212

77. Sharma R (2012) Enzyme Inhibition and Bioapplications IntechOpen. DOI 10:39273

78. Lam E, Luong JHT (2014) Carbon materials as catalyst supports and catalysts in the transformation of biomass to fuels and chemicals. ACS Catal 4:3393–3410

79. Liu J, Wickramaratne NP, Qiao SZ, Jaroniec M (2015) Molecular-based design and emerging applications of nanoporous carbon spheres. Nat Mater 14:763–774

80. Hu FP, Wang Z, Li Y, et al (2008) Improved performance of Pd electrocatalyst supported on ultrahigh surface area hollow carbon spheres for direct alcohol fuel cells. J Power Sources 177:61–66. https://doi.org/10.1016/j.jpowsour.2007.11.024

81. Liu R, Qu F, Guo Y, et al (2014) Au@carbon yolk-shell nanostructures via one-step core-shell-shell template. Chem Commun 50:478–480. https://doi.org/10.1039/c3cc47050d

82. de la Peña O'Shea VA, Álvarez-Galván MC, Campos-Martin JM, et al (2006) Surface and Structural Features of Co-Fe Oxide Nanoparticles Deposited on a Silica Substrate. Eur J Inorg Chem 2006:5057–5068

83. Ikeda S, Ishino S, Harada T, et al (2006) Ligand-free platinum nanoparticles encapsulated in a hollow porous carbon shell as a highly active heterogeneous hydrogenation catalyst. Angew Chemie - Int Ed 45:7063–7066. https://doi.org/10.1002/anie.200602700

84. Harada T, Ikeda S, Ng YH, et al (2008) Rhodium nanoparticle encapsulated in a porous carbon shell as an active heterogeneous catalyst for aromatic hydrogenation. Adv Funct Mater 18:2190–2196

85. Jacobs G, Das TK, Zhang Y, et al (2002) Fischer-Tropsch synthesis: Support, loading, and promoter effects on the reducibility of cobalt catalysts. Appl Catal A Gen 233:263–281. https://doi.org/10.1016/S0926-860X(02)00195-3

86. Beaumont SK, Alayoglu S, Specht C, et al (2014) Combining in situ NEXAFS spectroscopy and CO2methanation kinetics to study Pt and Co nanoparticle catalysts reveals key insights into the role of platinum in promoted cobalt catalysis. J Am Chem Soc 136:9898–9901. https://doi.org/10.1021/ja505286j

87. Sh Y, Noskov AS, Chem R (1990) Related content Procedures for making gaseous industrial waste safe

88. Shimura K, Miyazawa T, Hanaoka T, Hirata S (2013) Fischer–Tropsch synthesis over TiO2 supported cobalt catalyst: Effect of TiO2 crystal phase and metal ion loading. Appl Catal A Gen 460:8–14

89. Liu C, He Y, Wei L, et al (2018) Effect of TiO2 Surface Engineering on the Performance of Cobalt-Based Catalysts for Fischer–Tropsch Synthesis. Ind Eng Chem Res 58:1095–1104

90. Yu S-Y, Huang W-L, Ma Y, et al (2012) Characterization of cobalt-based catalyst supported on CeO2 nanocubes for Fischer-Tropsch synthesis. Integr Ferroelectr 138:32–37

91. Pan Z, Parvari M, Bukur DB (2014) Fischer–Tropsch Synthesis on Co/Al 2 O 3 Catalyst: Effect of Pretreatment Procedure. Top Catal 57:470–478

92. Garcilaso V, Barrientos J, Bobadilla LF, et al (2019) Promoting effect of CeO2, ZrO2 and Ce/Zr mixed oxides on Co/γ-Al2O3 catalyst for Fischer-Tropsch synthesis. Renew energy 132:1141–1150

93. Xu R, Hou C, Xia G, et al (2020) Effects of Ag promotion for Co / Al 2 O 3 catalyst in Fischer-Tropsch synthesis. Catal Today 342:111–114. https://doi.org/10.1016/j.cattod.2019.04.004

94. Huang X, Guo C, Zuo J, et al (2009) An assembly route to inorganic catalytic nanoreactors containing sub-10-nm gold nanoparticles with anti-aggregation properties. Small 5:361–365. https://doi.org/10.1002/smll.200800808

95. Mehrbod M, Martinelli M, Martino AG, et al (2019) Fischer-Tropsch synthesis: Direct cobalt nitrate reduction of promoted Co/TiO2 catalysts. Fuel 245:488–504

96. Nabaho D, Niemantsverdriet JWH, Claeys M, Steen E Van (2016) Hydrogen spillover in the Fischer – Tropsch synthesis : An analysis of platinum as a promoter for cobalt – alumina catalysts. Catal Today 261:17–27. https://doi.org/10.1016/j.cattod.2015.08.050

97. Mandal S, Maity S, Gupta PK, et al (2018) Synthesis of middle distillate through low temperature Fischer-Tropsch (LTFT) reaction over mesoporous SDA supported cobalt catalysts using syngas equivalent to coal gasification. Appl Catal A Gen 557:55–63

98. Jermwongratanachai T, Jacobs G, Shafer WD, et al (2014) Fischer – Tropsch synthesis : TPR and XANES analysis of the impact of simulated regeneration cycles on the

reducibility of Co / alumina catalysts with different promoters (Pt , Ru , Re , Ag , Au , Rh , Ir). Catal Today 228:15–21. https://doi.org/10.1016/j.cattod.2013.10.057

99. Shannon MD, Lok CM, Casci JL (2007) Imaging promoter atoms in Fischer–Tropsch cobalt catalysts by aberration-corrected scanning transmission electron microscopy. J Catal 249:41–51

100. Zsoldos Z, Hoffer T, Guczi L (1991) Structure and catalytic activity of alumina-supported platinum-cobalt bimetallic catalysts. 1. Characterization by x-ray photoelectron spectroscopy. J Phys Chem 95:798–801

101. Diehl F, Khodakov AY (2009) Promotion of cobalt Fischer-Tropsch catalysts with noble metals: a review. Oil Gas Sci Technol l'IFP 64:11–24

102. Tsubaki N, Sun S, Fujimoto K (2001) Different functions of the noble metals added to cobalt catalysts for Fischer–Tropsch synthesis. J Catal 199:236–246

103. Guczi L, Bazin D, Kovacs I, et al (2002) Structure of Pt–Co/Al 2 O 3 and Pt–Co/NaY bimetallic catalysts: characterization by in situ EXAFS, TPR, XPS and by activity in Co (carbon monoxide) hydrogenation. Top Catal 20:129–139

104. Guczi L, Schay Z, Stefler G, Mizukami F (1999) Bimetallic catalysis: CO hydrogenation over palladium–cobalt catalysts prepared by sol/gel method. J Mol Catal A Chem 141:177–185

105. Chu W, Chernavskii PA, Gengembre L, et al (2007) Cobalt species in promoted cobalt alumina-supported Fischer–Tropsch catalysts. J Catal 252:215–230

106. Nabaho D, Niemantsverdriet JWH, Claeys M, van Steen E (2016) Hydrogen spillover in the Fischer–Tropsch synthesis: An analysis of platinum as a promoter for cobalt–alumina catalysts. Catal Today 261:17–27

107. Wedepohl KH (1995) The composition of the continental crust. Geochim Cosmochim Acta 59:1217–1232

108. Barnes CE (2003) Inorganic Chemistry (Catherine E. Housecroft and Alan G. Sharpe). J Chem Educ 80:747

109. Basset JM, Besson B, Choplin A, et al (1984) Supported cluster and Mechanism of CO Reduction, in Fundam. Res. Homogeneous Catal. New-York

110. Ede SR, Nithiyanantham U, Kundu S (2014) Enhanced catalytic and SERS activities of CTAB stabilized interconnected osmium nanoclusters. Phys Chem Chem Phys 16:22723–22734. https://doi.org/10.1039/c4cp03068k

111. Nithiyanantham U, Ede SR, Kundu S (2014) Self-assembled wire-like and honeycomb-like osmium nanoclusters (NCs) in DNA with pronounced catalytic and SERS activities. J Mater Chem C 2:3782–3794

112. Anantharaj S, Nithiyanantham U, Ede SR, Kundu S (2014) Osmium organosol on DNA: application in catalytic hydrogenation reaction and in SERS studies. Ind Eng Chem Res 53:19228–19238

113. Boyd EP, Ketchum DR, Deng H, Shore SG (1997) Chemical vapor deposition of metallic thin films using homonuclear and heteronuclear metal carbonyls. Chem Mater 9:1154–1158

114. Odebunmi EO, Zhao Y, Knözinger H, et al (1984) CO hydrogenation with alumina-supported catalysts prepared from [Os(CO)5]. J Catal 86:95–107. https://doi.org/10.1016/0021-9517(84)90351-8

115. Bungane N, Welker C, van Steen E, Claeys M (2008) Fischer-Tropsch CO-hydrogenation on SiO2-supported osmium complexes. Zeitschrift für Naturforsch B 63:289–292

116. Molefe T, Forbes RP, Coville NJ (2021) Osmium@ Hollow carbon spheres as Fischer–Tropsch synthesis catalysts. Catal Letters 151:875–887

117. Lueking AD, Yang RT (2004) Hydrogen spillover to enhance hydrogen storage—study of the effect of carbon physicochemical properties. Appl Catal A Gen 265:259–268

118. Choi M, Yook S, Kim H (2015) Hydrogen spillover in encapsulated metal catalysts: new opportunities for designing advanced hydroprocessing catalysts. ChemCatChem 7:1048–1057

119. Srinivas ST, Rao PK (1994) Direct observation of hydrogen spillover on carbon-supported platinum and its influence on the hydrogenation of benzene. J Catal 148:470–477

120. Qian L, Cai W, Zhang L, et al (2015) The promotion effect of hydrogen spillover on CH4 reforming with CO2 over Rh/MCF catalysts. Appl Catal B Environ 164:168–175

121. Konda SK, Chen A (2016) Palladium based nanomaterials for enhanced hydrogen spillover and storage. Mater Today 19:100–108

122. Boudart M, Vannice MA, Benson JE (1969) Adlineation, portholes and spillover. Zeitschrift für Phys Chemie 64:171–177

123. Khoobiar S (1964) Particle to particle migration of hydrogen atoms on platinum—alumina catalysts from particle to neighboring particles. J Phys Chem 68:411–412

124. Benson JE, Kohn HW, Boudart M (1966) On the reduction of tungsten trioxide accelerated by platinum and water. J Catal 5:307–313

125. Delmon B, Pouchot MT (1966) LA CINETIQUE DES REACTIONS HETEROGENES. LA GERMINATION ET LAVANCEMENT DE LINTERFACE REACTIONNEL DANS LA REDUCTION DES OXYDES DE NICKEL ET DE CUIVRE PULVERULENTS. Bull Soc Chim Fr 2677

126. Sermon PA, Bond GC (1974) Hydrogen spillover. Catal Rev 8:211–239

127. Conner Jr WC, Pajonk GM, Teichner SJ (1986) Spillover of sorbed species. Adv Catal 34:1–79

128. Conner Jr WC, Falconer JL (1995) Spillover in heterogeneous catalysis. Chem Rev 95:759–788

129. D S (1931) Scholar (4). 167–168

130. Rozanov V V, Krylov O V (1997) Hydrogen spillover in heterogeneous catalysis. Russ Chem Rev 66:107

131. Wang S, Zhao Z, Chang X, et al (2019) Activation and Spillover of Hydrogen on Sub-1 nm Palladium Nanoclusters Confined within Sodalite Zeolite for the Semi-Hydrogenation of Alkynes. Angew Chemie Int Ed 58:7668–7672

132. Wang C, Guan E, Wang L, et al (2019) Product selectivity controlled by nanoporous environments in zeolite crystals enveloping rhodium nanoparticle catalysts for CO2 hydrogenation. J Am Chem Soc 141:8482–8488

133. Carter JL, Lucchesi PJ, Corneil P, et al (1965) Exchange of deuterium with the hydroxyl groups of alumina. J Phys Chem 69:3070–3074

134. Phaahlamohlaka TN, Kumi DO, Dlamini MW, et al (2017) Effects of Co and Ru

Intimacy in Fischer-Tropsch Catalysts Using Hollow Carbon Sphere Supports: Assessment of the Hydrogen Spillover Processes. ACS Catal 7:1568–1578. https://doi.org/10.1021/acscatal.6b03102

135. Karim W, Spreafico C, Kleibert A, et al (2017) Catalyst support effects on hydrogen spillover. Nature 541:68–71

136. Kyriakou G, Boucher MB, Jewell AD, et al (2012) Isolated metal atom geometries as a strategy for selective heterogeneous hydrogenations. Science (80-) 335:1209–1212

137. Lucci FR, Marcinkowski MD, Lawton TJ, Sykes ECH (2015) H2 activation and spillover on catalytically relevant Pt–Cu single atom alloys. J Phys Chem C 119:24351–24357

138. Lewis EA, Marcinkowski MD, Murphy CJ, et al (2014) Hydrogen dissociation, spillover, and desorption from Cu-supported Co nanoparticles. J Phys Chem Lett 5:3380–3385

139. Yin H, Zheng L-Q, Fang W, et al (2020) Nanometre-scale spectroscopic visualization of catalytic sites during a hydrogenation reaction on a Pd/Au bimetallic catalyst. Nat Catal 3:834–842

140. Bulavchenko OA, Gerasimov EY, Afonasenko TN (2018) Reduction of double manganese–cobalt oxides: in situ XRD and TPR study. Dalt Trans 47:17153–17159

141. Liu K, Yan P, Jiang H, et al (2019) Silver initiated hydrogen spillover on anatase TiO2 creates active sites for selective hydrodeoxygenation of guaiacol. J Catal 369:396–404

142. Yu Q, Yu T, Chen H, et al (2020) The effect of Al3+ coordination structure on the propane dehydrogenation activity of Pt/Ga/Al2O3 catalysts. J Energy Chem 41:93–99

143. Du C, Su J, Luo W, Cheng G (2014) Graphene supported Ag@ Co core–shell nanoparticles as efficient catalysts for hydrolytic dehydrogenation of amine boranes. J Mol Catal A Chem 383:38–45

144. Nabaho D, Niemantsverdriet JWH, Claeys M, van Steen E (2016) Hydrogen spillover in the Fischer–Tropsch synthesis: an analysis of gold as a promoter for cobalt–alumina catalysts. Catal Today 275:27–34

145. Yao Y, Goodman DW (2014) Direct evidence of hydrogen spillover from Ni to Cu on

Ni–Cu bimetallic catalysts. J Mol Catal A Chem 383:239–242

146. Yang F, Hu B, Xia W, et al (2018) On the nature of spillover hydrogen species on platinum/nitrogen-doped mesoporous carbon composites: A temperature-programmed nitrobenzene desorption study. J Catal 365:55–62

147. Pajonk GM (2000) Contribution of spillover effects to heterogeneous catalysis. Appl Catal A Gen 202:157–169

148. Rozanov V V (1997) Hydrogen spillover in heterogeneous catalysis. Russ Chem Rev 66:107. https://doi.org/10.1070/RC1997v066n02ABEH000308

149. Rodriguez NM, Baker RTK (1993) Interaction of hydrogen with metal sulfide catalysts-direct observation of spillover. J Catal 140:287–301

150. Baumgarten E, Lentes-Wagner C, Wagner R (1989) Hydrogen spillover through gas phase transport of hydrogen atoms. J Catal 117:533–541

151. Lenz DH, Conner WC (1988) Hydrogen spillover on silica: II. Kinetics and mechanism of the induction of catalytic activity. J Catal 112:116–125

152. Lapidus A, Krylova A, Kazanskii V, et al (1991) Hydrocarbon synthesis from carbon monoxide and hydrogen on impregnated cobalt catalysts Part I. Physico-chemical properties of 10% cobalt/alumina and 10% cobalt/silica. Appl Catal 73:65–81

153. Neikam WC, Vannice MA (1972) Hydrogen spillover in the Pt black/Ce Y zeolite/perylene system. J Catal 27:207–214

154. Lenz DH, Conner Jr WC, Fraissard JP (1989) Hydrogen spillover on silica III. Detection of spillover by proton NMR. J Catal 117:

155. Keren E, Soffer A (1977) Simultaneous electronic and ionic surface conduction of catalyst supports: A general mechanism for spillover: The role of water in the Pd-catalyzed hydrogenation of a carbon surface. J Catal 50:43–55

156. Levy R, Boudart M (1973) Mobility of solvated protons during catalytic reduction of WO3. Ind Chim BELGE-BELGISCHE Chem Ind 38:506

157. Levy RB, Boudart M (1974) The kinetics and mechanism of spillover. J Catal 32:304–314

158. Prins R (2012) Hydrogen spillover. Facts and fiction. Chem Rev 112:2714–2738

159. Prins R, Pálfi VK, Reiher M (2012) Hydrogen spillover to nonreducible supports. J Phys Chem C 116:14274–14283

160. Im J, Shin H, Jang H, et al (2014) Maximizing the catalytic function of hydrogen spillover in platinum-encapsulated aluminosilicates with controlled nanostructures. Nat Commun 5:1–8

161. Beaumont SK, Alayoglu S, Specht C, et al (2014) A nanoscale demonstration of hydrogen atom spillover and surface diffusion across silica using the kinetics of CO2 methanation catalyzed on spatially separate Pt and Co nanoparticles. Nano Lett 14:4792–4796

162. Delmon B (1980) A new concept explaining catalytic synergy between two solid phases. React Kinet Catal Lett 13:203–208

163. Delmon B (1979) A new hypothesis explaining synergy between two phases in heterogeneous catalysis the case of hydrodesulfurization catalysts. Bull des Soc Chim Belges 88:979–987

164. Karroua M, Matralis H, Grange P, Delmon B (1993) Synergy between" NiMoS" and Co9S8 in the hydrogenation of cyclohexene and hydrodesulfurization of thiophene. J Catal 139:371–374

165. Kim S Il, Woo SI (1991) Effect of sulfiding temperatures on the formation of sulfides ofMo/Al2O3 and CoMo/Al2O3. Appl Catal 74:109–123

166. Topsøe H, Clausen BS, Massoth FE (1996) Hydrotreating catalysis. In: Catalysis. Springer, pp 1–269

167. Inamura K, Prins R (1994) The role of Co in unsupported Co-Mo sulfides in the hydrodesulfurization of thiophene. J Catal 147:515–524

168. Rozanov V V, Yamin T, Krylov O V (1996) Heterogeneous catalytic processes on cobalt, molybdenum and cobalt-molybdenum catalysts studied by temperature-programmed desorption and temperature-programmed reaction. 27 HD exchange between adsorbed hydrogen and various coadsorbed molecules on the surf. Kinet i Katal 37:

169. Juarez-Mosqueda R, Mavrandonakis A, Kuc AB, et al (2015) Theoretical analysis of hydrogen spillover mechanism on carbon nanotubes. Front Chem 3:2

170. Psofogiannakis GM, Froudakis GE (2009) DFT study of hydrogen storage by spillover on graphite with oxygen surface groups. J Am Chem Soc 131:15133–15135

171. Nishihara H, Ittisanronnachai S, Itoi H, et al (2014) Experimental and theoretical studies of hydrogen/deuterium spillover on Pt-loaded zeolite-templated carbon. J Phys Chem C 118:9551–9559

172. Mitchell PCH, Ramirez-Cuesta AJ, Parker SF, et al (2003) Hydrogen spillover on carbon-supported metal catalysts studied by inelastic neutron scattering. Surface vibrational states and hydrogen riding modes. J Phys Chem B 107:6838–6845

173. Psofogiannakis GM, Froudakis GE (2011) Fundamental studies and perceptions on the spillover mechanism for hydrogen storage. Chem Commun 47:7933–7943

174. Chung T-Y, Tsao C-S, Tseng H-P, et al (2015) Effects of oxygen functional groups on the enhancement of the hydrogen spillover of Pd-doped activated carbon. J Colloid Interface Sci 441:98–105

175. Lei N, Zhao X, Hou B, et al (2019) Effective Hydrogenolysis of Glycerol to 1, 3-Propanediol over Metal-Acid Concerted Pt/WOx/Al2O3 Catalysts. ChemCatChem 11:3903–3912

176. Zhou M, Yang M, Yang X, et al (2020) On the mechanism of H2 activation over single-atom catalyst: An understanding of Pt1/WOx in the hydrogenolysis reaction. Chinese J Catal 41:524–532

177. Li Z, Ji S, Liu Y, et al (2019) Well-defined materials for heterogeneous catalysis: from nanoparticles to isolated single-atom sites. Chem Rev 120:623–682

178. Park J, Lee S, Kim H, et al (2019) Investigation of the support effect in atomically dispersed Pt on WO3− x for utilization of Pt in the hydrogen evolution reaction. Angew Chemie Int Ed 58:16038–16042

179. Baker LR, Kennedy G, Van Spronsen M, et al (2012) Furfuraldehyde hydrogenation on titanium oxide-supported platinum nanoparticles studied by sum frequency generation vibrational spectroscopy: acid–base catalysis explains the molecular origin of strong metal–support interactions. J Am Chem Soc 134:14208–14216

180. Lachawiec AJ, Qi G, Yang RT (2005) Hydrogen storage in nanostructured carbons by spillover: bridge-building enhancement. Langmuir 21:11418–11424

181. Su F, Lee FY, Lv L, et al (2007) Sandwiched ruthenium/carbon nanostructures for highly active heterogeneous hydrogenation. Adv Funct Mater 17:1926–1931

182. George SM (2010) Atomic layer deposition: an overview. Chem Rev 110:111–131

183. Zhang B, Qin Y (2018) Interface tailoring of heterogeneous catalysts by atomic layer deposition. ACS Catal 8:10064–10081

184. Zhang B, Guo X-W, Liang H, et al (2016) Tailoring Pt–Fe2O3 interfaces for selective reductive coupling reaction to synthesize imine. ACS Catal 6:6560–6566

185. Liang H, Zhang B, Ge H, et al (2017) Porous TiO2/Pt/TiO2 sandwich catalyst for highly selective semihydrogenation of alkyne to olefin. ACS Catal 7:6567–6572

186. Hu Q, Wang S, Gao Z, et al (2017) The precise decoration of Pt nanoparticles with Fe oxide by atomic layer deposition for the selective hydrogenation of cinnamaldehyde. Appl Catal B Environ 218:591–599

187. Gao Z, Dong M, Wang G, et al (2015) Multiply confined nickel nanocatalysts produced by atomic layer deposition for hydrogenation reactions. Angew Chemie 127:9134–9138

188. Wang M, Gao Z, Zhang B, et al (2016) Ultrathin coating of confined Pt nanocatalysts by atomic layer deposition for enhanced catalytic performance in hydrogenation reactions. Chem Eur J 22:8438–8443

189. Xue X, Liu J, Rao D, et al (2017) Double-active site synergistic catalysis in Ru–TiO 2 toward benzene hydrogenation to cyclohexene with largely enhanced selectivity. Catal Sci Technol 7:650–657

190. Jiao F, Guo H, Chai Y, et al (2018) Synergy between a sulfur-tolerant Pt/Al2O3@ sodalite core–shell catalyst and a CoMo/Al2O3 catalyst. J Catal 368:89–97

191. Tang T, Zhang L, Fu W, et al (2013) Design and synthesis of metal sulfide catalysts supported on zeolite nanofiber bundles with unprecedented hydrodesulfurization activities. J Am Chem Soc 135:11437–11440

192. Lee S, Lee K, Im J, et al (2015) Revisiting hydrogen spillover in Pt/LTA: Effects of physical diluents having different acid site distributions. J Catal 325:26–34

193. Zhang S, Gan J, Xia Z, et al (2020) Dual-active-sites design of Co@ C catalysts for ultrahigh selective hydrogenation of N-heteroarenes. Chem 6:2994–3006

194. Wei J, Qin S, Liu J, et al (2020) In situ Raman monitoring and manipulating of interfacial hydrogen spillover by precise fabrication of Au/TiO2/Pt sandwich structures. Angew Chemie Int Ed 59:10343–10347

195. Zhang J, Gao Z, Wang S, et al (2019) Origin of synergistic effects in bicomponent cobalt oxide-platinum catalysts for selective hydrogenation reaction. Nat Commun 10:1–8

Chapter 3

Note: the experimental methods and characterizations are covered in chapters 4-7 in a journal paper format.

3. Experimental Methods

3.1. Materials

All samples were of analytical grade and they were purchased from various sources. The cobalt nitrate hexahydrate (Aldrich), potassium osmate (Anglo American Research Laboratories, Johannesburg), ammonia solution (25%; Fluka), ethanol (98%; Merck), hexadecyltrimethylammonium bromide (CTAB; Aldrich), styrene (Aldrich),

polyvinylpyrollidone (PVP, MW 40 K, Aldrich) formaldehyde (37%; Aldrich), potassium persulfate (Eimer and Amend), hydrazine (35% Aldrich), and deionized water were used as received in the experiments.

3.2. Synthesis of Co@HCS and CoOs@HCS catalysts

3.2.1. Synthesis of polystyrene spheres (PSSs)

Styrene (8 mL) and polyvinylpyrollidone (PVP, 0.2 g) was dispersed and dissolved in a mixture of 200 mL ethanol and 50 mL deionized water by in a round bottom flask. The mixture was sonicated and stirred for 15 min. Thereafter, potassium persulfate (KPS, 0.3 g in 10 mL deionized water) was added to the prepared reaction mixture while stirring. The mixture was then heated at 80 ^{o}C for 24 hours. After the reaction the product was cooled, filtered and washed successively using deionized water. The obtained yield was ~ 6 g.

3.2.2. Synthesis of ammonium hexachloroosmate (IV), $(NH_4)_2OsCl_6$ [43]

Potassium osmate (5.00 g, 19.36 mmol) and 200 mL concentrated hydrochloric acid (35%) were placed in a 500 mL round bottom flask. The reaction mixture was stirred and heated at reflux for 2 h after which 50 mL 20% (w/v) ammonium chloride (186.9 mmol) solution was added, followed by cooling the mixture in ice. The solid that formed was isolated and washed with 80% ethanol to remove potassium. Potassium was removed because it could act as a promoter in FTS. The precipitate was recrystallized from hot concentrated hydrochloric acid. Ammonium hexachloroosmate (IV) ($(NH_4)_2OsCl_6$)) crystallised as deep red-brown cubes which were washed with absolute ethanol (8.1 g, 95% yield).

3.2.3. Synthesis of Co or CoOs on the polystyrene spheres (10% Co/PSSs or 10%Co 1% Os/PSSs)

PSSs (3g) were dissolved in a mixture of 75 mL deionized water and 25 ml ethanol. To this mixture cobalt nitrate hexahydrate (0.45 g) was added while stirring until the solution turned red. Thereafter, 10 mL of hydrazine (2M) was slowly added to the prepared solution dropwise, the solution was stirred for 12 hours to ensure complete deposition of Co nanoparticles onto the PSSs. The synthesis of the bimetallic CoOs/PSSs composite was prepared by adding both the cobalt (0.45 g) precursor and the ammonium hexachloroosmate (0.012 g) before the nanoparticle precipitation step.

3.2.4. Synthesis of Co or CoOs nanoparticles encapsulated inside hollow carbon spheres (10% Co@HCS and 10%Co 1% Os@HCS).

Co/PSSs or CoOs/PSSs (1 g) and ammonia solution (25%; 4 mL) were dissolved and dispersed in a mixture of 70 mL ethanol and 15 ml deionized water by sonication for 30 min. Subsequently, resorcinol (0.5 g), formaldehyde (0.5 mL) and hexadecyltrimethylammonium bromide (3 g) were added to make the resorcinol-formaldehyde core-shell structure. The solution was allowed to stir at room temperature for 24 hours. The formed resorcinol-formaldehyde (RF) core shell structure around Co/PSSs or CoOs/PSSs was filtered and washed successively with water and ethanol, followed by drying at 80 ^{o}C for 12 hours. Template removal and carbonization of the prepared composites was performed at a two-step horizontal chemical vapour deposition procedure, where template removal was done under a flow of nitrogen gas (50 ml/min) at 350 ^{o}C for 1 hour to decompose the PSSs. This was followed by the carbonization of the RF core shell structure under a flow of nitrogen gas (50 ml/min) at 600 ^{o}C for 2 hours. The resulting products were called Co@HCS and CoOs@HCS.

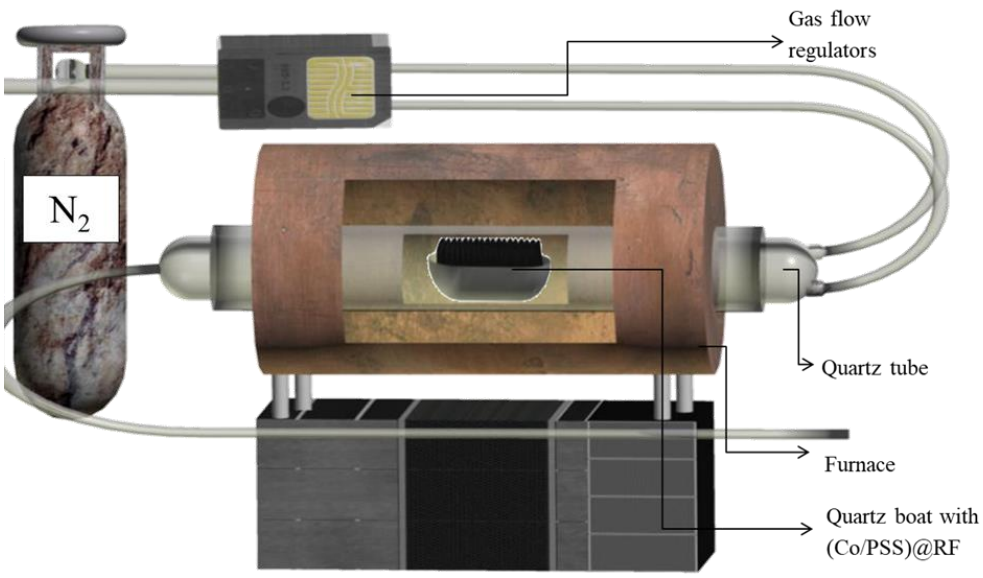

Figure 3.1: Schematic illustration of the chemical vapour deposition (CVD).

3.3. Synthesis of Os/(Co@HCS) catalyst

The Co@HCS (1.5 g) catalyst was dispersed in 250 mL of deionized water by sonication. To this mixture was added the Os (0.035 g) precursor and urea (0.4 g) followed by 30 min sonication. The mixture was then stirred at 95 ^{o}C in a round bottom flask for 12 hours. The product was collected by filtration and washing successively with water, followed by drying at 80 ^{o}C for 12 hours.

3.4. Synthesis of Co@HCS and CoPt@HCS catalysts

3.4.1. Synthesis of Co or CoPt on the polystyrene spheres (10Co/PSSs; 10CoxPt/PSSs) (x = 0.1, 0.5, 1)

PSSs (3 g) were added to a mixture of 75 mL deionized water and 25 ml ethanol. Cobalt nitrate hexahydrate (0.45 g) was added to this mixture while stirring, until the solution turned red. Thereafter, 10 mL of hydrazine (2M) was slowly added to the prepared solution dropwise, and the solution was stirred for 12 h to ensure complete deposition of Co nanoparticles onto the PSSs. The sample was called 10Co/PSS.

The bimetallic CoPt/PSSs composite was prepared by adding both the cobalt (0.45 g) precursor and the ammonium hexachloroplatinic acid hexahydrate (0.05M, 3 ml) onto the PSS, followed by hydrazine addition as stated above. This is expected to give a catalyst with a nominal Co/Pt mol or wt ratio of 10:1. The sample was called 10Co1Pt/PSS. Two further catalysts with ratios of Co:Pt of 20:1 and 100:1 (0.5Pt/10Co/PSS and 0.1Pt/10Co/PSS) were made by the same

method as above but using, 1.5 ml and 0.3 ml of ammonium hexachloroplatinic acid hexahydrate (0.05M), respectively.

3.4.2. Synthesis of Co or CoPt nanoparticles encapsulated inside hollow carbon spheres (10Co@HCS and 10CoxPt@HCS).

10Co/PSSs or 10Co1Pt/PSSs (1 g) and ammonia solution (25%; 4 mL) were added to a mixture of 70 mL ethanol and 15 ml deionized water and the mixture was sonicated for 30 min. Subsequently, resorcinol (0.5 g), formaldehyde (0.5 mL) and hexadecyltrimethylammonium bromide (3 g) were added to the above solution. The solution was allowed to stir at room temperature for 24 h. A resorcinol-formaldehyde (RF) core shell structure formed around the 10Co/PSSs or 10Co1Pt/PSSs and the material was filtered and washed successively with water and ethanol, followed by drying at 80 ^{o}C for 12 h. Template removal and carbonization of the prepared composites was performed using a two-step horizontal chemical vapour deposition procedure. Template removal was done under a flow of nitrogen gas (50 ml/min) at an isothermal temperature of 350 ^{o}C for 1 h to decompose and remove the PSSs. This was followed by carbonization of the RF core shell structure under a flow of nitrogen gas (50 ml/min) at 600 ^{o}C for 2 h. The resulting products were called 10Co@HCS and 10Co1Pt@HCS. The same method was used to make 10Co0.5Pt/PSS and 10Co0.1Pt/PSS samples to give the products 10Co0.5Pt@HCS and 10Co0.1Pt@HCS.

3.5. Synthesis of xPt/(Co@HCS) (x = 0.1, 0.5, 1) catalyst

To achieve a nominal 1 wt.% loading of Pt onto the surface of a 10Co@HCS catalyst (containing 10 wt%Co), platinum acetylacetonate [$Pt(acac)_2$, 97%] (13.5 mg) was added to the 10Co@HCS (0.4 g) catalyst and this was sonicated for 10 min to thoroughly dry-mix the two solids. The mixed composite was then transferred into a cylindrical quartz tube that was placed in a tubular horizontal furnace under a steady argon (50 ml/min) stream. The furnace was ramped to 100 ^{o}C and kept isothermal for 30 min to remove any moisture from the sample. The furnace was further ramped up to 350 ^{o}C at a heating rate of 2.5 ^{o}C/min and kept isothermal for 2 h. After 2 h, the reactor was left to cool down naturally to room temperature to produce 1Pt/(10Co@HCS) [1].

For the 0.5Pt/(10Co@HCS) and 0.1Pt/(10Co@HCS) products the same method as above was used, however, 6.75 mg and 1.35 mg of platinum acetylacetonate [Pt(acac)2, 97%] was used, respectively.

3.6. Catalyst characterization

TEM analysis was performed on a Tecnai spirit (T12) transmission electron microscope operating at 120 kV. The samples were dispersed in methanol by ultra-sonication and loaded onto a copper grid for TEM analysis. The particle size distribution of the materials formed was determined by counting at least 200 randomly selected particles per sample from different TEM images. Gaussian statistics yielded values for the average particle sizes. SEM analysis was performed on a FEI Nova Nanolab 600 FIB/SEM instrument operating at 30 kV. The samples were collected on a carbon tape and were coated with a gold−palladium layer prior to analysis.

N_2 adsorption−desorption experiments were conducted at −195 °C using a Micromeritics Tristar 3000 surface area and porosity analyser. Prior to an experiment, the sample was outgassed at 150 °C for 4 h under N_2 gas. The BET surface areas were obtained from adsorption data in a relative pressure range from 0.05 to 0.30. The total pore volumes were calculated from the amount of N_2 vapour adsorbed at a relative pressure of 0.99. The pore size distributions were evaluated from the desorption branches of the isotherms using the Barrett−Joyner−Halenda (BJH) method. The micropore surface area and volume were calculated using t-plot data.

TPR experiments were carried out with a Micromeritics Auto Chem II unit. The catalyst (approximately 50 mg) was placed in a tubular quartz reactor, fitted with a thermocouple for continuous temperature measurement. The reactor was heated in a furnace. Prior to the temperature-programmed reduction measurement, the calcined catalysts were flushed with high purity Ar gas at 200 °C for 30 min, to remove water and impurities, followed by cooling to ambient temperature. Then, the gas supply was switched to 5% H_2/Ar, and the temperature was raised at a rate of 10 °C min^{-1} from 50 to 850 °C. The gas flow rate through the reactor was controlled by three Brooks mass flow controllers and was kept constant at 50 $mL.min^{-1}$. The H_2 consumption (TCD signal) was recorded automatically. Pulse chemisorption was performed using the Micromeritics Auto Chem II instrument, to compute the number of active sites on the catalysts.

Ex-situ PXRD data were collected at the BXDS-WLE beamline at the Canadian Light Source using a photon energy of 15.144 keV and a 1k Mythen detector. The samples were measured in transmission geometry held inside Kapton capillaries. For all PXRD data presented, the crystalline phase identification was done using DIFFRAC.EVA (Version 4.2. Release 2016) using the crystallography open database (COD) (Release 2020). Phase analysis was done using the Rietveld method as implemented in Bruker AXS TOPAS software (Version 5, 2014).

Total scattering data were collected on the Canadian Light Source (CLS) Brockhouse high-energy wiggler beamline using a wavelength of $\lambda = 0.2081$ Å and a Perkin Elmer XRD1621 area detector placed 160 mm after the sample. The data were processed using GSAS-II software. The Qmax used to produce the pair distribution function (PDF) of the measured samples was 16 $Å^{-1}$. The instrumental resolution parameters Qdamp and Qbroad, as defined in PDFgui software, were determined by fitting a Ni powder standard measurement. Further data analysis was done using xPDFsuite. The PDF method is used to study short- and intermediate-range order in materials on the nanoscale. It is obtained from total scattering measurements using X-rays, neutrons, or electrons, and provides structural details when defects, disorder, or structural ambiguities obscure their elucidation directly in reciprocal space [2].

The catalyst (ca. 100 mg) was placed in a tubular quartz reactor. The sample was reduced at 350 °C for 2 h under a H_2 flow of 50 $mL.min^{-1}$. Before injection of the active gas, the sample was purged using helium gas at 350 °C for 1 h, followed by cooling to ambient conditions.

3.7. Fischer-Tropsch catalyst evaluation

3.7.1. Gases

All gases used in the Fischer-Tropsch synthesis (FTS) experiments were supplied by AFROX (African Oxygen) Ltd and were of ultra-high purity (UHP) grade. The synthesis gas (syngas) used comprised of a gas mixture of 60% hydrogen, 30% carbon monoxide and 10% nitrogen gas. This was done to ensure a H_2:CO ratio of approximately 2:1 in the feed gas. Nitrogen was used as an internal standard gas to ensure accurate mass balance calculations since it was non-reactive under FTS conditions. Hydrogen gas was used to reduce the catalyst prior to FTS reaction. Argon gas was used for the offline gas chromatography, whereas, air, nitrogen and hydrogen gasses were used for online gas chromatography analysis.

3.7.2. Reactor setup

The reactor setup for the FTS is shown schematically in Fig 3.2. The system consists of a fixed bed reactor, with all gases supplied from a gas cylinder with pressure regulators installed at different location, before and after the reactor. The pressure regulators ensured that the gas going into the reactor was of the required pressure at any given moment. The fixed bed reactor was made up of a 16 mm stainless steel tube with a frit inserted in the middle to serve as a support for the catalyst bed, Fig 3.3. A thermocouple was inserted into the catalyst bed for

temperature regulation, and Swagelok fittings were used for all gas line fittings. All gas lines used in the system consisted of a 1/4“ and 1/8“ stainless steel tubing. Quartz wool was placed on the frit and the catalyst rested on the wool (sieved by 150 µm sieve). Then the reactor was filled with steel balls so as to serve as a heat conductor to enable homogenous heat distribution in the reactor. All gas lines after the reactor were kept at 150 ℃. Two knockout pots or traps were installed after the reactor. The first knockout pot was maintained at 150 ℃ to serve as a wax trap and to avoid line blockage. The second knockout pot was set at room temperature to serve as a cold trap and used to trap water and high molecular weight hydrocarbons (i.e oil products). The gaseous products were directed to an online gas chromatograph equipped with a thermal conductivity detector (TCD) and the oil products were directed to an offline gas chromatograph equipped with a flame ionization detector (FID).

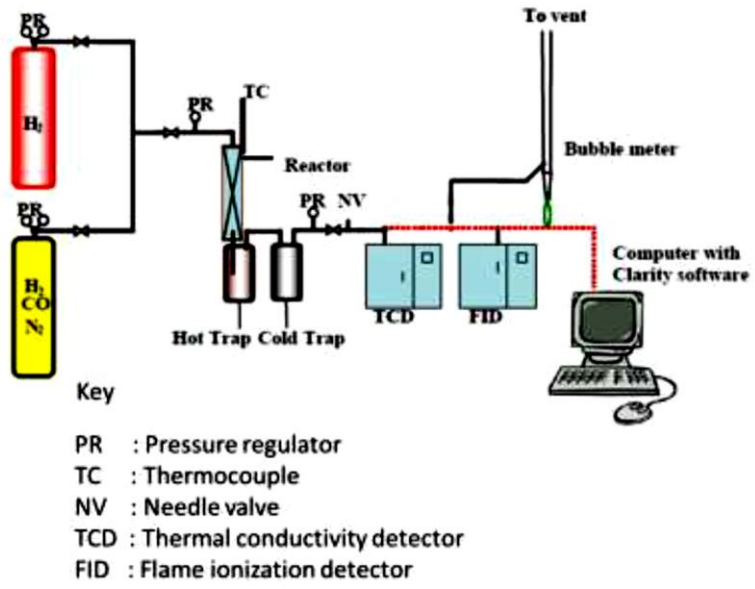

Figure 3. 1: Schematic illustration of the reactor and rig setup.

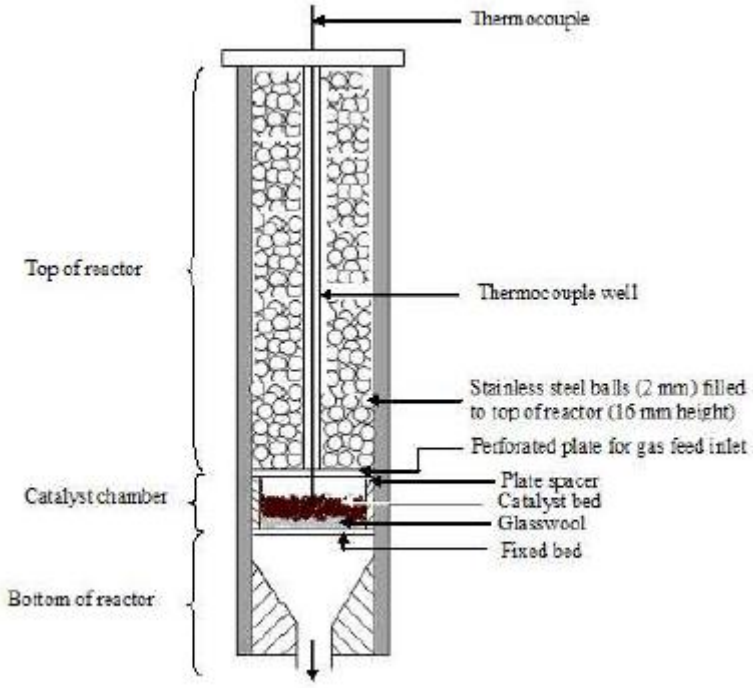

Figure 3. 2: Schematic diagram of a fixed bed reactor.

3.7.3. Catalytic experiments

The Fischer−Tropsch synthesis was performed in a fixed-bed micro-reactor. A gas cylinder containing a H2/CO/N2 mixture (~60/30/10 vol %; purity 99.99) was used to supply the reactant gas stream to the catalyst with a specific space velocity of 1800 mL h−1 g−1. N2 was used as an internal standard in order to ensure accurate mass balances. Catalyst (0.5 g, sieved through a 150 μm mesh, without pelletizing) was added to the reactor (resulting catalyst bed ~4 cm in length) and reduced in situ at 350 °C for 2 h under a stream of H2 (1.5 bar at 50 mL min−1). After reduction, the reactor temperature was decreased to ambient temperature under a hydrogen flow and then heated up to 220 °C under synthesis gas at a pressure of 10 bar. A hot trap placed immediately after the reactor was held at 150 °C in order to collect wax. A second trap kept at ambient temperature was used to collect the oil and water mixture. All gas lines after the reactor were kept at 100 °C. The flow was controlled using a metering valve and measured by a bubble meter. The product stream was analysed online using two gas chromatographs. A thermal conductivity detector (TCD), equipped with a Porapak Q (1.50 m × 3 mm) packed column, was used to analyse H2, N2, and CO, and a flame ionization detector (FID), equipped with a Porapak Q packed column, was used for the analysis of the hydrocarbons online. Gas chromatography calibration and product analysis have been described elsewhere.

3.7.4. Gas chromatography calibration and product analysis

Prior to all catalytic experiments, the gas chromatograph equipment was calibrated using two gases: syngas (29.2% CO, 10.3 of %N_2 and balance of H_2) and a six-gas mixture (2.5% CH_4, 0.2% C_2H_4, 0.5% C_2H_6, 10% CO, 5% CO_2 and balance of Ar). Typical GC traces are shown in Fig 3.4, Fig 3.5, Fig 3.6 and Fig 3.7. The data was recorded from the TCD and FID detectors during calibration and FT synthesis. The peak areas corresponding to each analyte detected during the calibration was used to compute the amount that corresponded with each analyte in the FT product stream. Clarity (v.2.5) software was used to compute the gas traces. GC conditions for analysis are summarized in Table 3.1

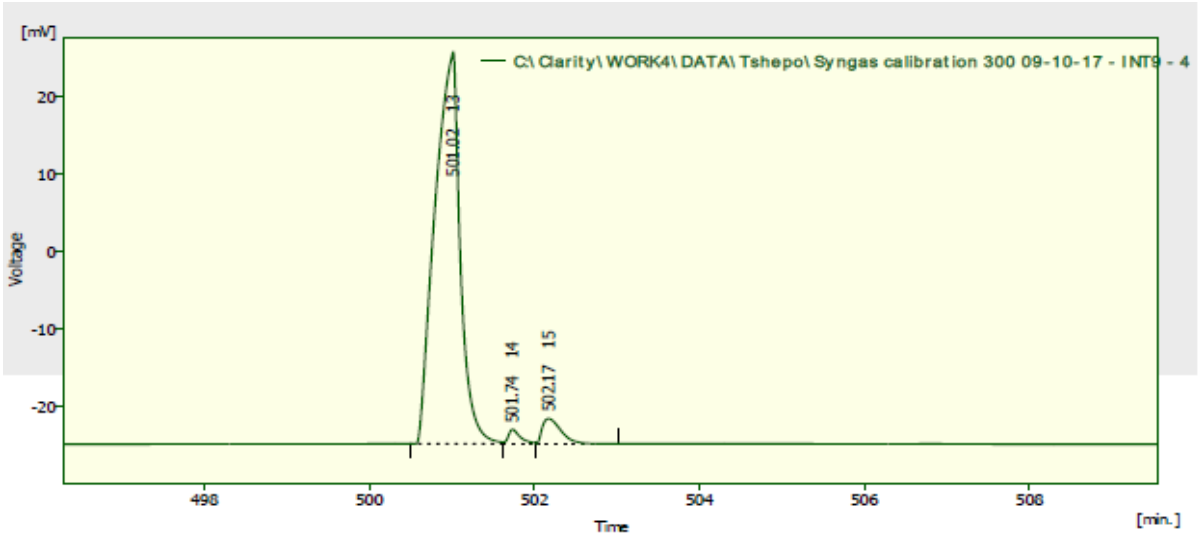

Figure 3. 3: A GC-TCD trace recorded during syngas calibration H_2 (60%), N_2 (10%) and CO (30%).

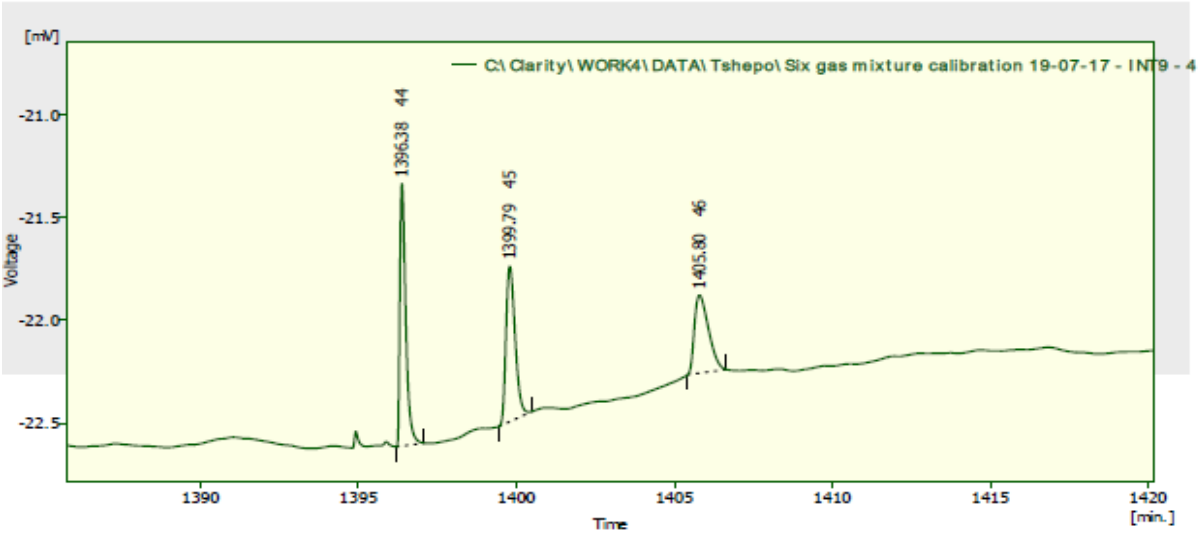

Figure 3. 4: A GC-FID trace recorded during the six-gas mixture calibration

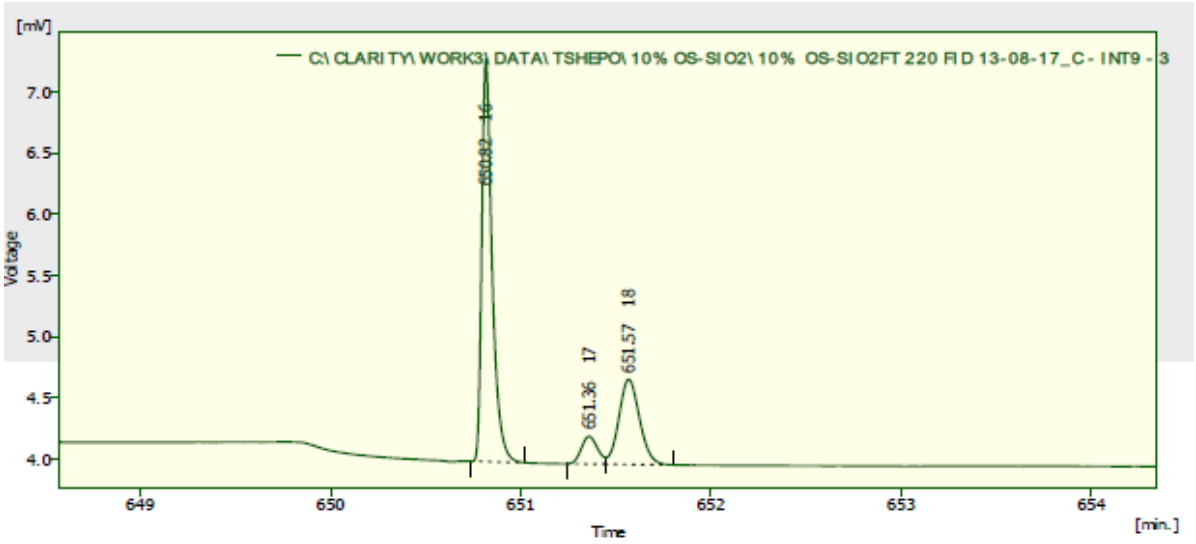

Figure 3. 5: A GC-FID trace recorded during a typical FTS run.

Table 3. 1: Specification of the GC operating conditions

Gas chromatograph (on-line)	
Make	PYE Unicam (Series 204)
Detector	Thermal conductivity detector (TCD)
Detector temperature	220 ^{0}C
Column type	Packed, stainless steel, 2 m x 2.2 mm, O.D. = 1/8”
Stationary phase	Carbosieve, S-II, 60-80 mesh
Sample valve temperature	150 ^{0}C
Carrier gas	Ar, 20 ml/min
Oven temperature	250 ^{0}C (isothermal)
Gas chromatography (on-line)	
Make	Hewlett Packard 5890
Detector	Flame ionization detector (FID)
Detector temperature	220 ^{0}C
Column type	Packed, stainless steel, 2 m x 2.2 mm, O.D. = 1/8”
Stationary phase	ZB-5, 80/100 mesh

Sample valve temperature	150 ^{0}C
Carrier gas	Ar, 20 ml/min
Oven temperature	250 ^{0}C (isothermal)
Gas chromatography (off-line)	
Make	Varian 3700
Detector	Flame ionization detector (FID)
Detector temperature	350 ^{0}C
Column type	30 m x 5 μFT, O.D. = 0.53 mm
Stationary phase	ZB-1
Sample valve temperature	250 ^{0}C
Carrier gas	N_2, 20 ml/min
Oven temperature	Heat to 300 ^{0}C (ramping rate: 10 ^{0}C/min), and hold at temperature for 3 hours

3.7. Mass balance calculations

Before carrying out the FTS, the amount of syngas in the inlet stream was determined as outlined in section 3.4.4. The mass balance calculation performed were similar to those performed by Bahome, Hexana, Phadi and Price [3–6]. Mass balance calculations were performed based on the carbon content under steady state conditions for about 50 hours. During FTS the amount of unreacted syngas and the low boiling products from the outlet stream were analysed on-line.

The percentage of CO converted was calculated as follows:

$$\%CO = \left\{\frac{CO_{in} - CO_{out} \times \left[\frac{N_{2,in}}{N_{2,out}}\right]}{CO_{in}}\right\} \times 100\% \qquad \text{Eqn 3.1}$$

Where Co_{in} and $N_{2,in}$ are the calibration peak areas for CO and N_2 from the inlet stream, respectively, and Co_{out} and $N_{2,out}$ are the peak areas measured for CO and N_2 during FTS as outlet stream, respectively.

The outlet flow rate (F_{out}) from the reactor was measured using a bubble soap flow meter. From this the calculation of the inlet feed flow rate (F_{in}) was calculated. A gas contraction factor was used;

$$F_{in} = \left\{\frac{N_{2,out}}{N_{2,in}}\right\} F_{out}$$ Eqn 3.2

where $X_{N_{2,in}}$ and $X_{N_{2,out}}$ are the mole fraction of N_2 in the six gas mixture (calibration gas) and the FTS run, respectively. F_{in} and F_{out} are the total feed inlet and exit flow rates, respectively, and expressed in mols/s.

The total number of carbon moles in the feed stream in the entire mass balance period was calculated as follows;

$$N_{C,in} = F_{in}.t.X_{CO,in}$$ Eqn 3.3

Where - $N_{c,in}$ are the total number of moles fed into the reactor

F_{in} is the total feed flow rate in mol/s

t is the total mass balance time

$X_{CO,in}$ is the mole fraction of CO in the feed gas

The mass balance calculations were accepted within the range 100 $\pm$ 5% in each case and calculated as follows;

$$\%\ carbon\ balance = \left\{\frac{N_{C,out}}{N_{C,in}}\right\} \times 100$$ Eqn 3.4

For the mass balance to be correct, $N_{C,in}$ should be equal or approximately equal to $N_{C,out}$.

The rate of CO conversion during the steady state period was computed as follows;

$$-r_{CO} = \frac{F_{CO,in} - F_{CO,out}}{m_{cat}}$$ Eqn 3.5

where $F_{CO,in}$ and $F_{CO,out}$ are the molar flow rates (mol/min) of CO fed into the reactor or exiting the reactor, respectively, r_{CO} is the rate of CO conversion ($mol.min^{-1}.g_{catalyst}^{-1}$), and m_{cat} is the mass (g) of the catalyst.

From the gaseous products, the selectivity of individual hydrocarbons were calculated as follows;

$$Sel(\theta) = \frac{[n_C]_\theta}{-r_{CO}.t.m_{cat}}$$ Eqn 3.6

where $[n_c]_\Theta$ are the moles of carbon in product θ.

The selectivity of the heavy hydrocarbons (C_{5+}) was calculated based on the moles of carbon as follows;

$$S_{5+} = 100 - \Sigma(S_{CH_4} + S_{C_2} + S_{C_3} + S_{C_4}) \quad \text{Eqn 3.7}$$

where S_{CH_4} is the selectivity for methane, and S_{C_2}, S_{C_3}, S_{C_4} are the selectivity's for hydrocarbons ranging from C_2 to C_4 products.

3.8. Reference

1. Mohamed R, Binninger T, Kooyman PJ, et al (2018) Facile deposition of Pt nanoparticles on Sb-doped SnO 2 support with outstanding active surface area for the oxygen reduction reaction. Catal Sci Technol 8:2672–2685
2. Terban MW, Billinge SJL (2021) Structural analysis of molecular materials using the pair distribution function. Chem Rev 122:1208–1272
3. Price JG (1994) An Investigation Into Novel Bimetallic Catalysts for Use in the Fischer-Tropsch Reaction
4. Bahome MC (2007) Synthesis and use of carbon nanotubes as a support for the Fischer-Tropsch Synthesis
5. Phadi TT (2012) Titanium dioxide-carbon spheres composites for use as supports in cobalt Fischer-Tropsch synthesis
6. Hexana WM (2009) A Systematic Study of the Effect of Chemical Propmotors on the Precipitated Fe-based Fischer-Tropsch Synthesis Catalyst

Chapter 4

Fischer-Tropsch synthesis: osmium promoted Co@HCS catalysts

Chapter published:

4.1. Introduction

Fischer-Tropsch synthesis (FTS) is a promising route to produce synthetic lubricants, synthetic fuels, and importantly aviation fuels [1], from a variety of carbon-containing feedstocks such as coal, oil and natural gas, but also importantly, from biomass. It is thus a process that can be harnessed as an important sustainable method for making multiple carbon containing compounds for humankind at an industrial scale [2,3]. In the FTS process, syngas ($CO_{(g)}$ and $H_{2(g)}$), is catalytically transformed into a broad range of hydrocarbons through a surface polymerisation reaction [4,5]. Cobalt FT catalysts are preferred for making aviation fuels due to their high intrinsic activity, higher per-pass conversion, selectivity for heavy hydrocarbon products, and longer lifetimes than Fe catalysts for the conversion of syngas derived from carbon sources with a 1:2 $CO:H_2$ gas ratio [6]. The Co catalyst required to make non-oxygenate products is metallic Co. The face-centred cubic (fcc) crystal structure and the less common hexagonal close-packed (hcp) crystal structure are the two different crystalline forms in which metallic Co can be found [7].

Typically, the dispersion of an FT catalyst on support is performed to improve its catalytic performance. In FTS, support metal oxides such as Al_2O_3, TiO_2, SiO_2 and MgO have previously been utilized for FT catalysts [8]. The use of these support materials does produce a required strong metal-support interaction (SMSI) with the catalyst, but it also forms irreducible compounds that are not active in the FT reaction [9–15]. The use of a carbon-based support material provides an approach to overcome the problems related to supports that show SMSIs because carbon-based supports show a poorer interaction with metals [16]. The carbons can have many shapes and sizes and a wide range of these carbons have been used to support Co for use in the FTS reaction [17–19]. Hollow carbon spheres (HCSs) are one of these carbons. This carbon allows for metals to be placed both inside and outside the HCS and thus allows the study of many typical properties associated with catalysts such as spillover effects,

diffusion and catalyst agglomeration [20]. Indeed, the HCSs can also be used as a nanoreactor when the active metal phase is placed inside the carbon shell [16,21,22].

To make the Co sites more active, metals like Ru, Pt, and Re are typically used to promote cobalt FTS catalysts [23–25]. One role of a promoter is to enhance the reducibility of a catalyst and this occurs by means of a spillover effect in which the promoter is first reduced, and then H atoms are transferred from the reduced promoter atoms to the catalyst [26]. Two types of hydrogen spillover processes can be envisaged. The first of these is a primary hydrogen spillover process, where the promoter (i.e., initiator) is in direct contact with the acceptor (e.g., Co_3O_4) and dissociated H atoms can migrate to the acceptor from the initiator directly. In the second type, a secondary hydrogen spillover process, the initiator and acceptor materials are separated by a distance (in this study, a carbon shell) and the atomic H migrates from the initiator to the acceptor through the carrier (i.e., a carbon catalyst support). An example of the two processes is shown in Scheme 1 where a HCS shell is shown to separate the Co from a promoter (Os). The reduction promoter for the metal oxide (e.g. Co_3O_4) can also play a role in the reaction selectivity [27,28]. Some studies to explore the spillover effect using HCSs have been reported. Thus, work performed by Phaahlamohlaka et al. investigated hydrogen spillover effects of Ru promoted Co FT catalysts using a mesoporous hollow carbon sphere (MHCS) as a physical barrier to spillover [29]. While the acceptor (Co_3O_4) was loaded onto the MHCS (with and without Ru), the initiator/promoter (Ru) was loaded both inside and outside of the MHCS [29]. The use of the two catalysts, CoRu/MHCS and Co(Ru@MHCS), made it possible to separate the processes of primary and secondary spillover, and indicated the importance of the primary spillover effect in FT catalysts.

Os and Ru both belong to the same Periodic Table group and share many similar chemical characteristics. While many FTS studies have been performed using Ru as a promoter in FTS [30], there are no studies on the use of Os as a promoter. Importantly, Os ions, like Ru ions, can be reduced below the Co FTS reaction temperature [31]. Furthermore, since Ru is a known FT catalyst while Os has shown poor FTS behaviour (it produces mainly CH_4) [32], the use of Os should allow for an evaluation of the effect of Os on both the reducibility of Co and its effect on product selectivity.

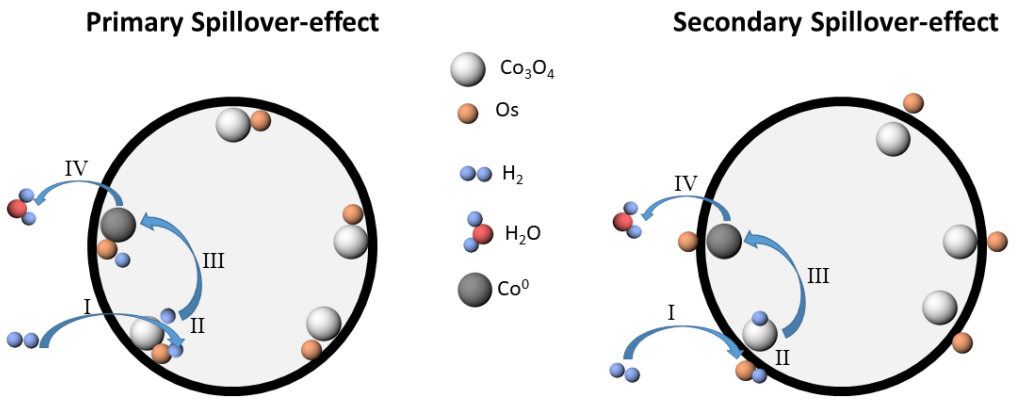

Scheme 1: Schematic illustration of the primary and secondary spillover effects using HCS support (I, hydrogen dissociation; II hydrogen adsorption; III, hydrogen transfer from initiator to acceptor or spillover; and IV, Co reduction and water removal).

In this study the synthesis and use of Os nanoparticles as a promoter supported on/in a Co@HCS catalyst for use in FTS is reported. The hollow morphology of the HCSs was used to investigate how the location of the Os nanoparticles in relation to the Co_3O_4 nanoparticles affected the reduction behaviour and activity/selectivity of the Co FT catalyst.

4.2. Experimental

4.2.1 Materials

All reagents used for the syntheses described here were of analytical grade and were purchased from various chemical suppliers. All reagents used in these syntheses were used as received. This includes the following chemical reagents: cobalt nitrate hexahydrate ($Co(NO_3)_2.6H_2O$) (Aldrich), potassium osmate ($K_2[OsO_2(OH)_2]$) (Anglo American Research Laboratories, Johannesburg), ammonia solution (25%; Fluka), ethanol (98%; Merck), hexadecyltrimethylammonium bromide ($C_{19}H_{42}BrN$) (CTAB; Aldrich), styrene (Aldrich), polyvinylpyrrolidone ($(C_6H_9NO)_n$) (PVP, MW 40 K, Aldrich) formaldehyde (37%; Aldrich), potassium persulfate ($K_2S_2O_8$) (Eimer and Amend), hydrazine (35% Aldrich), and deionized water.

4.2.2 Synthesis of Co@HCS and CoOs@HCS catalysts

4.2.2.1 Synthesis of Synthesis of polystyrene spheres (PSSs)

Styrene (8 mL) and polyvinylpyrrolidone (PVP, 0.2 g) were added to a mixture comprised of 200 mL of ethanol and 50 mL of deionized water contained in a round bottom flask [33]. The mixture was sonicated and stirred for 15 min. Thereafter, potassium persulfate (KPS, 0.3 g in

10 mL deionized water) was added to the prepared reaction mixture while stirring. The mixture was then heated at 80 ^{o}C for 24 h. After the reaction, the product was cooled, filtered, and washed successively using deionized water [33]. The product (PSSs), produced in high yield, was then dried in an oven at 60 °C for 12 h, crushed with a mortar and pestle and stored in a glass sample vial.

4.2.2.2 Synthesis of ammonium hexachloroosmate (IV), $(NH_4)_2OsCl_6$

Potassium osmate (5.00 g, 19.36 mmol) and 200 mL of concentrated hydrochloric acid (35%) were added to a 500 mL round bottom flask. The reaction mixture was stirred and heated at reflux for 2 h after which 50 mL 20% (w/v) ammonium chloride (186.9 mmol) solution was added, followed by cooling of the mixture in ice. The solid which formed was isolated and washed with 80% ethanol to remove residual potassium ions. Potassium ions were removed because they could act as a promoter in FTS. The precipitate was recrystallized from hot concentrated hydrochloric acid. Ammonium hexachloroosmate (IV) ($(NH_4)_2OsCl_6$) crystallised as red-brown cubes which were washed with absolute ethanol (8.1 g, 95% yield) [34].

4.2.2.3 Synthesis of Co or OsCo on the polystyrene spheres (Co/PSSs or xOsCo/PSSs)

PSSs (3 g) were added to a mixture of 75 mL deionized water and 25 ml ethanol. To this mixture was added cobalt nitrate hexahydrate (0.45 g), while stirring, until the solution turned red. Thereafter, 10 mL of hydrazine (2M) was slowly added dropwise to the prepared solution and the solution was then stirred for 12 hours to ensure complete deposition of Co nanoparticles onto the PSSs to give Co/PSSs. The synthesis of the bimetallic xOsCo/PSSs composite was achieved by adding both the Co (0.45 g) precursor and the ammonium hexachloroosmate (0.012 g, Os = 0.1 wt%; 0.035 g, Os = 0.5 wt%; 0.069 g, Os = 1 wt%) before the nanoparticle precipitation step to give xOsCo/PSSs (Co = 10% Co; xOs with x = 0.1%, 0.5% 1.0% Os).

4.2.2.4 Synthesis of Co or OsCo nanoparticles encapsulated inside hollow carbon spheres (Co@HCS and xOsCo@HCS)

The Co/PSSs or OsCo/PSSs (Co = 10% Co; Os = 0.1%, 0.5% 1.0%) (1 g) and ammonia solution (25%; 4 mL) were dissolved/dispersed in a mixture of 70 mL ethanol and 15 ml deionized water by sonication for 30 min. Subsequently, resorcinol (0.5 g), formaldehyde (0.5 mL) and hexadecyltrimethylammonium bromide (3 g) were added to make the resorcinol-formaldehyde core-shell structure. The solution was allowed to stir at room temperature for 24 h. The formed resorcinol-formaldehyde (RF) core shell structure around the Co/PSSs or OsCo/PSSs was filtered and washed successively with water and ethanol, followed by drying at 80 ^{o}C for 12 h. Template removal and carbonization of the prepared composites were performed in a two-step horizontal chemical vapour deposition apparatus. The template removal was done under a flow of nitrogen gas (50 ml/min) at 350 ^{o}C for 1 h to decompose the PSSs. This was followed by the carbonization of the RF core shell structure under a flow of nitrogen gas (50 ml/min) at 600 ^{o}C for 2 h. The resulting products were called Co@HCS and xOsCo@HCS (Co = 10% Co; xOs with x = 0.1%, 0.5% 1.0% Os).

4.2.2.5 Synthesis of xOs/(Co@HCS) catalyst

The Co@HCS (1.5 g) catalyst was dispersed in 250 mL of deionized water by sonication. To this mixture was added the Os salt precursor (0.012 g, Os = 0.1 wt%; 0.035 g, Os = 0.5 wt%; 0.069 g, Os = 1 wt%) and urea (0.4 g) followed by 30 min sonication. The mixture was then stirred at 95 ^{o}C in a round bottom flask for 12 h. The product xOs/(Co@HCS) was collected after filtration and washing with water, followed by drying at 80 ^{o}C for 12 h.

4.2.3 Catalyst characterization

TEM analysis was performed on a Tecnai spirit (T12) transmission electron microscope operating at 120 kV. The samples were dispersed in methanol by ultra-sonication and loaded

onto a copper grid for TEM analysis. The particle size distribution of the materials formed was determined by counting at least 200 randomly selected particles per sample from different TEM images. Gaussian statistics yielded values for the average particle sizes. SEM analysis was performed on an FEI Nova Nanolab 600 FIB/SEM instrument operating at 30 kV. The samples were collected on carbon tape and coated with a gold−palladium layer before analysis.

N_2 adsorption−desorption experiments were conducted at −195 °C using a Micromeritics Tristar 3000 surface area and porosity analyser. Prior to the experiment, the sample was outgassed at 150 °C for 4 h under N_2 gas. The BET surface areas were obtained from adsorption data in a relative pressure range from 0.05 to 0.30. The total pore volumes were calculated from the amount of N_2 vapour adsorbed at a relative pressure of 0.99. The pore size distributions were evaluated from the desorption branches of the isotherms using the Barrett−Joyner−Halenda (BJH) method. The micropore surface area and volume were calculated using t-plot data.

TPR experiments were carried out with a Micromeritics Auto Chem II unit. The catalyst (approximately 50 mg) was placed in a tubular quartz reactor, fitted with a thermocouple for continuous temperature measurement. The reactor was heated in a furnace. Prior to the temperature-programmed reduction measurement, the calcined catalysts were flushed with high purity Ar gas at 200 °C for 30 min, to remove water and impurities, followed by cooling to ambient temperature. Then, the gas supply was switched to 5% H_2/Ar, and the temperature was raised at a rate of 10 °C min^{-1} from 50 to 850 °C. The gas flow rate through the reactor was controlled by three Brooks mass flow controllers and was kept constant at 50 $mL.min^{-1}$. The H_2 consumption (TCD signal) was recorded automatically. Pulse chemisorption was performed using the Micromeritics Auto Chem II instrument, to compute the number of active sites on the catalysts.

Ex-situ PXRD data were collected at the BXDS-WLE beamline at the Canadian Light Source using a photon energy of 15.144 keV and a 1k Mythen detector. The samples were measured in transmission geometry held inside Kapton capillaries. For all PXRD data presented, the crystalline phase identification was done using DIFFRAC.EVA (Version 4.2. Release 2016) using the crystallography open database (COD) (Release 2020). Phase analysis was done using the Rietveld method as implemented in Bruker AXS TOPAS software (Version 5, 2014).

Total scattering data were collected on the Canadian Light Source (CLS) Brockhouse high-energy wiggler beamline using a wavelength of $\lambda = 0.2081$ Å and a Perkin Elmer XRD1621

area detector placed 160 mm after the sample. The data were processed using GSAS-II software. The Qmax used to produce the pair distribution function (PDF) of the measured samples was 16 $Å^{-1}$. The instrumental resolution parameters Qdamp and Qbroad, as defined in PDFgui software, were determined by fitting a Ni powder standard measurement. Further data analysis was done using xPDFsuite. The PDF method is used to study short- and intermediate-range order in materials on the nanoscale. It is obtained from total scattering measurements using X-rays, neutrons, or electrons, and provides structural details when defects, disorder, or structural ambiguities obscure their elucidation directly in reciprocal space [35].

4.2.4 Fischer-Tropsch Synthesis catalyst evaluation

The FTS reaction was performed in a fixed-bed micro-reactor. A gas cylinder containing an $H_2/CO/N_2$ mixture (~60/30/10 vol %; purity 99.99%) was used to supply the reactant gas stream to the catalyst with a specific space velocity of 1800 mL h^{-1} g^{-1}. N_2 was used as an internal standard to ensure accurate mass balances. Catalyst (0.5 g, sieved through a 150 μm mesh, without pelletizing) was added to the reactor (resulting catalyst bed ~4 cm in length) and reduced in situ at 350 °C for 2 h under a stream of H_2 (1.5 bar at 50 mL min^{-1}). After reduction, the reactor temperature was decreased to ambient temperature under a hydrogen flow and then heated up to 220 °C under synthesis gas at a pressure of 10 bar. A hot trap was placed immediately after the reactor was held at 150 °C to collect wax. A second trap kept at ambient temperature was used to collect the oil and water mixture. All gas lines after the reactor were kept at 100 °C. The flow was controlled using a metering valve and measured by a bubble meter. The product stream was analysed online using two gas chromatographs. A thermal conductivity detector (TCD), equipped with a Porapak Q (1.50 m × 3 mm) packed column, was used to analyse H_2, N_2, and CO, and a flame ionization detector (FID), equipped with a Porapak Q packed column, was used for the analysis of the hydrocarbons online using the Clarity software package.

4.3. Results

4.3.1 Transmission electron microscopy

The hollow carbon spheres (HCSs) were prepared by coating polystyrene spheres (PSS) with resorcinol-formaldehyde. Thereafter the sample was heated to remove the sacrificial PSS template leaving a hollow spherical carbon shell [36,37]. The Os nanoparticles were loaded both inside and outside the HCSs, while the Co_3O_4 particles (ca. Co 10 wt % loading) were only loaded inside the HCSs resulting in the synthesis of OsCo@HCS and Os/(Co@HCS) catalysts. The synthesized catalyst was promoted with different Os loadings (0.1%, 0.5% and

1% Os) both inside and outside the 10%Co@HCSs. Electron microscopy images were collected on samples of the xOsCo@HCS (x = 0.1%, 0.5% and 1% Os) and xOs/(Co@HCS) (x = 0.1%, 0.5% and 1% Os) catalysts as shown in Fig 4.1.

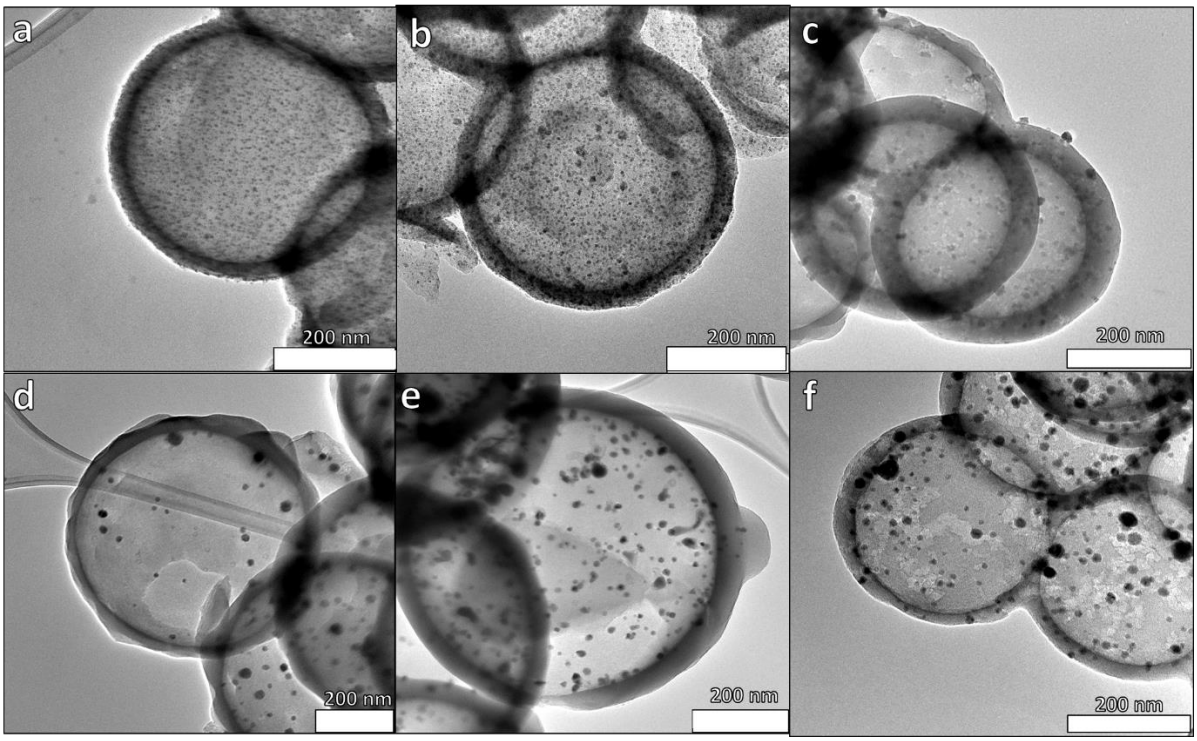

Figure 4.1: TEM images of xOs/(Co@HCS) with xOs = (a) 0.1% Os, (b) 0.5% Os, (c) 1% Os, and xOsCo@HCS with xOs = (d) 0.1% Os, (e) 0.5% Os, and (f) 1% Os (Co loading 10%).

Fig 4.1 (a), (b) and (c), show that the Co nanoparticles are reasonably well dispersed and successfully encapsulated inside the HCSs, while the loading of the Os promoter on the outer carbon shell can also be seen. As the promoter loading increased the dispersion of the Co nanoparticles inside the HCSs decreased. In Fig 4.1 (c) the cobalt nanoparticles show some agglomeration while the loading of Os on the outer shell is more visibly pronounced. The average particle size of (a) 0.1%Os/(Co@HCS), (b) 0.5%Os/(Co@HCS), and (c) 1%Os/(Co@HCS) were 6 ± 2 nm, 9 ± 4 nm and 10 ± 4 nm, were calculated (Fig S4.1) from the TEM images respectively.

Figs 4.1 (d) to (f), show images for samples in which both the Co and the Os promoter were encapsulated inside the HCSs. Interestingly, the carbon shell of the HCSs for Fig 4.1 (d) shows the presence of little to no metal loading. It can be observed that as the Os loading increased, agglomeration of the Co particles occurred. The average Co particle size in the xOsCo@HCS

catalysts was calculated (Fig S.4.1) to be 11± 5 nm, 12 ± 6 nm and 14 ± 4 nm, for the 0.1% Os (d), 0.5% Os (e), and 1% Os (f) catalysts respectively.

The HCSs were mesoporous and had a shell thickness range of 39 – 48 nm and a diameter range of 506 – 570 nm, as shown in Table 4.1. This distance was chosen so as to ensure that secondary hydrogen spillover could take place with the hydrogen species required to travel a short distance on/through the carbon material. The mesoporous carbon shell also facilitated permeability, thus providing easy access for small molecules to enter and exit the catalyst as the FTS reaction occurred.

Table 4.1: Average particle size of the synthesized catalysts and their shell diameter and thickness.

Sample	TEM Particle size (nm)	Rietveld Refinement Average Crystallite Size (nm)[a]	TEM HCS diameter (nm)	TEM HCS shell thickness (nm)
Co@HCS	4	3.5	570	40
0.1%OsCo@HCS	11	9.1	557	41
0.5%OsCo@HCS	12	11.9	526	40
1%OsCo@HCS	14	12.5	565	41
0.1%Os/(Co@HCS)	6	4.7	506	39
0.5%Os/(Co@HCS)	9	10.5	568	41
1%Os/(Co@HCS)	10	8.4	541	48

[a] Average crystallite sizes of the crystalline Co containing Co_3O_4 phase were calculated from Rietveld refinement of the PXRD data.

EDX analysis showed the elemental composition of the synthesized nanostructure catalysts. The EDX spectra (Fig. S4.3) confirmed that both Co and Os nanoparticles were indeed present in both the xOsCo@HCS and xOs/(Co@HCS) catalysts.

4.3.2 Powder X-Ray Diffraction (PXRD)

Syncrotron powder X-ray diffraction (PXRD) patterns of the catalysts, are shown in Fig 4.2. The broad feature(s) observed in the PXRD patterns, at ca. 2θ <10^{o} are due to diffuse X-ray scattering arising from the HCSs. Based on a comparison to similar results found in the literature, this feature indicated a defective nanostructure associated with the carbon spheres [38]. No Os diffraction peaks were observed in any of the PXRD patterns due to the low Os loading and very small crystallite sizes.

The Co@HCS catalyst showed the presence of both CoO (database reference code: COD 1533087) and Co(fcc) **(**database reference code: COD 9008466). This indicates that the Co can be reduced by the carbon shell [39–41]. Phase identification of the diffractograms of the Co catalysts with Os outside the carbon shell (0.5%Os/Co@HCS and 1%Os/(Co@HCS) showed that these samples contained primarily Co_3O_4 (database reference code: COD 1526734) as shown in Fig 4.2a and Table 4.2.

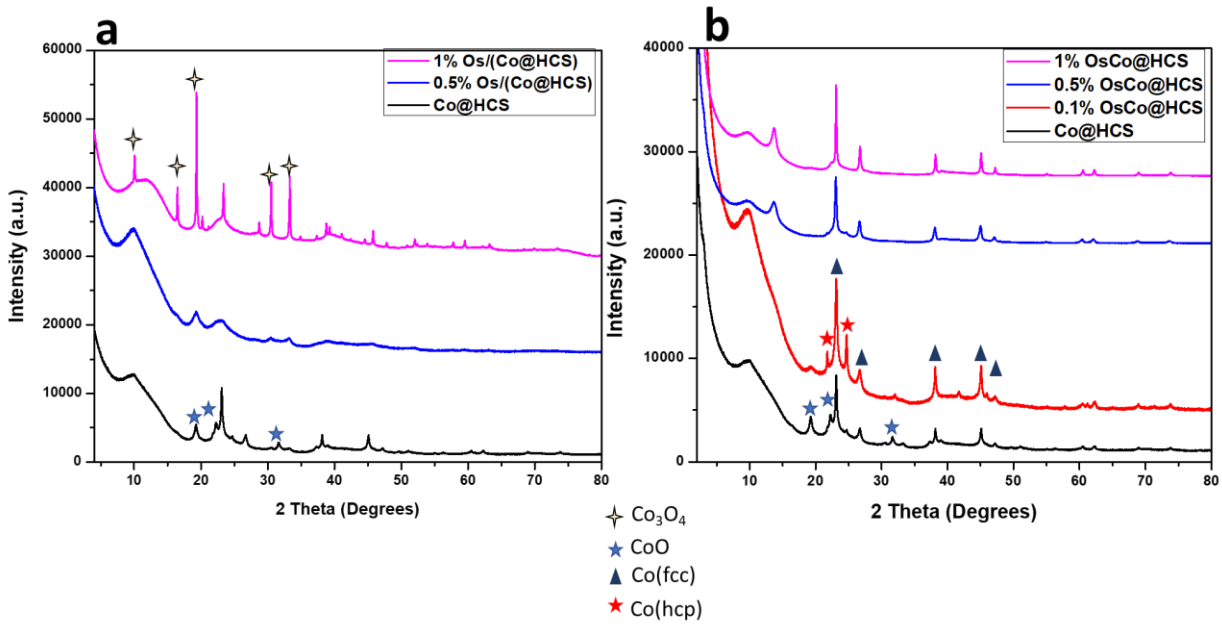

Figure 4.2: PXRD patterns for (a) Os loaded on the outside and (b) Os loaded on the inside of the 10% Co@HCS catalyst with different percentage Os loadings.

The PXRD patterns of the Co@HCS loaded with Os inside the HCS shell gave dramatically different results. The patterns showed peaks belonging predominantly due to the fcc Co phase (Fig 4.2 (b)) with the presence of some hcp Co phase (database reference code: COD 9008492). This indicated that the reduction of the Co_3O_4 and CoO further progressed, when Os was in close proximity, to form metallic Co (hcp/fcc) in these samples.

Table 4.2: Relative Co phase abundances (wt. %)

Sample	Co fcc	Co hcp	CoO	Co3O4
Co@HCS	53.2	-	46.8	-
0.1%OsCo@HCS	88.8	11.2	-	-
0.5%OsCo@HCS	100	-	-	-
1%OsCo@HCS	100	-	-	-
0.5%Os/(Co@HCS)	-	-	50	50
1%Os/(Co@HCS)	-	-	-	100

4.3.3 Total Scattering measurements

Total scattering measurements were undertaken to further examine the local structure of the catalysts. The resulting pair distribution functions (PDFs) for the xOs/(Co@HCS) and xOsCo@HCS catalysts are shown in Fig 4.3, Fig S4.4, Fig 4.4, and Fig S4.5, respectively.

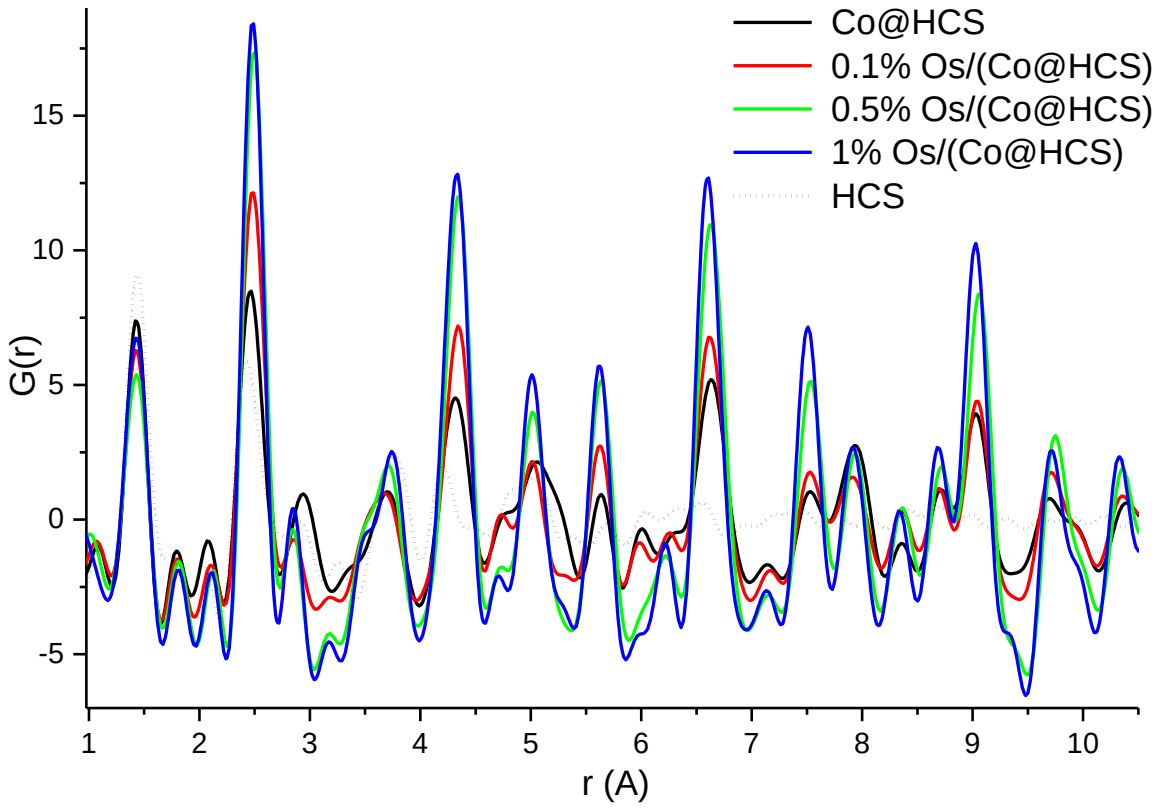

Figure 4.3. Zoomed view of the experimental PDF from 1-10 Å of the catalysts with Os supported outside the HCS.

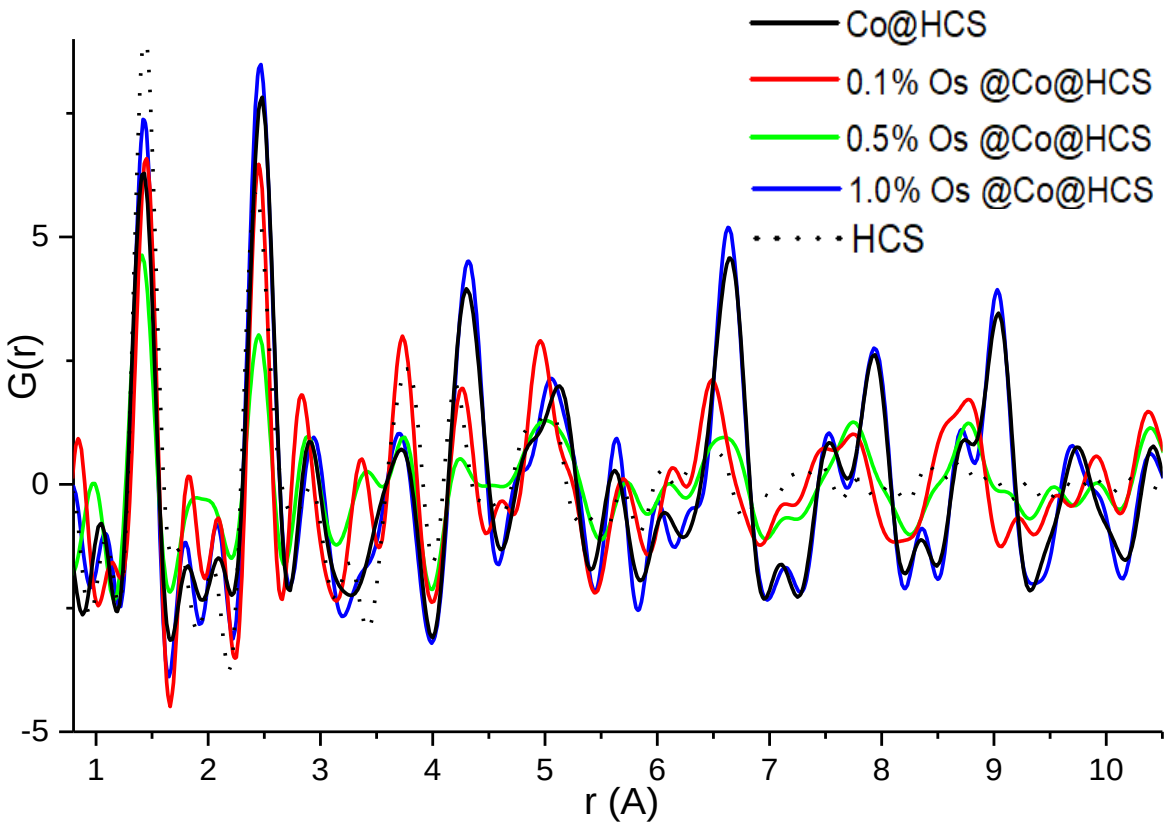

Figure 4.4. Zoomed view of the experimental PDF from 1-10 Å of the catalysts with Os supported inside the HCS.

Fig S4.4 shows the PDFs of samples xOs/(Co@HCS) (x = 0.1% - 1.0%) as well as Co@HCS and the HCS support. Likewise, Fig S4.5 shows the PDFs of samples xOsCo@HCS (x = 0.1% - 1.0%) as well as Co@HCS and the HCS support. When comparing the extended PDF ranges (Fig S4.4 and S4.5), it is clear that the oscillations in the PDF signal are significantly more attenuated when Os is loaded outside of the HCS. This dampening of the PDF signal with increasing distance from the scatterer is a direct measure of the lack of coherence and therefore a measure of the disorder of the structures comprising the catalyst.

It is best to first consider the structure of the HCS support. The PDFs shown in Figs 4.3 and 4.4 give information regarding the first, second and third coordination spheres of the carbon nanostructures. The expected real space values for in-plane carbon-carbon bond distances in the aromatic-type ring of graphite/graphene structures for the first three coordination spheres as shown in Fig 4.5 [42,43].

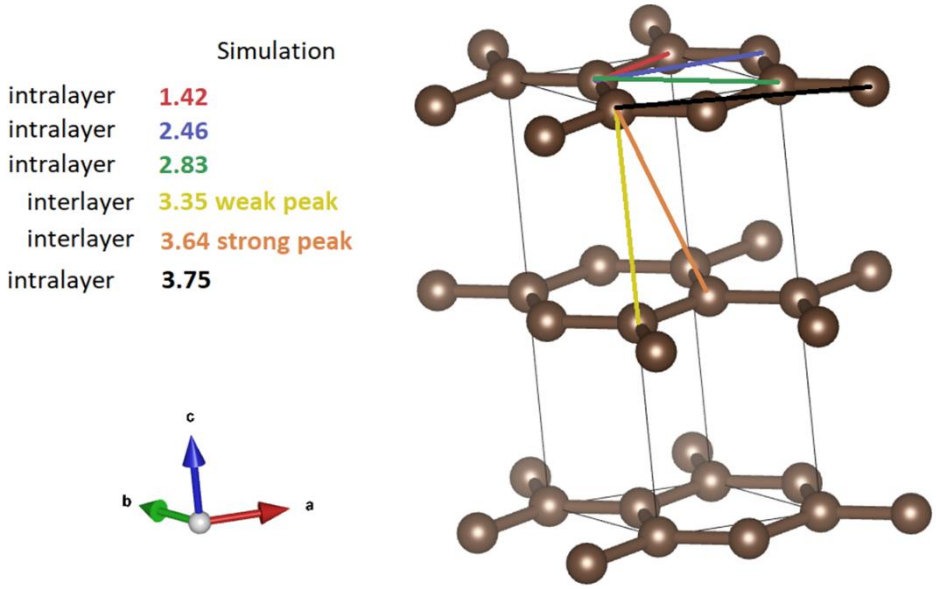

Figure 4.5. C-C bond lengths of graphite corresponding to peaks in PDF of the HCS.

The first peak in G(r), at 1.42 Å, corresponds to the C-C bonds with the three nearest neighbours in carbon with sp^2 bonding, Fig 4.6. The second peak at 2.46 Å represents the distance between the three atoms coordinating the central carbon or the shortest diagonal in the hexagon. The third peak at 2.83 Å, which is twice the first C-C distance, is the second, long diagonal in the hexagon. Deviations or peak broadening from these values imply non-uniform ring structures common in graphitic materials with defective structures. The reduction in structural coherence with increasing distance along the graphene sheet is noted in all samples and is due to the required curvature of the sheets to form spheres as well as from the distribution of varying curvatures in the sample from the inner layers to the outer layers of the shell, rather than from the termination of sheet fragments [44–46]. The increased deformation, tilting or folding of the layers to form spheres combined with weak van der Waals bonds between the layers, reveals that the structures are prone to turbostratic disorder [47].

It is important to note that the signal originating from the HCS support attenuates rapidly in comparison to samples containing Co, or Os and Co, indicating that the support is highly defective and lacks any medium to long-range order. Therefore, the signal observed extending to higher r values originates from the various metallic phases and their oxides.

The addition of Co and Os to the HCSs shows interesting changes to the PDFs. Firstly, considering the Co@HCS catalyst with no Os shows a peak at ca. 4.32 Å, arising from the CoO phase (Figs. 4.3 and 4.4, and Table 4.3). Various peaks in the PDF were used to identify the

aforementioned phases as well as phases which correspond to various Co-O, Co-Co, O-O distances associated with the three cobalt oxide phases found in catalysts. These include peaks at; 2.11, 3.70, 4.32, 6.63 and 2.85, 3.35, 4.95 Å for the Co_3O_4 (database reference code: COD 1526734) and the cubic CoO phase (database reference code: COD 1533087)], respectively [48,49].

When examining the sample set xOs/(Co@HCS), (min 0.1 % Os, max 1.0% Os), the Co remained primarily in its oxidized form as Co^{3+} or Co^{2+} as found in Co_3O_4/CoO. The data shows that the CoO content decreased with increasing Os content, as also verified later by TPR data.

The PDFs for xOsCo@HCS show the presence of metallic Co (4.3 Å) and some CoOx species with the 1% Os loaded catalyst completely reducing the Co phase to its metallic state. The reduction of Co occurs via a spillover effect from the close proximity of the Os promotor particles to the Co particles both held within the HCS. This further confirms that a primary spillover occurs when Os is in close contact with Co. Metallic Co was present for all loadings of Os in the xOsCo@HCS catalysts. It is difficult to accurately determine the exact interaction between Co and Os from the PDF data, and thus it is unclear if alloying or solid solutions of these phases have occurred or not.

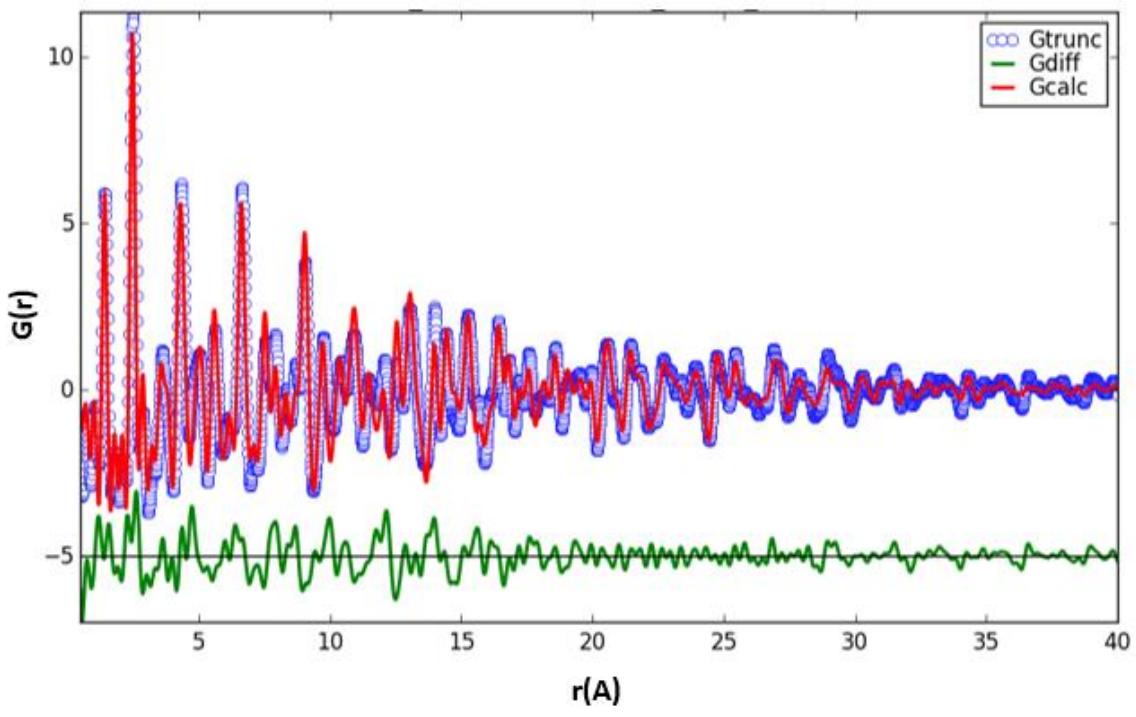

Figure 4.6: PDF fitting of 0.1% OsCo@HCS with Co, CoO, and graphite phases fitted.

The data in Table 4.3 shows the PDF fit results and the calculated Co/CoOx particle sizes (Fig 4.6). The fits show that larger particles are reduced more readily than the smaller particles as expected. The particle size determined from the PDFs was smaller and differed from the TEM particle size but showed the same trends with respect to Os loading. PDF is more sensitive to particle size changes over the bulk sample than TEM resulting in some variations in particle sizes between the two methods, however, the information is complementary. Similarly, in certain samples, Co containing phases detected by PDF analysis may differ from that found from similar synchrotron PXRD data due to the differences in sensitivity of the two techniques with PDF being more sensitive to nanostructures with reduced crystalinity.

Table 4.3: Atomic Pair Distribution Function **(**PDF) fit results

Sample	Graphene	Co	CoO	Co_3O_4
Co@HCS	✓	✓ (5.0)	✓ (5.9)	X
0.1%OsCo@HCS	✓	✓ (5.0)	✓ (2.6)	X
0.5%OsCo@HCS	✓	✓ (6.6)	✓ (1.6)	X
1%OsCo@HCS	✓	✓ (5.8)	X	X
0.5%Os/(Co@HCS)	✓	X	✓ (2.5)	✓ (4.1)
1%Os/(Co@HCS)	✓	X	X	✓ (9.1)

The format of the table is as follows: "contains phase (✓/X), particle size (nm)".

4.3.4 N_2 absorption-desorption analysis (BET)

The N_2 absorption-desorption isotherm curves and pore distribution curves for the HCS, Co@HCS, xOsCo@HCS and xOs/(Co@HCS) catalysts were recorded and representative data are shown in Figs S4.6 and Fig S4.7. All the catalysts presented the type I/IV adsorption isotherms which reveal both micropores and mesopores [50,51].

In Table 4.4, the specifics of the textural properties of the synthesized catalysts are listed. The values of the pore sizes show that the HCSs were mesoporous with a 2–50 nm pore size. The high surface areas (415–532 m^2/g) were due to the presence of micropores in the HCS shell (Fig S4.6). The decomposition of the polystyrene and the loss of small molecules during the

carbonization process resulted in the formation of these micropores. The high porosity of the synthesized catalysts is required for catalytic reactions (e.g. FTS) in that it enables the diffusion of reactants and products both in and out of the HCS cavity [19]. The surface area of the HCSs was shown to decrease with the addition of metals loaded inside or outside the HCS support material, presumably due to pore blockage.

Table 4.4: Summary of the N_2 physisorption data

Sample	Surface area (m^2/g)	Pore volume (cm^3/g)	Pore size (nm)
HCS only	532	0.51	5.0
Co@HCS	508	0.20	8.7
0.1%Os/Co@HCS	486	0.22	8.3
0.5%Os/Co@HCS	470	0.18	8.5
1%Os/Co@HCS	463	0.56	7.8
0.1%Os/(Co@HCS)	441	0.87	7.7
0.5%Os/(Co@HCS)	428	0.71	9.3
1% Os/(Co@HCS)	415	0.83	8.1

4.3.5 Temperature programmed reduction (TPR)

Reduction profiles of the synthesized catalysts are shown in Fig 4.7 and Fig 4.8. The behaviour of these catalysts followed a normal two-step reduction of Co_3O_4 with the CoO formed as an intermediate phase [52]. The two-step reduction equations are as follows:

First reduction step: $Co_3O_4 + H_2 \rightarrow 3CoO + H_2O$ (ca. 148 – 273 ^oC)

Second reduction step: $3CoO + 3H_2 \rightarrow 3Co + 3H_2O$ (ca. 285 – 415 ^oC) [10,52]

The presence of the Os promoter was observed to influence the TPR profile of Co_3O_4 by reducing the above reduction temperatures. The reduction of the Co_3O_4 was also affected by the relative location of the Os and the mechanism can be explained by primary and secondary hydrogen spillover effects.

A peak ratio of 1:3 is anticipated in a two-step reduction of Co_3O_4, which uses one H_2 molecule in the first reduction step and three H_2 molecules in the second reduction step. However, the 1:3 peak ratio was not observed in our study since the carbon can also reduce the Co and this complicates the reduction process. This has also previously been observed in other studies. For example, Ru ions doped inside a Co_3O_4 lattice can assist with the low temperature reduction of the oxide [53].

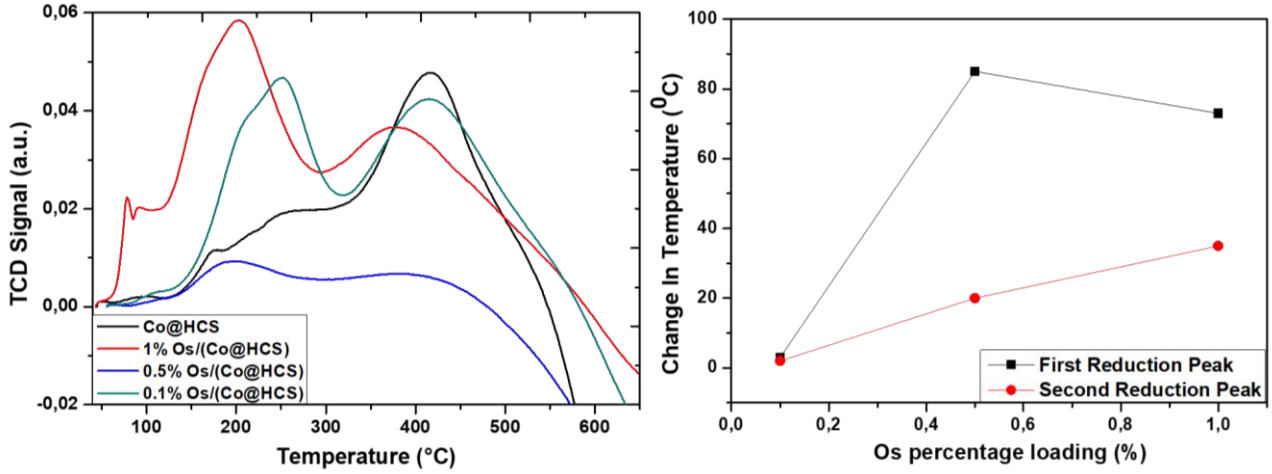

Figure 4.7: (a) TPR profiles showing the secondary hydrogen spillover effect and (b) the relative change in reduction temperature with Os % loading.

The TPR profiles of the xOs/(Co@HCS) (x = 0.1%, 0.5% and 1% Os loading) and the Co@HCS catalysts are shown in Fig 4.7 (a). The Co@HCS catalyst shows the two step reduction of Co_3O_4 to CoO at 275 ^oC followed by the reduction of CoO to Co at 415 ^oC [53]. The increase in Os loading on the outer HCS shell resulted in a temperature shift of the first reduction step, relative to the reduction step of Co@HCS, as shown in Fig 4.7 (b). This decrease was approximately 3, 85, and 73 ^oC for the three Os catalysts, xOs/(Co@HCS) (x = 0.1%, 0.5% and 1%, respectively). The second reduction step showed the expected smaller change in the reduction temperature with an increase of Os percentage loadings, as seen for other promoters (Pt, Ru, etc.) [54]. Here the changes were approximately 2, 20 and 35 ^oC for xOs/(Co@HCS) (x = 0.1%, 0.5% and 1%, respectively).

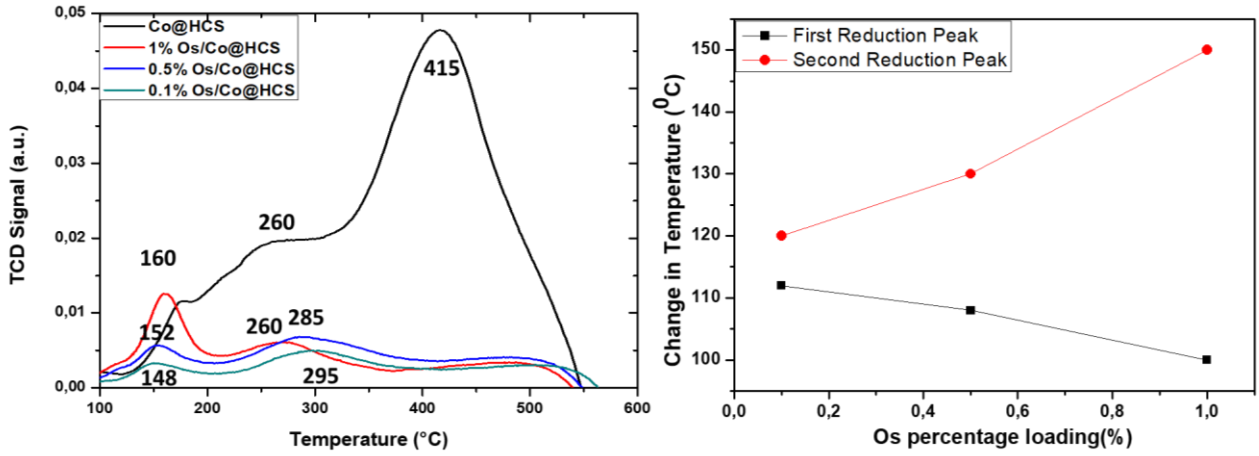

Figure 4.8. (a) TPR profile of the primary hydrogen spillover effect and (b) the change in temperature with Os percentage loading.

The TPR profiles of the xOsCo@HCS (x = 0.1%, 0.5%, 1%), and the Co@HCS catalysts are shown in Fig 4.8 (a). The effect of the close proximity of Os and Co leads to a change in the first reduction step of Co_3O_4 by 113, 108 and 99 ^oC for the xOsCo@HCS catalysts (x = 0.1%, 0.5%, 1%, respectively), Fig 4.8 (b). The second reduction step showed a larger change in the reduction temperature with Os percentage loading, with changes of approximately 120, 130 and 155 ^oC for the three xOsCo@HCS catalysts. It is also noted that the peaks in Fig 4.8 are much smaller than in Fig 4.7; this is because most of the CoOx has been reduced by the Os when the Co and Os were in close contact during the synthesis process (see Fig 4.2). It is clear that (i) the Co can be reduced more easily when the Co is inside the HCSs relative to when the Os is outside the HCSs and ii) even at low Os loadings (0.1% Os) the Os has the ability to reduce the Co ($T < 300\ ^oC$).

The total hydrogen consumption (THC) was calculated from the peak areas of the Co reduction peaks (Table S4.2). The highest THC was obtained from the 0.5%OsCo@HCS catalyst (20.83 mmol/g) and the lowest from the 1%Os(Co@HCS) catalyst (4.39 mmol/g). The xOsCo@HCS catalysts had higher THCs than the the xOs/(Co@HCS) catalysts. This observation indicates the importance of the Os promoter intimacy with the Co_3O_4 catalyst.

From the reduction profiles observed and the THC data it can be confirmed that Os facilitates both the primary and secondary hydrogen spillover effects. Additionally, it was found that the promoter effects of Os were not as prominent when Co_3O_4 and Os were separated by a carbon shell relative to when the metals were close to one another inside the HCS.

4.3.6 Fischer Tropsch Synthesis (FTS) evaluation

FTS studies on the catalyst were performed at 220 ^{o}C (50 h, 10 bar pressure). Table 4.5 shows the %CO conversion, turnover frequency (TOF), FT activity, C_1, C_2-C_4, and C_5+ selectivity for all the catalysts. Comparing the Os promoted catalysts to the unpromoted catalysts, all the Os promoted catalysts showed a similar or slightly higher %CO conversion than the unpromoted catalysts, Co@HCS (1.6 %). FTS %CO conversion of the OsCo@HCS catalysts are higher than those of the xOs/(Co@HCS) catalysts (Table 4.5). A similar trend was observed, catalysts with Co and Os close together (primary spillover process) gave a higher FT activity (38.5 – 46.4 x10^{-6} $mol_{CO}/g_{Co}.s$) than both the unpromoted catalyst (27.8 x10^{-6} $mol_{CO}/g_{Co}.s$), and the catalysts where Os and Co were separated (25.1 – 36.4 x10^{-6} $mol_{CO}/g_{Co}.s$) by the mesoporous carbon shell (secondary spillover effect). This can be attributed to the reducibility induced by the close proximity of Os to the Co oxide nanoparticles [55]. Previous studies of Os in FTS have been conducted and showed Os to be a poor FT catalyst with high methane production, Table 4.6 [56,57]. Of note as well, is the observation that the Co has larger particles when inside the HCSs, suggesting that the effect of Os location on the % syngas conversion is even larger than measured when assuming equal Co particle sizes. Another explanation for the higher rate might be related to the Co phase present viz. the xOsCo@HCS catalysts had a higher intrinsic activity for CO hydrogenation reaction in its hcp phase than in its fcc Co phase [54].

The catalytic performance in FTS suggests that the primary spillover effect due to Os gives rise to synergistic electronic effects, that are more effective in giving a highly active FT catalyst compared to the catalytic performance of Os via a secondary spillover effect. A similar observation has been reported by Nabaho et al [58], for a Pt promoted Co catalysts when the Pt and Co were separated by some distance using an alumina support. The addition of a promoter, such as Pt, to Co oxide nanoparticles, has been reported to alter the catalyst morphology [59], and this appears to also occur for Os.

The presence of the Os promoter has also been shown to affect the selectivity of the catalysts (Table 4.5). The methane selectivity was shown to decrease with increased contact between Os and Co viz. Co@HCS (18.8%) > 1%Os/(Co@HCS) (13%) > 1%OsCo@HCS (7.6%). A decrease in methane selectivity was also noted when Co and Os were in close contact. The results could also be related to the Co particle size since larger Co particles are more selective to higher molecular weight hydrocarbons and the smaller particles are more selective towards methane production [60–65]. As the methane selectivity decreased, the selectivity to C_5+ liquid

hydrocarbons increased after the promotion of the Co catalyst with Os. Os itself is highly selective for methane production [56], but when used as a promoter and in close contact with Co, the Os-Co catalyst produces high molecular weight hydrocarbons. The increased selectivity to C_5+ hydrocarbons could also be due to Os enhancement on the Co crystallite surface, similar to what has been reported for a Ru promoted Co catalyst [66,67]. The xOs/(Co@HCS) catalyst had a higher selectivity to methane production compared to the Co@HCS catalyst.

Table 4.5: Fischer-Tropsch catalytic performance and selectivity (H_2/CO ratio = 2, P = 10 bar, Temperature = 220 °C).

Sample	CO Conversion (%)	TOF ($x10^{-3}$ s)[a]	Activity ($x10^{-6}$) ($mol_{CO}/g_{Co}.s$)	Selectivity (C mol) %		
				C_1	C_2-C_4	C_{5+}
10Co@HCS	4.2	6.01	27.8	18.8	11.1	70.1
0.1%OsCo@HCS	5.3	7.23	38.5	13.2	4.9	81.9
0.5%OsCo@HCS	6	11.5	39.8	11.4	6.9	81.7
1%OsCo@HCS	6.8	44.7	46.4	7.6	3.8	88.6
0.1%Os/(Co@HCS)	4.8	29.3	25.1	15	10.6	74.4
0.5%Os/(Co@HCS)	4.7	41.1	27.1	22.9	14.8	62.3
1%Os/(Co@HCS)	5	23.4	36.4	13	3.4	83.6

[a]Calculated using the data obtained from Co crystallite sizes of the spent catalysts as determined by Rietveld refinement (Table 6). Surface atoms were calculated using the Van Hardeveld and Hartog statistical method [68].

In table 4.6, the %CO conversion and selectivity data is reported based on studies conducted on related Co and Os catalysts. The studies have shown that both Os and Co show FT activity with the Os catalyst showing mainly methane selectivity. The Co catalysts generally had high C_{5+} selectivity, consistent with reports on many other unpromoted.

Table 4.6: Reactivity data of Os vs Co encapsulated in HCS.

Sample 220 °C	Reaction Temperature	CO conversion (%)	Selectivity (C mol) (%)		
			C_1	C_2-C_4	C_{5+}

Co@MHCS [29]	220	11.2	20.1	7.9	72.0
Co@HCS (this study)	220	4.2	18.8	11.1	70.1
Os@HCS [56]	220	13.9	92.8	7.2	1.30
Os/SiO_2 [57]	220	4.1	64.3	35.7	0.34

4.3.7 Transmission electron microscopy studies of the spent FT catalysts

The TEM images of the six spent catalysts are shown in Fig 4.9. The images reveal that the HCSs maintained their morphology and the Co nanoparticles remained encapsulated during and after the FTS reaction. This shows the effectiveness of the HCS as a thermally stable support material that can withstand high pressures under the FTS reaction conditions. It was also observed that the Co nanoparticles underwent some sintering during the FTS reaction and formed agglomerated particles known to result in Co catalyst deactivation [69].

The average particle size of the Co in the spent xOs/(Co@HCS) catalysts was 26 ± 8 nm, 20 ± 5 nm and 21 ± 9 nm for the 0.1% Os, 0.5% Os, and 1% Os catalysts, respectively (Table 4.7, Fig S4.2). Furthermore, carbon formation on the Co agglomerates was observed that formed in the synthesis gas environment (Fig 4.9; blue circle) [70].

Sintering during FTS at elevated temperatures is common. A study by Bian et al. showed the sintering of Co crystallites from 10 to 17 nm and from 29 to 32 particle size for Co/SiO_2 catalysts occurred during FTS (10 bar and 200 ^oC and 240 ^oC) [71]. A study by Davis et al. showed the sintering of Co in spent Co/Al_2O_3 catalysts. X-ray absorption fine structure (EXAFS) studies showed that high pressure and FTS reaction conditions caused an increase in the first Co-Co shell of the metallic phase's coordination number from 2.7 to 7.6. The catalyst had Co crystallites with a size of 5–6 nm. [72].

Post analysis of the TEM images of the three xOsCo@HCS catalysts gave average particle sizes of 21 ± 7 nm, 11 ± 5 nm and 17 ± 9 nm for the 0.1% Os, 0.5% Os, and 1% Os loadings, respectively (Fig 4.9 d, e, f and Table 4.7). A similar observation of Co metal agglomeration and subsurface carbon formation (only at 0.1% Os) can be seen in Fig 9. The data showed that sintering was reduced when the Os and Co are in close contact indicating that the Os may hinder this reaction [46].

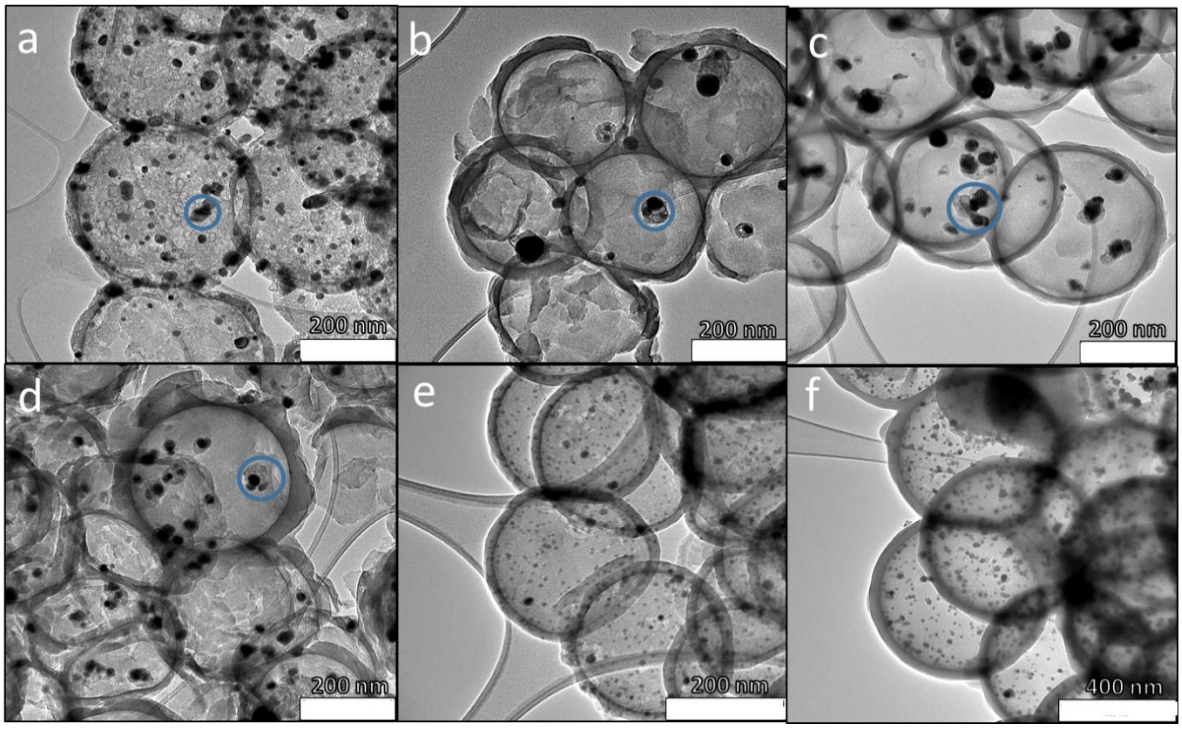

Figure 4.9: Post FTS TEM images of xOs/(Co@HCS) with xOs = (a) 0.1% Os, (b) 0.5% Os, (c) 1% Os, and xOsCo@HCS with xOs = (d) 0.1% Os, (e) 0.5% Os, and (f) 1% Os (Co loading 10%).

Table 4.7: Average particle size of the FTS spent catalysts size.

Sample	TEM Particle size (nm)	Rietveld Refinement Particle Size (nm) [a]
0.1%OsCo@HCS	17	13
0.5%OsCo@HCS	11	12.1
1%OsCo@HCS	21	14.2
0.1%Os/(Co@HCS)	21	21
0.5%Os/(Co@HCS)	20	22.3
1%Os/(Co@HCS)	21	24.2

[a] Average crystallite sizes of the crystalline Co (hcp) phase were calculated from Rietveld refinements of the PXRD data

4.3.8 Powder X-ray diffraction studies of the spent FT catalysts

PXRD analyses were performed on the spent catalysts to identify the crystalline phases present in Os promoted Co nanoparticles supported on HCSs. PXRD patterns of post FT catalysts are shown in Fig 4.10. In all the PXRD patterns the broad feature expected of carbonaceous materials was observed at approximately $2\theta = 25^{o}$.

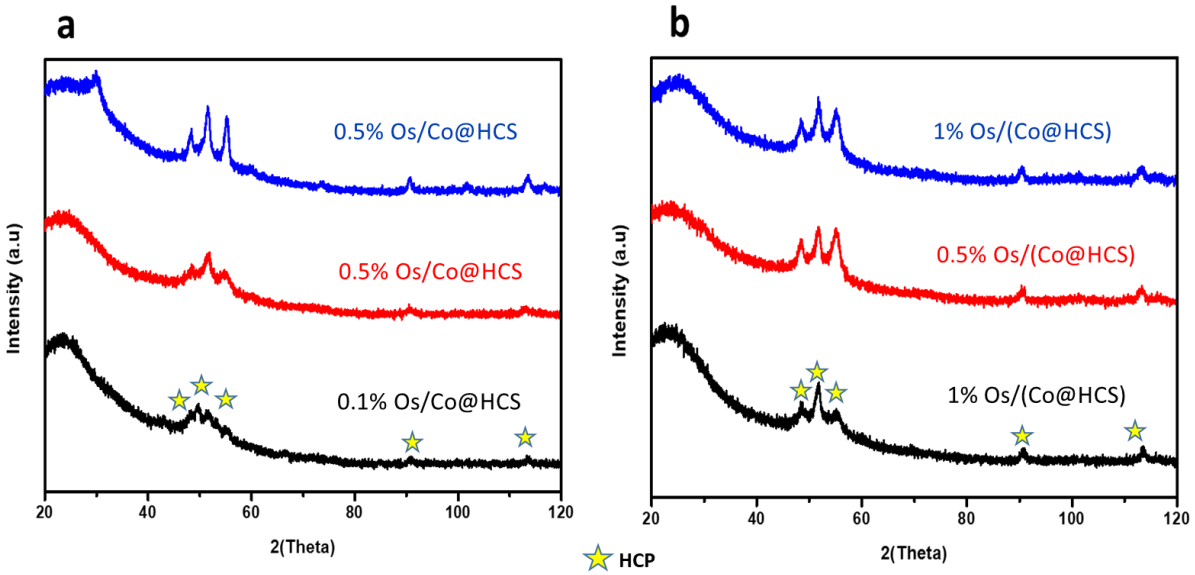

Figure 4.10: Post FTS PXRD patterns of (a) Os promoter loaded on the inside and (b) Os promoter loaded on the outside of the Co@HCS catalyst with different percentage Os loadings. The stars mark the position of the Co hcp phase.

All the PXRD patterns of the post-reaction analysed FTS catalysts, Fig 4.10, showed a predominant Co hcp phase (COD: 9010967). The Co hcp phase was formed in the reducing FTS environment. Similar results were noted from a study of Co/Al_2O_3; after FTS the Co also crystallized as the Co hcp phase [73–75]. X-ray scattering by Os in these PXRD patterns was again not observed, due to its low concentration. The Rietveld refinement was conducted on the XRD patterns of the catalysts and showed that the particle sizes increased under the FTS conditions resulting in metal agglomeration and possibly catalyst deactivation [76]. The Co

particle sizes determined by Rietveld refinement correspond with the data obtained from the TEM study, confirming the occurrence of metal sintering (Table 4.7).

4. Conclusion

Co FT catalysts, promoted with Os, were synthesized using hollow carbon spheres (HCS) as a nanoreactor support material. Co nanoparticles were encapsulated inside the HCSs and the promoter was loaded both inside and outside of the HCSs. The mesoporous and defective nature of HCSs was exploited to investigate the effect of primary (both Co and Os inside a HCS) and secondary (Co inside and Os outside of a HCS) spillover effects. The synthesis of Co@HCS, xOsCo@HCS, and xOs/(Co@HCS) porous catalysts was successful. The particle sizes of the Co catalysts increased with closer proximity of the Co catalyst and the Os promoter in the following order: Co@HCS < xOs/(Co@HCS) < xOsCo@HCS.

The PXRD, PDF and TPR data showed that the intimate contact of Co and Os, when both metals were inside the HCS, enhanced the reducibility of the Co catalyst more than when the Os promoter was loaded on the outside of the HCS. The Os promoter was shown to produce both primary and secondary spillover effects and Os was shown to promote the Co FT catalyst. The intimacy of the Os promoter with the Co catalyst was shown to affect the particle size of Co, and the crystalline phase of Co, with the Co fcc metallic phase being dominant when the promoter was in close proximity with Co. The Co oxide particle size decreased as the Os content grew inside the HCS. At the same time, the Co particle size increased. Both point to the reduction role of the Os on the Co catalyst.

The Os promoter improved the Co FTS reaction selectivity towards higher molecular weight hydrocarbons and improved its FTS catalytic performance. This can be readily explained by the presence of more reduced Co particles. Although the utilization of Os as a promoter may offer an alternative to the use of the Ru and Pt promoted Co FT catalyst, the agglomeration of Co in the presence of Co is substantial.

Lastly, post FTS studies showed that HCS support material was stable and could withstand high pressures and the FTS conditions. The HCSs maintained their morphology and the Co nanoparticles remained encapsulated during the reaction. The Co hcp phase was observed in the analysis of all post FT catalysts under the reducing FTS conditions. The sintering of encapsulated Co nanoparticles showed higher Co reduction in xOsCo@HCS catalysts,

compared to the xOs/(Co@HCS) catalysts during the FTS reaction. Subsurface carbon formation was also found in the xOs/(Co@HCS) catalyst when compared to xOsCo@HCS.

Reference

[1] N. Montoya Sánchez, F. Link, G. Chauhan, C. Halmenschlager, H.E.M. El-Sayed, R. Sehdev, R. Lehoux, A. de Klerk, Conversion of waste to sustainable aviation fuel via Fischer–Tropsch synthesis: Front-end design decisions, Energy Sci. Eng. 10 (2022) 1763–1789.

[2] V. Vosoughi, S. Badoga, A.K. Dalai, N. Abatzoglou, Modification of mesoporous alumina as a support for cobalt-based catalyst in Fischer-Tropsch synthesis, Fuel Process. Technol. 162 (2017) 55–65.

[3] D. Dhamo, D. Hess, M. Rubin, R. Dittmeyer, SOEC-based production of e-fuels via the Fischer–Tropsch route, in: High-Temperature Electrolysis From Fundam. to Appl., IOP Publishing, 2023.

[4] E. Iglesia, Design, synthesis, and use of cobalt-based Fischer-Tropsch synthesis catalysts, Appl. Catal. A Gen. 161 (1997) 59–78. https://doi.org/10.1016/S0926-860X(97)00186-5.

[5] R. Pestman, W. Chen, E. Hensen, Insight into the rate-determining step and active sites in the Fischer–Tropsch reaction over cobalt catalysts, ACS Catal. 9 (2019) 4189–4195.

[6] V. Subramanian, K. Cheng, C. Lancelot, S. Heyte, S. Paul, S. Moldovan, O. Ersen, M. Marinova, V. V. Ordomsky, A.Y. Khodakov, Nanoreactors: An Efficient Tool to Control the Chain-Length Distribution in Fischer-Tropsch Synthesis, ACS Catal. 6 (2016) 1785–1792. https://doi.org/10.1021/acscatal.5b01596.

[7] N.O. Elbashir, P. Dutta, A. Manivannan, M.S. Seehra, C.B. Roberts, Impact of cobalt-based catalyst characteristics on the performance of conventional gas-phase and supercritical-phase Fischer-Tropsch synthesis, Appl. Catal. A Gen. 285 (2005) 169–180. https://doi.org/10.1016/j.apcata.2005.02.023.

[8] F. Rodríguez-Reinoso, The role of carbon materials in heterogeneous catalysis, Carbon N. Y. 36 (1998) 159–175. https://doi.org/10.1016/S0008-6223(97)00173-5.

[9] T. Mochizuki, T. Hara, N. Koizumi, M. Yamada, Surface structure and Fischer–Tropsch synthesis activity of highly active Co/SiO2 catalysts prepared from the impregnating solution modified with some chelating agents, Appl. Catal. A Gen. 317 (2007) 97–104.

[10] G. Jacobs, J.A. Chaney, P.M. Patterson, T.K. Das, B.H. Davis, Fischer-Tropsch synthesis: Study of the promotion of Re on the reduction property of Co/Al2O3 catalysts by in situ EXAFS/XANES of Co K and Re LIII edges and XPS, Appl. Catal. A Gen. 264 (2004) 203–212. https://doi.org/10.1016/j.apcata.2003.12.049.

[11] B. Jongsomjit, J. Panpranot, J.G. Goodwin, Effect of zirconia-modified alumina on the properties of Co/γ -Al2O3catalysts, J. Catal. 215 (2003) 66–77. https://doi.org/10.1016/S0021-9517(02)00102-1.

[12] J. Li, N.J. Coville, The effect of boron on the catalyst reducibility and activity of Co/TiO2Fischer-Tropsch catalysts, Appl. Catal. A Gen. 181 (1999) 201–208. https://doi.org/10.1016/S0926-860X(98)00434-7.

[13] Y. Jin, A.K. Datye, Phase transformations in iron Fischer-Tropsch catalysts during temperature-programmed reduction, J. Catal. 196 (2000) 8–17. https://doi.org/10.1006/jcat.2000.3024.

[14] M. Boudart, A. Delbouille, J.A. Dumesic, S. Khammouma, H. Topsøe, Surface, catalytic and magnetic properties of small iron particles. I. Preparation and characterization of samples, J. Catal. 37 (1975) 486–502. https://doi.org/10.1016/0021-9517(75)90184-0.

[15] Z. Luo, G. Zhao, H. Pan, W. Sun, Strong Metal–Support Interaction in Heterogeneous Catalysts, Adv. Energy Mater. 12 (2022) 2201395.
[16] T.N. Phaahlamohlaka, D.O. Kumi, M.W. Dlamini, L.L. Jewell, N.J. Coville, Ruthenium nanoparticles encapsulated inside porous hollow carbon spheres: A novel catalyst for Fischer–Tropsch synthesis, Catal. Today. 275 (2016) 76–83. https://doi.org/10.1016/j.cattod.2015.11.034.
[17] T. Fu, Z. Li, Review of recent development in Co-based catalysts supported on carbon materials for Fischer-Tropsch synthesis, Chem. Eng. Sci. 135 (2015) 3–20. https://doi.org/10.1016/j.ces.2015.03.007.
[18] Y. Chen, J. Wei, M.S. Duyar, V. V Ordomsky, A.Y. Khodakov, J. Liu, Carbon-based catalysts for Fischer–Tropsch synthesis, Chem. Soc. Rev. 50 (2021) 2337–2366.
[19] T. Hlabathe, J. Gorimbo, M. Moyo, X. Liu, Carbon Supported Catalysts in Fischer-Tropsch Synthesis: Structural Properties of Carbon Supports, Adv. Mater. Sci. Technol. 4 (2022).
[20] S. Ikeda, S. Ishino, T. Harada, N. Okamoto, T. Sakata, H. Mori, S. Kuwabata, T. Torimoto, M. Matsumura, Ligand-free platinum nanoparticles encapsulated in a hollow porous carbon shell as a highly active heterogeneous hydrogenation catalyst, Angew. Chemie. 118 (2006) 7221–7224.
[21] Z. Yu, N. Ji, J. Xiong, Y. Han, X. Li, R. Zhang, Y. Qiao, M. Zhang, X. Lu, Ultrafine Ruthenium Clusters Shell-Embedded Hollow Carbon Spheres as Nanoreactors for Channel Microenvironment-Modulated Furfural Tandem Hydrogenation, Small. 18 (2022) 2201361.
[22] W. Zhan, Y. Wang, J. Chen, Z. Chen, Y. Li, Boosting the Fischer-Tropsch synthesis performances of cobalt-based catalysts via geometric and electronic engineering: Construction of hollow structures, Appl. Catal. B Environ. 313 (2022) 121469.
[23] G. Jacobs, T.K. Das, Y. Zhang, J. Li, G. Racoillet, B.H. Davis, Fischer-Tropsch synthesis: Support, loading, and promoter effects on the reducibility of cobalt catalysts, Appl. Catal. A Gen. 233 (2002) 263–281. https://doi.org/10.1016/S0926-860X(02)00195-3.
[24] S.K. Beaumont, S. Alayoglu, C. Specht, W.D. Michalak, V. V. Pushkarev, J. Guo, N. Kruse, G.A. Somorjai, Combining in situ NEXAFS spectroscopy and CO2methanation kinetics to study Pt and Co nanoparticle catalysts reveals key insights into the role of platinum in promoted cobalt catalysis, J. Am. Chem. Soc. 136 (2014) 9898–9901. https://doi.org/10.1021/ja505286j.
[25] F. Diehl, A.Y. Khodakov, Promotion of cobalt Fischer-Tropsch catalysts with noble metals: a review, Oil Gas Sci. Technol. l'IFP. 64 (2009) 11–24.
[26] D.H. Chun, G.B. Rhim, M.H. Youn, D. Deviana, J.E. Lee, J.C. Park, H. Jeong, Brief review of precipitated iron-based catalysts for low-temperature Fischer–Tropsch synthesis, Top. Catal. 63 (2020) 793–809.
[27] K. Jalama, N.J. Coville, D. Hildebrandt, D. Glasser, L.L. Jewell, J.A. Anderson, S. Taylor, D. Enache, G.J. Hutchings, Effect of the addition of Au on Co/TiO 2 catalyst for the Fischer–Tropsch reaction, Top. Catal. 44 (2007) 129–136.
[28] J. Gahtori, G. Singh, C.L. Tucker, E. van Steen, A. V Biradar, A. Bordoloi, Insights into promoter-enhanced aqueous phase CO hydrogenation over Co@ TiO2 mesoporous nanocomposites, Fuel. 310 (2022) 122402.
[29] T.N. Phaahlamohlaka, D.O. Kumi, M.W. Dlamini, R. Forbes, L.L. Jewell, D.G. Billing, N.J. Coville, Effects of Co and Ru Intimacy in Fischer-Tropsch Catalysts Using Hollow Carbon Sphere Supports: Assessment of the Hydrogen Spillover Processes, ACS Catal. 7 (2017) 1568–1578. https://doi.org/10.1021/acscatal.6b03102.
[30] K.M. Mazurova, A.F. Miyassarova, R. V Kazantsev, O.L. Eliseev, A. V Stavitskaya,

Influence of the Promoter Deposition Conditions on the Catalytic Properties of Ruthenium–Cobalt Systems in the Fischer–Tropsch Synthesis, Pet. Chem. (2022) 1–7.
[31] D. Eliche-Quesada, J.M. Mérida-Robles, E. Rodríguez-Castellón, A. Jiménez-López, Ru, Os and Ru–Os supported on mesoporous silica doped with zirconium as mild thio-tolerant catalysts in the hydrogenation and hydrogenolysis/hydrocracking of tetralin, Appl. Catal. A Gen. 279 (2005) 209–221.
[32] T. Molefe, R. Forbes, N.J. Coville, Osmium as a potential Fischer-Tropsch catalyst using hollow carbon spheres as support, (2018) 148.
[33] J. Fu, Q. Xu, J. Chen, Z. Chen, X. Huang, X. Tang, Controlled fabrication of uniform hollow core porous shell carbon spheres by the pyrolysis of core/shell polystyrene/cross-linked polyphosphazene composites, Chem. Commun. 46 (2010) 6563–6565.
[34] H. Chiririwa, E. Muzenda, The Preparation and Characterisation of Osmium(IV), Osmium(II) and Osmium(0) Complexes from Refinery Materials, (2015) 0–4. https://doi.org/10.15242/iie.e1114015.
[35] M.W. Terban, S.J.L. Billinge, Structural analysis of molecular materials using the pair distribution function, Chem. Rev. 122 (2021) 1208–1272.
[36] F.P. Hu, Z. Wang, Y. Li, C. Li, X. Zhang, P.K. Shen, Improved performance of Pd electrocatalyst supported on ultrahigh surface area hollow carbon spheres for direct alcohol fuel cells, J. Power Sources. 177 (2008) 61–66. https://doi.org/10.1016/j.jpowsour.2007.11.024.
[37] X. Li, M. Puttaswamy, Z. Wang, C.K. Tan, A.C. Grimsdale, N.P. Kherani, A.I.Y. Tok, A pressure tuned stop-flow atomic layer deposition process for MoS2 on high porous nanostructure and fabrication of TiO2/MoS2 core/shell inverse opal structure, Appl. Surf. Sci. 422 (2017) 536–543.
[38] X. Chen, K. Kierzek, K. Cendrowski, I. Pelech, X. Zhao, J. Feng, R.J. Kalenczuk, T. Tang, E. Mijowska, CVD generated mesoporous hollow carbon spheres as supercapacitors, Colloids Surfaces A Physicochem. Eng. Asp. 396 (2012) 246–250.
[39] W. Chen, X. Pan, M.-G. Willinger, D.S. Su, X. Bao, Facile autoreduction of iron oxide/carbon nanotube encapsulates, J. Am. Chem. Soc. 128 (2006) 3136–3137.
[40] F. Morales, B.M. Weckhuysen, J.J. Spivey, K.M. Dooley, Promotion effects in Co-based Fischer-Tropsch catalysis, Catalysis. 19 (2006) 1–40.
[41] H.M. Koo, X. Wang, A.R. Kim, C.-H. Shin, J.W. Bae, Effects of self-reduction of Co nanoparticles on mesoporous graphitic carbon-nitride to CO hydrogenation activity to hydrocarbons, Fuel. 287 (2021) 119437.
[42] H. Krzton, M. Niewiara, Studies on commercial carbon black by radial distribution function and rietveld refinement, Phys. Scr. 1995 (1995) 98.
[43] D.F.R. Mildner, J.M. Carpenter, On the short range atomic structure of non-crystalline carbon, J. Non. Cryst. Solids. 47 (1982) 391–402.
[44] M.S. Kane, J.F. Goellner, H.C. Foley, R. DiFrancesco, S.J.L. Billinge, L.F. Allard, Symmetry breaking in nanostructure development of carbogenic molecular sieves: Effects of morphological pattern formation on oxygen and nitrogen transport, Chem. Mater. 8 (1996) 2159–2171.
[45] V. Petkov, R.G. DiFrancesco, S.J.L. Billinge, M. Acharya, H.C. Foley, Local structure of nanoporous carbons, Philos. Mag. B. 79 (1999) 1519–1530.
[46] V. Mashindi, P. Mente, T.N. Phaahlamohlaka, N. Mpofu, O. Makgae, B.D. Moreno, D.H. Barrett, R.P. Forbes, P.B. Levecque, K.I. Ozoemena, Platinum nanocatalysts supported on defective hollow carbon spheres: oxygen reduction reaction durability studies, Front. Chem. (2022) 101.
[47] G. Ramos-Sanchez, P.B. Balbuena, Interactions of platinum clusters with a graphite substrate, Phys. Chem. Chem. Phys. 15 (2013) 11950–11959.

[48] W. Li, O.J. Borkiewicz, M. Saubanère, M.-L. Doublet, D. Flahaut, P.J. Chupas, K.W. Chapman, D. Dambournet, Atomic structure of 2 nm size metallic cobalt prepared by electrochemical conversion: An in situ pair distribution function study, J. Phys. Chem. C. 122 (2018) 23861–23866.
[49] P. Du, O. Kokhan, K.W. Chapman, P.J. Chupas, D.M. Tiede, Elucidating the domain structure of the cobalt oxide water splitting catalyst by X-ray pair distribution function analysis, J. Am. Chem. Soc. 134 (2012) 11096–11099.
[50] S.J. Gregg, K.S.W. Sing, H.W. Salzberg, Adsorption surface area and porosity, J. Electrochem. Soc. 114 (1967) 279C.
[51] Y. Tian, C. Xing, W. Wang, S. Zhang, Y. Zhang, A highly crosslinked, mesoporous poly (ionic liquid) containing salen–Pd for efficient, eco-friendly Suzuki–Miyaura coupling reactions, New J. Chem. 46 (2022) 8855–8862.
[52] A.I.M. Rabee, C.B.A. Gaid, G.A.H. Mekhemer, M.I. Zaki, Combined TPR, XRD, and FTIR studies on the reduction behavior of Co3O4, Mater. Chem. Phys. 289 (2022) 126367.
[53] J. Hong, E. Marceau, A.Y. Khodakov, L. Gaberová, A. Griboval-Constant, J.-S. Girardon, C. La Fontaine, V. Briois, Speciation of ruthenium as a reduction promoter of silica-supported Co catalysts: a time-resolved in situ XAS investigation, ACS Catal. 5 (2015) 1273–1282.
[54] S.K. Beaumont, S. Alayoglu, C. Specht, N. Kruse, G.A. Somorjai, A nanoscale demonstration of hydrogen atom spillover and surface diffusion across silica using the kinetics of CO2 methanation catalyzed on spatially separate Pt and Co nanoparticles., Nano Lett. 14 (2014) 4792–4796.
[55] A. Kogelbauer, J.G. Goodwin Jr, R. Oukaci, Ruthenium Promotion of Co/Al2O3Fischer–Tropsch Catalysts, J. Catal. 160 (1996) 125–133.
[56] T. Molefe, R.P. Forbes, N.J. Coville, Osmium@ Hollow carbon spheres as Fischer–Tropsch synthesis catalysts, Catal. Letters. 151 (2021) 875–887.
[57] N. Bungane, C. Welker, E. van Steen, M. Claeys, Fischer-Tropsch CO-hydrogenation on SiO2-supported osmium complexes, Zeitschrift Für Naturforsch. B. 63 (2008) 289–292.
[58] D. Nabaho, J.W.H. Niemantsverdriet, M. Claeys, E. Van Steen, Hydrogen spillover in the Fischer – Tropsch synthesis : An analysis of platinum as a promoter for cobalt – alumina catalysts, Catal. Today. 261 (2016) 17–27. https://doi.org/10.1016/j.cattod.2015.08.050.
[59] H. Romar, E. Rivoire, P. Tynjälä, U. Lassi, Effect of Calcination Conditions on the Dispersion of Cobalt Over Re, Ru and Rh Promoted Co/γ-Al 2 O 3 Catalysts, Top. Catal. 60 (2017) 1408–1414.
[60] M.S. Eluyemi, M.A. Eleruja, A. V Adedeji, B. Olofinjana, O. Fasakin, O.O. Akinwunmi, O.O. Ilori, A.T. Famojuro, S.A. Ayinde, E.O.B. Ajayi, Synthesis and characterization of graphene oxide and reduced graphene oxide thin films deposited by spray pyrolysis method, Graphene. 5 (2016) 143–154.
[61] N.T. Tung, T. Van Khai, M. Jeon, Y.J. Lee, H. Chung, J.-H. Bang, D. Sohn, Preparation and characterization of nanocomposite based on polyaniline and graphene nanosheets, Macromol. Res. 19 (2011) 203–208.
[62] Q. Sun, S. Kim, Synthesis of nitrogen-doped graphene supported Pt nanoparticles catalysts and their catalytic activity for fuel cells, Electrochim. Acta. 153 (2015) 566–573.
[63] S.E.M. Pourhosseini, O. Norouzi, H.R. Naderi, Study of micro/macro ordered porous carbon with olive-shaped structure derived from Cladophora glomerata macroalgae as efficient working electrodes of supercapacitors, Biomass and Bioenergy. 107 (2017)

287–298.
[64] A. Tavasoli, S. Taghavi, Performance enhancement of bimetallic Co-Ru/CNTs nano catalysts using microemulsion technique, J. Energy Chem. 22 (2013) 747–754.
[65] A. Olivo, V. Trevisan, E. Ghedini, F. Pinna, C.L. Bianchi, A. Naldoni, G. Cruciani, M. Signoretto, CO2 photoreduction with water: Catalyst and process investigation, J. CO2 Util. 12 (2015) 86–94.
[66] A. Tavasoli, A. Karimi, A.A. Khodadadi, Y.A.D.E. MORTAZAVI, S.M.A.L.I. MOUSAVIAN, Accelerated deactivation and activity recovery studies of ruthenium and rhenium promoted cobalt catalysts in Fischer-Tropsch synthesis, (2005).
[67] M. Trépanier, A. Tavasoli, A.K. Dalai, N. Abatzoglou, Co, Ru and K loadings effects on the activity and selectivity of carbon nanotubes supported cobalt catalyst in Fischer–Tropsch synthesis, Appl. Catal. A Gen. 353 (2009) 193–202.
[68] R. Van Hardeveld, F. Hartog, The statistics of surface atoms and surface sites on metal crystals, Surf. Sci. 15 (1969) 189–230.
[69] J. Van de Loosdrecht, B. Balzhinimaev, J.-A. Dalmon, J.W. Niemantsverdriet, S. V Tsybulya, A.M. Saib, P.J. Van Berge, J.L. Visagie, Cobalt Fischer-Tropsch synthesis: deactivation by oxidation?, Catal. Today. 123 (2007) 293–302.
[70] J. Wilson, C. de Groot, Atomic-scale restructuring in high-pressure catalysis, J. Phys. Chem. 99 (1995) 7860–7866.
[71] G.-Z. Bian, N. Fujishita, T. Mochizuki, W.-S. Ning, M. Yamada, Investigations on the structural changes of two Co/SiO2 catalysts by performing Fischer–Tropsch synthesis, Appl. Catal. A Gen. 252 (2003) 251–260.
[72] T.K. Das, G. Jacobs, P.M. Patterson, W.A. Conner, J. Li, B.H. Davis, Fischer–Tropsch synthesis: characterization and catalytic properties of rhenium promoted cobalt alumina catalysts☆, Fuel. 82 (2003) 805–815.
[73] J. Hong, P.A. Chernavskii, A.Y. Khodakov, W. Chu, Effect of promotion with ruthenium on the structure and catalytic performance of mesoporous silica (smaller and larger pore) supported cobalt Fischer–Tropsch catalysts, Catal. Today. 140 (2009) 135–141.
[74] H. Romar, A.H. Lillebø, P. Tynjälä, T. Hu, A. Holmen, E.A. Blekkan, U. Lassi, Characterisation and Catalytic Fischer–Tropsch Activity of Co–Ru and Co–Re Catalysts Supported on γ-Al 2 O 3, TiO 2 and SiC, Top. Catal. 58 (2015) 887–895.
[75] R.-S. Zhou, R.L. Snyder, Structures and transformation mechanisms of the η, γ and θ transition aluminas, Acta Crystallogr. Sect. B Struct. Sci. 47 (1991) 617–630.
[76] D.J. Moodley, J. Van de Loosdrecht, A.M. Saib, M.J. Overett, A.K. Datye, J.W. Niemantsverdriet, Carbon deposition as a deactivation mechanism of cobalt-based Fischer–Tropsch synthesis catalysts under realistic conditions, Appl. Catal. A Gen. 354 (2009) 102–110.

Chapter 5

Fischer-Tropsch synthesis: platinum promoted Co@HCS catalysts.

Chapter submitted for publication:

5.1. Introduction

Fischer-Tropsch synthesis (FTS) is an alternative and assuring route for transforming nonpetroleum and non-coal feedstocks, such as natural gas and biomass, into petroleum products and fine chemicals using syngas (CO/H_2) [1, 2]. FTS is known to produce cleaner fuels (low sulphur content) and is more economically friendly in cost compared to other routes derived from crude oil [3, 4]. Environmental problems that arise today due to the energy crises has led to the development of sophisticated and effective catalysts being developed by researchers to address the energy challenges faced in the world by moving away from coal to make fuels, but rather to make chemicals [5, 6]. FTS provides one route to achieve this.

Cobalt catalyst dispersed on a support material are renowned for their catalytic activity and selectivity in the FT reaction [7–9]. Co catalyst preference for syngas conversion in FTS is due to the high intrinsic activity, higher per pass conversion, good selectivity toward higher molecular weight hydrocarbons and a long lifetime of a Co catalyst relative to a Fe catalyst [10]. The active Co catalyst in FTS exists in two different metallic crystalline phases, namely the face centred cubic (fcc) structure and the hexagonal closed packed (hcp) structure [11]. The catalytic activity of Co is influenced by the number of Co active sites that are available on the surface of the catalyst. Optimization of the Co catalyst FT performance can be achieved by reactor design modification and process conditions, improving catalyst preparation methods, as well as introducing efficient support materials and promotors [12–16]. The support material interaction with the Co catalyst enhances metal dispersion and provides the anchorage to prevent catalyst sintering or agglomeration, and therefore assists in minimizing the associated loss in catalytic activity. However, support materials such as alumina and silica form strong metal support interactions (SMSI) with the Co, resulting in the formation of aluminate and silicate spinel compounds, respectively, which favour high Co dispersion at the expense of reducibility. Low reducibility of supported Co results in a decreased number of active sites, and this reduces the catalytic properties of a catalyst.

Well-known alternative support materials that reduce SMSI effects, are carbon-based materials. Carbon materials are relatively inert and hence a moderate interaction with the metal catalyst occurs that can result in a low SMSI [17]. In FTS reaction, a catalyst is supported by a wide variety of carbons [17]. One of these, the hollow carbon sphere (HCS) has a core-shell structure in which the core is empty. HCSs have a high surface area, excellent electronic conductivity, low weight, are mesoporous and are chemically inert. The encapsulation of active metal nanoparticles inside the HCSs can restrict metal sintering to the metal in the core, and can also lead to containment of fragmented catalyst particles [18–20]. The hollow morphology and defective mesoporous carbon structure of HCSs make them an interesting carbon support for use as a Co FT catalyst. The HCSs can be used as nanoreactors for the active phase metal encapsulated by the carbon structure; a heterogeneous catalyst in which mass transportation of reactants (e.g., H_2 and Co) and products to/from the HCS may influence the reaction outcome [21–24]. The relative chemical inertness of HCSs can reduce the SMSI effect and enable simpler reducibility and enhanced metal catalytic activity [25, 26].

Co catalyst reducibility and catalytic performance can be enhanced by an incorporation of a promoter [27]. Generally, Co promoters are noble metals (ruthenium, platinum, palladium and rhenium) that are added in small amounts to the supported Co catalyst. The promoter can significantly improve the Co reducibility thus improving the Co catalyst activity, selectivity and stability [28, 29]; the promoter itself may not necessarily possess catalytic activity. One of the more commonly used promoters is Pt. Pt's high affinity for H_2 activation (i.e. adsorption and dissociation) has been attributed to catalyse the reduction of Co oxide nanoparticles where the possibility of electronic/ligand effects from Pt-Co interactions may arise. Proposed mechanism(s) for the promotion effect(s) are linked to the promoter's location (direct or indirect contact) relative to the Co crystallites [30].

Hydrogen spillover is one of the proposed mechanisms which involves the dynamic movement of species that have been adsorbed to the surface of a solid's surface at various sites through dissociative adsorption of a H_2 molecule [31]. Scheme 1, illustrates the intrinsic primary and secondary hydrogen spillover steps, two possible effects, that may occur during the reduction of a Co oxide nanoparticle in the presence of a promoter (Pt). In primary hydrogen spillover, the promoter is in direct contact with the Co oxide and dissociation of hydrogen occurs on the promoter surface (step 2) into hydrogen atoms which migrate (step 3, Scheme 1(a)) to reduce Co oxide into Co^0 (metallic) and form water (step 4, Scheme 1(a)). In secondary hydrogen spillover, the promoter and Co oxide are separated by varying distances. Here the dissociated

hydrogen atom on the promoter has to migrate on the surface of the support material (step 3, Scheme 1(b)) (e.g., via hydroxyl groups on oxidic supports) with spillover to the Co oxide (step 4, Scheme 1(b)) which results in the reduction of Co oxide. This was demonstrated by Nebaho et al. [32] using a hybrid mixture of Co/Al_2O_3 and Pt/Al_2O_3. Despite the physical separation of the Co catalyst and Pt promoter, they observed an enhancement in Co reducibility. There have been reports of hydrogen species spilling over a distance ranging from a few nanometres to several centimetres. [33–39].

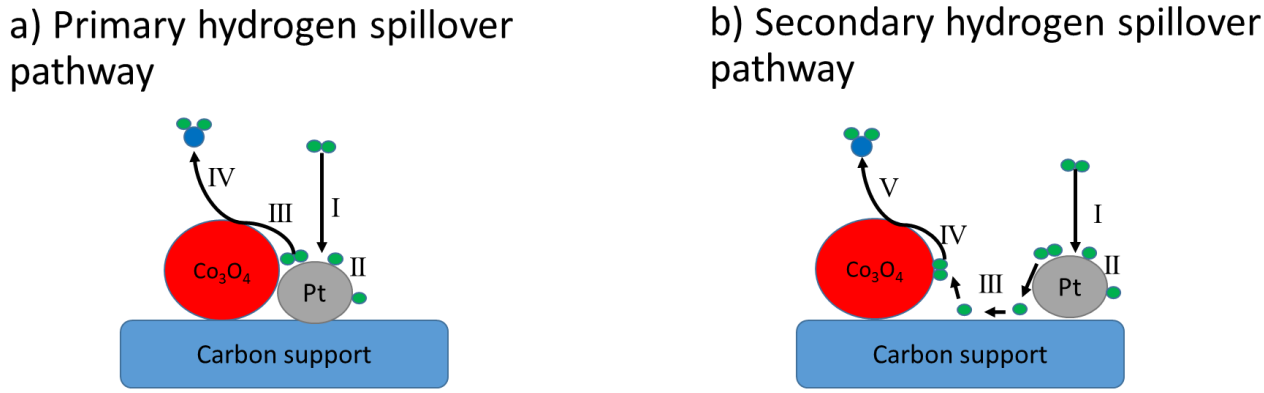

Scheme 1: (a) Primary and (b) secondary hydrogen spillover mechanism (pathways) [40, 41].

The aim of this study was to evaluate the Pt promoter effect on Co encapsulated inside a HCS (Co@HCS) catalyst during reduction experiments and Fischer-Tropsch synthesis reactions. Two hybrid catalysts were prepared which include a bimetallic PtCo@HCS catalyst where both Pt and Co metals were encapsulated inside HCS, and a Pt/(Co@HCS) catalyst where Co was inside, and Pt was outside the HCS. The PtCo@HCS was used to study the primary hydrogen spillover effect, while Pt/(Co@HCS) was used to study the secondary hydrogen spillover effect with the HCS carbon shell as a physical barrier between Pt and Co [42]. The HCS encapsulation ability thus enabled the study of the hydrogen spillover mechanism. Investigations were also conducted into the impact of the spillover effect on the catalysts' FT performance.

5.2. Experimental

5.2.1 Materials

All samples were of analytical grade and they were purchased from various sources. The cobalt nitrate hexahydrate (Aldrich), hexachloroplatinic acid hexahydrate (Merck), platinum

acetylacetonate [$Pt(acac)_2$, 97%], ammonia solution (25%; Fluka), ethanol (98%; Merck), hexadecyltrimethylammonium bromide (CTAB; Aldrich), styrene (Aldrich), polyvinylpyrollidone (PVP, MW 40 K, Aldrich), formaldehyde (37%; Aldrich), potassium persulfate (Eimer and Amend), hydrazine (35% Aldrich), and deionized water were used as received for the experiments.

5.2.2 Synthesis of Co@HCS and CoPt@HCS catalysts

3.4.3. Synthesis of polystyrene spheres (PSSs) [43]

Styrene (8 mL) and polyvinylpyrollidone (PVP, 0.2 g) was dispersed and dissolved in a mixture of 200 mL ethanol and 50 mL deionized water by in a round bottom flask. The mixture was sonicated and stirred for 15 min. Thereafter, potassium persulfate (KPS, 0.3 g in 10 mL deionized water) was added to the prepared reaction mixture while stirring. The mixture was then heated at 80 ^{o}C for 24 hours. After the reaction the product was cooled, filtered, and washed successively using deionized water. The obtained yield was ~ 6 g.

3.4.4. Synthesis of Co or CoPt on the polystyrene spheres (10Co/PSSs; 10CoxPt/PSSs) (x = 0.1, 0.5, 1)

PSSs (3 g) were added to a mixture of 75 mL deionized water and 25 ml ethanol. Cobalt nitrate hexahydrate (0.45 g) was added to this mixture while stirring, until the solution turned red. Thereafter, 10 mL of hydrazine (2M) was slowly added to the prepared solution dropwise, and the solution was stirred for 12 h to ensure complete deposition of Co nanoparticles onto the PSSs. The sample was called 10Co/PSS.

The bimetallic CoPt/PSSs composite was prepared by adding both the cobalt (0.45 g) precursor and the ammonium hexachloroplatinic acid hexahydrate (0.05M, 3 ml) onto the PSS, followed by hydrazine addition as stated above. This is expected to give a catalyst with a nominal Co/Pt mol or wt ratio of 10:1. The sample was called 10Co1Pt/PSS. Two further catalysts with ratios of Co:Pt of 20:1 and 100:1 (0.5Pt/10Co/PSS and 0.1Pt/10Co/PSS) were made by the same method as above but using, 1.5 ml and 0.3 ml of ammonium hexachloroplatinic acid hexahydrate (0.05M), respectively.

3.4.5. Synthesis of Co or CoPt nanoparticles encapsulated inside hollow carbon spheres (10Co@HCS and 10CoxPt@HCS).

10Co/PSSs or 10Co1Pt/PSSs (1 g) and ammonia solution (25%; 4 mL) were added to a mixture of 70 mL ethanol and 15 ml deionized water and the mixture was sonicated for 30 min. Subsequently, resorcinol (0.5 g), formaldehyde (0.5 mL) and hexadecyltrimethylammonium bromide (3 g) were added to the above solution. The solution was allowed to stir at room temperature for 24 h. A resorcinol-formaldehyde (RF) core shell structure formed around the 10Co/PSSs or 10Co1Pt/PSSs and the material was filtered and washed successively with water and ethanol, followed by drying at 80 ^{o}C for 12 h. Template removal and carbonization of the prepared composites was performed using a two-step horizontal chemical vapour deposition procedure. Template removal was done under a flow of nitrogen gas (50 ml/min) at an isothermal temperature of 350 ^{o}C for 1 h to decompose and remove the PSSs. This was followed by carbonization of the RF core shell structure under a flow of nitrogen gas (50 ml/min) at 600 ^{o}C for 2 h. The resulting products were called 10Co@HCS and 10Co1Pt@HCS. The same method was used to make 10Co0.5Pt/PSS and 10Co0.1Pt/PSS samples to give the products 10Co0.5Pt@HCS and 10Co0.1Pt@HCS.

5.2.3 Synthesis of xPt/(Co@HCS) (x = 0.1, 0.5, 1) catalyst

To achieve a nominal 1 wt.% loading of Pt onto the surface of a 10Co@HCS catalyst (containing 10 wt%Co), platinum acetylacetonate [$Pt(acac)_2$, 97%] (13.5 mg) was added to the 10Co@HCS (0.4 g) catalyst and this was sonicated for 10 min to thoroughly dry-mix the two solids. The mixed composite was then transferred into a cylindrical quartz tube that was placed in a tubular horizontal furnace under a steady argon (50 ml/min) stream. The furnace was ramped to 100 ^{o}C and kept isothermal for 30 min to remove any moisture from the sample. The furnace was further ramped up to 350 ^{o}C at a heating rate of 2.5 ^{o}C/min and kept isothermal for 2 h. After 2 h, the reactor was left to cool down naturally to room temperature to produce 1Pt/(10Co@HCS) [44].

For the 0.5Pt/(10Co@HCS) and 0.1Pt/(10Co@HCS) products the same method as above was used, however, 6.75 mg and 1.35 mg of platinum acetylacetonate [Pt(acac)2, 97%] was used, respectively.

5.3 Results

5.3.1 Transmission electron microscopy (TEM)

The synthesis of the hollow carbon spheres (HCS) was achieved by using monodispersed polystyrene spheres (PSSs) as a template using a standard procedure [43]. The TEM image of the PSSs showed that they were uniform, spherical in shape, and had a smooth surface (Fig.

5.1 (a)). The particle size distribution was between 350 and 600 nm with an average diameter of 490 nm (Fig. 5.1 (b)). The PSSs were prepared to be larger than 200 nm in diameter to prevent coagulation from occuring and the formation of large, connected nanospheres [45]. The PSS template was then coated with Co (10 wt.%) and Pt (0.1, 0.5 and 1 wt.%) to form 10Co/PSSs or 10Co-xPt/PSSs (x = 0.1, 0.5, 1 wt.%).

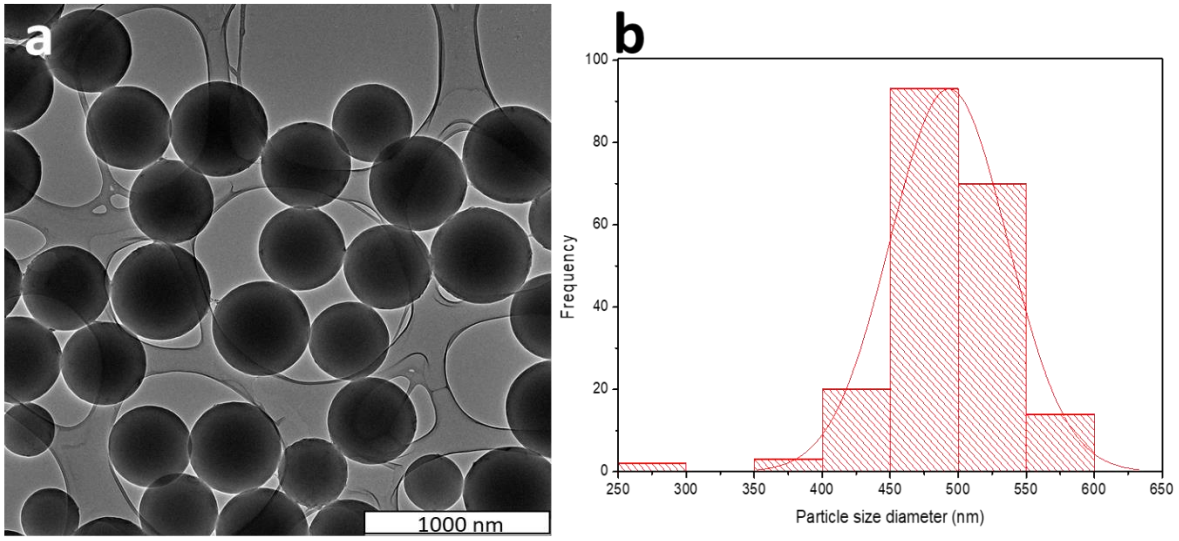

Fig 5.1: (a) TEM image of PSSs and (b) particle size distribution

The 10Co/PSSs or 10Co1Pt/PSSs template was then covered with RF (resorcinol formaldehyde) and CTAB. The addition and RF polymerization steps led to the Co/PSS coating as previously reported [46, 47]. The synthesized RF coated template was then heated to decompose the PSS template and carbonization took place to form the 10Co@HCS or 10Co1Pt@HCS. The same method was used to convert the RF covered in 10Co0.5Pt/PSS and 10Co0.1Pt/PSS prepared samples to give the products 10Co0.5Pt@HCS and 10Co0.1Pt@HCS.

The average nanoparticle size, HCS diameter and carbon shell thickness were determined using the TEM images and the ImageJ software. Fig. 5.2 shows the TEM images of the (a) HCS's support and the (b) shell thickness. The HCS diameter ranged between 350 and 400 nm with the average size of 380 nm and the carbon shell thickness had an average width of 28 ± 5 nm. It was important for the carbon shell of the support to be porous with short dimensions to enable both primary and secondary hydrogen spillover to take place by traveling a short distance through the HCS carbon shell. The average HCS diameter (380 nm) was lower than that of the polystyrene spheres (495 nm) and this was due to a shrinkage that occurs during the

carbonization process [48]. This decrease can also be caused by the dehydration of the cross-linked carbon precursor that occurs during carbonization [49, 50].

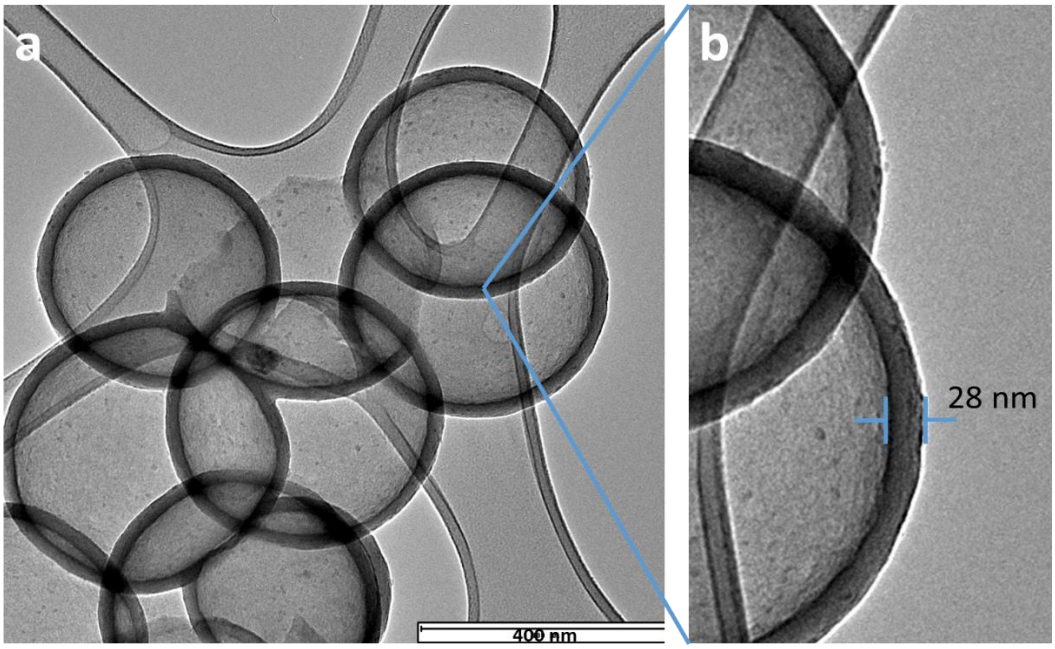

Figure 5.2: TEM images of (a) HCSs and (b) carbon shell thickness (28 ± 5 nm)

Electron microscopy measurements were performed to verify the architectures of the synthesised Co catalysts (Fig. 5.3). The synthesised Co@HCS catalyst had well dispersed Co nanoparticles (3.5 ± 2 nm) inside the HCS support. The TEM images, Fig. 5.3, revealed a spherical HCS morphology with metal nanoparticles in the core shell structure for the bimetallic PtCo@HCS catalysts (Fig. 5.3 d, e, and f) and a similar morphology for the Pt/(Co@HCS) catalysts (Fig. 5.3 a, b, and c). TEM images of the catalysts revealed that the majority (> 90%) of the HCS's support structure was still intact and undamaged. [19, 51].

The average size of the Co nanoparticles in (a) 10Co0.1Pt@HCS, (b) 10Co0.5Pt@HCS, and (c) 1% Pt/10%Co@HCS catalysts were 5 ± 3 nm, 6 ± 3 nm and 7 ± 2 nm. The Co@HCS catalyst (chapter 4, Fig 4.1) had a smaller average Co particle size (3.5 nm). From this observation it can be confirmed that incorporation of Pt promoter to Co@HCS catalyst did result in a small change in the size of Co nanoparticles (close to experimental error) that showed some increase as the Pt content increased. This is consistent with literature studies involving Pt addition to Co which showed little to no significant effect on the size of Co nanoparticles. For instance, Zhang et al. reported that a Pt promoter added to Co catalyst, supported on carbon nanotubes, gave no Co size increase of note. The small size effect seen was attributed to a chemical interaction between the Co oxide nanoparticles and the support resulting from the

decomposition of the Co precursor on the support [52]. Chu et al. also confirmed that no significant effect was observed from adding Pt to Co_3O_4 nanoparticles supported on Al_2O_3 and attributed the size of the Co_3O_4 nanoparticles to the pore diameter of the support [53]. Similar observations of a limited change in size of Co nanoparticle size by Pt was observed for the Pt/(Co@HCS) catalysts. The average particle size of Co nanoparticles in (d) 0.1Pt/(10Co@HCS), (e) 0.5Pt/(10Co@HCS), and (f) 1Pt/(10Co@HCS) catalysts were 5 ± 3 nm, 6 ± 2 nm and 6 ± 3 nm, respectively. A similar trend was observed in a study where the effects of Co and Ru intimacy in FT catalysts was investigated using HCS supports in that the Co change in particle size was insignificant with introduction of a Ru promoter [42]. In contrast, the introduction of an Os promoter showed a change in the particle size of Co in relation to intimacy and Os percentage loading (chapter 4).

The Pt nanoparticles in the xPt/(10Co@HCS) were difficult to observe due to their low loadings and the carbon shell thickness [54].

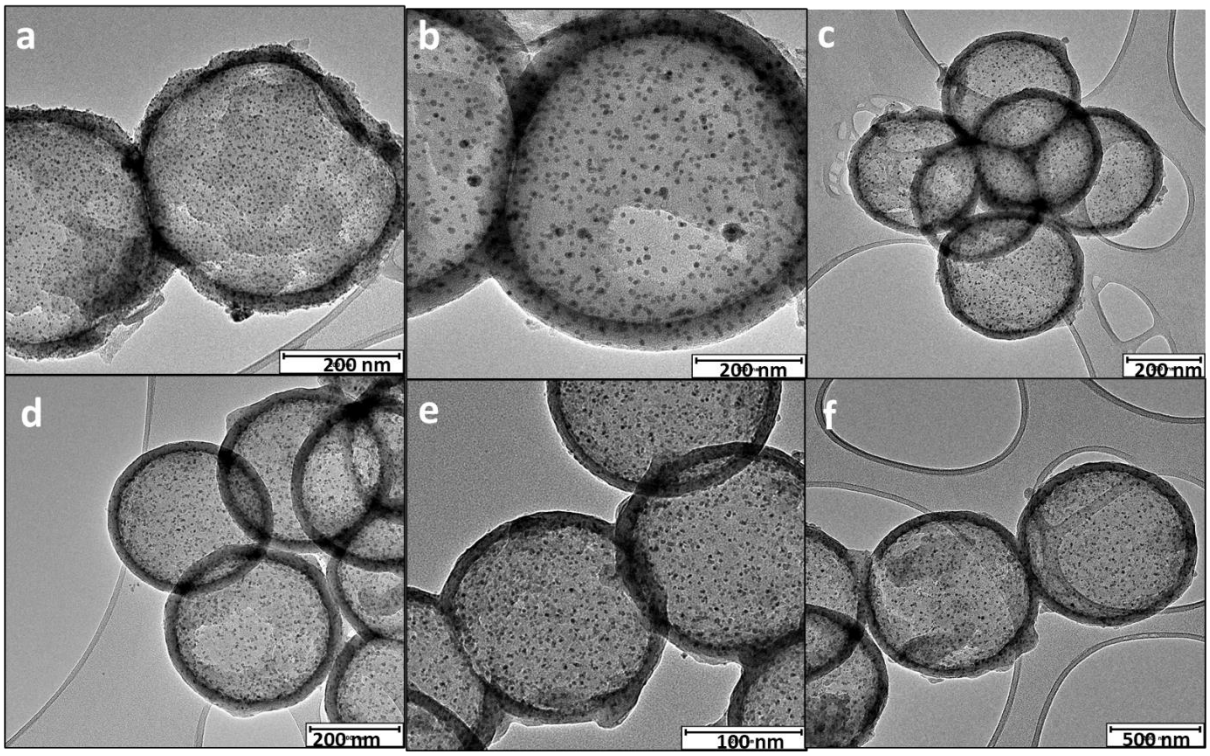

Figure 5.3: TEM images of (a) 10Co0.1Pt@HCS, (b) 10Co0.5Pt@HCS, (c) 10Co1Pt@HCS, (d) 0.1Pt/(10Co@HCS), (e) 0.5Pt/(10Co@HCS), and (f) 1Pt/(10Co@HCS)

5.3.2 Scanning electron microscopy (SEM) and energy dispersive X-ray (EDX) spectroscopy

The synthesised catalysts were confirmed to be spherical and hollow in structure, as confirmed from the SEM images of some partially broken and non-broken HCS's. The EDX analysis showed the elemental composition of the synthesized nanostructure catalysts. Fig. S5.1 (a), Fig S5.2 (a) and Fig S5.3 (a) shows the SEM images of 10Co@HCS, 1Pt/10Co@HCS, and 1Pt/(10Co@HCS) respectively. From EDX spectrum 1 (Fig. S5.1 (b)) it can be confirmed that Co nanoparticles were indeed present in Co@HCS, and both Co and Pt nanoparticles were present in the Pt/Co@HCS and Pt/(Co@HCS) catalysts (Fig S5.2 (b) and S5.3 (b)). The other Pt (0.5% and 0.1%) loaded catalysts showed similar results.

5.3.3 Powder X-ray diffraction (XRD)

PXRD patterns of 10Co@HCS, Pt/10Co@HCS and Pt/(10Co@HCS) catalysts are shown in Fig 5.3 (a) and (b). The broad peak at 2θ between 25^{o} and 30^{o} observed for all the synthesised catalysts was attributed to the disorderd sp^2 hybridized carbon shell structure [55]. Due to the very small quantities (metal loadings or concentration) of Pt promoter and to the small Pt particle sizes, no PXRD patterns of Pt were observed.

The various PXRD spectra showed the presence of Co_3O_4, CoO and fcc/hcp Co phases (Fig 5.3, Table 5.1 and S5.1). A comparison of the patterns of the synthesised catalysts showed that the peaks due to the Co_3O_4 as well as the CoO phase (ICSD (9362) and COD (9008618) collection files) decreased with Pt loading. The presence of the CoO phase was due to the autoreduction of the Co_3O_4 phase when it in contact with the carbon shell. This reduction process was also observed for Co@HCS catalysts promted by Os (chapter 4) [56].

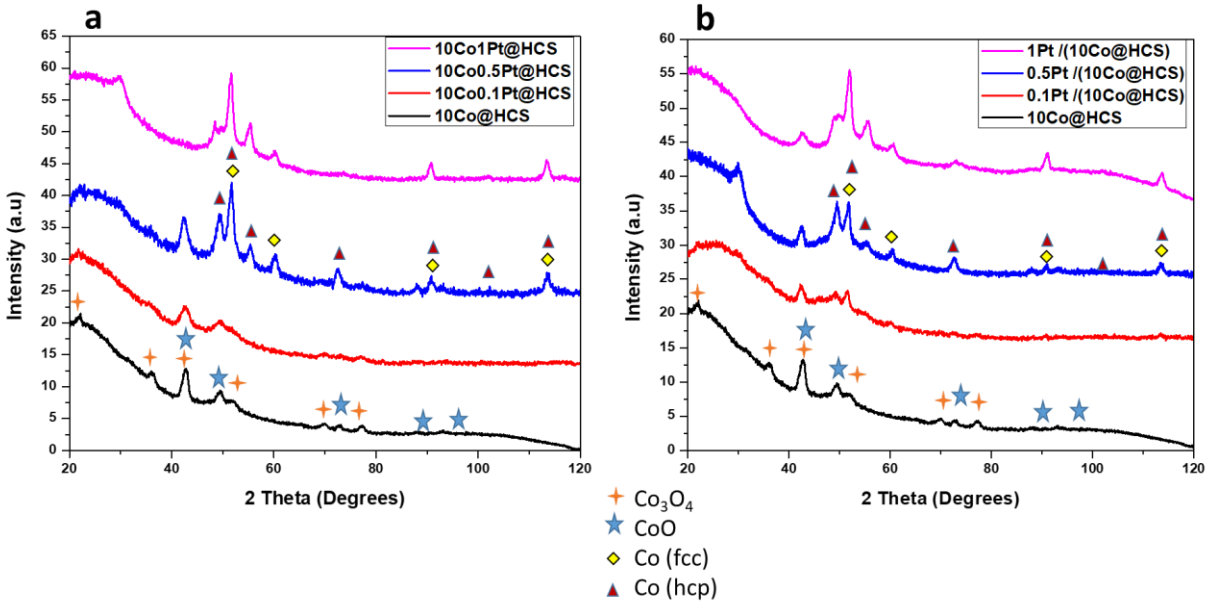

Figure 5.3: PXRD pattern of Co@HCS, (a) Pt/Co@HCS and (b) Pt/(Co@HCS) catalysts.

The Co (fcc and hcp) phases were present in the Pt promoted catalysts (Table 5.1) and the peaks due to these phases increased with an increase in CoO reduction with Pt loading. This observation indicates further reduction of the Co oxides to Co metal. The data gathered suggests that Pt (and carbon) promoted the reduction of Co oxides, with no significant Co particle size change (TEM particle size). The 10CoxPt@HCS catalysts Co (hcp/fcc) ratios followed the pattern: 10Co0.1Pt@HCS (0.19) < 10Co0.5Pt@HCS (0.23) < 10Co1Pt@HCS (0.75) suggesting that the Pt induced an increase in the hcp Co content. In contrast,, the 10CoxPt@HCS catalyst Co (hcp/fcc) ratios followed the pattern: 0.1Pt/(10Co@HCS) (n/a) > 0.5Pt/(10Co@HCS) (0.60) > 1Pt/(10Co@HCS) (0.52) suggesting that when the pt was removed from the Co the hcp ratio did not increase. The 0.1Pt/(10Co@HCS) catalyst can be assumed to show a similar Co (hcp/fcc) ratio to that of 0.5Pt/(10Co@HCS) and 1Pt/(10Co@HCS) catalysts based on the trend given. In summary, the comparison of the Co (hcp/fcc) ratios between 10CoxPt@HCS and xPt/(10Co@HCS) cataysts showed that with an increase in Pt loading the 10CoxPt@HCS catalysts tended to have more hcp Co than the xPt/(10Co@HCS) catalysts which had more fcc Co. The data are consistent with the literature which has indicated that a low reduction temperatures usually leads to the formation of Co (hcp) while a high reduction temperatures lead to Co (fcc) formation [40]. The Co (hcp) phase has been reported in the literature to be the more FT catalytically active than the Co phase.

The data thus suggets that Pt can facilitate the formation of Co (hcp) with an increase in Pt loading via a primary hydrogen spillover effect, but when Pt promotion occurs via migration of the atomic H occurs from the initiator to the acceptor via the carrier it facilitates the formation of Co (fcc) with increase in Pt loading via a secondary spillover effect (Table 5.1). This data suggests that the role Pt plays in the improvement of Co reducibility and formation of the highly active Co (hcp) phase for the FT process can be explained by both the primary and secondary hydrogen spillover effects.

Earlier hydrogen spillover process studies were conducted on Ru/Co systems in order to explain the Ru promoter effects [57]. A study by Hong et al., used X-ray spectroscopy (XAS) and their data suggested that a Co_3O_4 nanoparticle lattice with Ru ions implanted inside of it acted as a promoter for Co_3O_4 reduction at low temperatures. [27]. Another study proposed that an intimate interaction or close proximity between the Co_3O_4 and the Ru nanoparticles resulted in promoter effects that gave a lowering of the reduction temperature of Co_3O_4 [58]. Data in Chapter 4 also showed that the close proximity of the Os promoter to Co enhanced the reduciblity of Co_3O_4 nanoparticles and that the Co phase was affected by the presence of the Os promoter nanoparticle. The change in phase at low Pt loading is explained by a competitive effect between direct H_2 reduction (to give hcp Co) and Pt induced H_2 reduction (to give hcp Co). Clearly as the Pt concentration is increased the preferred phase (hcp) is formed in a competitive reaction. This is a desirable effect due to the phase being more FT catalytically active.

Table 5.1. Relative Co phase abundances (wt. %)

SAMPLE	CO_3O_4	CoO	CO(FCC)	CO(HCP)	OTHER	HCP/FCC RATIO
10%Co@HCS	56.554	43.45	-	-	-	-
10Co0.1Pt@HCS	-	63.24	30.96	5.81	-	0.19
10Co0.5Pt@HCS	-	55.87	35.92	8.21	-	0.23
10Co1Pt@HCS	-	31.37	39.206	29.43	-	0.75
0.1Pt/Co@HCS	**Not enough useable information in data – poor peak info**					n/a
0.5Pt/(10Co@HCS)	-	17.83	20.78	12.49	**Graphite** 48.90	0.60
1Pt/(10Co@HCS)	-	5.83	31.18	16.09	**Graphite** 46.89	0.52

5.3.4 Nitrogen absorption-desorption analysis

Textural properties of the HCSs and prepared catalysts was analysed using the nitrogen absorption-desorption method (BET). Fig S4, illustrates the N_2 absorption-desorption isotherm curves of the HCS and the Co@HCS, CoxPt@HCS and xPt/(Co@HCS) catalysts. All the catalysts presented the type I/IV adsorption isotherms which reveal both micropores and mesopores [59].

Table 5.2 shows the data collected for the surface area, pore volume and pore size for HCSs of the prepared catalysts. The porous nature of the HCS carbon shell was enhanced by the porogen (CTAB) that was used during the carbon shell synthesis [60]. A similair observation of high surface area and microporosity of HCS materials has been reported as a result of using microporous spherical templates [19, 61]. The surface area of the HCSs was shown to decrease with the introduction of metals loaded inside or outside the HCS support material, which can be accounted for by the metal nanoparticles obstructing some of the micropores, thus altering the carbon shell's pore structure.

Table 5.2. Textural properties (surface area, pore volume and average pore size) of the hollow carbon sphere support and the Co encapsulated catalysts.

SAMPLE	**SURFACE AREA (M^2/G)**	**PORE VOLUME (CM^3/G)**	**MESOPORE SIZE (NM)**
HCSs	532	0.51	5.0
10Co@ HCS	508	0.59	9.8
10Co0.1Pt@HCS	371	0.54	8.7
10Co0.5Pt@HCS	358	0.63	6.8
10Co1Pt@HCS	323	0.21	3.1
0.1Pt/(10Co@HCS)	495	0.73	6.9
0.5Pt/(10Co@HCS)	435	0.67	5.4
1Pt/(10Co@HCS)	389	0.48	4.2

5.3.5 Temperature programmed reduction (TPR)

A TPR study was conducted to elucidate Co's reduction behaviour and the impact of the Pt promotor on the synthesized catalysts. The peaks present at a temperature greater than 600 °C, in all the catalysts, are due to the gasification of the carbon material to CH_4 (Fig. S5) [18]. Peaks above 600 °C for catalysts supported on carbon materials are usually assigned to the gasification of the carbon support when using CNTs [3, 57] and solid carbon spheres [18].

To observe the Co reduction peaks, the TPR profiles were expanded in the region < 500 ^oC (Fig 5.10 and Fig 5.11). All the catalysts showed a peak at temperatures below 150 ^oC and this peak is attributed to the evolution of water. Another possibility could be NO and the reduction of nitrate species. Nitrates are the remnants of the $Co(NO_3)_2$ precursor. The $Co(NO_3)_2$ peaks were not observed using XRD which implies low nitrate concentrations were probably present as tiny, finely dispersed, and/or amorphous particles with no long-range ordering. It is also possible that this peak could be attributed to the reduction of CoOOH species to Co_3O_4 [62]. These catalysts' TPR behaviour exhibited the typical two-step reduction of Co_3O_4 species via conversion to a CoO intermediate phase with the final step being converted from CoO to metallic Co. The two-step reduction equations are as follows [63]:

First reduction step: $Co_3O_4 + H_2 \rightarrow 3CoO + H_2O$ (ca. 230 – 320 ^oC) Eqn: 1

Second reduction step: $3CoO + 3H_2 \rightarrow 3Co + 3H_2O$ (ca. 325 – 430 ^oC) Eqn: 2

The TPR first reduction and second reduction peaks are shown in Table 5.3. The unpromoted Co@HCS catalyst had a first reduction peak at 320 ^oC, followed by the second reduction peak at 430 ^oC. The Pt promoter reduced the reduction temperature of both the first and second reduction peaks [52, 64]. The extent of the downward shift of the reduction peak to lower temperatures was impacted by the distance between the Pt and Co relative to each other.

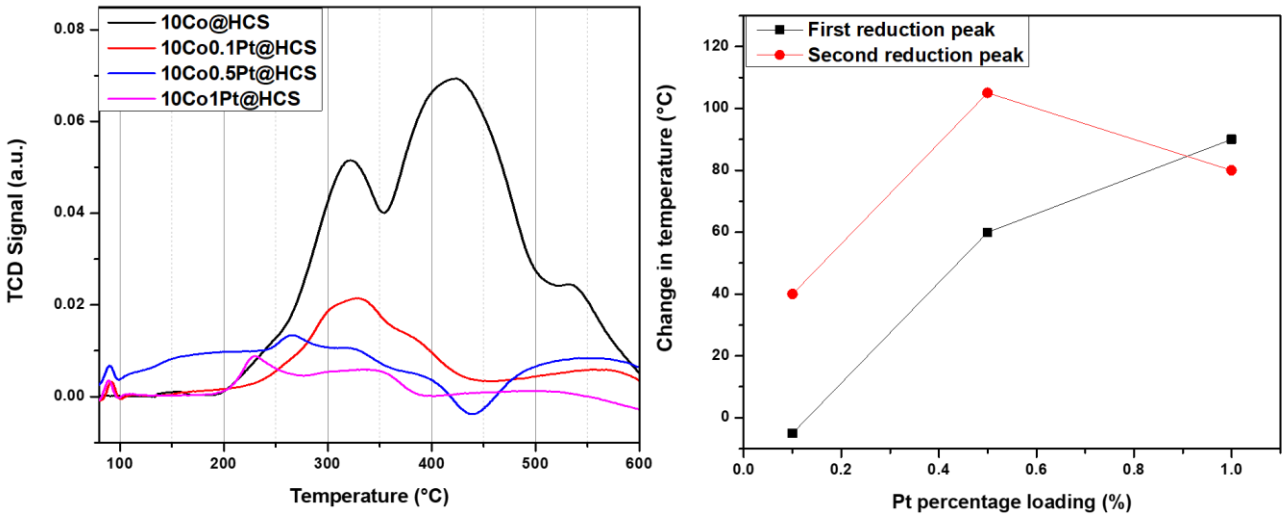

Figure 5.10: (a) TPR profile of the secondary hydrogen spillover effect and (b) the relative change in temperature with Pt percentage loading.

The TPR profiles of the (0.1, 0.5 and 1% Pt loading), and 10%Co@HCS catalysts are shown in Fig 5.10 (a). As can be seen from the intensity of all the Pt promoted Co samples, the peaks are small due to some reduction that occurred during the synthesis stages when Co is close to Pt. The TPR profiles showed significant lower reduction temperatures when the Pt promoter was placed inside the HCSs along with the Co catalyst. The addition of Pt had an effect on both these reduction steps, causing a shift in the peaks assigned to them, to lower temperatures. This is in agreement with reports in the literature on the effect of Pt on Co reducibility [52]. A change in temperature for the first reduction step of Co_3O_4 was approximately by 5, 58 and 95 ^oC for the CoxPt@HCS catalysts (x = 0.1%, 0.5%, 1%, respectively), Fig 5.10 (b). The second reduction step showed a larger change in the reduction temperature with Pt percentage loading, with changes of approximately 40, 108 and 79 ^oC for the three xOsCo CoxPt@HCS catalysts. This observation is in agreement with a study on co-impregnation of SiO_2 and Al_2O_3 with $Co(NO_3)_2 \cdot 6H_2O$ and $Pt(NH_3)_4(NO_3)_2$ which revealed a significant enhancement in the reduction of Co oxide [65].

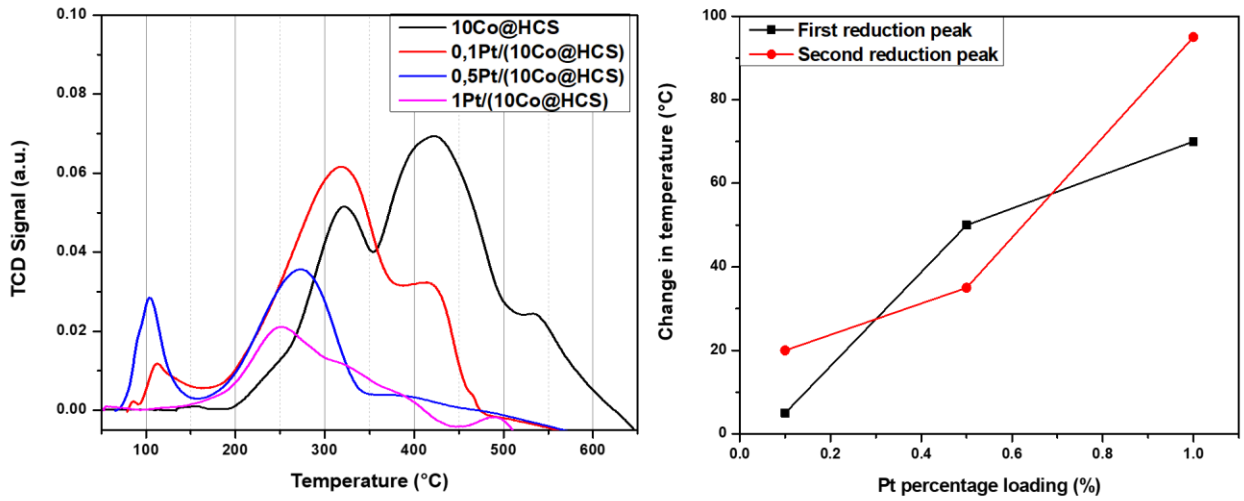

Figure 5.11. (a) TPR profile of the primary hydrogen spillover effect and (b) the change in temperature with Pt percentage loading.

The TPR profiles of the Pt/(10Co@HCS), (0.1, 0.5 and 1% Pt loading) and the 10% Co@HCS catalysts are shown in Fig. 5.10 (a). The Pt/(Co@HCS) catalysts followed a two-step reduction of Co_3O_4 to Co^0, with CoO being the intermediate phase. It is noted that when a higher percentage loading of Pt is added to the Co@HCS, Fig. 5.11 (b), a temperature reduction or downward shift of the reduction peaks, relative to the reduction step of Co@HCS, occurs (Fig 5.7 (b)). As the percentage loading increased the change in the first reduction step temperature was approximately 5, 52, 70 ^oC for the three Os catalysts, xPt/(Co@HCS) (x = 0.1%, 0.5% and 1%, respectively). The second reduction step temperature change was approximately 20, 34, 98 ^oC, respectively.

The downward shift to lower temperature of the reduction peaks is due to a secondary spillover effect. A physical barrier (carbon shell) separated the Co_x and Pt, with Pt being outside and Co oxide being inside the HCS's. The apparent decrease in the amount of hydrogen uptake suggests the occurrence of diffusion limitations of the H atoms when the Co oxide is separated from the Pt [30]. This could be due to some of the Co already being reduced. The secondary hydrogen spillover effect has been observed, in a hybrid Pt-Co [66] and hybrid Rh-Co [67] catalyst where the promoters, Pt and Rh were separated from Co oxide by some distance using alumina supports. The secondary hydrogen spillover effect was also observed for the Ru@MHCS@Co sample, where the carbon shell served as a barrier separating Ru and Co, with Ru inside and Co oxide outside [42].

Generally, one hydrogen molecule is consumed in the first reduction step of Co_3O_4 nanoparticles (Eqn 1), followed by consumption of three hydrogen molecules in the second reduction step (Eqn 2). A reduction peak ratio is thus expected to be 1:3 and such observation are seen in the TPR profile of Co@HCS catalyst. On the promoted catalysts first reduction peak had a peak area ratio that was greater than the second reduction peak. As seen in earlier studies, this discrepancy can be attributed to the noble metal promoter. For example, Ru ions doped inside a Co_3O_4 lattice can assist with the low temperature reduction of the oxide [27].

From the reduction profiles observed it can be confirmed that Pt does facilitate both the primary and secondary hydrogen spillover effects. Additionally, it was found that the promoter effects of Pt were not as prominent when Co_3O_4 and Pt were separated by a carbon shell compared to when the two metals were in close proximity. This observation is in agreement with a study on the effect of Ru on Co in FTS in that the reduction profiles showed that the Ru promoter effects were not as prominent in a catalyst where Co (15% wt) and Ru (5% wt) were separated by a HCS shell (Co first reduction peak: 310 ^oC, second reduction peak: 430 ^oC) as in the catalyst where the two metals were in close proximity (Co first reduction peak: 247 ^oC, second reduction peak: 482 ^oC) [68]. A similar trend was observed with the Os promoter in chapter 4.

Table 5.3: The first and second reduction temperatures of the synthesised catalysts

SAMPLE	FIRST REDUCTION PEAK (°C)	SECOND REDUCTION PEAK (°C)
10%Co@ HCS	320	430
10Co0.1Pt@HCS	325	390
10Co0.5Pt@HCS	260	325
10Co1Pt@HCS	230	350
0.1Pt/(10Co@HCS)	315	410
0.5Pt/(10Co@HCS)	270	395
1Pt/(10Co@HCS)	250	335

5.3.6 Fischer-Tropsch Synthesis (FTS) evaluation

The FTS performance and promoter effect on the synthesised catalysts were evaluated at 220 (Table 5.4) and 250 °C (Table S5.2) for 50 hours at each reaction temperature. Prior to FTS evaluation, a pre-treatment *in-situ* hydrogen reduction of the catalysts was performed at a temperature of 350 °C for 18 hours [42, 69, 70]. FTS CO conversion and selectivity data were then obtained for Co@HCS, CoPtx@HCS and Ptx/(Co@HCS) catalysts as shown in Table 5.4.

According to the table the catalytic activities of the catalysts followed the following order 10Co1Pt@HCS (15.0%) > 1Pt/(10Co@HCS) (6.7%) >10Co@HCS (4.2%). This trend was consistent at both reaction temperatures. As the temperature rose, CO conversion increased for all of the catalysts. The unpromoted catalyst showed to have the lowest CO conversion compared to the Pt promoted catalysts, thus showing that both primary and secondary spillover effect resulted in increased CO conversions. This observation can be attributed to the Pt promoter [71]. A significant increase in CO conversion was observed with intimacy between the Co and Pt promoter. Due to the direct contact or close proximity of Pt with Co, easy reduction of the Co oxide was expected which subsequently resulted in the generation of active Co (hcp) particles [11]. The generation of active Co (hcp) phase has a higher intrinsic activity for CO hydrogenation reactions compared to the Co (fcc) phase [30]. An increase in Pt percentage loading in 10CoxPt@HCS catalysts, which had high Co hcp/fcc ratios showed an increase in the CO conversion. In this study, promoted catalysts with higher Pt loading showed noticeably improved CoOx reducibility and Co dispersion.

It is worth noting that promoters, such as Pt, can also have a "cleansing effect" on the Co surface by removing unreactive species such as carbon, which can enhance the CO conversion [29, 72, 73]. This effect is likely to be more pronounced when Co and Pt are in close contact, as in the primary hydrogen spillover process which was observed with CoPt@HCS catalysts.

The Pt/(Co@HCS) catalysts showed lower activity than the CoPt@HCS catalyst. This could be due to a number of interlinked factors observed in catalysts that undergo secondary spillover, such as the lowered ability to reduce the Co oxide, resulting in lowered concentration of Co (hcp) (due to Co(fcc) formation), or simply the distance that the spillover hydrogen has to travel (~30 nm) [19, 68]. Additionally, the carbon shell separating the Co and Pt may block some of the pores of the support, limiting the diffusion of the spillover H atoms which was observed in the BET studies.

A diminished Pt promoter effect in the secondary hydrogen spillover process was also observed by Nabaho et al. for their catalyst, where Pt and Co were separated by an alumina support [72]. They attributed this effect to CO poisoning of the Pt surface, which can inhibit the hydrogenation reaction [74]. This phenomenon is well-known in olefin hydrogenation reactions and PEM fuel cells [75].

The hydrogen spillover effect was also observed to affect the hydrocarbon selectivity of the catalysts. In the case of the catalysts studied in Table 5.4, the methane selectivity increased with increased contact between Pt and Co: 10%Co@HCS (18.8%) < 1Pt/(10Co@HCS) (22.5%) < 10Co1Pt@HCS (31.3%). Another observation was that an increase in Pt loading resulted in increased methane selectivity and a decrease in C_5+ liquid hydrocarbons. A high selectivity for the production of high molecular weight hydrocarbons was demonstrated by the unpromoted catalyst, C_5+, compared to Pt promoted Co catalysts and this is likely due to the high hydrogenation activity of the Pt promoter, which is generally expected in catalysts with Pt loadings greater than 0.1% [76]. The close contact between Co and Pt in the CoPt@HCS catalyst resulted in a higher methane selectivity, which is undesirable.

Overall, the catalytic activity and selectivity of the Co catalyst were both impacted by the primary and secondary spillover effects of the Pt nanoparticles in FTS.

Table 5.4: Fischer-Tropsch synthesis performance of the catalysts**.**

Sample	CO Conversion (%)	TOF ($x10^{-3}$ s)[a]	Activity ($x10^{-6}$) ($mol_{CO}/g_{Co}.s$)	Selectivity (C mol) %		
				C_1	C_2-C_4	C_{5+}
10Co@HCS	4,2	6	27,8	18.8	11.1	70.1
0.1%PtCo@HCS	11,3	6,1	42,1	24.6	12.3	63.1
0.5%PtCo@HCS	13,3	10.0	52,8	26.8	11.7	61.5
1%PtCo@HCS	15	18.0	59,6	31.3	12.4	56.3
0.1%Pt/(Co@HCS)	5,1	3,9	20,6	20.8	8.3	70.9
0.5%Pt/(Co@HCS)	6	6,9	24,8	21.6	8.8	69.6

1%Pt/(Co@HCS)	6,7	9,9	33.0	22.5	9.2	68.3

Table 5.5: Catalysts relative Co phase abundance (wt %)

SAMPLE	CO(FCC)	CO(HCP)	HCP/FCC RATIO
10%Co@HCS	**-**	**-**	**-**
10Co0.1Os@HCS	**37.10**	**4.68**	**0.13**
10Co0.Os@HCS	**81.35**	**18.65**	**0.23**
10Co1Os@HCS	**43**	**57**	**1.33**
0.1%Os/(Co@HCS)	**100**	**-**	**-**
0.5%Os/(Co@HCS)	**63.74**	**-**	**-**
1%Os/(Co@HCS)	**-**	**-**	**-**
10Co0.1Pt@HCS	**30.96**	**5.81**	**0.19**
10Co0.5Pt@HCS	**35.92**	**8.21**	**0.23**
10Co1Pt@HCS	**39.206**	**29.43**	**0.75**
0.1Pt/Co@HCS	**-**	**-**	**-**
0.5Pt/(10Co@HCS)	**20.78**	**12.49**	**0.60**
1Pt/(10Co@HCS)	**31.18**	**16.09**	**0.52**

5.4 Conclusion

In conclusion, several Co-based catalysts were successfully synthesized, including Co@HCS, CoPt@HCS and Pt/(Co@HCS). EDX spectra confirmed the presence of the Co and Pt nanoparticles in the catalysts.

The catalysts were evaluated using various techniques, including TPR, in-situ XRD, and FT performance, and the results showed that Pt has a positive effect on the Co catalysts, enhancing their reducibility and improving their performance in CO conversion and hydrocarbon selectivity. The primary hydrogen spillover effect was found to make a significant contribution

in reducing Co_3O_4 to metallic active phase Co^0, while the secondary hydrogen spillover effect had a lesser effect, possibly due to the carbon shell (~28 nm) distance between Pt and Co and the limitations of hydrogen atom gas and surface diffusion. A higher Co (hcp) to Co (fcc) ratio was achieved from the reduction of the Co_3O, when Pt and Co were in intimate contact. As a result, the highest degree of CO conversion was observed for CoPt@HCS (FT data) and the hydrocarbon selectivity also showed that the primary hydrogen spillover effect increased methane production which was undesirable.

Overall, these findings confirms that Pt can be effectively used as a promoter for Co oxide catalysts, and further, that the distance between Pt and Co plays a role in the efficiency of the hydrogen spillover effect.

5.5 Reference

1. Iglesia E, Reyes SC, Madon RJ, Soled SL (1993) Selectivity control and catalyst design in the Fischer-Tropsch synthesis: sites, pellets, and reactors. Adv Catal 39:221–302

2. Khodakov AY, Chu W, Fongarland P (2007) Advances in the development of novel cobalt Fischer-Tropsch catalysts for synthesis of long-chain hydrocarbons and clean fuels. Chem Rev 107:1692–1744. https://doi.org/10.1021/cr050972v

3. Bahome MC (2007) Synthesis and use of carbon nanotubes as a support for the Fischer-Tropsch Synthesis

4. Snavely K, Subramaniam B (1997) On-Line gas chromatographic analysis of Fischer−Tropsch synthesis products formed in a supercritical reaction medium. Ind Eng Chem Res 36:4413–4420

5. Cheng L, Xiang Q, Liao Y, Zhang H (2018) CdS-based photocatalysts. Energy Environ Sci 11:1362–1391

6. Yilmaz G, Peh SB, Zhao D, Ho GW (2019) Atomic-and Molecular-Level Design of Functional Metal–Organic Frameworks (MOFs) and Derivatives for Energy and Environmental Applications. Adv Sci 6:1901129

7. Dalai AK, Davis BH (2008) Fischer–Tropsch synthesis: a review of water effects on the performances of unsupported and supported Co catalysts. Appl Catal A Gen 348:1–15

8. Khodakov AY, Griboval-Constant A, Bechara R, Villain F (2001) Pore-size control of cobalt dispersion and reducibility in mesoporous silicas. J Phys Chem B 105:9805–9811

9. Bertole CJ, Mims CA, Kiss G (2004) Support and rhenium effects on the intrinsic site activity and methane selectivity of cobalt Fischer–Tropsch catalysts. J Catal 221:191–203

10. Subramanian V, Cheng K, Lancelot C, et al (2016) Nanoreactors: An Efficient Tool to Control the Chain-Length Distribution in Fischer-Tropsch Synthesis. ACS Catal 6:1785–1792. https://doi.org/10.1021/acscatal.5b01596

11. Lyu S, Wang L, Zhang J, et al (2018) Role of active phase in Fischer–Tropsch synthesis: Experimental evidence of CO activation over single-phase cobalt catalysts. ACS Catal 8:7787–7798

12. Chu W, Chernavskii PA, Gengembre L, et al (2007) Cobalt species in promoted cobalt alumina-supported Fischer–Tropsch catalysts. J Catal 252:215–230

13. Zhang Y, Yoneyama Y, Fujimoto K, Tsubaki N (2003) A new preparation method of bimodal catalyst support and its application in Fischer–Tropsch synthesis. Top Catal 26:129–137

14. Voß M, Borgmann D, Wedler G (2002) Characterization of alumina, silica, and titania supported cobalt catalysts. J Catal 212:10–21

15. Spadaro L, Arena F, Granados ML, et al (2005) Metal–support interactions and reactivity of Co/CeO2 catalysts in the Fischer–Tropsch synthesis reaction. J Catal 234:451–462

16. Iglesia E, Soled SL, Fiato RA (1992) Fischer-Tropsch synthesis on cobalt and ruthenium. Metal dispersion and support effects on reaction rate and selectivity. J Catal 137:212–224

17. Phaahlamohlaka TN, Kumi DO, Dlamini MW, et al (2016) Ruthenium nanoparticles encapsulated inside porous hollow carbon spheres: A novel catalyst for Fischer–Tropsch synthesis. Catal Today 275:76–83. https://doi.org/10.1016/j.cattod.2015.11.034

18. Liu R, Qu F, Guo Y, et al (2014) Au@ carbon yolk–shell nanostructures via one-step core–shell–shell template. Chem Commun 50:478–480

19. Nongwe I, Bepete G, Shaikjee A, et al (2014) Synthesis of gold encapsulated in spherical carbon capsules with a mesoporous shell structure. A robust catalyst in a nanoreactor. Catal Commun 53:77–82

20. Li S, Niu J, Zhao YC, et al (2015) High-rate aluminium yolk-shell nanoparticle anode for Li-ion battery with long cycle life and ultrahigh capacity. Nat Commun 6:1–7

21. Fang X, Zang J, Wang X, et al (2014) A multiple coating route to hollow carbon spheres with foam-like shells and their applications in supercapacitor and confined catalysis. J Mater Chem A 2:6191–6197

22. Qiao Z-A, Guo B, Binder AJ, et al (2013) Controlled synthesis of mesoporous carbon nanostructures via a “silica-assisted” strategy. Nano Lett 13:207–212

23. He G, Evers S, Liang X, et al (2013) Tailoring porosity in carbon nanospheres for lithium–sulfur battery cathodes. ACS Nano 7:10920–10930

24. Wang G-H, Hilgert J, Richter FH, et al (2014) Platinum–cobalt bimetallic nanoparticles in hollow carbon nanospheres for hydrogenolysis of 5-hydroxymethylfurfural. Nat Mater 13:293–300

25. Xiong H, Motchelaho MAM, Moyo M, et al (2013) Cobalt catalysts supported on a micro-coil carbon in Fischer–Tropsch synthesis: A comparison with CNTs and CNFs. Catal today 214:50–60

26. Trepanier M, Dalai AK, Abatzoglou N (2010) Synthesis of CNT-supported cobalt nanoparticle size on reducibility, activity and selectivity in Fischer-Tropsch reactions. Appl Catal A Gen 374:79–86

27. Hong J, Marceau E, Khodakov AY, et al (2015) Speciation of ruthenium as a reduction promoter of silica-supported Co catalysts: a time-resolved in situ XAS investigation. ACS Catal 5:1273–1282

28. Jacobs G, Das TK, Zhang Y, et al (2002) Fischer-Tropsch synthesis: Support, loading, and promoter effects on the reducibility of cobalt catalysts. Appl Catal A Gen 233:263–281. https://doi.org/10.1016/S0926-860X(02)00195-3

29. Beaumont SK, Alayoglu S, Specht C, et al (2014) Combining in situ NEXAFS spectroscopy and CO2methanation kinetics to study Pt and Co nanoparticle catalysts reveals key insights into the role of platinum in promoted cobalt catalysis. J Am Chem Soc 136:9898–9901. https://doi.org/10.1021/ja505286j

30. Beaumont SK, Alayoglu S, Specht C, et al (2014) A nanoscale demonstration of hydrogen atom spillover and surface diffusion across silica using the kinetics of CO2

methanation catalyzed on spatially separate Pt and Co nanoparticles. Nano Lett 14:4792–4796

31. Conner Jr WC, Falconer JL (1995) Spillover in heterogeneous catalysis. Chem Rev 95:759–788

32. Nabaho D (2015) Hydrogen spillover in the Fischer-Tropsch synthesis: the role of platinum and gold as promoters in cobalt-based catalysts

33. Khoobiar S (1964) Particle to particle migration of hydrogen atoms on platinum—alumina catalysts from particle to neighboring particles. J Phys Chem 68:411–412

34. Karim W, Spreafico C, Kleibert A, et al (2017) Catalyst support effects on hydrogen spillover. Nature 541:68–71

35. Lachawiec AJ, Qi G, Yang RT (2005) Hydrogen storage in nanostructured carbons by spillover: bridge-building enhancement. Langmuir 21:11418–11424

36. Teichner SJ (1993) The history and perspectives of spillover. In: Studies in Surface Science and Catalysis. Elsevier, pp 27–43

37. Lueking A, Yang RT (2002) Hydrogen spillover from a metal oxide catalyst onto carbon nanotubes—implications for hydrogen storage. J Catal 206:165–168

38. Hirscher M, Becher M (2003) Hydrogen storage in carbon nanotubes. J Nanosci Nanotechnol 3:3–17

39. Liu Y-Y, Zeng J-L, Zhang J, et al (2007) Improved hydrogen storage in the modified metal-organic frameworks by hydrogen spillover effect. Int J Hydrogen Energy 32:4005–4010

40. Rozanov V V, Krylov O V (1997) Hydrogen spillover in heterogeneous catalysis. Russ Chem Rev 66:107

41. Prins R (2012) Hydrogen spillover. Facts and fiction. Chem Rev 112:2714–2738

42. Phaahlamohlaka TN, Kumi DO, Dlamini MW, et al (2017) Effects of Co and Ru intimacy in Fischer–Tropsch catalysts using hollow carbon sphere supports: assessment of the hydrogen spillover processes. ACS Catal 7:1568–1578

43. Fu J, Xu Q, Chen J, et al (2010) Controlled fabrication of uniform hollow core porous shell carbon spheres by the pyrolysis of core/shell polystyrene/cross-linked

polyphosphazene composites. Chem Commun 46:6563–6565

44. Mohamed R, Binninger T, Kooyman PJ, et al (2018) Facile deposition of Pt nanoparticles on Sb-doped SnO 2 support with outstanding active surface area for the oxygen reduction reaction. Catal Sci Technol 8:2672–2685

45. Qi G, Wang Y, Estevez L, et al (2010) Facile and scalable synthesis of monodispersed spherical capsules with a mesoporous shell. Chem Mater 22:2693–2695

46. Li N, Zhang Q, Liu J, et al (2013) Sol–gel coating of inorganic nanostructures with resorcinol–formaldehyde resin. Chem Commun 49:5135–5137

47. Fang X, Liu S, Zang J, et al (2013) Precisely controlled resorcinol–formaldehyde resin coating for fabricating core–shell, hollow, and yolk–shell carbon nanostructures. Nanoscale 5:6908–6916

48. Li S, Pasc A, Fierro V, Celzard A (2016) Hollow carbon spheres, synthesis and applications–a review. J Mater Chem A 4:12686–12713

49. Zheng M, Cao J, Chang X, et al (2006) Preparation of oxide hollow spheres by colloidal carbon spheres. Mater Lett 60:2991–2993

50. Stober W, Fink A (1968) Controlled Growth of Monodispersed Silica Spheres in the Micron Size Range. J Colloid Interface Sci 26:62–69. https://doi.org/10.1016/0021-9797(68)90272-5

51. Petkovich ND, Stein A (2013) Controlling macro-and mesostructures with hierarchical porosity through combined hard and soft templating. Chem Soc Rev 42:3721–3739

52. Zhang H, Chu W, Zou C, et al (2011) Promotion effects of platinum and ruthenium on carbon nanotube supported cobalt catalysts for Fischer–Tropsch synthesis. Catal Letters 141:438–444

53. Girardon J-S, Lermontov AS, Gengembre L, et al (2005) Effect of cobalt precursor and pretreatment conditions on the structure and catalytic performance of cobalt silica-supported Fischer–Tropsch catalysts. J Catal 230:339–352

54. Masilo J (2019) Investigation of the hydrogen spillover effect in platinum promoted cobalt/hollow carbon spheres

55. Chen X, Kierzek K, Cendrowski K, et al (2012) CVD generated mesoporous hollow

carbon spheres as supercapacitors. Colloids Surfaces A Physicochem Eng Asp 396:246–250

56. Chen W, Pan X, Willinger M-G, et al (2006) Facile autoreduction of iron oxide/carbon nanotube encapsulates. J Am Chem Soc 128:3136–3137

57. Bruce LA, Hoang M, Hughes AE, Turney TW (1993) Ruthenium promotion of Fischer-Tropsch synthesis over coprecipitated cobalt/ceria catalysts. Appl Catal A Gen 100:51–67

58. Park J-Y, Lee Y-J, Karandikar PR, et al (2011) Ru promoted cobalt catalyst on γ-Al2O3 support: Influence of pre-synthesized nanoparticles on Fischer–Tropsch reaction. J Mol Catal A Chem 344:153–160

59. Gregg SJ, Sing KSW, Salzberg HW (1967) Adsorption surface area and porosity. J Electrochem Soc 114:279C

60. Galeano C, Güttel R, Paul M, et al (2011) Yolk-shell gold nanoparticles as model materials for support-effect studies in heterogeneous catalysis: Au, @C and Au, @ZrO2 for CO oxidation as an example. Chem - A Eur J 17:8434–8439. https://doi.org/10.1002/chem.201100318

61. Chen X, Kierzek K, Wenelska K, et al (2013) Electrochemical Characteristics of Discrete, Uniform, and Monodispersed Hollow Mesoporous Carbon Spheres in Double-Layered Supercapacitors. Chem Asian J 8:2627–2633

62. Van de Loosdrecht J, Barradas S, Caricato EA, et al (2003) Calcination of Co-based Fischer–Tropsch synthesis catalysts. Top Catal 26:121–127

63. Rosynek MP, Polansky CA (1991) Effect of cobalt source on the reduction properties of silica-supported cobalt catalysts. Appl Catal 73:97–112

64. Nabaho D, Niemantsverdriet JWH, Claeys M, van Steen E (2016) Hydrogen spillover in the Fischer–Tropsch synthesis: an analysis of gold as a promoter for cobalt–alumina catalysts. Catal Today 275:27–34

65. Schanke D, Vada S, Blekkan EA, et al (1996) Study of Pt-promoted cobalt CO hydrogenation catalysts

66. Nabaho D, Niemantsverdriet JWH, Claeys M, van Steen E (2016) Hydrogen spillover

in the Fischer–Tropsch synthesis: An analysis of platinum as a promoter for cobalt–alumina catalysts. Catal Today 261:17–27

67. Hilmen AM, Schanke D, Holmen A (1996) TPR study of the mechanism of rhenium promotion of alumina-supported cobalt Fischer-Tropsch catalysts. Catal Letters 38:143–147

68. Phaahlamohlaka TN, Kumi DO, Dlamini MW, et al (2017) Effects of Co and Ru Intimacy in Fischer-Tropsch Catalysts Using Hollow Carbon Sphere Supports: Assessment of the Hydrogen Spillover Processes. ACS Catal 7:1568–1578. https://doi.org/10.1021/acscatal.6b03102

69. Bezemer GL, Radstake PB, Falke U, et al (2006) Investigation of promoter effects of manganese oxide on carbon nanofiber-supported cobalt catalysts for Fischer–Tropsch synthesis. J Catal 237:152–161

70. Xu X, Oosterbeek H, Bitter JH, et al (2006) Cobalt Particle Size Effects in the Fischer−Tropsch Reaction Studied with Carbon Nanofiber Supported Catalysts. J Am Chem Soc 128:3956–3964. https://doi.org/10.1021/ja058282w

71. Kogelbauer A, Goodwin Jr JG, Oukaci R (1996) Ruthenium Promotion of Co/Al2O3Fischer–Tropsch Catalysts. J Catal 160:125–133

72. Nabaho D, Niemantsverdriet JWH, Claeys M, Steen E Van (2016) Hydrogen spillover in the Fischer – Tropsch synthesis : An analysis of platinum as a promoter for cobalt – alumina catalysts. Catal Today 261:17–27. https://doi.org/10.1016/j.cattod.2015.08.050

73. Iglesia E, Soled SL, Fiato RA, Via GH (1993) Bimetallic synergy in cobalt ruthenium Fischer-Tropsch synthesis catalysts. J Catal 143:345–368

74. Hwang KS, Yang M, Zhu J, et al (2003) The molecular mechanism of the poisoning of platinum and rhodium catalyzed ethylene hydrogenation by carbon monoxide. J Mol Catal A Chem 204:499–507

75. Baschuk JJ, Li X (2001) Carbon monoxide poisoning of proton exchange membrane fuel cells. Int J Energy Res 25:695–713

76. Diehl F, Khodakov AY (2009) Promotion of cobalt Fischer-Tropsch catalysts with noble metals: a review. Oil Gas Sci Technol l'IFP 64:11–24

Chapter 6

The effect of shell thickness on hydrogen spillover in Os promoted Co@HCS

Chapter to be published:

6.1. Introduction

Heterogeneous catalysis is of high importance to the modern chemical and energy industries [1]. These industries, however, are facing a series of problems that relate to energy use and pollution of the environment, and as a result thereof scientists and engineers are working to develope more effective catalysts to solve these issues [2, 3]. In recent years, the evolution of catalysts in their operational states has received considerable attention from scientific and engineering researchers such as their surface composition, phase transformation, sintering and

the geometric restructuring of reaction sites, and reaction intermediates during catalysis [5-9]. Research has been done on the dynamic behaviour of the intermediates involved catalytic processes in order to better understand how catalysts evolve in their operational states.

In 1964, the hydrogen spillover effect was first observed on a WO_3/Pt catalyst where the hydrogen atoms that migrated from the metal phase (Pt) to the support phase (WO_3) [4]. Hydrogen spillover occurred due to the dynamic migration of surface adsorbed H^+ species from a surface site on which they were generated or absorbed (the activator surface), onto another surface site (the acceptor surface) that would not otherwise generate or absorb them under the same conditions [4–7]. The spillover process consists of three connective steps: (i) dissociative chemisorption of the molecular hydrogen onto a metal catalyst (activator surface), (ii) migration of the H species or atomic hydrogen (H^+) species from the surface of the metal to another surface (acceptor surface), and (iii) H species or atoms that move and/or adsorb on the surface of the support or another metal [8]. The mobile surface on which the adsorbed H species travels has a specific reactivity that depends on the support material, which may change the way the surface reacts catalytically and physically to the species being adsorbed [9]. Therefore, the efficiency and spatial extent of hydrogen spillover strongly depends on the types of support materials utilized in the reaction [5, 10]. Different types of support materials have been used to explore the spillover effect.

In this study carbon has been used as the support. Activated carbon [11–14], carbon nanofibers [15–17], carbon nanotubes [18–25], fullerenes [26], carbon nanospheres [27], graphene-like materials [28–32], and templated carbon [28, 33–35] have all been the subject of experimental studies on hydrogen spillover with carbon materials.

Support materials in catalysis facilitate crystallization and stabilization of the catalytically active metal species, and also affect metal-support interactions, metal dispersion, mechanical strength, thermal stability, crystallite size, and mass transfer of the reactants/products of the active metal catalyst through its physicochemical and textural properties. [36, 37] In general, noble metal catalysts, in particular Pt-based, are supported by carbonaceous support materials [38]. Carbon support materials with oxygen groups on their surface are thought to improve the metal-carbon interaction and to allow better active metal dispersion. One type of carbon that has been used has been the hollow carbon sphere (HCS) support material. This has a spherical hollow structure and the inside can be used as a nanoreactor, by encapsulating an active metal phase within the carbon shell. These structures have been used in different catalysed chemical

reactions such as oxidation, nitroarene reduction, hydrogenation, FTS, and the integration of multiple catalytic reactions.

The shell porosity can be controlled and both meso- and micropores can be built into the shell [39]. Mesoporosity is preferred if diffusion issues to/from the core are to be minimized. Mesoporous core-shell carbon spheres have been reported to contain an active metal precursor encapsulated inside the core of a mesoporous carbon shell that is a suitable candidate for immobilizing nanoparticles. The core can be either totally filled with a single metal particle or partially filled with one or more metal particles. The porous shell prevents particle aggregation and can ensure a short diffusion distant for reagent molecules [40]. Core-shell composites are known. For example, Ikeda et al. reported on the use of Pt nanoparticles enclosed in a hollow porous carbon shell (Pt@hmC) as a highly effective heterogenous hydrogenation catalyst [41]. Another study by Phaahlamohlaka et al. studied the hydrogen spillover effect of ruthenium loaded on Co encapsulated inside mesoporous hollow carbon spheres (Ru@MHCS@Co) and their findings showed that hydrogen spillover from Ru to Co via the carbon layer was possible, when the Co oxide encapsulated became reduced [42]. Carbon shells can provide for a tuneable pore structure and have relative chemical inertness.

Although hydrogen spillover has been studied over the past two decades, a thorough comprehension of the phenomenon is still lacking; thus, further studies are on supports that show spillover are still needed. Two types of spillover are known: the primary and secondary spillover effects, and both have been studied (illustrations in chapters 4 and 5). In primary hydrogen spillover, the promoter is in direct contact with a metal oxide. For example, when the reduction of CoOx is considered, the dissociation of hydrogen occurs on the promoter surface into hydrogen atoms that migrate to reduce CoOx into Co^0 (metallic) and concurrently to form water. In secondary hydrogen spillover, the promoter and CoOx are separated by varying distances. Here the dissociated hydrogen atom on the promoter has to migrate on the surface of the support material (e.g., via hydroxyl groups on a support) with spillover to the Co oxide which results in the reduction of CoOx. In the spillover of hydrogen species, migration distances ranging from a few nanometres to several centimetres have been reported [4, 5, 9, 43–46].

In this study hollow carbon spheres supported Co catalysts were utilized to study the secondary hydrogen spillover effect *by varying the distance between an Os promoter and a Co catalyst*. The carbon shell thickness was varied between the two metals so that the distance the H species

travelled in a spillover reaction could be varied. Secondary spillover materials provide an opportunity to examine the carbon substrate's physical and chemical properties independently from the effects of how the hydrogen, metal promoter (Os), and the metal substrate (Co_3O_4) interact with one another. The catalysts were tested using the FTS to evaluate the effect of the different carbon shells on the reaction.

6.2. Experimental

6.2.1. Materials

All reagents used for the syntheses described here were of analytical grade and were purchased from various chemical suppliers. All reagents used in these syntheses were used as received. This includes the following chemical reagents: cobalt nitrate hexahydrate ($Co(NO_3)_2.6H_2O$) (Aldrich), potassium osmate ($K_2[OsO_2(OH)_2]$) (Anglo American Research Laboratories, Johannesburg), ammonia solution (25%; Fluka), ethanol (98%; Merck), hexadecyltrimethylammonium bromide ($C_{19}H_{42}BrN$) (CTAB; Aldrich), styrene (Aldrich), polyvinylpyrollidone ($(C_6H_9NO)_n$) (PVP, MW 40 K, Aldrich) formaldehyde (37%; Aldrich), potassium persulfate ($K_2S_2O_8$) (Eimer and Amend), hydrazine (35% Aldrich), and deionized water. All reagents were used as received.

6.2.2. Synthesis of Co@HCS catalyst

6.2.2.1. Synthesis of polystyrene spheres (PSS) [47]

Styrene (8 mL) and polyvinylpyrollidone (PVP, 0.2 g) was added to a mixture comprised of 200 mL of ethanol and 50 mL of deionized water contained in a round bottom flask. The mixture was sonicated and stirred for 15 min. Thereafter, potassium persulfate (KPS, 0.3 g in 10 mL deionized water) was added to the prepared reaction mixture while stirring. The mixture was then heated at 80 ^oC for 24 h. After the reaction the product was cooled, filtered and washed successively using deionized water. The product (PSSs), produced in high yield, was then dried in an oven at 60 °C for 12 h, crushed with a mortar and pestle and stored in a glass sample vial.

6.2.2.2. Synthesis of ammonium hexachloroosmate (IV), $(NH_4)_2OsCl_6$ [48]

Potassium osmate (5.00 g, 19.36 mmol) and 200 mL of concentrated hydrochloric acid (35%) were added to a 500 mL round bottom flask. The reaction mixture was stirred and heated at reflux for 2 h after which 50 mL 20% (w/v) ammonium chloride (186.9 mmol) solution was added, followed by cooling of the mixture in ice. The solid which formed was isolated and washed with 80% ethanol to remove residual potassium ions. Potassium ions were removed because they could act as a promoter in FTS. The precipitate was recrystallized from hot

concentrated hydrochloric acid. Ammonium hexachloroosmate (IV) ($(NH_4)_2OsCl_6$) crystallised as red-brown cubes which were washed with absolute ethanol (8.1 g, 95% yield).

6.2.2.3. **Synthesis of 10% Co loaded on PSS (Co/PSS)**

PSS's (3 g) were dissolved in a mixture of 75 mL deionized water and 25 ml ethanol. To this mixture was added cobalt nitrate hexahydrate (0.45 g), while stirring, until the solution turned red. Thereafter, 10 mL of hydrazine (2M) was slowly added to the prepared solution dropwise and the solution was then stirred for 12 h to ensure complete deposition of Co nanoparticles onto the PSSs to give Co/PSSs.

6.2.2.4. **Synthesis of Co@HCS** [42]

The Co/PSSs (Co = 10%) (3 g) and ammonia solution (25%; 12 mL) were dissolved/dispersed in a mixture of 150 mL ethanol and 76 ml deionized water by sonication for 30 min. Subsequently, resorcinol (1.1 g), formaldehyde (2.3 mL) and hexadecyltrimethylammonium bromide (2.5 g) were added to make the resorcinol-formaldehyde core-shell structure. The solution was allowed to stir at room temperature for 24 h. The formed resorcinol-formaldehyde (RF) core shell structure around the Co/PSSs was filtered and washed successively with water and ethanol, followed by drying at 80 ^{o}C for 12 h. Template removal and carbonization of the prepared composites was performed in a two-step horizontal chemical vapour deposition apparatus. The template removal was done under a flow of nitrogen gas (50 ml/min) at 350 ^{o}C for 1 h to decompose the PSSs. This was followed by the carbonization of the RF core shell structure under a flow of nitrogen gas (50 ml/min) at 600 ^{o}C for 2 h. The resulting products were called Co@HCS.

6.2.2.5. **Synthesis of Co@HCS with different shell thickness**

The RF resins can give a tailored carbon shell thickness [49]. The synthesis parameters used to tune the HCS shell are given below in Table 6.1. The method described in section 7.2.2.4 was used in preparing different shell thickness Co@HCS catalysts by adjusting the amount of RF utilized. A literature study on the variation of HCS shell thickness was reported by Li et al. where silica spheres were used as the template and RF as the carbon source [39]. In our study PSS was used as the template. Three different Co@HCS materials were made with three different diameters and are referred to as Co@HCS16, Co@HCS28, Co@HCS51, and with shell thicknesses of 16 ± 3 nm, 28 ± 5 nm, and 51 ± 6 nm respectively.

Table 6.1: Synthesis parameters for HCSs with different shell thicknesses.

Sample	PSS (g)	NH_3 (ml)	C_2H_5OH (ml)	H_2O (ml)	CTAB (g)	Resorcinol (g)	Formaldehyde (ml)
Co@HCS16	3	12	150	76	2	0.5	1.2
Co@HCS28	3	12	150	76	2.5	1.1	2.3
Co@HCS51	3	12	150	76	3	2.2	4.6

6.2.3. **Synthesis of 1% Os loaded on Co@HCS with different diameters**

The Co@HCSx (x = 16, 28, 51) (1.5 g) catalysts were dispersed in 250 mL of deionized water by sonication. To this mixture was added the Os salt precursor (0.069 g, Os = 1%) and urea (0.4 g) followed by 30 min sonication. The mixture was then stirred at 95 ^{o}C in a round bottom flask for 12 h. The product Os/(Co@HCS) was collected after filtration and washing with water, followed by drying at 80 ^{o}C for 12 h.

6.3. Results

6.3.1. Transmission electron microscopy (TEM)

The synthesis of the hollow carbon spheres (HCSs) was achieved by using monodispersed polystyrene spheres (PSSs) as a template using a standard procedure [47]. The TEM image of the PSSs shows that they were spherical in shape, uniform, and had a smooth surface (Fig 6.1 (a)). The particle size distribution was between 450 and 600 nm with an average diameter of 493 nm (Fig 6.1 (b)). The PSSs were synthesized to be larger than 200 nm in diameter in order to avoid the occurrence of coagulation and the formation of large indistinguishable nanopheres [50].The PSS template was then coated with 10% Co loading to form 10%Co/PSS

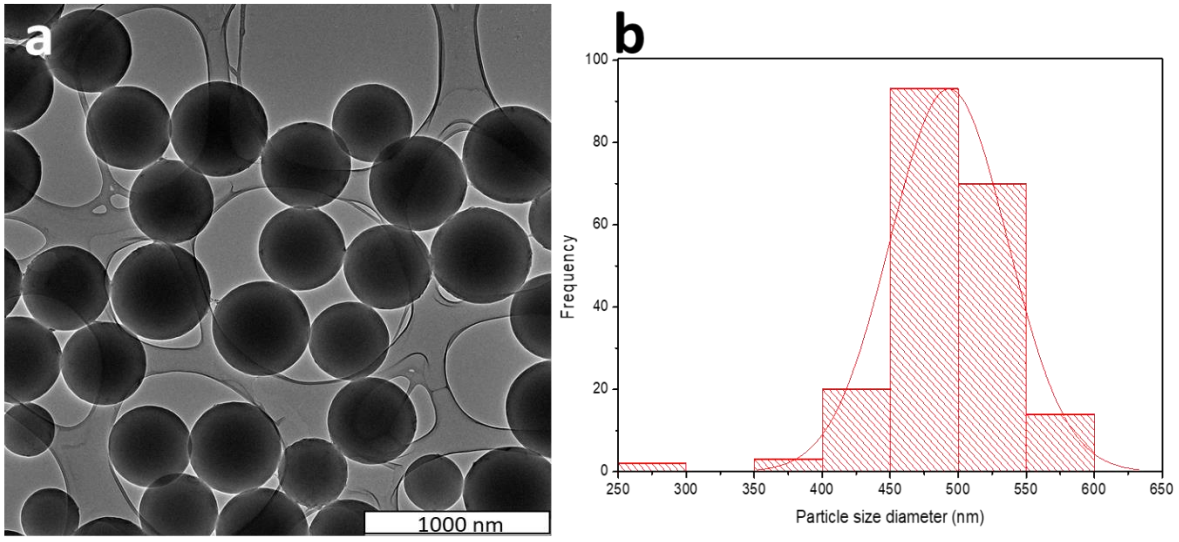

Fig 6.1: (a) TEM image of PSSs and (b) their particle size distribution

The 10%Co/PSS template was then covered by RF (resorcinol formaldehyde) and CTAB. This was done with three different resorcinol formaldehyde amounts to coat the 10%Co/PSSs (Table 6.1).

The addition and RF polymerization steps led to the 10%Co/PSS coating as previously reported [39, 49]. The synthesized RF coated template was then heated to decompose the PSS template

and carbonization took place to form the 10%Co@HCSx (x = 16, 28, 51 materials with three different shell thicknesses (16 nm, 28 nm, 51 nm).

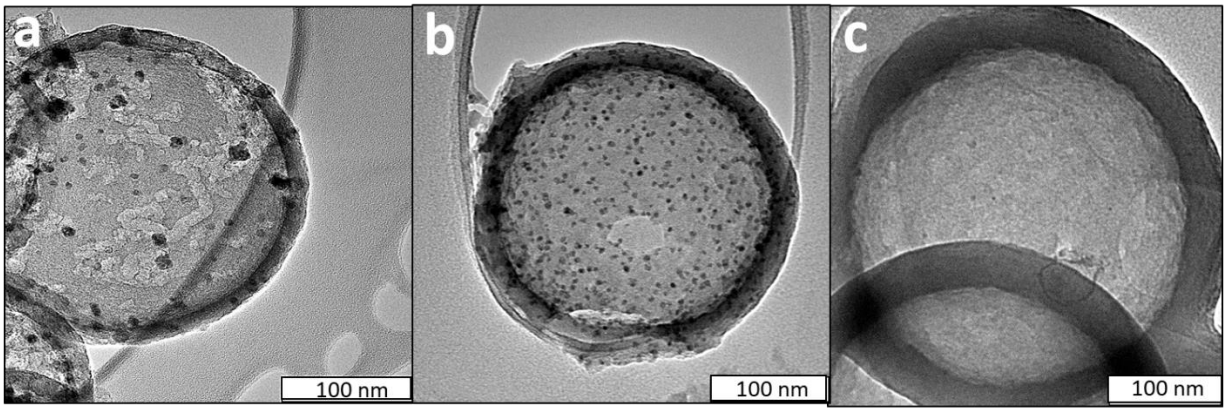

Fig 6.2: TEM images of (a) 10%Co@HCS16, (b) 10%Co@HCS28 and (c) 10%Co@HCS51 catalysts.

In Fig 6.2, TEM images of the Co nanoparticles encapsulated inside the HCS catalysts are shown with varied carbon shell thickness. The HCS diameter ranged between 400 and 500 nm with the average size of 448 nm, Table 6.2. The size of the HCSs was shown to be less than that of the PSS template and this observation is due to a shrinkage occurring during the carbonization process [51]. This can be attributed to the dehydration of the cross-linked carbon precursor that occurs during carbonization [52, 53].

The Co nanoparticles were well dispersed and successfully encapsulated inside the HCS support. The carbon shell thickness was 16 ± 3 nm, 28 ± 5 nm, and 51 ± 6 nm for the 10%Co@HCS16, 10%Co@HCS28 and 10%Co@HCS51 catalysts, respectively. The Co nanoparticles size distribution was 7 ± 3 nm, 4 ± 1 nm, and 3.6 ± 2 for the 10%Co@HCS16, 10%Co@HCS28 and 10%Co@HCS51 catalysts, respectively (Table 6.2).

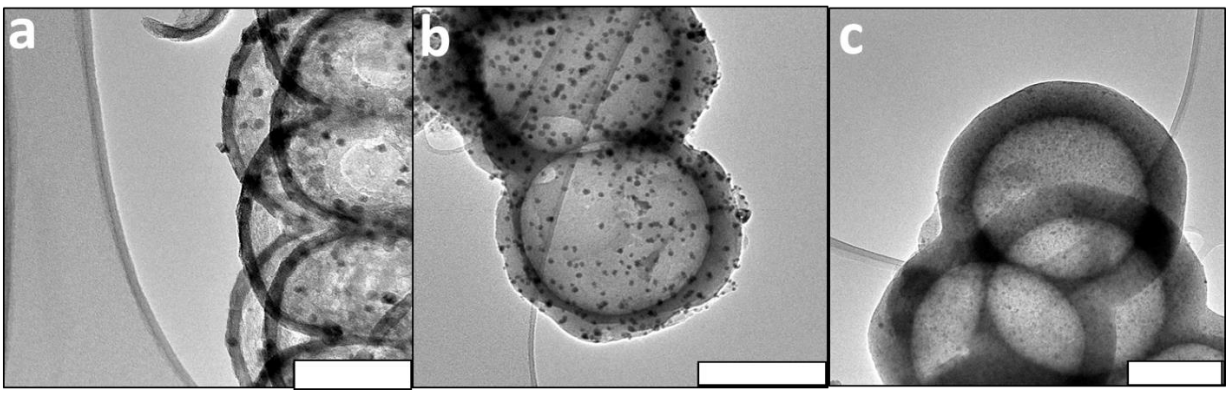

Fig 6.3: TEM images of (a) 1%Os/10%Co@HCS16, (b) 1%Os/10%Co@HCS28 and (c) 1%Os/10%Co@HCS51 catalysts.

Fig 6.3 shows the TEM images of three synthesized catalysts after Os promoter addition. The loading of the Os promoter on the outer carbon shell can be seen in Fig 6.3. The Co nanoparticles size distribution was 10 ± 8 nm, 6 ± 3 nm, and 3.7 ± 2 for the 1%Os/(10%Co@HCS16), 1%Os/(10%Co@HCS28) and 1%Os/(10%Co@HCS51) catalysts, respectively (Table 6.2). The decrease in the size of the encapsulated metal nanoparticles with an increase in the RF amount and the corresponding carbon shell was as a result of the growth mechanism of the RF shell with an increase in the amount of RF. The nanoparticles decreased in size with increased amounts of RF; the mechanism behind such observation will require further investigation. The Os nanoparticle size distribution was estimated by measuring the metal particles outside the HCSs and was found to be 11 ± 4 nm on average for the three catalysts. The introduction of Os on the outer shell resulted in a very small increase in the Co particle size; a similar trend was observed in the data for Co-Os catalysts described in chapter 4. It is not clear whether this was due to a Co-Os interaction or due to the modified reaction conditions on addition of the Os (e.g. changes in solution pH).

Table 6.2: Average particle size of the synthesized catalysts and their shell diameter and thickness.

Sample	TEM Co particle size (nm)	TEM HCS diameter (nm)	TEM HCS shell thickness (nm)
10%Co@HCS16	7	470	16
10%Co@HCS28	4	457	28
10%Co@HCS51	5	466	51
1%Os/(10%Co@HCS16)	10	426	16
1%Os/(10%Co@HCS28)	6	468	28
1%Os/(10%Co@HCS51)	5	465	51

6.3.2 Thermogravimetric analysis

Thermogravimetric analysis (TGA) was performed to study the thermal stability and efficacy of template removal of the prepared samples and the carbon support, Fig 6.4. The analysis was

done under air and the carbon support underwent decomposition through the oxidation reaction emitting CO_2 as a byproduct.

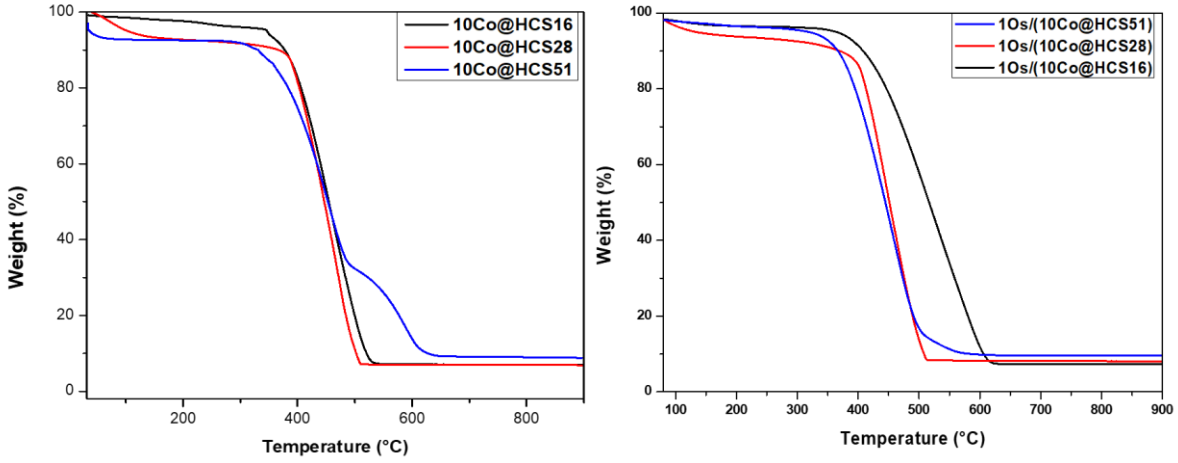

Figure 6.4: TGA profiles of (a) Co@HCSx and (b) Os/(Co@HCSx) catalysts.

The percentage weight loss of the synthesized catalysts was compared relative to the amount of Co metal loaded, as a function of temperature as shown in Fig 6.4 (a) and (b). The remaining residue for the Co@HCSx and Os/Co@HCSx catalysts was attributed to the Co oxide particles, allowing an estimation of the Co metal loading percentage (~ 10%) inside the HCS support. Since small amounts of Os (ca. 1%) was loaded on the outer carbon shell, no difference in overall weight percentage loading was observed for the Os/Co@HCSx catalysts in comparison to that of Co@HCSx catalysts. Another reason for the lack of observation of an Os loading can be attributed to Os being known to undergo oxidation at 350 °C to form OsO_4 under oxidative conditions [54]. OsO_4 is volatile and is thus removed from TGA under the experimental conditions.

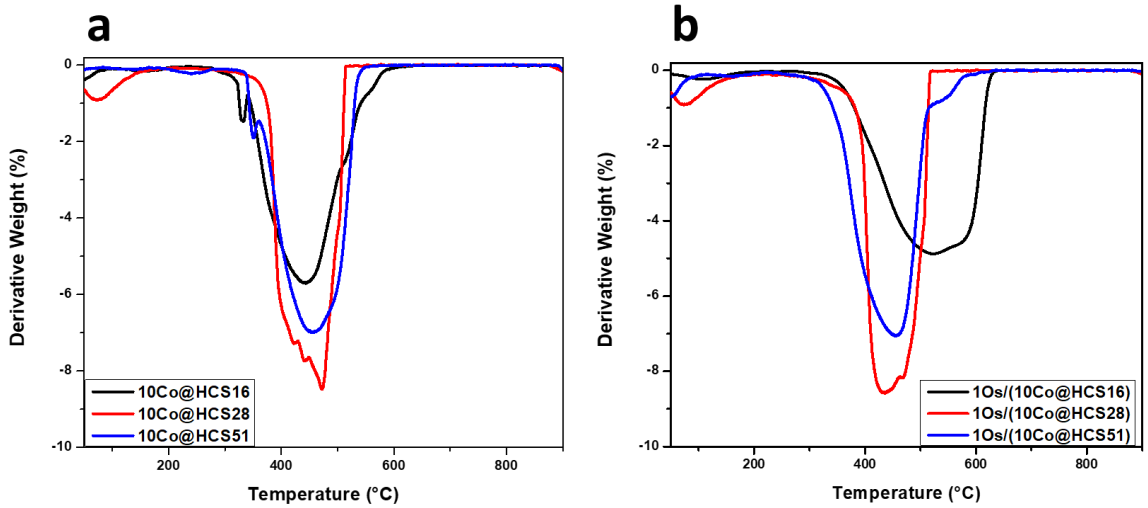

Figure 6.5: TGA derivative profiles of (a) Co@HCSx and (b) Os/(Co@HCSx) catalysts.

The first derivate of the TGA profile for the bulk assembled synthesized catalyst curves allowed the analysis to determine the temperature at which the maximum weight loss took place. Thermal decomposition profiles of the catalysts are shown in Fig 6.5. The TGA profiles show that the PSS template was completely removed from the RF shell core during the carbonization procedure and ~10% CoOx metal loading was the remaining residue left after thermal decomposition. This observation emphasizes the efficacy of template removal by thermal decomposition during the CVD process as well as the quality of the synthesized carbon shell. The efficacy of template removal by thermal decomposition is also supported by TEM and XRD studies.

The first derivative profile for Co@HCSx catalysts shown in Fig 6.5 (a) and (b) occurred between 400 and 500 ℃ thus showing that the HCS was thermally stable. The Co@HCSx catalysts showed a decomposition temperature which agreed with other studies [55, 56]. Furthermore, the Os/(Co@HCS28) and Os/(Co@HCS51) catalysts decomposed at temperatures in the range of 400–500 ℃ while that of the Os/(Co@HCS16) catalyst decomposed above 500 ℃. This was not expected as the carbon shell is thinner in Os/(Co@HCS16) and must relate to the enhanced oxidation of the Co that led to a poorer catalyst to assist any carbon oxidation. The data obtained suggests that the presence of Os on the outer shell did not impact the thermal decomposition of these catalysts as the data were similar to those of the unpromoted Co@HCSx catalysts. Overall, from the TGA profiles it can be deduced that the prepared catalysts were thermally stable for use under FTS reaction conditions.

6.3.3 Nitrogen absorption-desorption analysis (BET)

Table 6.3 shows a summary of the nitrogen absorption-desorption analysis data used to determine the surface area, pore volume and pore size characteristics of the prepared catalysts. The prepared catalyst follow type I/IV isotherms (chapter 4) which is due to the presence of a carbon framework that is both mesoporous and microporous (Fig S6.1).

All of the synthesized catalysts were shown to have large BET surface areas (349 – 491 m^2/g). The surface area of the catalysts was 392 m^2/g, 468 m^2/g, and 491 m^2/g for the

10%Co@HCS16, 10%Co@HCS28 and 10%Co@HCS51 catalysts, respectively and showed to increase with shell thickness. The promoted catalysts had a surface area of 418 m^2/g, 415 m^2/g, and 389 m^2/g for the 1%Os(10%Co@HCS16), 1%Os(10%Co@HCS28) and 1%Os(10%Co@HCS51) catalysts, respectively and showed a decrease with shell thickness. The high specific surface area was mainly due to the microporous nature of the carbon support. Micropores were also present in the HCS framework (2-10 nm). The pore size of the catalysts was 8.7 nm, 7.3 nm, and 4.3 nm for the 10%Co@HCS16, 10%Co@HCS28 and 10%Co@HCS51 catalysts, respectively. The pore sizes of the promoted catalysts were 9.8 nm, 8.1 nm, and 6.7 nm for the 1%Os(10%Co@HCS16), 1%Os(10%Co@HCS28) and 1%Os(10%Co@HCS51) catalysts, respectively. The formation of catalysts with mesopore size less than 2 nm, Fig S6.2, can be attributed to the decomposition of RF and loss of small molecules during carbonization of the HCS [57].

In general, for each type of carbon support, the measured surface area would rise with an increase in pore volume, number of pores, and deacrease with pore width. Based upon the data in Table 6.3, it can be seen that the specific surface area of the HCSs increased with an increase in carbon shell thickness. As the carbon shell thickness was increased, the average pore volume and average pore size decreased due to some blockage of the pore channels as the carbon content increased. Another observation was that the addition of Os on the surface of the HCSs resulted in a decrease in surface area of the catalysts as well as a decrease in pore size and this observation might be due to Os nanoparticles on the outer surface of the carbon shell blocking macropores thus leaving micropores which gives a decrease in pore size [42]. Due to the low porosity and decrease in pore size, studies have shown that mass transfer limitations may be found [58]

Table 6.3: Summary of the N_2 physisorption data

Sample	Surface area (m^2/g)	Pore volume (cm^3/g)	Pore size (nm)	Micropore volume (cm^3/g)
10%Co@HCS16	392	0.44	8.7	0.16
10%Co@HCS28	468	0.32	7.3	0.18
10%Co@HCS51	491	0.12	4.3	0.20

1% Os/(10%Co@HCS16)	418	0.83	9.8	0.08
1% Os/(10%Co@HCS28)	415	0.70	8.1	0.12
1% Os/(10%Co@HCS51)	389	0.53	6.7	0.15

6.3.4 Powder X-ray diffraction (PXRD)

Powder X-ray diffraction (PXRD) data were collected on the prepared catalysts for the purpose of identifying the crystalline phases that are present in the samples, Fig 6.6. A summary of the XRD data is given in supplementary Table S6.1. All of the PXRD patterns contained a broad feature c.a. 22.5° 2θ which is attributed to the disordered sp^2 hybridized carbon (002) reflection [59]. No notable diffraction peaks belonging to the Os phase were observed in any of the PXRD patterns due to the low promoter metal loadings.

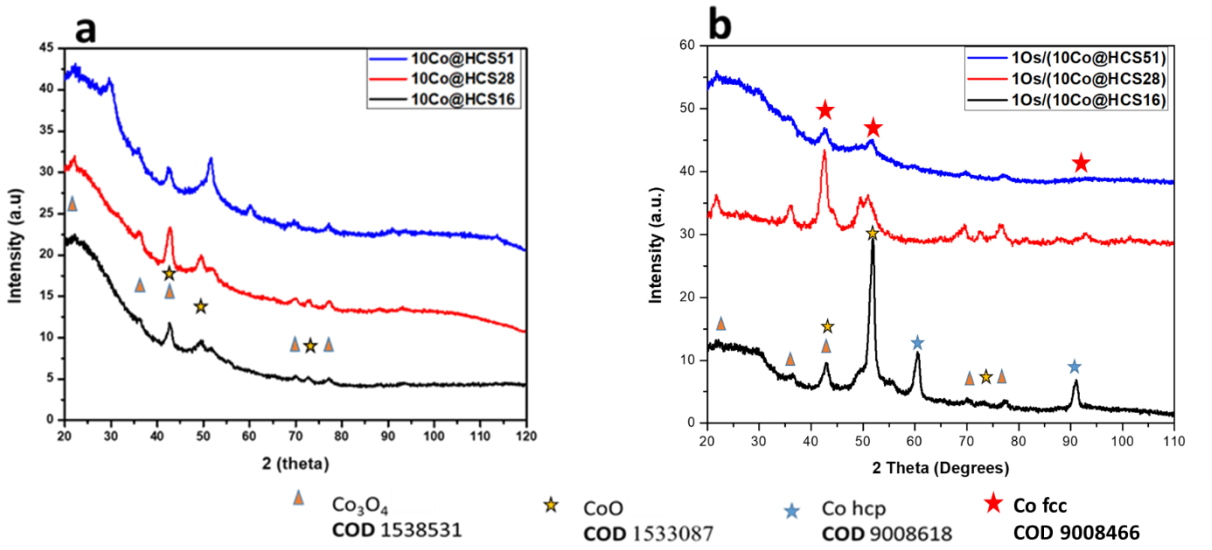

Figure 6.6: PXRD patterns of (a) Co@HCS (16 nm, 28 nm, and 51 nm) and (b) Os/(Co@HCS) (16 nm, 28 nm, and 51 nm)

The Co@HCSx (x = 16, 28 and 51) catalysts showed peaks belonging to the cubic Co_3O_4 phase and cubic CoO metal phase corresponding with **COD:1526734** and **COD:1533087** collection files, respectively, Fig 6.6 (a). The contact between Co_3O_4 and the HCSs resulted in the formation of the CoO phase observed due to an auto reduction process. In a related study by

Chen et al., it was observed that above 600 °C, the CNT host could reduce the Fe oxide supported both inside and outside of multi-walled carbon nanotubes (CNTs). [60]. Another observation for the Co@HCSx (x = 16, 28 and 51) catalysts was that the Co_3O_4 phase showed particles that were in a nanoscale range, as well as having a narrow size distribution [61].

Similar peaks were observed after addition of the Os promoter to the outer shell of the Co@HCSx catalysts with an addition of the metallic Co (fcc) phase, Fig 6.6 (b). The Co (fcc) phase was present in the Os promoted catalysts and the peaks due to the phase decreased with an increase in shell thickness resulting in CoO reduction being limited. This observation indicates further reduction of the Co oxides to Co metal by Os promoter was impeaded by an increase in carbon shell thickness. This suggests that the presence of Os on the outer shell had little impact on the phase of the Co encapsulated inside the HCS support with an increase in carbon shell thickness. The PXRD pattern of the Co@HCS16 catalyst, surprisingly, had strong peaks that were assigned to CoO and the hcp Co phase (**COD:9008492).** This contrasts with the studies in chapter 4 where the hcp Co phase was observed only for CoOs@HCS materials. This suggests that the presence of Os on the outer shell where the carbon shell with a thin width resulted in a close intimacy between Os and Co and this impacted on the enhanced reduction of the Co_3O_4 to CoO and generation of the hcp Co phase.

Overall, the information obtained from the PXRD data suggested that the intimacy of the Os promoter with the Co catalyst in a thin carbon shell (Os/(Co@HCS16) and (Os/(Co@HCS16)) promoted the reduction of CoOx to give the hcp and fcc metallic Co phase. Whereas, when the Os promoter and Co were separated by a thicker carbon shell (Os/(Co@HCS51)) no metallic Co phase was observed. More interesting was the observation of the Co hcp phase in the Os/(Co@HCS16)) catalyst, indicating the importance of the promoter-Co interaction.

6.3.5 Temperature programmed reduction (TPR)

TPR studies were conducted to study the reducibility of the Co_3O_4 catalyst and how the presence of the Os promoter affected the Co_3O_4 catalyst. The difference in carbon shell thickness can influence the distance travelled by H species and affect the reducibility of the Co_3O_4 catalyst. Previous studies conducted on Co catalysts have shown that the reduction of Co_3O_4 to metallic Co^0 proceeds via intermediate formation of CoO [62–66]:

$$Co_3O_4 \rightarrow CoO \rightarrow Co$$

TPR profiles of the Co@HCSx catalysts with different carbon shell thickness are shown in Fig 6.7 and 6.8. The TPR profiles of all the catalysts > 450 ℃ showed a peak that corresponds to the methanation of the carbon support (Fig S6.2). The TPR profiles (Fig 6.7) of the different Co@HCSx catalysts showed that with a decrease in the carbon shell thickness, the low temperature reducibility showed the following order Co@HCS16 < Co@HCS28 < Co@HCS51. This observation revealed that a change in carbon shell thickness affected the reduction of the Co oxide. This trend can be due to a decrease in permeability with a corresponding increase in the carbon shell thickness thus limiting the ability of H_2 molecules to enter inside the HCS in order to reduce the Co_3O_4 into Co^0 metal. It is to be noted that the data reveal that the the first reduction peak is more affected by the carbon shell thickness than the second reduction peak. A study by Nabaho et al. showed that the effect of Pt on Co in TPR indicated a similar effect [67]. This suggest that H_2 diffusion may be implicated in spillover effects with an increase in carbon shell thickness.

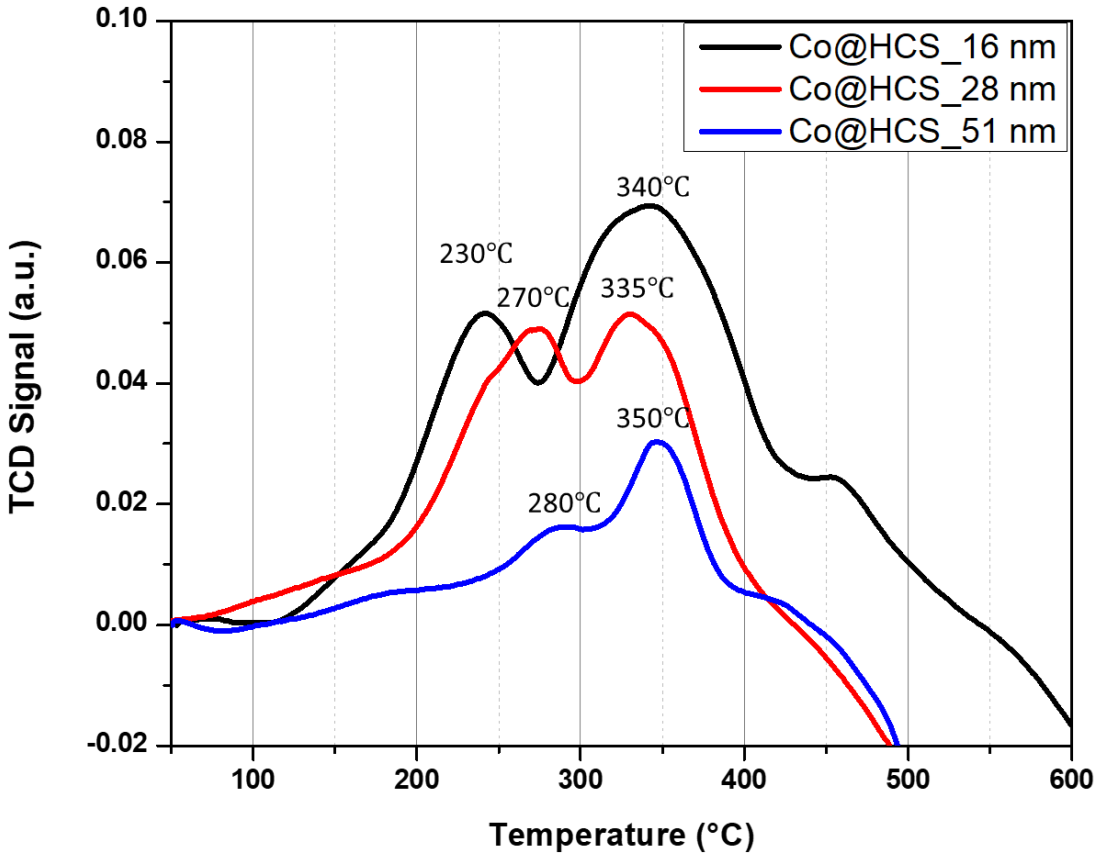

Figure 6.7: TPR profiles of Co@HCS16, Co@HCS28 and Co@HCS51

The TPR profiles of Os/(Co@HCSx) catalysts with different carbon shell thickness are shown in Fig 6.8. The Os/(10%Co@HCSx) (x = 16 nm, and 51 nm) catalysts showed a peak at

temperatures below 120 ^{o}C and this peak can be attributed to evolution of water. Another possibility is that the peak could be due to the formation of NO or other reduced species formed from reduction of residual nitrate species which were the remnants of the $Co(NO_3)_2$ precursor. It is also possible that this peak could be attributed to the reduction of CoOOH species to Co_3O_4 [68].

The TPR profiles of the catalysts allowed the study of the secondary spillover effect and how a change in shell thickness between the Os promoter and Co_3O_4 catalyst affected the reducibility of Co_3O_4. The Os promoter was shown to enhance the reducibility of the Co_3O_4 catalyst in comparison to the non-promoted Co_3O_4 catalyst. This observation was observed from the decrease in reduction temperature required to reduce the Co_3O_4 catalyst in a two-step reduction.

The TPR first reduction and second reduction peaks are shown in Table 6.4. The increase in carbon shell thickness on Os/(Co@HCS) catalyst resulted in a decrease of the temperature of the first reduction step relative to the Co@HCSx catalysts and the catalysts had first reduction temperatures of 180 ^{o}C, 206 and 230 ℃ for Os/(10%Co@HCSx) (x = 16 nm, 28 nm and 51 nm) respectively. The decrease of the temperature of the first reduction step relative to the Co@HCSx catalysts was by approximately 50 ^{o}C, 64 and 50 ℃ for Os/(10%Co@HCSx) (x = 16 nm, 28 nm and 51 nm) respectively. All three catalysts show a similar change that can be due to the similar % Os loaded on the Co catalyst. The data are consistent with Os 'acting at a distance' with the Co reduction dependent of the shell thickness.

The second reduction step occurred at temperatures of 250, 380 and 340 ℃. The data suggest that as the thickness increases the impact on the second peak is such as to have little effect on its location for the thicker carbon shells. The peaks have a similar position to when Os is not present. Only for the thin carbon shell is an effect seen.

The shift in temperature relative to Co@HCSx catalyst decreased by 90 and 10 ˚C for the Os/(10%Co@HCSx) (x = 16 nm, and 51 nm) catalysts but increased by 45 ˚C for the Os/(10%Co@HCS28 nm) catalyst. This latter result was unexpected and suggests a number of explanations: (i) the proximity of the peak due to the methane formation can distort the second TPR peak. However, no evidence for this is seen. (ii) the influence of the CoOx species on the peak.

The 10%Co@HCS51nm catalyst was shown to have existed in a CoO phase due to carbon auto-reduction since a minor second reduction peak was observed in the presence of the Os

promoter [60]. Carbon spheres (CSs) are known to be made up of randomly twisted, curling graphitic flakes that range in size from 1 to 10 nm and are not closed shells [69]. The graphitic flakes' edges make excellent sites for hydrogen absorption to occur thus reducing the CoO to metallic Co [70]. The decrease in shell thickness lowered the reduction temperature required of Co_3O_4 through via a secondary spillover effect involving Os. The catalyst showed a significant downward shift in reduction temperature due to the high permeability and the short distance for the H^+ species to travel for secondary spillover to occur.

A similar study of varying the distance between two metals was conducted on Fe oxide and Pt promoter [5]. A surface-sensitive and space-resolved in situ single nanoparticle iron edge XAS measurement was performed simultaneously on each of the 16 Fe nanoparticles to reveal their degree of reduction as a function of distance from the Pt particle [71–73]. The metals were supported on a nonreducible aluminium oxide support and the inter-particle distance between Fe oxide and Pt promoter was 45 nm to 0 nm where they overlapped on one another. Hydrogen spillover was noticed at inter-particle distances below 15 nm and the reduction of Fe oxide increased with decrease in distance. Overall, the observations from the TPR showed that secondary spillover is limited by distance the H atoms travel in order to reduce the Co oxide.

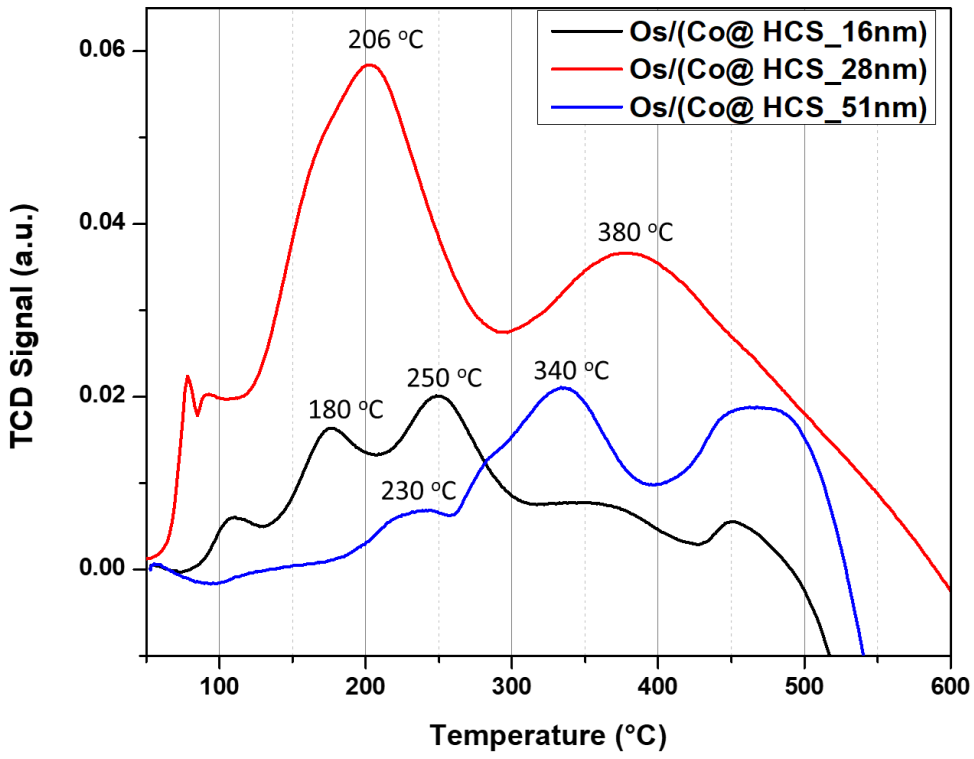

Figure 6.8: TPR profiles of Os/(Co@HCS16), Os/(Co@HCS28) and Os/(Co@HCS51)

Table 6.4: Summary of the TPR first and second reduction data.

Sample	First reduction (˚C)	Second reduction (˚C)
10%Co@HCS16	230	340
10%Co@HCS28	260	335
10%Co@HCS51	280	350
1% Os/(10%Co@HCS16)	180	250
1% Os/(10%Co@HCS28)	206	380
1% Os/(10%Co@HCS51)	230	340

6.3.6 Fischer Tropsch Synthesis (FTS)

In a fixed-bed micro-reactor at 220 (Table 6.4) and 250 °C (Table S6.1) for a total of 50 h at each reaction temperature, the FTS activity was assessed to determine the promoter's impact on the catalysts. Pre-treatment of the four catalysts was done by reducing the catalysts at 350 ℃ to assess the FTS catalytic performance. A summary of the catalytic performance and selectivity obtained is given in Table 6.5.

The Co nanoparticles encapsulated inside HCS (10%Co@HCS28) was used as a standard to investigate the FTS performance when the Os promoter was loaded onto the outside of the HCS support with varying carbon shell thickness. The activity of all the promoted catalysts was higher compared to the unpromoted catalysts and this observation can be explained by the reducibility induced on by the Os promoter effects. (Table 6.4) This suggests that a secondary spillover effect was detected in FTS and could be varied as a function of change in shell thickness on the FTS performance. The shorter distance travelled by the H species in Os/(Co@HCS16 nm, between the Os promoter and the Co catalyst via the carbon shell during the secondary spillover was seen to give a higher CO conversion compared to the longer distance travelled by the H species (Os/(Co@HCS51 nm). The CO conversion thus increased in the following order: (Os/(Co@HCS51 nm) < (Os/(Co@HCS28 nm) < (Os/(Co@HCS16 nm). This observation was affected by various factors such as hydrogen species diffusion effects, the particle size and the phase of Co nanoparticles encapsulated inside the HCSs, and the permeability of the HCSs in releasing products.

This trend suggested that a thicker carbon shell inhibited the flow of reactants thus resulting in lower CO conversion. A similar trend was observed in the TPR studies where a decrease in permeability with correspondence to an increase in the carbon shell thickness resulted in a limit to the ability of H_2 molecules to enter inside the HCS in order to reduce the Co_3O_4 into Co^0 metal.

Generally, CO conversion increases with a decrease in Co particle size, however, the opposite was observed in that the CO conversion increased with an increase in particle size from 5 nm to 10 nm. A similar observation was obtained in a study where the CO conversion increased from 22.5% to 35.6% at 210 °C and from 54.9% to 91.2% at 230 °C as the size of the Co nanoparticles increased from 5 nm to 8 nm, using Co nanoparticles coated in a silica shell [74]. Another explanation for the higher CO conversion in the (Os/(Co@HCS16 nm) catalyst attributed to the Co phase present viz. which was a hcp phase which has a higher intrinsic activity for CO hydrogenation reactions compared to the fcc Co phase obtained in Os/(Co@HCS28 nm) and Os/(Co@HCS51 nm) catalysts [75].

The Co catalyst is usually selective towards the production of large quantities of of high molecular products (e.g. C_{5+}) [76]. The FTS measurements showed that Os promoted Co@HCS catalysts resulted in high molecular products being favoured. High reaction temperature was observed to result in high methane selectivity. The selectivity to C_5+ hydrocarbons is expected to be due to Os enrichment on the cobalt crystallite surface via secondary spillover effect. Similar to what has been reported for a Ru promoted Co catalyst [77, 78]. The increase in shell thickness did not show any significant change in hydrocarbon selectivity among the Os promoted catalysts (1%Os/(10%Co@HCSx, x = 16 and 28 nm). However, the 1%Os/(10%Co@HCS_51 nm) catalyst showed higher selectivity towards C_{5+} hydrocarbon compared to the other Os promoted catalysts and this could be a result of the thick carbon shell. This could suggest that a thicker carbon shell, Co@HCS_51nm, can inhibit the flow of reactants, leading to long chain growth forming within the HCS, thus resulting in high selectivity towards C_{5+} hydrocarbon being produced.

Table 6.5: A summary of the Fischer-Tropsch catalytic performance and selectivity.

Sample	CO Conversion (%)	TOF ($x10^{-3}$ s)[a]	Activity ($x10^{-6}$) ($mol_{CO}/g_{Co}.s$)	Selectivity (C mol) %

				C_1	C_2-C_4	C_{5+}
Co@HCS28	4.2	6.0	27.8	18.8	11.1	70.1
Os/(Co@HCS_16)	7.4	26,3	41.3	13.2	4.9	81.9
Os/(Co@HCS_28)	5.0	23.4	36.4	13.0	3.4	83.6
Os/(Co@HCS_51)	1.6	4.9	18.6	7.6	3.8	88.6

6.4. Conclusion

In this study, Co nanoparticles were successfully synthesized and encapsulated inside a carbon shell support (HCS) with varying thicknesses. The catalysts were then promoted with Os on the outside of the HCS to investigate any secondary hydrogen spillover effects. The catalysts were found to be thermally stable for use in a Fischer-Tropsch synthesis (FTS) reaction. The TPR studies showed that as the carbon shell thickness decreased the reducibility of Co_3O_4 to metallic Co in the following order: Co@HCS16 < Co@HCS28 < Co@HCS51. Further, the reducibility of Co_3O_4 was found to be enhanced by the addition of an Os promoter. Significant downward shifts in the reduction temperature of the Co was observed with decreasing carbon thickness. It thus appears that the ease of H_2 diffusion through the carbon shell impacts on the Co reduction.

BET results, showed that a lower surface area and higher FT CO conversion were associated with the thin carbon shell catalysts, Co@HCS_16 nm. The incorporation of the Os promoter improved the CO conversion and shifted the selectivity towards the production of longer chain hydrocarbons. The secondary hydrogen spillover effect was measured as a function of shell thickness and its impact on FTS performance. It was found that a shorter distance travelled by H species between the Os promoter and Co catalyst resulted in a higher CO conversion compared to when longer distances were travelled. A decrease in distance between the Os promoter and Co catalyst also impacted on the Co phase in that the reduction of CoO to metallic Co (fcc and hcp) XRD peak intensity increased. Furthermore, the Os/(Co@HCS_16 nm) catalyst had a Co hcp phase being observed due to intimacy between the metals, whereas, the Os/(Co@HCS_28 nm) and Os/(Co@HCS_51 nm) showed a Co fcc phase. This trend suggests that a thicker carbon shell, Co@HCS_51nm, can inhibit the flow of reactants, leading to lower CO conversions and long chain growth forming within the HCS, thus resulting in high selectivity towards C_{5+} hydrocarbon being produced.

6.5. Reference

1. Xie Z, Liu Z, Wang Y, Jin Z (2015) Applied catalysis for sustainable development of chemical industry in China. Natl Sci Rev 2:167–182

2. Cheng L, Xiang Q, Liao Y, Zhang H (2018) CdS-based photocatalysts. Energy Environ Sci 11:1362–1391

3. Yilmaz G, Peh SB, Zhao D, Ho GW (2019) Atomic-and Molecular-Level Design of Functional Metal–Organic Frameworks (MOFs) and Derivatives for Energy and Environmental Applications. Adv Sci 6:1901129

4. Khoobiar S (1964) Particle to particle migration of hydrogen atoms on platinum—alumina catalysts from particle to neighboring particles. J Phys Chem 68:411–412

5. Karim W, Spreafico C, Kleibert A, et al (2017) Catalyst support effects on hydrogen spillover. Nature 541:68–71

6. Conner Jr WC, Falconer JL (1995) Spillover in heterogeneous catalysis. Chem Rev 95:759–788

7. Gardes GEE, Pajonk GM, Teichner SJ (1974) Catalytic demonstration of hydrogen spillover from nickel-alumina catalyst to alumina. J Catal 33:145–148

8. Prins R (2012) Hydrogen spillover. Facts and fiction. Chem Rev 112:2714–2738

9. Teichner SJ (1993) The history and perspectives of spillover. In: Studies in Surface Science and Catalysis. Elsevier, pp 27–43

10. Zhan G, Zeng HC (2018) Hydrogen spillover through Matryoshka-type (ZIFs@) n− 1 ZIFs nanocubes. Nat Commun 9:1–12

11. Anson A, Lafuente E, Urriolabeitia E, et al (2006) Hydrogen capacity of palladium-loaded carbon materials. J Phys Chem B 110:6643–6648

12. Aksoylu AE, Madalena M, Freitas A, et al (2001) The effects of different activated carbon supports and support modifications on the properties of Pt/AC catalysts. Carbon N Y 39:175–185

13. Amorim C, Keane MA (2008) Palladium supported on structured and nonstructured carbon: A consideration of Pd particle size and the nature of reactive hydrogen. J Colloid Interface Sci 322:196–208

14. Park S-J, Lee S-Y (2010) Hydrogen storage behaviors of platinum-supported multi-walled carbon nanotubes. Int J Hydrogen Energy 35:13048–13054

15. Jain P, Fonseca DA, Schaible E, Lueking AD (2007) Hydrogen uptake of platinum-doped graphite nanofibers and stochastic analysis of hydrogen spillover. J Phys Chem C 111:1788–1800

16. Lupu D, Biriş AR, Mişan I, et al (2004) Hydrogen uptake by carbon nanofibers catalyzed by palladium. Int J Hydrogen Energy 29:97–102

17. Back C-K, Sandí G, Prakash J, Hranisavljevic J (2006) Hydrogen sorption on palladium-doped sepiolite-derived carbon nanofibers. J Phys Chem B 110:16225–16231

18. Yoo E, Gao L, Komatsu T, et al (2004) Atomic hydrogen storage in carbon nanotubes promoted by metal catalysts. J Phys Chem B 108:18903–18907

19. Zacharia R, Kim KY, Kibria AKMF, Nahm KS (2005) Enhancement of hydrogen storage capacity of carbon nanotubes via spill-over from vanadium and palladium nanoparticles. Chem Phys Lett 412:369–375

20. Chen C-H, Huang C-C (2008) Enhancement of hydrogen spillover onto carbon nanotubes with defect feature. Microporous Mesoporous Mater 109:549–559

21. Suttisawat Y, Rangsunvigit P, Kitiyanan B, et al (2009) Investigation of hydrogen storage capacity of multi-walled carbon nanotubes deposited with Pd or V. Int J Hydrogen Energy 34:6669–6675

22. Bhowmick R, Rajasekaran S, Friebel D, et al (2011) Hydrogen spillover in Pt-single-walled carbon nanotube composites: formation of stable C− H bonds. J Am Chem Soc 133:5580–5586

23. Zacharia R, Rather S, Hwang SW, Nahm KS (2007) Spillover of physisorbed hydrogen from sputter-deposited arrays of platinum nanoparticles to multi-walled carbon nanotubes. Chem Phys Lett 434:286–291

24. Reyhani A, Mortazavi SZ, Mirershadi S, et al (2011) Hydrogen storage in decorated multiwalled carbon nanotubes by Ca, Co, Fe, Ni, and Pd nanoparticles under ambient conditions. J Phys Chem C 115:6994–7001

25. Wu H, Wexler D, Liu H (2012) Effects of different palladium content loading on the hydrogen storage capacity of double-walled carbon nanotubes. Int J Hydrogen Energy 37:5686–5690

26. Saha D, Deng S (2011) Hydrogen adsorption on Pd-and Ru-doped C60 fullerene at an ambient temperature. Langmuir 27:6780–6786

27. Zubizarreta L, Menéndez JA, Pis JJ, Arenillas A (2009) Improving hydrogen storage in Ni-doped carbon nanospheres. Int J Hydrogen Energy 34:3070–3076

28. Campesi R, Cuevas F, Gadiou R, et al (2008) Hydrogen storage properties of Pd nanoparticle/carbon template composites. Carbon N Y 46:206–214

29. Chen C-H, Chung T-Y, Shen C-C, et al (2013) Hydrogen storage performance in palladium-doped graphene/carbon composites. Int J Hydrogen Energy 38:3681–3688

30. Vinayan BP, Sethupathi K, Ramaprabhu S (2013) Facile synthesis of triangular shaped palladium nanoparticles decorated nitrogen doped graphene and their catalytic study for renewable energy applications. Int J Hydrogen Energy 38:2240–2250

31. Vinayan BP, Sethupathi K, Ramaprabhu S (2012) Hydrogen storage studies of palladium decorated nitrogen doped graphene nanoplatelets. J Nanosci Nanotechnol 12:6608–6614

32. Parambhath VB, Nagar R, Ramaprabhu S (2012) Effect of nitrogen doping on hydrogen storage capacity of palladium decorated graphene. Langmuir 28:7826–7833

33. Giasafaki D, Charalambopoulou G, Bourlinos A, et al (2013) A hydrogen sorption study on a Pd-doped CMK-3 type ordered mesoporous carbon. Adsorption 19:803–811

34. Zlotea C, Cuevas F, Paul-Boncour V, et al (2010) Size-dependent hydrogen sorption in ultrasmall Pd clusters embedded in a mesoporous carbon template. J Am Chem Soc 132:7720–7729

35. Yang Y-X, Bourgeois L, Zhao C, et al (2009) Ordered micro-porous carbon molecular sieves containing well-dispersed platinum nanoparticles for hydrogen storage. Microporous mesoporous Mater 119:39–46

36. Bukur DB, Lang X, Mukesh D, et al (1990) Binder/support effects on the activity and selectivity of iron catalysts in the Fischer-Tropsch synthesis. Ind Eng Chem Res 29:1588–1599

37. Regalbuto J (2016) Catalyst preparation: science and engineering. CRC press

38. Sharma R (2012) Enzyme Inhibition and Bioapplications IntechOpen. DOI 10:39273

39. Li N, Zhang Q, Liu J, et al (2013) Sol–gel coating of inorganic nanostructures with resorcinol–formaldehyde resin. Chem Commun 49:5135–5137

40. de la Peña O'Shea VA, Álvarez-Galván MC, Campos-Martin JM, et al (2006) Surface and Structural Features of Co-Fe Oxide Nanoparticles Deposited on a Silica Substrate. Eur J Inorg Chem 2006:5057–5068

41. Ikeda S, Ishino S, Harada T, et al (2006) Ligand-free platinum nanoparticles encapsulated in a hollow porous carbon shell as a highly active heterogeneous hydrogenation catalyst. Angew Chemie - Int Ed 45:7063–7066. https://doi.org/10.1002/anie.200602700

42. Phaahlamohlaka TN, Kumi DO, Dlamini MW, et al (2017) Effects of Co and Ru Intimacy in Fischer-Tropsch Catalysts Using Hollow Carbon Sphere Supports: Assessment of the Hydrogen Spillover Processes. ACS Catal 7:1568–1578. https://doi.org/10.1021/acscatal.6b03102

43. Lachawiec AJ, Qi G, Yang RT (2005) Hydrogen storage in nanostructured carbons by spillover: bridge-building enhancement. Langmuir 21:11418–11424

44. Lueking A, Yang RT (2002) Hydrogen spillover from a metal oxide catalyst onto carbon nanotubes—implications for hydrogen storage. J Catal 206:165–168

45. Hirscher M, Becher M (2003) Hydrogen storage in carbon nanotubes. J Nanosci Nanotechnol 3:3–17

46. Liu Y-Y, Zeng J-L, Zhang J, et al (2007) Improved hydrogen storage in the modified metal-organic frameworks by hydrogen spillover effect. Int J Hydrogen Energy 32:4005–4010

47. Fu J, Xu Q, Chen J, et al (2010) Controlled fabrication of uniform hollow core porous shell carbon spheres by the pyrolysis of core/shell polystyrene/cross-linked polyphosphazene composites. Chem Commun 46:6563–6565

48. Chirariwa H, Muzenda E (2015) The Preparation and Characterisation of Osmium(IV), Osmium(II) and Osmium(0) Complexes from Refinery Materials. 0–4. https://doi.org/10.15242/iie.e1114015

49. Fang X, Liu S, Zang J, et al (2013) Precisely controlled resorcinol–formaldehyde resin coating for fabricating core–shell, hollow, and yolk–shell carbon nanostructures. Nanoscale 5:6908–6916

50. Qi G, Wang Y, Estevez L, et al (2010) Facile and scalable synthesis of monodispersed spherical capsules with a mesoporous shell. Chem Mater 22:2693–2695

51. Li S, Pasc A, Fierro V, Celzard A (2016) Hollow carbon spheres, synthesis and applications–a review. J Mater Chem A 4:12686–12713

52. Zheng M, Cao J, Chang X, et al (2006) Preparation of oxide hollow spheres by colloidal carbon spheres. Mater Lett 60:2991–2993

53. Stober W, Fink A (1968) Controlled Growth of Monodispersed Silica Spheres in the Micron Size Range. J Colloid Interface Sci 26:62–69. https://doi.org/10.1016/0021-9797(68)90272-5

54. Livingstone SE (2016) The Chemistry of Ruthenium, Rhodium, Palladium, Osmium, Iridium and Platinum: Pergamon Texts in Inorganic Chemistry. Elsevier

55. Jacobs G, Patterson PM, Zhang Y, et al (2002) Fischer–Tropsch synthesis: deactivation of noble

metal-promoted Co/Al2O3 catalysts. Appl Catal A Gen 233:215–226

56. Xiong H, Moyo M, Motchelaho MA, et al (2014) Fischer–Tropsch synthesis: Iron catalysts supported on N-doped carbon spheres prepared by chemical vapor deposition and hydrothermal approaches. J Catal 311:80–87

57. Ma X, Gan L, Liu M, et al (2014) Mesoporous size controllable carbon microspheres and their electrochemical performances for supercapacitor electrodes. J Mater Chem A 2:8407–8415

58. Khodakov AY, Griboval-Constant A, Bechara R, Zholobenko VL (2002) Pore size effects in Fischer Tropsch synthesis over cobalt-supported mesoporous silicas. J Catal 206:230–241

59. Ferrari AC, Robertson J (2000) Interpretation of Raman spectra of disordered and amorphous carbon. Phys Rev B 61:14095

60. Chen W, Pan X, Willinger M-G, et al (2006) Facile autoreduction of iron oxide/carbon nanotube encapsulates. J Am Chem Soc 128:3136–3137

61. Weidenthaler C (2011) Pitfalls in the characterization of nanoporous and nanosized materials. Nanoscale 3:792–810

62. Van't Blik HFJ, Koningsberger DC, Prins R (1986) Characterization of supported cobalt and cobalt-rhodium catalysts: III. Temperature-Programmed Reduction (TPR), Oxidation (TPO), and EXAFS of Co□ RhSiO2. J Catal 97:210–218

63. Castner DG, Watson PR, Chan IY (1990) X-ray absorption spectroscopy, X-ray photoelectron spectroscopy, and analytical electron microscopy studies of cobalt catalysts. 2. Hydrogen reduction properties. J Phys Chem 94:819–828

64. Ernst B, Bensaddik A, Hilaire L, et al (1998) Study on a cobalt silica catalyst during reduction and Fischer–Tropsch reaction: in situ EXAFS compared to XPS and XRD. Catal today 39:329–341

65. Bechara R, Balloy D, Dauphin J-Y, Grimblot J (1999) Influence of the characteristics of γ-aluminas on the dispersion and the reducibility of supported cobalt catalysts. Chem Mater 11:1703–1711

66. Khodakov AY, Lynch J, Bazin D, et al (1997) Reducibility of cobalt species in silica-supported Fischer–Tropsch catalysts. J Catal 168:16–25

67. Nabaho D, Niemantsverdriet JWH, Claeys M, van Steen E (2016) Hydrogen spillover in the Fischer–Tropsch synthesis: an analysis of gold as a promoter for cobalt–alumina catalysts. Catal Today 275:27–34

68. Van de Loosdrecht J, Barradas S, Caricato EA, et al (2003) Calcination of Co-based Fischer–Tropsch synthesis catalysts. Top Catal 26:121–127

69. Kang ZC, Wang ZL (1996) On accretion of nanosize carbon spheres. J Phys Chem 100:5163–5165

70. Wang ZL, Kang ZC (1997) Graphitic structure and surface chemical activity of nanosize carbon spheres. Carbon N Y 35:419–426

71. Karim W, Kleibert A, Hartfelder U, et al (2016) Size-dependent redox behavior of iron observed by in-situ single nanoparticle spectro-microscopy on well-defined model systems. Sci Rep 6:1–8

72. Van Bokhoven JA, Lamberti C (2016) X-ray absorption and X-ray emission spectroscopy: theory and applications. John Wiley & Sons

73. Vaz CAF, Balan A, Nolting F, Kleibert A (2014) In situ magnetic and electronic investigation of the early stage oxidation of Fe nanoparticles using X-ray photo-emission electron microscopy. Phys Chem Chem Phys 16:26624–26630

74. Zeng B, Hou B, Jia L, et al (2013) Studies of Cobalt Particle Size Effects on Fischer–Tropsch Synthesis over Core–Shell-Structured Catalysts. ChemCatChem 5:3794–3801

75. Beaumont SK, Alayoglu S, Specht C, et al (2014) A nanoscale demonstration of hydrogen atom spillover and surface diffusion across silica using the kinetics of CO2 methanation catalyzed on spatially separate Pt and Co nanoparticles. Nano Lett 14:4792–4796

76. Van Der Laan GP, Beenackers AACM (1999) Kinetics and Selectivity of the Fischer-Tropsch Synthesis: A Literature Review. Catal Rev - Sci Eng 41:255–318. https://doi.org/10.1081/CR-100101170

77. Tavasoli A, Karimi A, Khodadadi AA, et al (2005) Accelerated deactivation and activity recovery studies of ruthenium and rhenium promoted cobalt catalysts in Fischer-Tropsch synthesis

78. Trépanier M, Tavasoli A, Dalai AK, Abatzoglou N (2009) Co, Ru and K loadings effects on the activity and selectivity of carbon nanotubes supported cobalt catalyst in Fischer–Tropsch synthesis. Appl Catal A Gen 353:193–202

Chapter 7

Osmium promoter effects on the hydrogen spillover and performance of nitrogen functionalized hollow carbon spheres supported cobalt Fischer-Tropsch synthesis catalysts

Chapter to be published:

7.1 Introduction

Low temperature Fischer-Tropsch synthesis (FTS) is an important route for the production of clean hydrocarbon fuels (contains very low sulphur) and fine chemicals from syngas (H_2 and CO), which can be generated from coal, natural gas or biomass [1, 2]. The emergence of the processes can be attributed to economic, socio-political, and climate change-related factors related to the use of crude oil. The process involves a metal catalyst such as cobalt (Co) being supported on a refractory oxide or carbonaceous material. Supported Co catalysts are well known for their activity and selectivity in the FT reaction [3–5]. From literature, most studies in FTS have been on Co-based (and Fe-based) catalysts supported on metal oxides such as alumina, titania and silica [6–8]. Carbon-based materials due to their special qualities of having a high thermal stability, tuneable surface chemistry, and potentially large surface area, have recently been researched as model supports for Co FT catalysts. Carbon-based materials properties are influenced by the carbon morphology [9], and carbon supports applied in FTS include activated carbon (AC), carbon spheres (CSs), carbon nanofibers (CNFs), carbon nanotubes (CNTs), hollow carbon spheres (HCSs) and graphene nanosheets (GNSs) [10, 11]. As a support material for FTS catalysts, HCSs have shown to have unique advantageous properties such as high surface area, a porous structure and low density. HCSs make interesting support materials for the design of highly dispersed catalysts for FTS because of their low density and high surface to volume ratios. Furthermore, the ability to encapsulate a metal catalyst within the HCS provides an excellent platform for research on metal-support interactions, the effects of catalyst size, and the impact of carbon framework surface functionalization or doping.

Functionalization is a common and reliable technique for converting a hydrophobic carbon surface into a hydrophilic one [12]. Functionalization of the carbon framework surface involves doping it with a heteroatom such as nitrogen or oxygen. It has been reported that the stabilization and interaction between a catalyst and its support are improved by functionalizing

carbon-based support materials, which enhances the catalyst's catalytic performance [13, 14]. When used as a support for Co catalyst in FTS, nitrogen doped carbons outperform oxygen functionalized carbon materials in terms of catalytic activity [15]. In general, the doping procedure can occur through either in-situ or ex-situ procedures. In the in-situ process the carbon is made to contain the N through the direct use of appropriate N containing carbon molecules. In the ex-situ method a carbon material is coated with N after the carbon has been synthesized. For instance, a nitrogen-containing precursor like ammonia or melamine can be used to treat the carbon material at a high temperature. This results in decomposition of the precursor to give free radicals like NH_2, NH, atomic nitrogen and hydrogen. The carbon framework is therefore attacked by the free radicals to form nitrogen-containing functional groups such as $–NH_2$, –CN, as well as pyrrolic and quaternary nitrogen [16]. N-doped carbon supported FT catalysts have drawn a lot of attention from researchers [17, 18, 27–29, 19–26]. One of the studies reported that Co supported on N-doped carbon can enhance the selectivity of heavy hydrocarbons being produced [30]. Even though nitrogen doping enhances the FTS catalytic performance and selectivity of a catalyst, another method for catalytic performance enhancement is through promotion effects.

Co FT catalysts are generally promoted with noble metals such a rhenium, platinum, and ruthenium in order enhance the catalytic activity of the Co active site [31–33]. Promoters can be categorised, according to their purpose, into two groups: 1) those that facilitate the desired reaction, for example, by increasing the activity of the catalyst; and 2) those that suppress any unwanted processes, for example, by increasing the selectivity of the catalyst [34]. A promoter metal can enhance the catalytic activity of, for example, Co. This is done by lowering the reduction temperature of the cobalt oxide through hydrogen dissociative/associative reactions, through a mechanism known as hydrogen spillover [35–38]. Two types of hydrogen spillover processes can be envisaged. In a (1) primary hydrogen spillover, the promoter (i.e initiator) is in direct contact with the Co oxide (i.e acceptor) and dissociation of hydrogen occurs on the promoter surface into hydrogen atoms which migrate to reduce Co oxide into Co^0 (metallic) and form water. In a (2) secondary hydrogen spillover, the promoter and Co oxide are separated by varying distances. Here the dissociated hydrogen atom on the promoter has to migrate on the surface of the support material (e.g., via hydroxyl groups on oxidic supports) with spillover to the Co oxide which results in the reduction of Co oxide. In literature, hydrogen spillover research including Co FT catalysts has been conducted on metal oxide support materials, which have shown to provide a minimal hydrogen effect over long hydrogen transfer distances. A

study by Prins et al. suggested that the flawed carbon sites have the ability to chemically adsorb hydrogen, and that hydrogen spillover on the defective carbon nanomaterials was viable [39]. A secondary hydrogen spillover process could be aided by nitrogen doping facilitating the surface diffusion of activated hydrogen species.

In the present work, HCSs and N-functionalized HCSs (NHCSs) were studied by using them as a support material for a Co FT catalyst under FTS conditions. In contrasting the non-doped HCSs with nitrogen doped HCSs as a support material for the Co FT catalyst, the impact of surface functionalization was investigated. Furthermore, both catalysts were promoted with osmium to study the secondary spillover effects on Co FT catalysts using both the HCS and NHCS supports as a physical barrier.

7.2 Experimental

7.3.1 Materials

All samples were of analytical grade and were purchased from various sources. The cobalt nitrate hexahydrate (Aldrich), potassium osmate (Anglo American Research Laboratories, Johannesburg), ammonia solution (25%; Fluka), ethanol (98%; Merck), hexadecyltrimethylammonium bromide (CTAB; Aldrich), styrene (Aldrich), polyvinylpyrollidone (PVP, MW 40 K, Aldrich) formaldehyde (37%; Aldrich), resorcinol, potassium persulfate (Eimer and Amend), hydrazine (35%; Aldrich), melamine (99%; Aldrich) and deionized water were used as received in the experiments.

7.3.2 Synthesis of polystyrene spheres (PSSs) [40]

Styrene (8 mL) and polyvinylpyrollidone (PVP, 0.2 g) was dispersed and dissolved in a mixture of 200 mL ethanol and 50 mL deionized water in a round bottom flask. The mixture was sonicated and stirred for 15 min. Thereafter, potassium persulfate (KPS, 0.3 g in 10 mL deionized water) was added to the prepared reaction mixture while stirring. The mixture was then heated at 80 ^{o}C for 24 h. After the reaction the product was cooled, filtered, and washed successively using deionized water. The obtained yield was ~ 6 g.

7.3.3 Synthesis of ammonium hexachloroosmate (IV), $(NH_4)_2OsCl_6$ [41]

Potassium osmate (5.00 g, 19.36 mmol) and 200 mL concentrated hydrochloric acid (35%) were placed in a 500 mL round bottom flask. The reaction mixture was stirred and heated at reflux for 2 h after which 50 mL 20% (w/v) ammonium chloride (186.9 mmol) solution was added, followed by cooling of the mixture in ice. The solid which formed was isolated and washed with 80% ethanol to remove the potassium. Potassium ions were removed as they can

act as a promoter in FTS. The precipitate was recrystallized from hot concentrated hydrochloric acid. Ammonium hexachloroosmate (IV) ($(NH_4)_2OsCl_6$) crystallised as deep red-brown cubes which were washed with absolute ethanol (8.1 g, 95% yield).

7.3.4 Synthesis of Co on the polystyrene spheres (Co/PSSs) [42]

PSSs (3 g) were dissolved in a mixture of 75 mL deionized water and 25 ml ethanol. To this mixture was added cobalt nitrate hexahydrate (0.45 g), while stirring, until the solution turned red. Thereafter, 10 mL of hydrazine (2 M) was slowly added to the prepared solution dropwise, and the solution was stirred for 12 h to ensure complete deposition of Co nanoparticles onto the PSSs to give Co/PSSs.

7.3.5 Synthesis of Co nanoparticles encapsulated inside hollow carbon spheres (Co@HCS)

The Co/PSSs (Co = 10% Co) (1 g) and ammonia solution (25%; 4 mL) were dissolved and dispersed in a mixture of 70 mL ethanol and 15 ml deionized water by sonication for 30 min. Subsequently, resorcinol (0.5 g), formaldehyde (0.5 mL) and hexadecyltrimethylammonium bromide (3 g) were added to make the resorcinol-formaldehyde core-shell structure. The solution was allowed to stir at room temperature for 24 h. The formed resorcinol-formaldehyde (RF) core shell structure around the Co/PSSs was filtered, and then washed successively with water and ethanol. This was followed by drying at 80 ^oC for 12 h to give Co/PSS@RF. Template removal and carbonization of the Co/PSS@RF was performed in a two-step horizontal chemical vapour deposition (CVD) procedure, where template removal was carried out under a flow of nitrogen gas (50 ml/min) at 350 ^oC for 1 h to decompose the PSSs. This was followed by the carbonization of the RF core shell structure under a flow of nitrogen gas (50 ml/min) at 600 ^oC for 2 h. The resulting product was called Co@HCS.

7.3.6 Synthesis of nitrogen-doped Co@HCSs (Co@NHCSs)

The Co/PSS@RF (3 g) composite was mixed with melamine (3 g) in a sample vial containing methanol (20 mL). The mixture was sonicated for 30 min followed by drying in an oven at 80 ^oC for 2 h. Template removal and carbonization of the prepared Co/PSS@RF@melamine composite was performed using the CVD steps and conditions listed in section 2.5. The resulting product (Co/PSS@RF@melamine) was called Co@NHCS to simplify the nomenclature.

7.3.7 Synthesis of Os/(Co@HCS) and Os/(Co@NHCS) catalyst

The Co@HCS or Co@NHCS (1.5 g) catalyst was dispersed in 250 mL of deionized water by sonication. To this mixture was added to the Os salt precursor (0.012 g, Os = 0.1%; 0.035 g, Os = 0.5%; 0.069 g, Os = 1%) and urea (0.4 g) followed by 30 min sonication. The mixture

was then stirred at 95 ^{o}C in a round bottom flask for 12 h. The product Os/(Co@HCS) or Os/(Co@NHCS) was collected after filtration and washing successively with water, followed by drying at 80 ^{o}C for 12 h.

7.3Results

7.3.1 Transmission electron microscopy

The hollow carbon spheres (HCSs) were prepared by coating polystyrene spheres (PSS) with resorcinol-formaldehyde (RF). Whereas, the Nitrogen doped HCSs (NHCS) were prepared by ex-situ method were a carbon material (RF) was coated with N after the carbon had been synthesized. Thereafter the sample was heated to remove the sacrificial PSS template leaving a hollow spherical carbon shell [43]. The HCS support material had a diameter of 469 $\pm$ 92 nm and a carbon shell thickness of 37 $\pm$ 5.7 nm. The NHCS support material had similar dimensions; a diameter of 464 $\pm$ 123 nm and a carbon shell thickness of 41 $\pm$ 13.6 nm. It thus appears that the addition of the N source did not affect the shell thickness substantially. It did modify the surface as seen from XPS data (see below). The thickness of the carbon shell was chosen so as to ensure that secondary hydrogen spillover could take place with the H^{+} species required to travel a short distance on/through the carbon material. The mesoporous carbon shell also facilitated permeability, thus providing easy access for small molecules to enter and exit the catalyst as the FTS reaction occurred [44].

TEM images of the Co and Os supported in/on the HCSs and NHCSs complexes show that the carbon shells are spherical and have good uniformity (Fig. 7.1). The Co nanoparticles were successfully encapsulated and were highly dispersed within both the HCSs and NHCSs (Fig. 7.1 (a)) and (b), respectively). Fig. 7.1 (b) and (d) shows the presence of Os promoter on the surface of the carbon shell for 1%Os/(10%Co@HCS) and 1%Os/(10%Co@NHCS) catalysts, respectively.

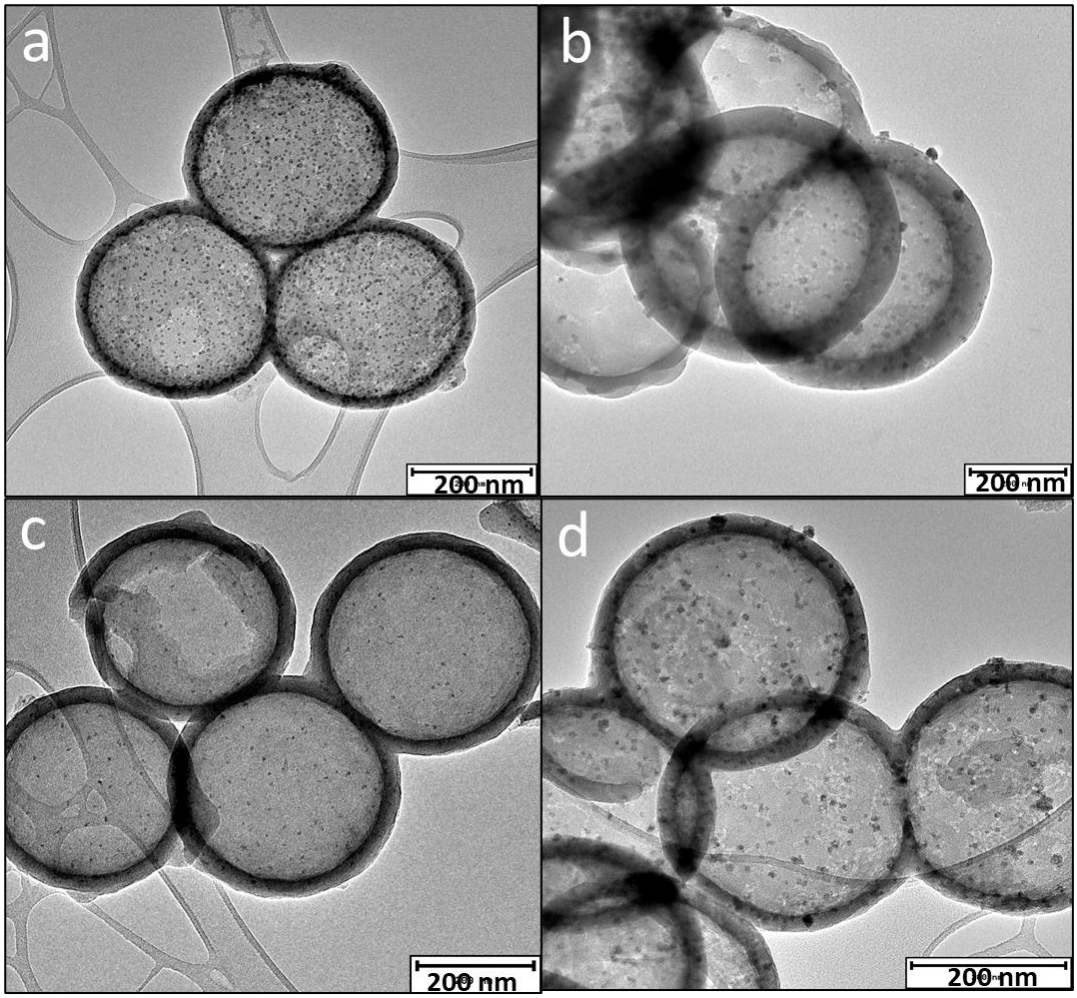

Figure 7.1: TEM images of (a) 10%Co@HCS, (b) 1%Os/(10%Co@HCS), (c) 10%Co@NHCS, and (d) 1%Os/(10%Co@NHCS)

The average particle size of the Co nanoparticles supported on the HCSs was observed to be 3.9 nm (Fig. 7.2 (a)), whereas those supported on NHCSs, had a smaller average particle size distribution of 3.4 nm (Fig 7.2 (b)); overall, the difference in particle size distribution was small. The same catalysts were further promoted with Os on the outer shell and the Co particle size distribution for 1%Os/(10%Co@HCS) and 1%Os/(10%Co@NHCS) catalysts were found to be 9.8 nm and 7.2 nm (Fig 7.2 (c) and (d)).

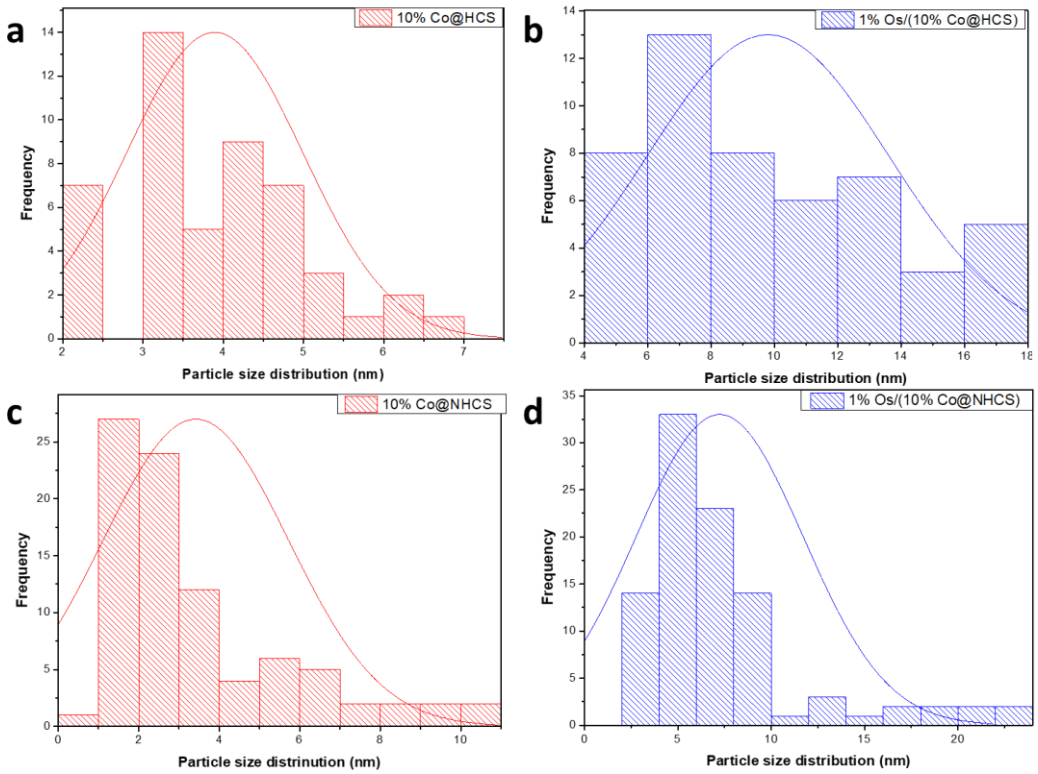

Figure 7.2: Co particle size distribution of a) 10%Co@HCS, b) 1%Os/(10%Co@HCS), c) 10%Co@NHCS, and d) 1%Os/(10%Co@HCS)

As expected, the Co nanoparticles showed better dispersion on the NHCS supports compared to HCS supports [45]. This is related to the nitrogen functional groups and the presence of more defects on the NHCS surface, which function as anchoring sites, increasing the interaction between the support and the metal precursor [45]. Another observation was that the Os promoted catalysts gave larger Co nanoparticles compared to the non-promoted catalysts. This observation suggests that the Os promoter's close proximity to the Co catalyst led to the growth of Co particles.

Energy dispersive X-ray analysis (EDX) was conducted using TEM and from the analysis confirmation of the presence of Co and C in the 10%Co@HCS and Co, C and N in the 10%Co@NHCS catalysts was obtained (Fig. S7.1 (a) and (b), respectively). Furthermore, Os was detected in the promoted catalysts, 1%Os/(10%Co@HCS), and 1%Os/(10%Co@NHCS) (Fig. S7.1 (c) and (d)), respectively.

7.3.2 X-ray photoelectron spectroscopy (XPS)

The chemical composition and oxidation state of the synthesized catalysts was investigated with the use of XPS. The XPS survey spectra showed the presence of C, N, O, Co and Os, as shown in Fig 7.3. The elemental quantification of the samples investigated by XPS was determined by taking the integrated peak areas of the C1s, N1s, O1s, Co2p, and Os4f from the XPS survey spectra (summarized in Table S7.1). The HCS and NHCS XPS signal had C and O for both samples, and that of NHCS had a N peak due to N-doping. A similar trend was observed for 10%Co@HCS and 10%Co@NHCS; and for 1%Os/(10%Co@HCS) and 1%Os/(10%Co@HCS). The 10%Co@HCS and 10%Co@NHCS catalysts showed a small to insignificant Co peak while the 1%Os/(10%Co@HCS) and 1%Os/(10%Co@HCS) catalysts showed the presence of Co (very low content, Table S7.1) and Os peak. This is expected as the Co was placed inside the HCSs. The findings also confirmed that N-doping was successful on the doped catalysts [46, 47].

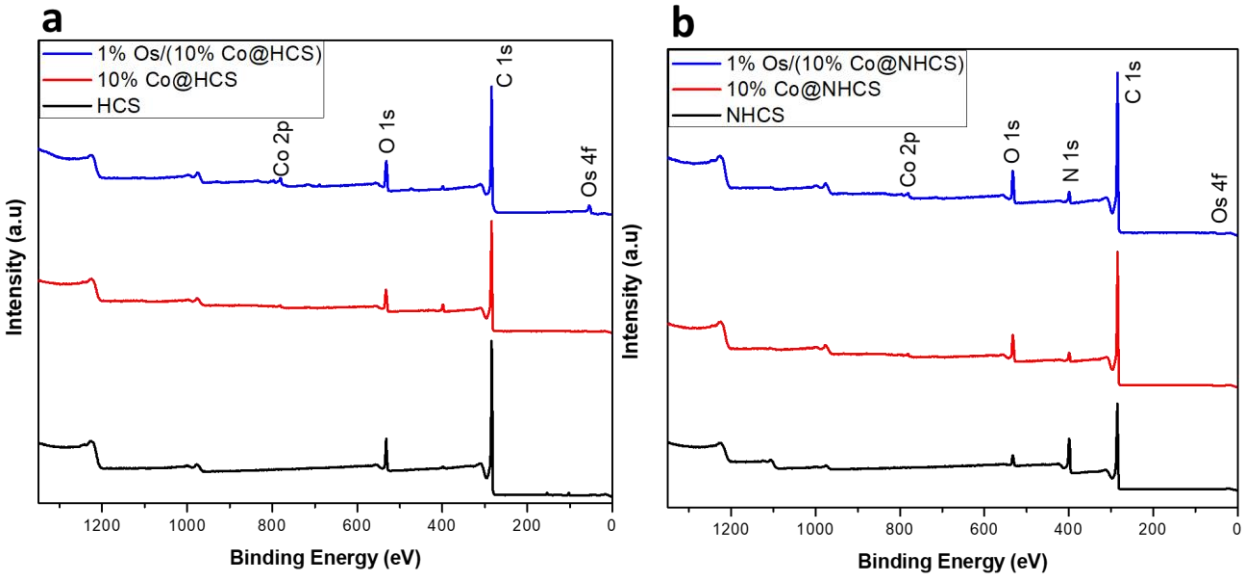

Figure 7.3: XPS survey spectra for the a) non-nitrogen doped and b) nitrogen doped samples

The N1s spectra of the 10%Co@NHCS and 1%Os/(10%Co@NHCS) catalysts were deconvoluted. Fig 7.4 shows the N1s spectra of the nitrogen doped catalysts and the schematic illustration of the nitrogen dopants and where they are located in the carbon framework structure. The deconvoluted N1s spectra showed three different peak types of N-configurations for the two catalysts which were attributed to pyridinic-N (397.6 – 398.1 Ev), pyrrolic-N (399.0 – 399.7 Ev) and substitutional/graphitic-N (400.6 – 401.7 Ev) [48–52] (Fig 7.4 (a) and (b)). While the pyrrolic-N atom is substituted into five-membered carbon rings, the pyridinic-N

atom has sp^2 hybridization with two nearby C atoms. The graphitic-N atom is a quaternary nitrogen and has sp^3 hybridization with three C atoms attached to the N and it is incorporated into the graphene layer with a high binding energy [53, 54] (Fig 7.4 (c)). From the peak deconvolution results, the relative percentage area of the nitrogen content could be determined, Table 7.1. The 10%Co@NHCS catalyst had nitrogen content of 4.4% (Table S 7.1) containing 29% pyridinic-N, 36% pyrrolic-N and 35% graphitic-N; and the 1%Os/(10%Co@NHCS) catalyst had a nitrogen content of 4.3% (Table S 7.1) containing 30% pyridinic-N, 36% pyrrolic-N and 34% graphitic-N. The relative percentage area of the three nitrogen peaks among the two catalysts was not significantly different. This confirms that the presence of Os on the outer carbon structure did not affect the relative percentage areas of the pyridinic-N, pyrrolic-N, and graphitic-N peaks. The two catalysts (10%Co@NHCS and 1%Os/(10%Co@NHCS)), when compared to the NHCS support (17.2% N content), had a significantly reduced nitrogen content. The fact that the surface N concentration in the 10%Co@NHCS catalyst significantly decreased suggests that the Os nanoparticles were specifically anchored on the N atoms [55].

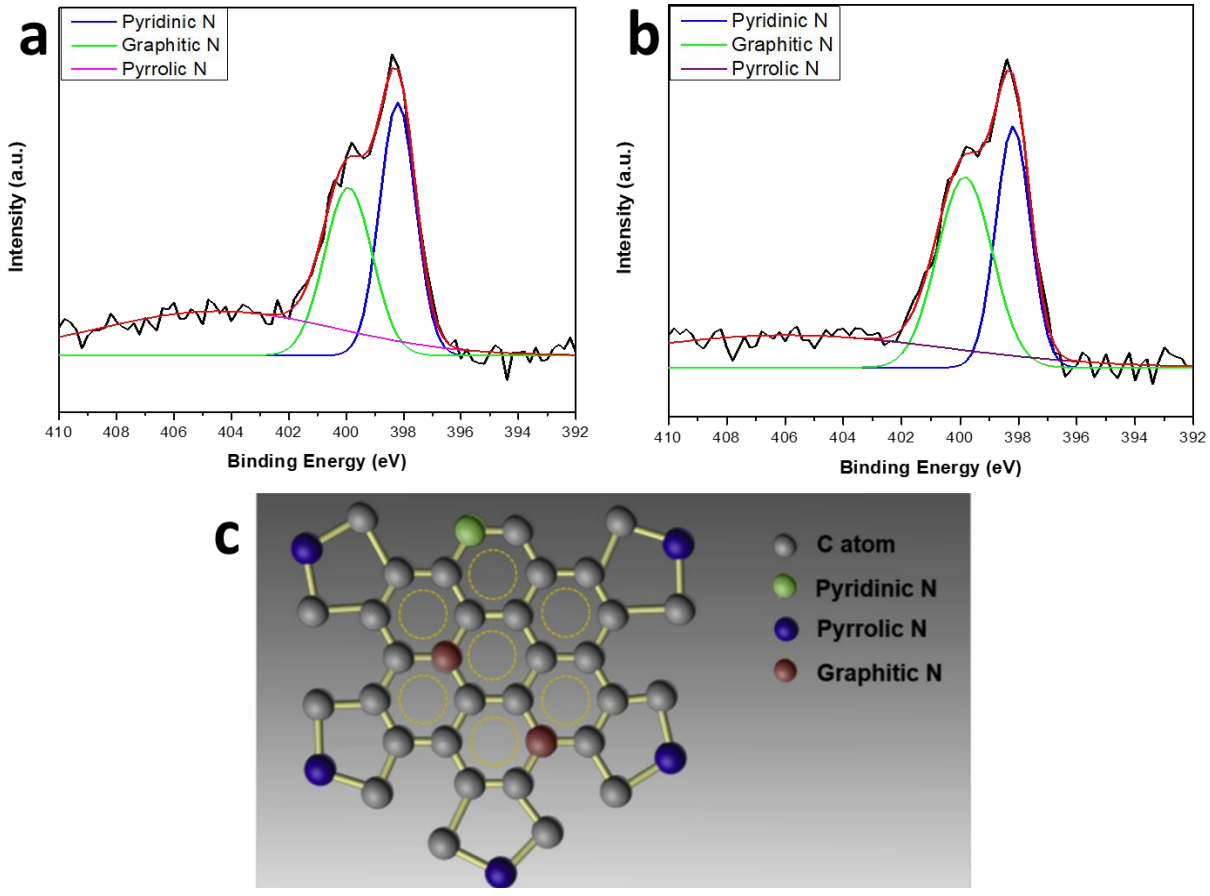

Figure 7.4: Deconvuluted XPS N1s spectra for 10%Co@NHCS (b) 1%Os/(10Co@NHCS), and c) schematic illustration of the nitrogen dopants [55].

Studies into how nitrogen doping affects the bonding arrangements of the surface carbon in HCS and NHCS supported catalysts were also conducted by performing the deconvolution of the C 1s spectra. Fig 7.5 (a-d) shows the deconvoluted C1s XPS spectra for a) 10%Co@HCS, b) 1%Os/(10%Co@HCS), c) 10%Co@NHCS, and d) 1%Os/(10%Co@HCS), respectively. The deconvoluted C1s spectra showed three different peak types with C-configurations which were due to graphitic carbon like C=C/C-H/C-H with sp^2 hybridization at ~283.6 – 283.8 eV, C-N/C-O with sp^2 hybridization at ~284.3 – 286.8 eV, and O=C-O/O=C-N with sp^3 hybridization ~287.9 – 288.8 eV surface functional groups [56, 57]. The nitrogen containing catalysts showed a decrease in the relative area percentage of graphitic carbon sp^2 hybridization and an increase in the amount of C-N sp^2 hybridization (Table 7.1). This observation was due to sp^2 sites being incorporated with nitrogen groups into the carbon network. The catalysts that were not nitrogen doped showed the opposite effect in that the graphitic carbon had a higher relative area percentage. This observation suggests successful nitrogen doping of the 10%Co@NHCS and 1%Os/(10Co@NHCS) catalysts.

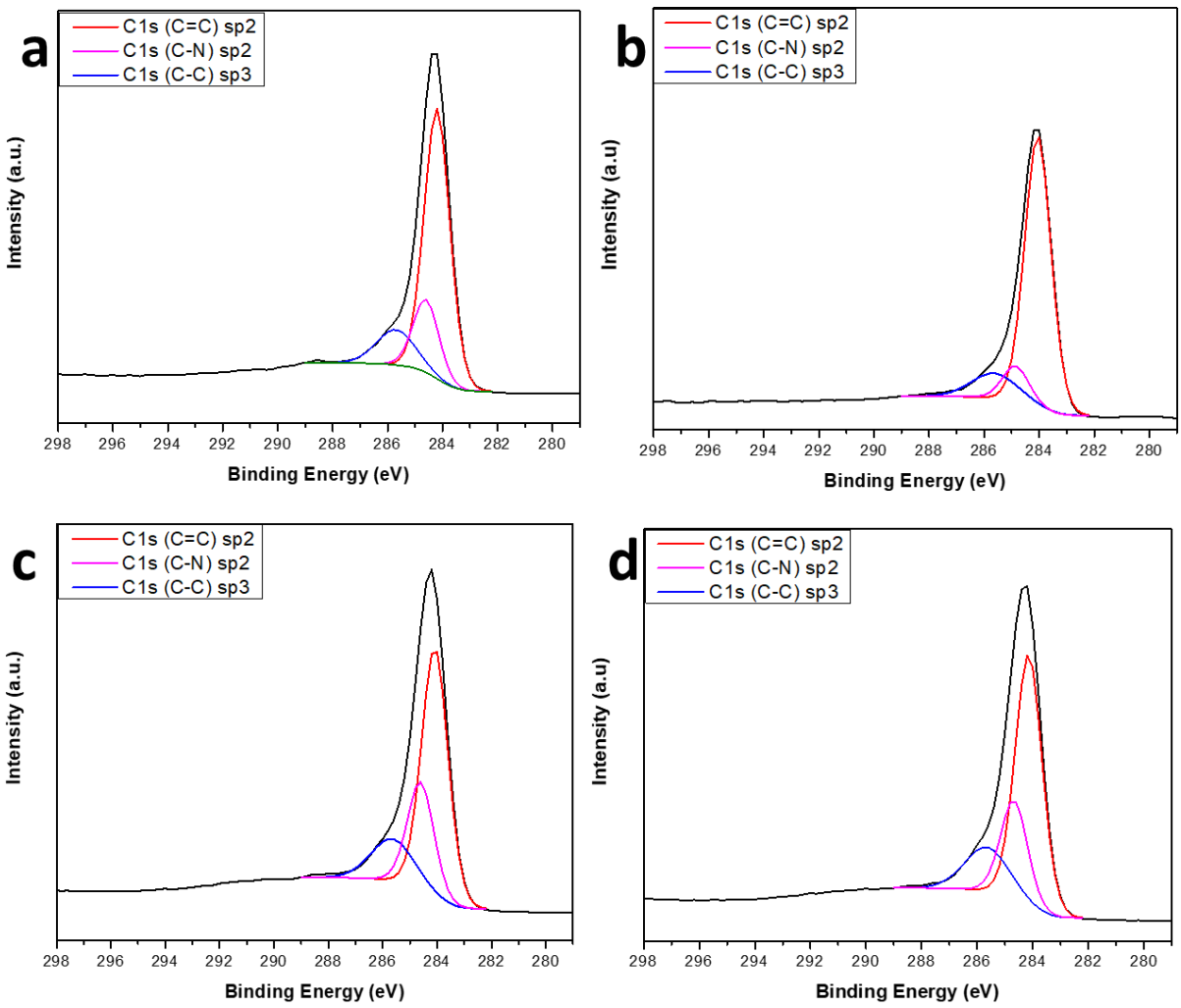

Figure 7.5: Deconvoluted C1s XPS spectra for a) 10%Co@HCS, b) 1%Os/(10%Co@HCS), c) 10%Co@NHCS, and d) 1%Os/(10%Co@NHCS)

In Fig 7.6, O 1s spectra was deconvoluted in a similar manner as done for the N1s and C1s peaks to study the effect of N dopants on the Co and Os metal dispersion. The O 1s spectra were deconvoluted into three peaks that represented the O containing the following functional groups: -C=O/O-N (~528.9 – 529.9 eV), O-C (~530.1 – 531.6 eV), and the N-C=O/O-C=O (~532.9 – 322.5 eV) [57, 58]. The overall contribution of the functional groups to the total O content are listed in Table S 7.1. The O content on the catalysts that were not nitrogen doped were higher than those of the nitrogen doped catalysts.

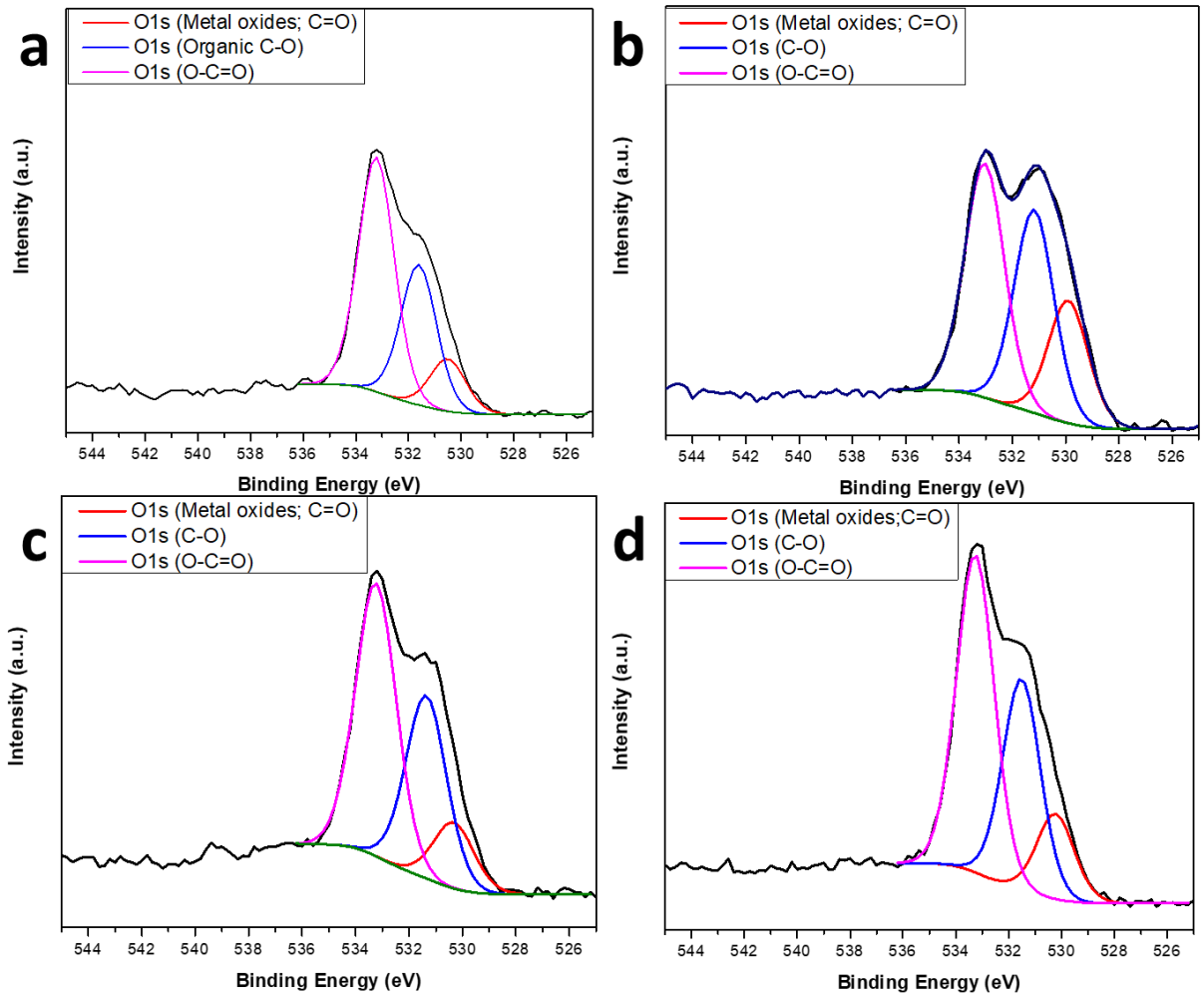

Figure 7.6: Deconvoluted O1s XPS spectra for a) 10%Co@HCS, b) 1%Os/(10%Co@HCS), c) 10%Co@NHCS, and d) 1%Os/(10%Co@NHCS)

In summary, the data suggests that the anchoring of Co and Os nanoparticles on the N atoms decreases in the following order of priority pyrrolic-N > graphitic-N > pyridinic-N. Further, the metal on the NHCS support reduces the nitrogen content measured by XPS, suggesting that the Os is bound to the N on the surface. The nitrogen doping on the HCS support showed a decrease in graphitic carbon and an increase in the amount of C-N functional groups in the carbon framework.

Table 7.1: N1s, C1s and O1s components of the samples collected from the XPS results

Sample Name	Relative area percentage (%)								
	Pyridinic N ~398 eV	Pyrrolic N ~399 eV	Graphitic N ~400 eV	C=C sp2 ~283 eV	C-N sp2 ~284 eV	C-C sp3 ~285 eV	C=O ~529 eV	C-O ~530 eV	O-C=O ~533 eV
10%Co@HCS	-	-	-	68	18	14	12	33	55
1%Os/(10%Co @HCS)	-	-	-	78	10	12	22	36	42
10%Co@NHCS	29	36	35	59	25	16	13	35	52
1%Os/(10%Co @NHCS)	30	36	34	60	23	17	14	35	51

7.3.3 Powder X-ray diffraction

Ex-situ powder X-ray diffraction (PXRD) data for the prepared catalysts are shown in Fig. 7.7. All the catalysts had a peak at 2θ values of ~ 25^o corresponding to the graphene like carbon and confirms the existence of a highly defective carbon structure as seen by the broad peak obtained [59]. The presence of Os was not observed in both osmium promoted catalysts and this was attributed to the small amounts of the promoter metal being loaded, and to the small Os particle sizes [28].

The 10%Co@HCS and 1%Co@HCS catalysts displayed peaks at 2θ values of 36.8^o, 42.3^o, 59.4^o, and 65.3^o that correspond to the crystal planes of Co_3O_4, as determined from the COD: 1526734 collection files. Peaks corresponding to CoO were also seen at 2θ values of 44^o and 52^o, this observation was due to the partial auto-reduction of the Co_3O_4 phase when it is in contact with the HCSs [60]. The broad peaks for the Co_3O_4 phase supported a narrow size distribution with an almost symmetric Co oxide peak shape, as well as the fact that the Co particles were in the nanoscale range. [61]. The PXRD data suggests that the presence of the Os promoted the reduction of the Co_3O_4, as well as caused particle growth.

The 10%Co@NHCS and 1%Os/(10%Co@NHCS) catalysts displayed peaks belonging to the CoO and Co (fcc) phase. This observation signifies the reduction of the Co oxides to Co metal. This suggests that surface nitrogen functionalization affected the reduction of CoO phase to the Co (fcc) phase. The peaks for the nitrogen doped catalysts were not apparent and this observation could be due to more surface-active sites being created or because active metals were distributed uniformly across the support material [62]. A decrease in Co crystallite sizes was observed with nitrogen-doping as seen from TEM particle size distribution. The decrease in Co particle size with the introduction of nitrogen doping is consistent with surface nitrogen atoms influencing catalyst nucleation sites on the HCS support material. Nitrogen-rich carbons

are known to provide a range of chemical binding site for a direct support interaction with nanoparticles thus resulting in improved dispersion and smaller particles [63].

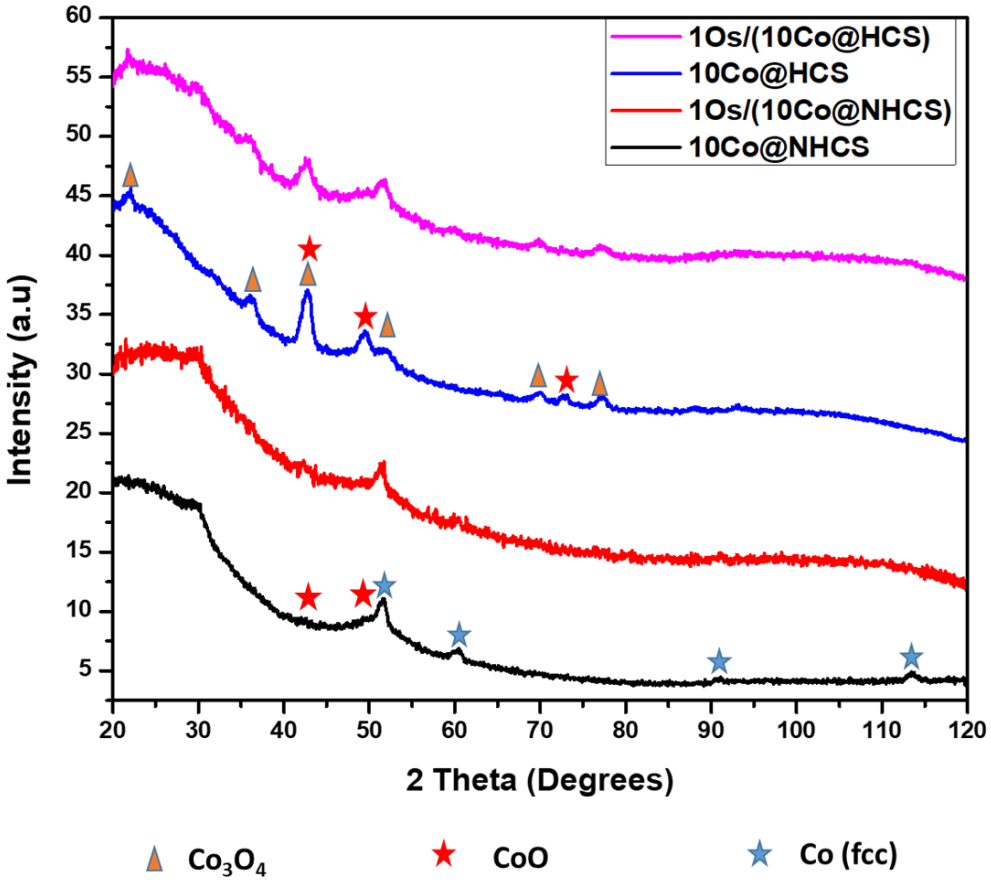

Figure 7.7: PXRD patterns for 10%Co@HCS, 1%Os/(10%Co@HCS), 10%Co@NHCS, and 1%Os/(10%Co@NHCS)

7.3.4 Nitrogen absorption-desorption analysis

The surface areas, pore volumes and pore sizes of the synthesised catalysts were determined by the BET technique and data are shown in Table 7.2. The encapsulation of Co nanoparticles inside the hollow carbon spheres led to a decrease in the surface area of the carbons. A further decrease in surface areas upon loading the catalyst with the Os promoter on the outer surface of the HCSs was observed. Another observation was that the nitrogen doped catalysts had lower surface areas compared to the non-doped catalysts. However, all the synthesised catalysts had relatively high surface areas (> 250 m^2/g).

Table 7.2. Textural properties (surface area, pore volume and average pore size) of the HCS support, nitrogen doped HCS and Os promoted inside the hollow carbon spheres.

sample	Surface area (m^2/g)	Pore volume (cm^3/g)	Pore size (nm)
HCS only	541	0,87	7,7
10%Co@ HCS	508	0.20	8.7
10%Co@ NHCS	354	0.43	4.9
1%Os/(10%Co@ HCS)	463	0.56	4.8
1%Os/(10%Co@ NHCS)	347	0.37	11.6

The microporosity of the HCSs supported catalysts were confirmed from the distribution graphs, Fig 7.8, which displayed pore sizes less than 2 nm. These findings were attributed to the decomposition of the RF and loss off polystyrene template during the carbonization procedure [64].

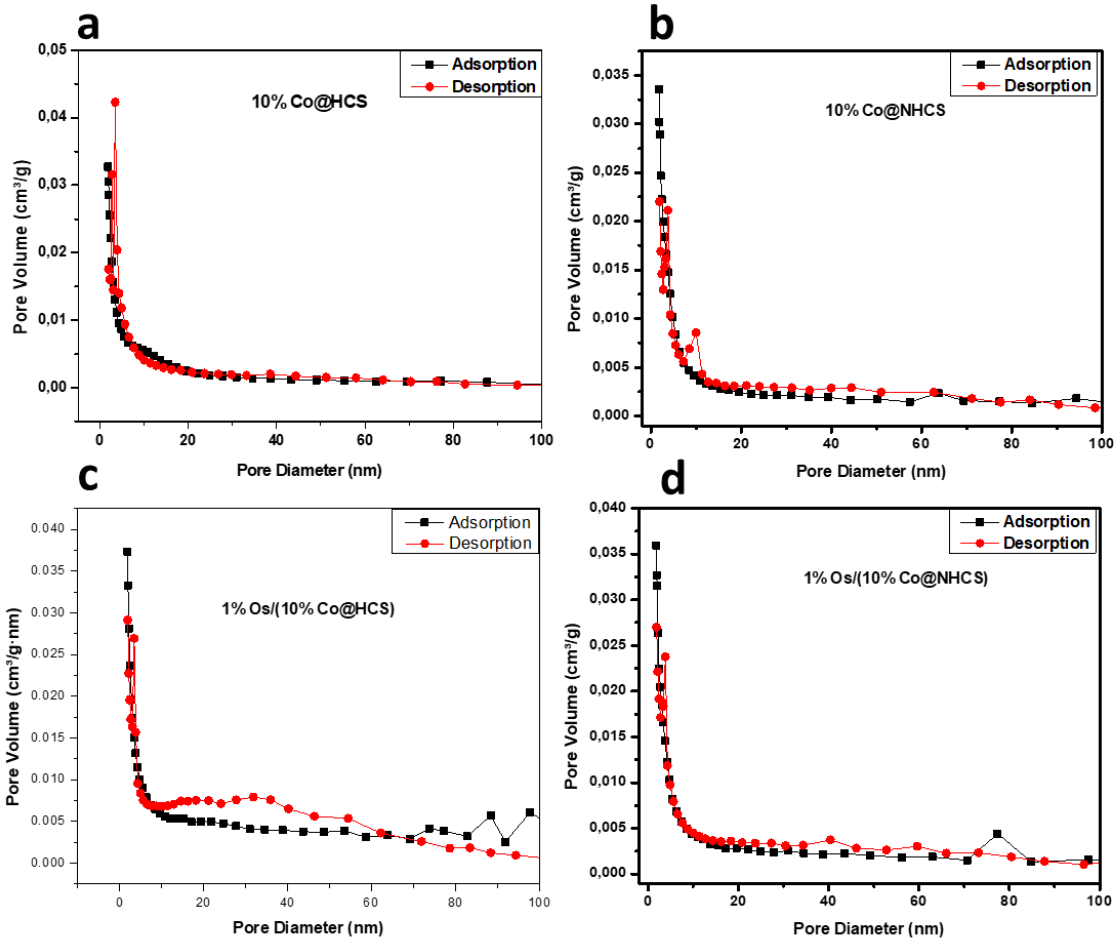

Figure 7.8: Pore size ditribution of a) 10%Co@HCS, b) 10%Co@NHCS c) 1%Os/(10%Co@HCS), and d) 1%Os/(10%Co@NHCS) catalysts.

7.3.5 Temperature programmed reduction

Temperature-programmed reduction (TPR) was used to track the impact of nitrogen doping on the stepwise reduction of Co oxide. Fig. 7.9 shows the TPR profiles for all the synthesised catalysts that revealed Co oxide reduction characteristics. Two peaks were detected for each catalyst and the first peak at lower temperature was attributed to the reduction of Co_3O_4 to CoO and the second peak at a higher temperature was attributed to CoO reduction to Co^0 species [65]. It can be seen in Fig. 7.9 that the Os promoter influenced the TPR profile of Co_3O_4 by reducing the reduction temperatures. Nitrogen-functionalization of the HCS resulted in a shift of the reduction peaks to higher temperatures and this observation was due to smaller particle sizes. The functionalization of the HCS with nitrogen combined with the promotion effects of Os showed a non-significant difference in the lowering of the reduction temperature of the Co oxide. Furthermore, the size of the cobalt oxide nanoparticles in functionalized catalysts played a role in the reduction temperature, in that smaller particles have a higher reduction temperature due to their larger surface area to volume ratio and higher surface energy. The reduction temperature from CoO to metallic Co gradually increased with the decrease in particle size, and this may explain why the second reduction peak was larger for the samples with smaller particle sizes. Smaller particles would have had a higher reduction temperature due to their increased surface energy [66].

The reduction of 10%Co@HCS occurred at 320 °C (first reduction step of Co_3O_4 to CoO species) followed by the second reduction step at a higher temperature of 430 °C for the conversion of CoO to Co^0 species. in contrast, the nitrogen functionalized 10%Co@NHCS catalyst occurred at higher temperatures of 418 °C and 550 °C for the first and second Co reduction steps, respectively. The addition of a promoter also improved the reduction of 1% Os/(10%Co@HCS) catalyst which had the reduction peaks at 202 °C and 380 °C for the first and second reduction steps, respectively. However, loading a promoter to the functionalized 1% Os/(10%Co@NHCS) catalyst did not lower the reduction temperatures significantly (425 °C and 560°C) for the first and second reduction steps, respectively.

One role of a promoter is to enhance the reducibility of a catalyst and this occurs by means of a spillover effect in which the promoter is first reduced, and then H atoms transfer from the

reduced promoter atoms to the catalyst [67]. The Os promoted catalyst enhanced the reduction and this can be attributed to a secondary spillover effect as the Os promoter is separated from the Co_3O_4 catalyst by a carbon barrier (HCS).

It is apparent that nitrogen-functionalization of the hollow carbon support is likely to have a significant impact on the reduction behavior of cobalt oxide due to the cobalt oxide nanoparticles' strong electronic interaction with the N-rich hollow carbon sphere surface. The presence of N atoms on the support led to an increase in the reduction temperature for both the $Co_3O_4 \rightarrow CoO$ and $CoO \rightarrow Co°$ transformations, due to the electron-withdrawing effect of the N atoms, which increased the energy required for the reduction reaction to occur [66]. This is supported by a study conducted on post doped nitrogen-decorated hollow carbon to serve as a support for Co Fischer-Tropsch catalysts, where it was found that the reduction temperature increased as the nitrogen content in the support increased [15]. As a result of the cobalt oxide nanoparticles' strong interfacial electronic interaction with the surface of the N-doped hollow carbon spheres, the Co oxide particles became more difficult to reduce, thus moving the reduction peaks to higher temperatures.

The methanation process was affected by both the functionalization and the promotion of the catalysts. The TPR profiles of the nitrogen doped catalysts showed a higher methanation temperature. The Os promoter, in contrast, showed a reduction in the methanation temperature compared to the non-promoted catalysts (ca. <600 °C) (Fig 7.9).

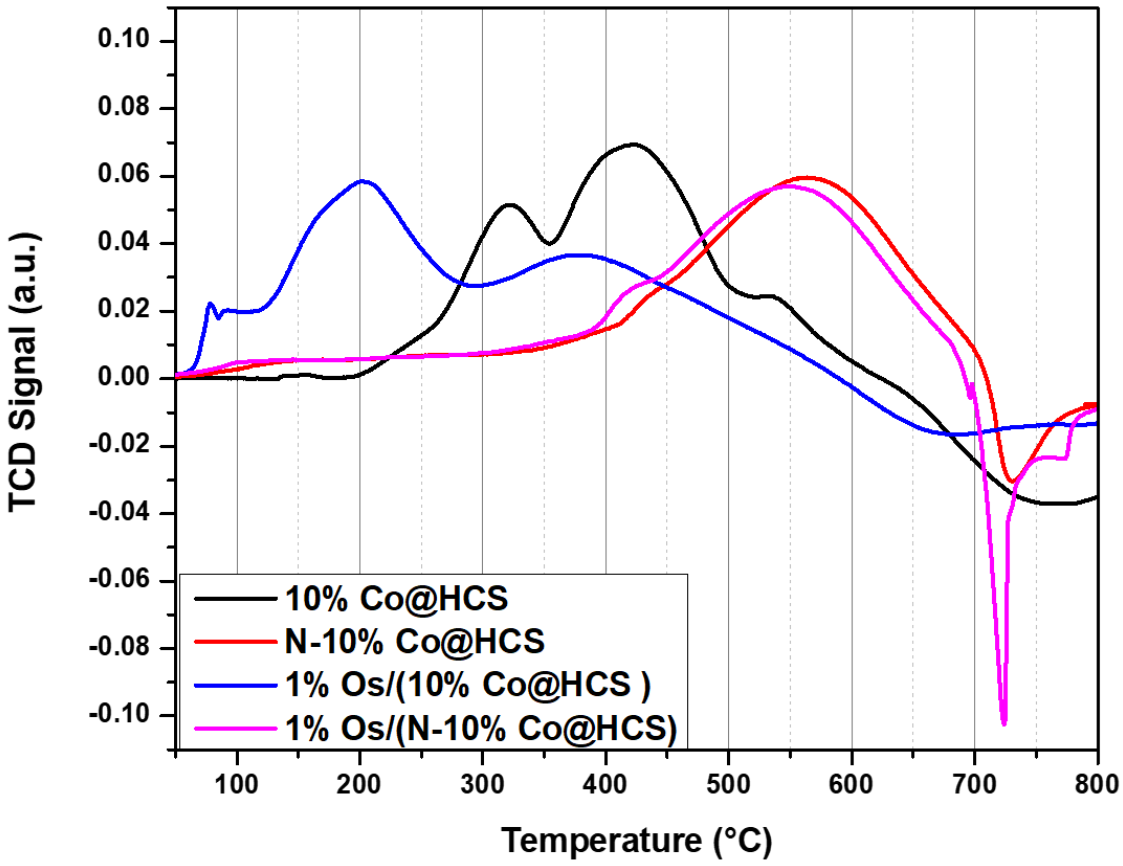

Figure 7.9: TPR profiles of 10%Co@HCS, 10%Co@NHCS, 1%Os/(10%Co@HCS), and 1%Os/(10%Co@NHCS) catalysts.

Table 7.3: The first and second reduction temperatures of the synthesised catalysts

Sample	First reduction peak (°C)	Second reduction peak (°C)
10%Co@HCS	320	430
10%Co@NHCS	418	550
1%Os/(10%Co@HCS)	206	380
1%Os/(10%Co@NHCS)	425	560

7.3.6 Fischer-Tropsch Synthesis (FTS) evaluation

FTS was performed on the synthesised catalysts at 220 ^{o}C and 250 ^{o}C (50 h, 10 bar pressure). Table 7.4 shows the %CO conversion, CH_4, C_1-C_4 and liquid C_5^+ selectivity for all the catalysts. In FTS, supports that have been doped with nitrogen typically affect catalysts performance

[68–70]. Nitrogen-doped HCSs supported catalysts (10%Co@NHCS, 1%Os/(10%Co@NHCS)) showed higher %CO conversion than the catalysts supported on undoped HCSs (10%Co@HCS, 1%Os/(10%Co@HCS)). At both reaction temperatures, this trend remained constant. The trend can be attributed to the small Co particle size, the higher metal dispersion and the increase in catalyst reducibility present in nitrogen-doped catalysts as seen from TEM, XRD, and TPR studies. All of these factors increased the number of surface Co sites, which increased the %CO conversion of the FTS reaction [71, 72]. A similar pattern was noticed in a study of post-doped nitrogen-decorated HCSs used as a support for Co FT catalysts [15]. In contrast, a study comparing 10 wt% Fe FT catalyst dispersed on nitrogen doped and undoped CNTs reported a decline in activity. The activity of the catalyst with nitrogen doping was 1.6 times greater than that of the catalyst without nitrogen-doping [28]. The behaviour of the doped and undoped Fe/CNT catalyst was attributed to substantial particle agglomeration which took place at high reaction temperatures. Whereas, in this study the catalysts were more stable with time on stream and this could be attributed to the unique nanoreactor properties of the HCSs. The HCSs possess properties such as high surface area, low density, and the ability to be used as a nanoreactor when active metal phase is placed inside the carbon shell [73]. By reducing catalyst agglomeration and enabling high dispersion of the catalyst particles on the support material, these properties lead to stable CO conversions under the FT reaction conditions.

The 1%Os/(10%Co@NHCS) had the highest %CO conversion and occurred when both nitrogen doping and Os promotion was incorporated to give a catalytic activity that was enhanced. The addition of a promoter to Co_3O_4 nanoparticles has been reported to alter the catalyst morphology [74]. The Os promoter enhanced the catalytic performance of both the 1%Os/(10%Co@HCS), and 1%Os/(10%Co@NHCS) catalysts which can be attributed to secondary spillover effect which gives rise to synergistic electronic effects [75].

The selectivity data shows that the presence of a promoter facilitated the production of long chain hydrocarbons, C_{5+} (Table 7.4). The long chain product selectivity at 220 ^{o}C increased with the presence of Os, e.g. 1%Os/(10%Co@NHCS) (75.1%) > 10%Co@NHCS (58.7%) and 1%Os/(10%Co@HCS) (83.6%) > 10%Co@HCS (70.1%). Os as a catalyst is known for its high selectivity for methane production [47], but when used as a promoter, the Co catalyst tends to produce high molecular weight hydrocarbons. The increased selectivity to C_{5+} hydrocarbons could also be due to Os enrichment on the cobalt crystallite surface, similar to what has been reported for a Ru promoted Co catalyst [48, 49]. Another explanation could be

as the Co particle size increases (e.g. 1% Os/(10%Co@HCS) and 1% Os/(10%Co@NHCS) catalysts) there tends to be an increase in the selectivity of liquid C_5^+ and a study by Borg et al. showed similar findings on the Co/γ–Al_2O_3 catalysts [76]. A study on particle size effect of Co catalyst using Co/δ-Al_2O_3 and Co/θ-Al_2O_3 catalysts showed similar findings as in this study in that unpromoted catalysts liquid C_5^+ content was generally low, due to the pore structure of the HCS support compared to the promoted catalyst [77]. A comparison of the Co catalysts supported on γ–Al_2O_3, with narrow pore size (7 nm) vs a wide pore size (13 nm), was investigated by Rytter et al. and demonstrated that wide pore sizes favoured the selectivity towards higher liquid C_5^+, which correlates with observations made in this study.

On the other hand, the selectivity data based on the incorporation of Co and Os on N-HCSs vs the undoped HCSs showed that the HCS catalysts had the highest C_{5+} selectivity and a low C_1 selectivity. This observation was anticipated since nitrogen doped catalyst supports provided chemically anchoring sites to increase metal dispersion thus resulting in small size Co particles [9, 49 tuning]. Therefore, methane production was more favoured by smaller particles, while higher molecular weight hydrocarbons were more favoured by larger particles. [45, 59, 76–79].

Overall, the catalysts evaluated at 220 ºC and 250 ºC showed an increase in CO% conversion with increase in temperature as well as with Os promotion via secondary spillover effect. The selectivity towards higher molecular weights decreased with an increase in temperature as well as with HCS nitrogen doping.

Table 7.4. Fischer-Tropsch Activity and Product selectivity of catalysts (T = 220, H_2/CO ratio = 2, P = 10 bar).

Sample	CO Conversion (%)	TOF (x10^{-3} s)^a	Activity (x10^{-6}) ($mol_{CO}/g_{Co}.s$)	Selectivity (C mol) %		
				C_1	C_2-C_4	C_{5+}
10%Co@HCS	4.2	6	27.8	18.8	11.1	70.1
10%Co@NHCS	5.3	10.7	39.9	13.2	4.9	81.9
1%Os/(10%Co@HCS)	6	23.4	36.4	11.4	6.9	81.7

1%Os/(10%Co@NHCS)	6.8	27.9	20.7	7.6	3.8	88.6

7.3.7 Post FTS transmission electron microscopy study

Generally, loss of catalytically activity of Co catalysts under FTS reaction conditions is due to metal sintering, poisoning, catalyst surface rearrangement, carbon effects (e.g. carbonization or coking) and the formation of metal-support compounds [72, 80]. Coalescence and Ostwald ripening are two mechanisms by which sintering takes place [81].

After the catalysts in FTS had been evaluated, the samples were examined to determine what had changed during the 100 h exposure of FTS reaction conditions. TEM images of the FTS spent catalysts are shown in Fig 7.10. The images reveal that for all the catalysts that the HCS and NHCS support materials were thermally stable at the high temperatures and pressures used during the FTS process and maintained their structural morphology. The spherical structure of the support was maintained and not broken, with Co nanoparticles remaining encapsulated inside the spheres. The maintenance of the morphology in NHCS supported catalysts suggests that nitrogen doping also retained the spherical carbon framework.

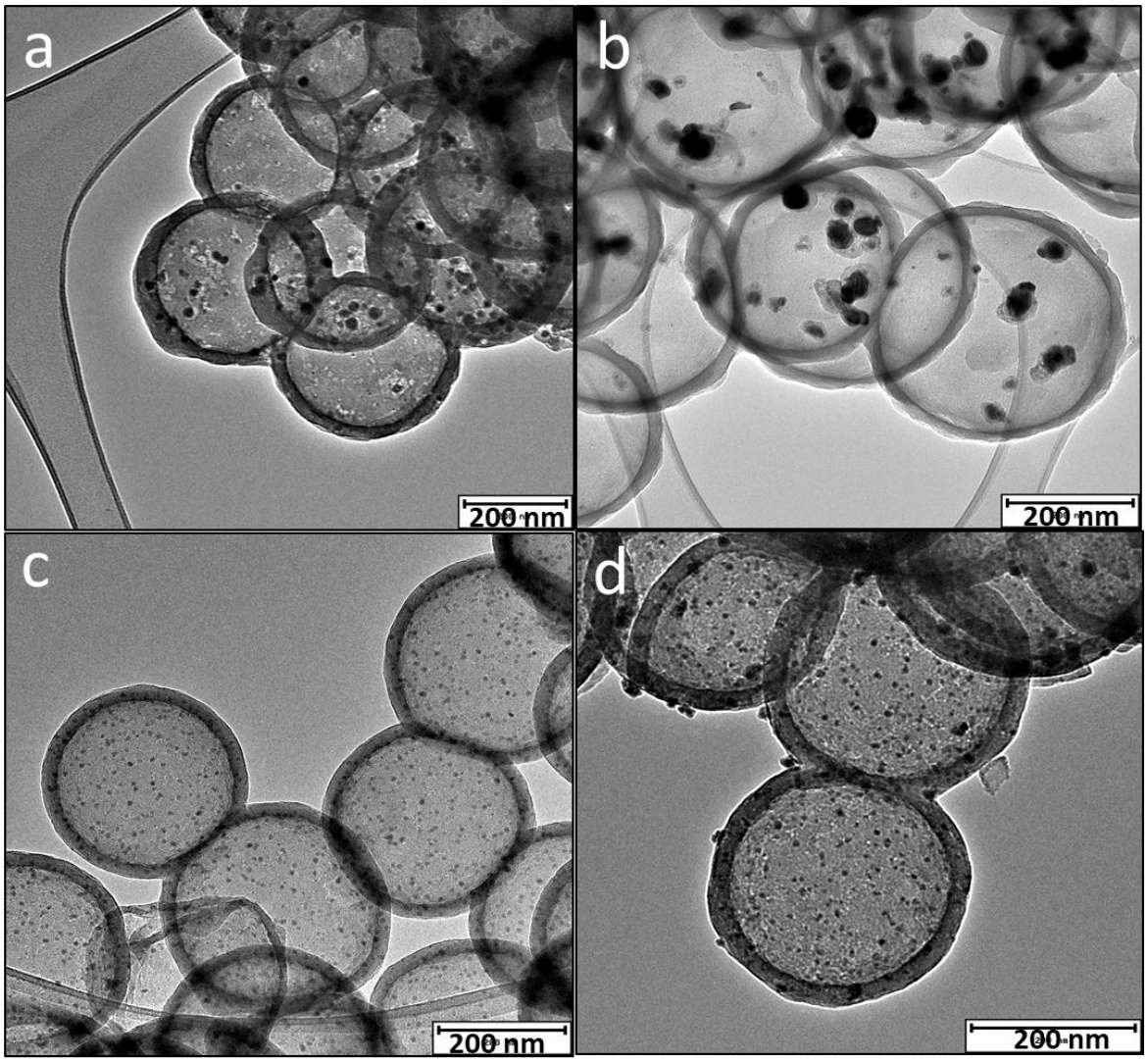

Figure 7.10: Post FTS TEM images of (a) 10%Co@HCS, (b) 1%Os/(10%Co@HCS), (c) 10%Co@NHCS, and (d) 0.1%Os/(10%Co@NHCS)

Particle size distributions of the spent FT catalysts were measured from the TEM images of the Co and the average particle size of the Co nanoparticles was determined, Fig 7.11. The average particle size of Co in the spent 10%Co@HCS, 10%Co@NHCS, 1%Os/(10%Co@HCS) and 1%Os/(10%Co@NHCS) catalyst was 12.1 ± 5 nm, 6.4 ± 3 nm, 26 ± 8 nm, and 11.8 ± 5 nm, respectively (Shown in Table 7.6).

From the data analysed on the spent catalysts it can be observed that nitrogen doping reduced the particle size growth during FTS as compared to the undoped catalysts. For instance, the average Co particle size increase change was 3 nm for 10%Co@NHCS catalyst and 4.6 nm for 1%Os/(10%Co@NHCS) catalyst. This was far less when compared to the particle size increase change of 8.2 nm for the 10%Co@HCS and 16.2 nm for the 1%Os/(10%Co@HCS) catalysts.

The large-scale sintering on undoped catalysts was expected to be due to Ostwald ripening effects in the presence of syngas.

The smaller particle size growth due to FTS for nitrogen doped catalysts is consistent with studies done in the past comparing the FT activities of the catalysts dispersed on N-doped and undoped carbons [28]. A study by Lu et al. on supported iron Fischer-Tropsch catalysts for lower olefins and the promotion effects of nitrogen doping into carbon nanotubes, reported that for the samples supported on the pristine carbon support, there was a steady decline in activity with time on stream. This behaviour was attributed to significant catalyst sintering on pristine carbon materials at high reaction temperatures vs reduced to low catalyst sintering occurrence on nitrogen doped carbon support [28]. A similar trend was observed in the study in that the activity of the undoped catalysts was lower than those of the N-doped catalysts. In a different study, the Fe-supported solid carbon spheres (SCSs) were contrasted which showed greater particle growth on the spent catalysts which ranged between 20-40 nm regardless of only having a 5 wt% metal loading [82]. Lastly, a study by Dlamini et al. showed similar findings on a 10Co/HCS spent catalyst compared to a 10Co/N−HCSs$_{900}$ spent catalyst, where the average particle sizes of the 10/Co@HCS sample increased from 7.7 to 10.2 nm, while that of 10Co/N−HCSs$_{900}$ increased from 6.4 to 8.9 nm.

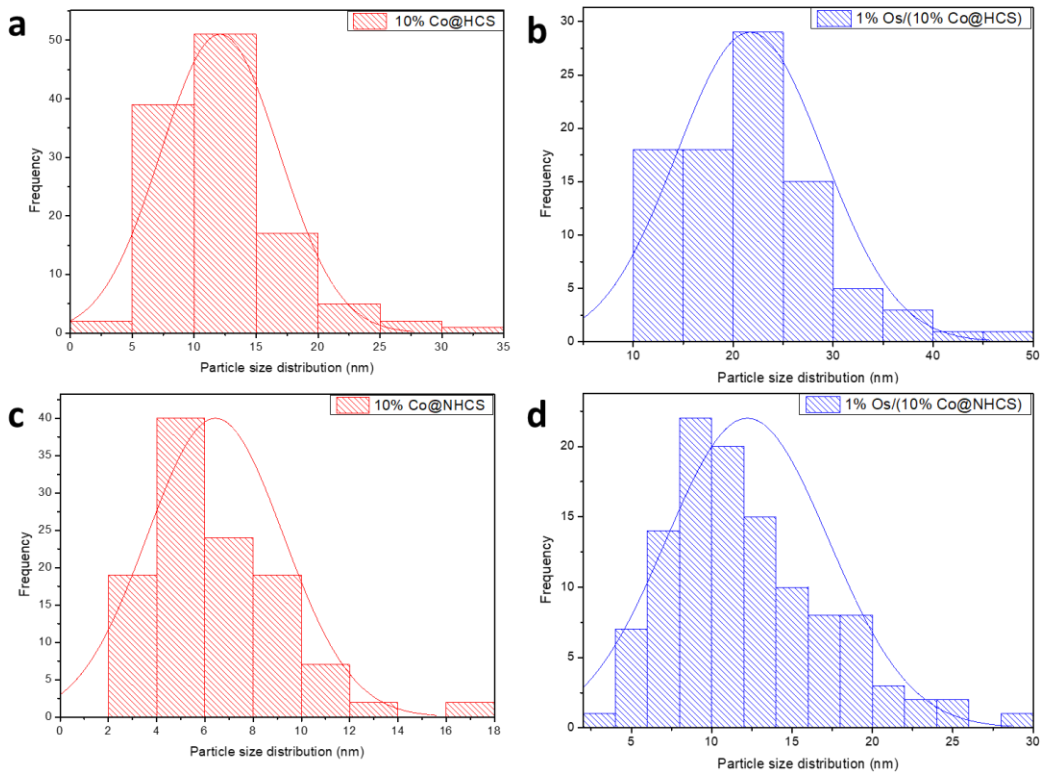

Figure 7.11: The FTS spent catalysts particle size distribution of a) 10%Co@HCS, b) 1%Os/(10%Co@HCS), c) 10%Co@NHCS, and d) 1%Os/(10%Co@NHCS)

Table 7.6: Pre and post reaction catalyst particle sizes

Sample Name	Pre-reaction particle size (nm)	Post-reaction particle size (nm)
10%Co@ HCS	3.9	12.1
10%Co@ NHCS	3.4	6.4
1%Os/(10%Co@ HCS)	9.8	26
1%Os/(10%Co@ NHCS)	7.2	11.8

7.4 Conclusion

Co Fischer-Tropsch catalysts, promoted with Os and functionalized with nitrogen were prepared using hollow carbon spheres (HCS) as a nanoreactor support material. Co nanoparticles were encapsulated inside the HCSs and the promoter was loaded on the outside of the HCSs. The mesoporous and defective nature of HCSs was exploited to study the effects of secondary (Co inside and Os outside of a HCS) spillover effects. Nitrogen- functionalization of the HCSs was done to study the effects of nitrogen doping on secondary spillover effects on Co FT catalysts. The synthesis of 10%Co@HCS, 10%Co@NHCS, 1%Os/(10%Co@HCS), and 1%Os/(10%Co@NHCS) porous catalysts was successful. The particle sizes of the Co catalysts decreased with nitrogen doping of the Co catalyst and increased with the Os promoter loading in the following order: 10%Co@NHCS > 10%Co@HCS > 1%Os/(10%Co@NHCS) < 1%Os/(10%Co@HCS).

The XPS data showed that C, N, O, Co, and Os were present even though Co and Os detection was insignificant. The data showed that the order for anchoring Co and Os nanoparticles on the N atoms decreased as follows: pyrrolic-N > graphitic-N > pyridinic-N. The TPR data showed that the Os promoter produced a secondary spillover effect. However, the nitrogen functionalized catalysts showed no significant spillover effects. Nitrogen doping increased the reduction temperature, while in contrast, the Os promoter lowered the reduction temperature.

The Os promoter and nitrogen doping increased the FTS catalytic performance. Nitrogen doping improved the selectivity of the Co FTS reaction to the production of higher molecular weight hydrocarbons. In the spent catalysts, nitrogen doped catalysts revealed less particle sintering.

Overall, nitrogen doping of hydrocarbon-based carbon (HCS) can provide a unique material that is suitable for use as a support for catalysts. Nitrogen doping can increase the number of catalyst anchoring sites on the support and help to immobilize the catalyst nanoparticles during the reaction. These properties can improve the efficiency and stability of the catalyst, making nitrogen-doped HCS an attractive material for use as a support in catalytic reactions.

7.5 Reference

1. Iglesia E, Reyes SC, Madon RJ, Soled SL (1993) Selectivity control and catalyst design in the Fischer-Tropsch synthesis: sites, pellets, and reactors. Adv Catal 39:221–302
2. Khodakov AY, Chu W, Fongarland P (2007) Advances in the development of novel cobalt Fischer-Tropsch catalysts for synthesis of long-chain hydrocarbons and clean fuels. Chem Rev 107:1692–1744. https://doi.org/10.1021/cr050972v
3. Bertole CJ, Mims CA, Kiss G (2004) Support and rhenium effects on the intrinsic site activity and methane selectivity of cobalt Fischer–Tropsch catalysts. J Catal 221:191–203
4. Dalai AK, Davis BH (2008) Fischer–Tropsch synthesis: a review of water effects on the performances of unsupported and supported Co catalysts. Appl Catal A Gen 348:1–15
5. Khodakov AY, Griboval-Constant A, Bechara R, Villain F (2001) Pore-size control of cobalt dispersion and reducibility in mesoporous silicas. J Phys Chem B 105:9805–9811
6. Joo SH, Park JY, Tsung CK, et al (2009) Thermally stable Pt/mesoporous silica core-shell nanocatalysts for high-temperature reactions. Nat Mater 8:126–131. https://doi.org/10.1038/nmat2329
7. Ikeda S, Ishino S, Harada T, et al (2006) Ligand-free platinum nanoparticles encapsulated in a hollow porous carbon shell as a highly active heterogeneous hydrogenation catalyst. Angew Chemie - Int Ed 45:7063–7066. https://doi.org/10.1002/anie.200602700
8. Harada T, Ikeda S, Ng YH, et al (2008) Rhodium nanoparticle encapsulated in a porous carbon shell as an active heterogeneous catalyst for aromatic hydrogenation. Adv Funct Mater 18:2190–2196
9. Xiong H, Jewell LL, Coville NJ (2015) Shaped carbons as supports for the catalytic conversion of syngas to clean fuels. ACS Catal 5:2640–2658
10. Tavasoli A, Abbaslou RMM, Trepanier M, Dalai AK (2008) Fischer–Tropsch synthesis over cobalt catalyst supported on carbon nanotubes in a slurry reactor. Appl Catal A Gen 345:134–142
11. Tavasoli A, Sadagiani K, Khorashe F, et al (2008) Cobalt supported on carbon nanotubes - A promising novel Fischer-Tropsch synthesis catalyst. Fuel Process Technol 89:491–498. https://doi.org/10.1016/j.fuproc.2007.09.008

12. Ribeiro H, Vilela DN, Almeida AH, Pinto MR (2018) Functionalized Graphene Process in Biotechnology: A Brief Landscape. J Nanomed Res 7:171

13. Yan Y, Miao J, Yang Z, et al (2015) Carbon nanotube catalysts: recent advances in synthesis, characterization and applications. Chem Soc Rev 44:3295–3346

14. Chernyak SA, Suslova E V, Egorov A V, et al (2016) Effect of Co crystallinity on Co/CNT catalytic activity in CO/CO2 hydrogenation and CO disproportionation. Appl Surf Sci 372:100–107

15. Dlamini MW, Phaahlamohlaka TN, Kumi DO, et al (2020) Post doped nitrogen-decorated hollow carbon spheres as a support for Co Fischer-Tropsch catalysts. Catal Today 342:99–110

16. Catalysis F, Synthesis F (1990) 303 RECENT TECHNOLOGICAL DEVELOPMENTS IN FISCHER-TROPSCH CATALYSIS Calvin H. BARTHOLOMEW. Catal Letters 7:303–315. https://doi.org/10.1007/BF00764511

17. Yang Y, Jia L, Hou B, et al (2014) The correlation of interfacial interaction and catalytic performance of N-doped mesoporous carbon supported cobalt nanoparticles for Fischer-Tropsch synthesis. J Phys Chem C 118:268–277. https://doi.org/10.1021/jp408174w

18. Qiu B, Yang C, Guo W, et al (2017) Highly dispersed Co-based Fischer–Tropsch synthesis catalysts from metal–organic frameworks. J Mater Chem A 5:8081–8086

19. Oschatz M, Hofmann JP, van Deelen TW, et al (2017) Effects of the Functionalization of the Ordered Mesoporous Carbon Support Surface on Iron Catalysts for the Fischer–Tropsch Synthesis of Lower Olefins. ChemCatChem 9:620–628. https://doi.org/10.1002/cctc.201601228

20. Taghavi S, Asghari A, Tavasoli A (2017) Chemical engineering research and design enhancement of performance and stability of graphene nano sheets supported cobalt catalyst in Fischer–Tropsch synthesis using graphene functionalization. Chem Eng Res Des 119:198–208

21. Chen X, Deng D, Pan X, et al (2015) N-doped graphene as an electron donor of iron catalysts for CO hydrogenation to light olefins. Chem Commun 51:217–220

22. Xiong H, Moyo M, Rayner MK, et al (2010) Autoreduction and Catalytic Performance of a Cobalt Fischer–Tropsch Synthesis Catalyst Supported on Nitrogen-Doped Carbon Spheres. ChemCatChem 2:514–518

23. Fu T, Li Z (2015) Review of recent development in Co-based catalysts supported on carbon materials for Fischer-Tropsch synthesis. Chem Eng Sci 135:3–20. https://doi.org/10.1016/j.ces.2015.03.007

24. Li Z, Liu R, Xu Y, Ma X (2015) Enhanced Fischer–Tropsch synthesis performance of iron-based catalysts supported on nitric acid treated N-doped CNTs. Appl Surf Sci 347:643–650

25. Fu T, Liu R, Lv J, Li Z (2014) Influence of acid treatment on N-doped multi-walled carbon nanotube supports for Fischer–Tropsch performance on cobalt catalyst. Fuel Process Technol 122:49–57

26. Fu T, Li Z (2014) Highly dispersed cobalt on N-doped carbon nanotubes with

improved Fischer–Tropsch synthesis activity. Catal Commun 47:54–57

27. Davari M, Karimi S, Tavasoli A, Karimi A (2014) Enhancement of activity, selectivity and stability of CNTs-supported cobalt catalyst in Fischer–Tropsch via CNTs functionalization. Appl Catal A Gen 485:133–142

28. Lu J, Yang L, Xu B, et al (2014) Promotion effects of nitrogen doping into carbon nanotubes on supported iron Fischer–Tropsch catalysts for lower olefins. ACS Catal 4:613–621

29. Xiong H, Motchelaho MA, Moyo M, et al (2014) Fischer–Tropsch synthesis: Iron-based catalysts supported on nitrogen-doped carbon nanotubes synthesized by post-doping. Appl Catal A Gen 482:377–386

30. Yang Y, Jia L, Hou B, et al (2014) The Effect of Nitrogen on the Autoreduction of Cobalt Nanoparticles Supported on Nitrogen-Doped Ordered Mesoporous Carbon for the Fischer–Tropsch Synthesis. ChemCatChem 6:319–327

31. Jacobs G, Das TK, Zhang Y, et al (2002) Fischer-Tropsch synthesis: Support, loading, and promoter effects on the reducibility of cobalt catalysts. Appl Catal A Gen 233:263–281. https://doi.org/10.1016/S0926-860X(02)00195-3

32. Diehl F, Khodakov AY (2009) Promotion of cobalt Fischer-Tropsch catalysts with noble metals: a review. Oil Gas Sci Technol l'IFP 64:11–24

33. Beaumont SK, Alayoglu S, Specht C, et al (2014) Combining in situ NEXAFS spectroscopy and CO2methanation kinetics to study Pt and Co nanoparticle catalysts reveals key insights into the role of platinum in promoted cobalt catalysis. J Am Chem Soc 136:9898–9901. https://doi.org/10.1021/ja505286j

34. Sh Y, Noskov AS, Chem R (1990) Related content Procedures for making gaseous industrial waste safe

35. Morales F, Weckhuysen BM (2006) In Catalysis; Spivey, JJ; Dooley, KM, Eds

36. Choi M, Yook S, Kim H (2015) Hydrogen spillover in encapsulated metal catalysts: new opportunities for designing advanced hydroprocessing catalysts. ChemCatChem 7:1048–1057

37. Nabaho D, Niemantsverdriet JWH, Claeys M, van Steen E (2016) Hydrogen spillover in the Fischer–Tropsch synthesis: An analysis of platinum as a promoter for cobalt–alumina catalysts. Catal Today 261:17–27

38. Nabaho D, Niemantsverdriet JWH, Claeys M, van Steen E (2016) Hydrogen spillover in the Fischer–Tropsch synthesis: an analysis of gold as a promoter for cobalt–alumina catalysts. Catal Today 275:27–34

39. Prins R (2012) Hydrogen spillover. Facts and fiction. Chem Rev 112:2714–2738

40. Eliche-Quesada D, Mérida-Robles JM, Rodríguez-Castellón E, Jiménez-López A (2005) Ru, Os and Ru–Os supported on mesoporous silica doped with zirconium as mild thio-tolerant catalysts in the hydrogenation and hydrogenolysis/hydrocracking of tetralin. Appl Catal A Gen 279:209–221

41. Chiririwa H, Muzenda E (2015) The Preparation and Characterisation of Osmium(IV), Osmium(II) and Osmium(0) Complexes from Refinery Materials. 0–4.

https://doi.org/10.15242/iie.e1114015

42. Fu J, Xu Q, Chen J, et al (2010) Controlled fabrication of uniform hollow core porous shell carbon spheres by the pyrolysis of core/shell polystyrene/cross-linked polyphosphazene composites. Chem Commun 46:6563–6565

43. Hu FP, Wang Z, Li Y, et al (2008) Improved performance of Pd electrocatalyst supported on ultrahigh surface area hollow carbon spheres for direct alcohol fuel cells. J Power Sources 177:61–66. https://doi.org/10.1016/j.jpowsour.2007.11.024

44. Phaahlamohlaka TN, Kumi DO, Dlamini MW, et al (2017) Effects of Co and Ru Intimacy in Fischer-Tropsch Catalysts Using Hollow Carbon Sphere Supports: Assessment of the Hydrogen Spillover Processes. ACS Catal 7:1568–1578. https://doi.org/10.1021/acscatal.6b03102

45. Sun Q, Kim S (2015) Synthesis of nitrogen-doped graphene supported Pt nanoparticles catalysts and their catalytic activity for fuel cells. Electrochim Acta 153:566–573

46. Daems N, Wouters J, Van Goethem C, et al (2018) Selective reduction of nitrobenzene to aniline over electrocatalysts based on nitrogen-doped carbons containing non-noble metals. Appl Catal B Environ 226:509–522

47. Chizari K, Janowska I, Houllé M, et al (2010) Tuning of nitrogen-doped carbon nanotubes as catalyst support for liquid-phase reaction. Appl Catal A Gen 380:72–80

48. Wei D, Liu Y, Wang Y, et al (2009) Synthesis of N-doped graphene by chemical vapor deposition and its electrical properties. Nano Lett 9:1752–1758

49. Ewels CP, Glerup M (2005) Nitrogen doping in carbon nanotubes. J Nanosci Nanotechnol 5:1345–1363

50. Jansen RJJ, Van Bekkum H (1995) XPS of nitrogen-containing functional groups on activated carbon. Carbon N Y 33:1021–1027

51. Nakayama Y, Soeda F, Ishitani A (1990) XPS study of the carbon fiber matrix interface. Carbon N Y 28:21–26

52. Casanovas J, Ricart JM, Rubio J, et al (1996) Origin of the large N 1s binding energy in X-ray photoelectron spectra of calcined carbonaceous materials. J Am Chem Soc 118:8071–8076

53. Ding W, Wei Z, Chen S, et al (2013) Space-confinement-induced synthesis of pyridinic-and pyrrolic-nitrogen-doped graphene for the catalysis of oxygen reduction. Angew Chemie 125:11971–11975

54. Zhang J, Ma L, Gan M, et al (2015) Well-dispersed platinum nanoparticles supported on hierarchical nitrogen-doped porous hollow carbon spheres with enhanced activity and stability for methanol electrooxidation. J Power Sources 288:42–52

55. Cheng Q, Zhao N, Lyu S, et al (2019) Tuning interaction between cobalt catalysts and nitrogen dopants in carbon nanospheres to promote Fischer-Tropsch synthesis. Appl Catal B Environ 248:73–83

56. Hellgren N, Haasch RT, Schmidt S, et al (2016) Interpretation of X-ray photoelectron spectra of carbon-nitride thin films: New insights from in situ XPS. Carbon N Y 108:242–252

57. Chen X, Wang X, Fang D (2020) A review on C1s XPS-spectra for some kinds of carbon materials. Fullerenes, Nanotub Carbon Nanostructures 28:1048–1058

58. Seredych M, Hulicova-Jurcakova D, Lu GQ, Bandosz TJ (2008) Surface functional groups of carbons and the effects of their chemical character, density and accessibility to ions on electrochemical performance. Carbon N Y 46:1475–1488

59. Pourhosseini SEM, Norouzi O, Naderi HR (2017) Study of micro/macro ordered porous carbon with olive-shaped structure derived from Cladophora glomerata macroalgae as efficient working electrodes of supercapacitors. Biomass and Bioenergy 107:287–298

60. Taghavi S, Tavasoli A, Asghari A, Signoretto M (2019) Loading and promoter effects on the performance of nitrogen functionalized graphene nanosheets supported cobalt Fischer-Tropsch synthesis catalysts. Int J Hydrogen Energy 44:10604–10615

61. Weidenthaler C (2011) Pitfalls in the characterization of nanoporous and nanosized materials. Nanoscale 3:792–810

62. Zhang G, Sun Y, Xu Y, Zhang R (2018) Catalytic performance of N-doped activated carbon supported cobalt catalyst for carbon dioxide reforming of methane to synthesis gas. J Taiwan Inst Chem Eng 93:234–244

63. Antonietti M, Oschatz M (2018) The Concept of "Noble, Heteroatom-Doped Carbons," Their Directed Synthesis by Electronic Band Control of Carbonization, and Applications in Catalysis and Energy Materials. Adv Mater 30:1706836

64. Ma X, Gan L, Liu M, et al (2014) Mesoporous size controllable carbon microspheres and their electrochemical performances for supercapacitor electrodes. J Mater Chem A 2:8407–8415

65. Hong J, Marceau E, Khodakov AY, et al (2015) Speciation of ruthenium as a reduction promoter of silica-supported Co catalysts: a time-resolved in situ XAS investigation. ACS Catal 5:1273–1282

66. Yang Y, Jia L, Hou B, et al (2014) The correlation of interfacial interaction and catalytic performance of N-doped mesoporous carbon supported cobalt nanoparticles for Fischer–Tropsch synthesis. J Phys Chem C 118:268–277

67. Everett DH (1972) Manual of symbols and terminology for physicochemical quantities and units, appendix II: Definitions, terminology and symbols in colloid and surface chemistry. Pure Appl Chem 31:577–638

68. Zhuang Z, Li Y, Li Z, et al (2018) MoB/g-C3N4 interface materials as a Schottky catalyst to boost hydrogen evolution. Angew Chemie 130:505–509

69. Borg Ø, Dietzel PDC, Spjelkavik AI, et al (2008) Fischer–Tropsch synthesis: Cobalt particle size and support effects on intrinsic activity and product distribution. J Catal 259:161–164

70. Rane S, Borg Ø, Rytter E, Holmen A (2012) Relation between hydrocarbon selectivity and cobalt particle size for alumina supported cobalt Fischer–Tropsch catalysts. Appl Catal A Gen 437:10–17

71. Rytter E, Eri S, Skagseth TH, et al (2007) Catalyst particle size of cobalt/rhenium on porous alumina and the effect on Fischer− Tropsch catalytic performance. Ind Eng

Chem Res 46:9032–9036

72. Karaca H, Safonova O V, Chambrey S, et al (2011) Structure and catalytic performance of Pt-promoted alumina-supported cobalt catalysts under realistic conditions of Fischer–Tropsch synthesis. J Catal 277:14–26

73. Phaahlamohlaka TN, Kumi DO, Dlamini MW, et al (2016) Ruthenium nanoparticles encapsulated inside porous hollow carbon spheres: A novel catalyst for Fischer–Tropsch synthesis. Catal Today 275:76–83. https://doi.org/10.1016/j.cattod.2015.11.034

74. Romar H, Rivoire E, Tynjälä P, Lassi U (2017) Effect of Calcination Conditions on the Dispersion of Cobalt Over Re, Ru and Rh Promoted Co/γ-Al 2 O 3 Catalysts. Top Catal 60:1408–1414

75. Nabaho D, Niemantsverdriet JWH, Claeys M, Steen E Van (2016) Hydrogen spillover in the Fischer – Tropsch synthesis : An analysis of platinum as a promoter for cobalt – alumina catalysts. Catal Today 261:17–27. https://doi.org/10.1016/j.cattod.2015.08.050

76. Tavasoli A, Taghavi S (2013) Performance enhancement of bimetallic Co-Ru/CNTs nano catalysts using microemulsion technique. J energy Chem 22:747–754

77. Olivo A, Trevisan V, Ghedini E, et al (2015) CO2 photoreduction with water: Catalyst and process investigation. J CO2 Util 12:86–94

78. Eluyemi MS, Eleruja MA, Adedeji A V, et al (2016) Synthesis and characterization of graphene oxide and reduced graphene oxide thin films deposited by spray pyrolysis method. Graphene 5:143–154

79. Tung NT, Van Khai T, Jeon M, et al (2011) Preparation and characterization of nanocomposite based on polyaniline and graphene nanosheets. Macromol Res 19:203–208

80. Karaca H, Hong J, Fongarland P, et al (2010) In situ XRD investigation of the evolution of alumina-supported cobalt catalysts under realistic conditions of Fischer-Tropsch synthesis. Chem Commun 46:788–790

81. Wan G, Sahm PR (1990) Particle growth by coalescence and ostwald ripening in rheocasting of Pbsn. Acta Metall Mater 38:2367–2372

82. Xiong H, Moyo M, Motchelaho MA, et al (2014) Fischer–Tropsch synthesis: Iron catalysts supported on N-doped carbon spheres prepared by chemical vapor deposition and hydrothermal approaches. J Catal 311:80–87

Chapter 8

Conclusion and recommendation

8.1. Conclusion

In this study, the synthesis and evaluation of various Co Fischer-Tropsch (FT) catalysts promoted with Os and Pt were investigated using hollow carbon spheres (HCS) as a nanoreactor support material. The study of the hydrogen spillover effect was investigated in Fischer-Tropsch synthesis (FTS).

In the first study (**Chapter 4**), Co nanoparticles were encapsulated inside the HCSs, and an Os promoter was loaded both inside and outside the HCSs. This was done to study the primary (Co and Os inside a HCS) and secondary (Co inside and Os outside a HCS) hydrogen spillover effects. The synthesis of Co@HCS, xOsCo@HCS, and xOs/(Co@HCS) porous catalysts was successful.

The TPR and PXRD data showed that the intimate contact of Co and Os enhanced the reducibility of the Co catalyst more than when the Os promoter was loaded on the outside of the HCS. The Os promoter was found to produce both primary and secondary hydrogen spillover effects, and Os was shown to promote the Co FT catalyst. The intimacy of the Os promoter with the Co catalyst was found to affect the crystalline phase of Co, with the Co fcc metallic phase being dominant when the promoter was in close proximity to Co. The Os promoter also increased the FTS catalytic performance and enhanced the selectivity of the Co FTS reaction towards higher molecular weight hydrocarbons. The particle sizes of the Co catalysts increased with the intimacy of the Co catalyst and the Os promoter in the following order: Co@HCS < xOs/(Co@HCS) < xOsCo@HCS.

In addition, post-FTS studies showed that the HCS support material was stable and able to withstand high pressures and FTS conditions. The HCSs maintained their morphology and the Co nanoparticles remained encapsulated during the reaction. The Co hcp phase was observed in the analysis of all post-FTS catalysts due to the reducing FTS conditions. The sintering of encapsulated Co nanoparticles showed higher Co reduction in xOsCo@HCS catalysts compared to xOs/(Co@HCS) type catalysts during the FTS reaction. Subsurface carbon formation was also found in the xOs/(Co@HCS) catalyst compared to xOsCo@HCS.

In the second study **(Chapter 5)**, the synthesis and evaluation of several Co-based catalysts was carried out, including ones with bimetallic CoPt@HCS and ones with Co and Pt separated by a carbon shell Pt/(Co@HCS). These catalysts were supported on hollow carbon spheres (HCS) and were used to investigate the effect of Pt as a promoter on Co oxide catalysts and the primary and secondary hydrogen spillover effect. Techniques such as TEM, TGA, EDX, XRD and TPR and FT performance were used to evaluate the catalysts.

The results showed that Pt has a positive effect on Co oxide catalysts, enhancing their reducibility and improving their performance in CO conversion and hydrocarbon selectivity. The CoPt@HCS catalysts were used to study the primary hydrogen spillover effect and it was found to have a significant contribution in reducing Co_3O_4 to its metallic active phase (Co^0). The Pt/(Co@HCS) catalysts were used to study the secondary hydrogen spillover effect and it had a lesser effect, possibly due to the distance between Pt and Co and the limitations of hydrogen atom surface diffusion. A high Co (hcp) to Co (fcc) ratio from the reduction of Co_3O_4, when Pt and Co were in intimate contact, was achieved, and this led to the highest degree of CO conversion being observed for the CoPt@HCS catalyst in the FTS. This catalyst also showed a decrease in C_{5+} hydrocarbon production due to the contribution of the primary hydrogen spillover effect compared to the secondary spillover effect.

In addition to these findings (**chapter 6**), the synthesis of Co nanoparticles encapsulated inside HCS of varying carbon shell thicknesses (16, 28 and 51 nm) was undertaken with catalysts promoted with Os on the outside of the carbon shell to investigate the secondary hydrogen spillover effect. The TPR studies showed that a decrease in the carbon shell thickness, resulted in low temperature reducibility of Co_3O_4 to metallic Co being achieved in the following order Co@HCS16 < Co@HCS28 < Co@HCS51. The reducibility of Co_3O_4 was found to be enhanced by the Os promoter and a significant downward shift in reduction temperature was observed. The Os promoter was found to induce a secondary spillover effect and to enhance the Co FT catalyst. The PXRD studies showed that the intimacy of the Os promoter with the Co catalyst affected the crystalline phase of Co, with the Co hcp phase being dominant when the promoter was in close proximity to the Co (Os/Co@HCS16). The Os promoter also increased the FTS catalytic performance. However, a non-significant difference in selectivity was obtained with the introduction of the Os promoter.

In the last study (**chapter 7**), the surface chemistry of the hollow carbon spheres (HCSs) was improved by nitrogen doping. The use of nitrogen-doped HCSs as a support material for Co

FT catalysts improved the efficiency and stability of the catalyst. Nitrogen doping increased the number of catalyst anchoring sites and helped to immobilize the catalyst nanoparticles during the FTS reaction.

The addition of an Os promoter to the nitrogen doped Co FT catalyst showed an improvement in catalytic performance, with increased selectivity towards higher molecular weight hydrocarbons and reduced particle sintering in the spent catalysts. Overall, the combination of nitrogen doping and Os promotion shows promise as a way to enhance the performance of Co FT catalysts.

Overall, the use of Os and Pt as promoters for Co oxide catalysts was shown to enhance their reducibility and improve their performance in CO conversion and hydrocarbon selectivity. The primary hydrogen spillover effect was found to have a significant contribution, while the secondary hydrogen spillover effect had a lesser effect, due to the distance between the promoter and Co and the limitations of hydrogen atom surface diffusion. The distance between the promoter and Co played a role in the efficiency of the hydrogen spillover effect. Nitrogen doping led to an increase in the number of anchoring sites on the support therefore improving thermal stability, improving Co dispersion, and enhancing selectivity towards the production of C_{5+} hydrocarbons and reducing metal agglomeration during FTS reaction conditions. These findings may have important implications for the development of more efficient and selective FT catalysts. The comparison of Co (hcp/fcc) ratios in promoter-Co@HCS and promoter/(10Co@HCS) catalysts showed that as the promoter loading increased, the promoter-Co@HCS catalysts had more hcp Co than the promoter/(10Co@HCS)) catalysts which had more fcc Co. The PXRD data revealed that the intimacy of the promoter to the Co catalyst (promoter-Co@HCS) promoted the reduction of CoOx to the hcp metallic Co phase. These observations were consistent with the literature in that it has been indicated that a low reduction temperature observed in primary spillover usually leads to the formation of Co (hcp) while a high reduction temperature observed in secondary spillover lead to Co (fcc) formation. The Co (hcp) phase has been reported in the literature to be the more FT catalytically active than the Co phase.

8.2. Recommendations

Based on the findings of this study, it is recommended that further research be conducted to better understand the role of osmium promoters in reducing Fischer-Tropsch catalysts. This could include encapsulating a single Co or Fe nanoparticle and a single Os promoter in hollow

carbon spheres (HCSs) to form a bimetallic catalyst, and using in situ magnetometer measurements with pure hydrogen to study the primary spillover effect. The use of HCSs as a support material in these studies is important for understanding the effects of morphology on the promoter's role in spillover effects. These additional studies could provide valuable insight into the mechanism behind the spillover effect and help to improve the performance of FT catalysts. The PDF studies, described in this thesis study, can also be conducted on Pt promoted Co catalysts to further examine the local structure of the Pt promoter to the Co catalyst. Various peaks in the PDF can also be used to identify the Co phases and how the Pt contributes to Co oxide reduction. The studies using PDFs can be compared to those of Os to further understand the Pt and Os promoter effects on Co catalyst.

Appendix 1 – List of symbols

The following is a list of abbreviations that were used in the thesis:

ASF - Anderson-Schulz-Flory

BET - Brunauer-Emmett-Teller

CNTs - Carbon nanotubes

CSs - Carbon spheres

CVD - Chemical vapour deposition

EDX - Energy dispersive X-ray spectroscopy

FID - Flame ionisation detector

FTIR - Fourier transform infrared spectroscopy

FT - Fischer-Tropsch

GC - Gas chromatography

HCSs - Hollow carbon spheres

N-HCSs - Nitrogen doped hollow carbon spheres

PDF – Pair distribution function

PSS – Polystyrene spheres

PXRD - Powder X-ray diffraction

RF - Resorcinol-formaldehyde

SEM - Scanning electron microscopy

TCD - Thermal conductivity detector

TEM - Transmission electron microscopy

TEOS - Tetraethyl orthosilicate

TGA-DTA - Thermogravimetric analysis with differential thermal gravimetry

TPR - Temperature programmed reduction

WGS - Water gas shift

wt.% - Weight percentage

XPS - X-ray photoelectron spectroscopy

Appendix 2 - Supplementary Information

Chapter 4: Fischer-Tropsch synthesis: osmium promoted Co@HCS catalysts

List of Figures

List of Tables

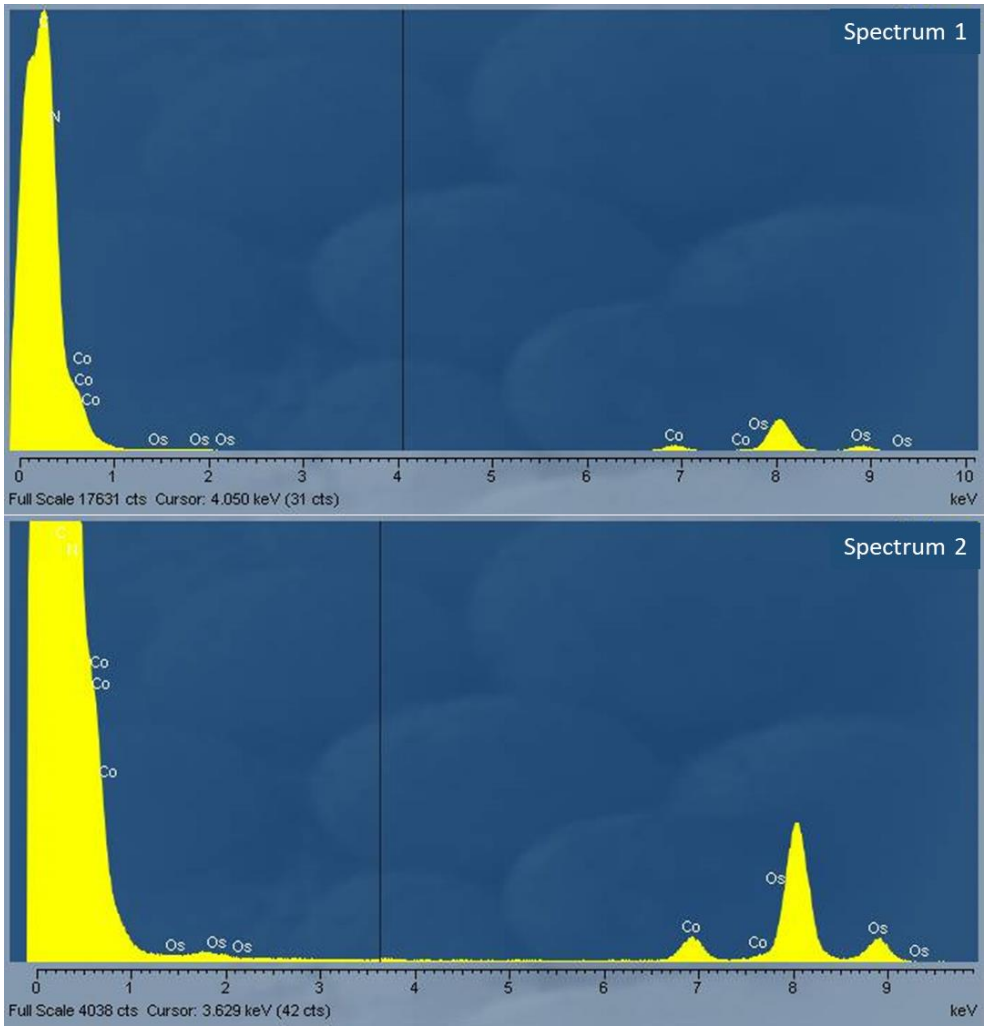

Figure S4.1. EDS spectrum of (a) Os@HCS and (b) Os/(Co@HCS) catalysts.

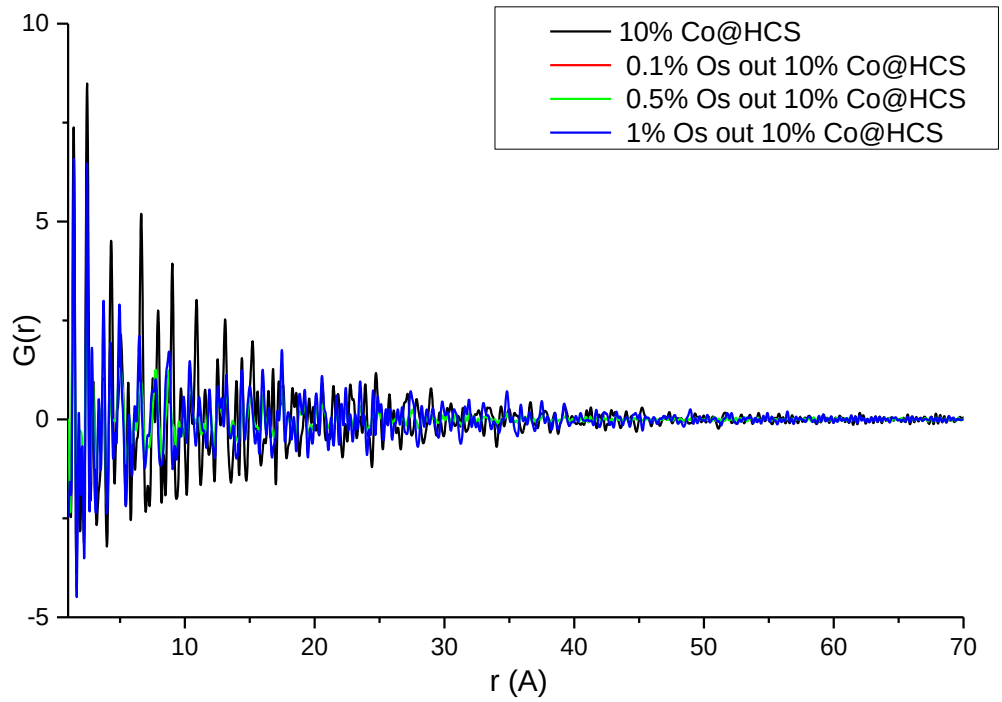

Figure S4.2. Experimental PDF of catalysts with Os supported outside the HCSs (need to have the 0.1% Os sample added).

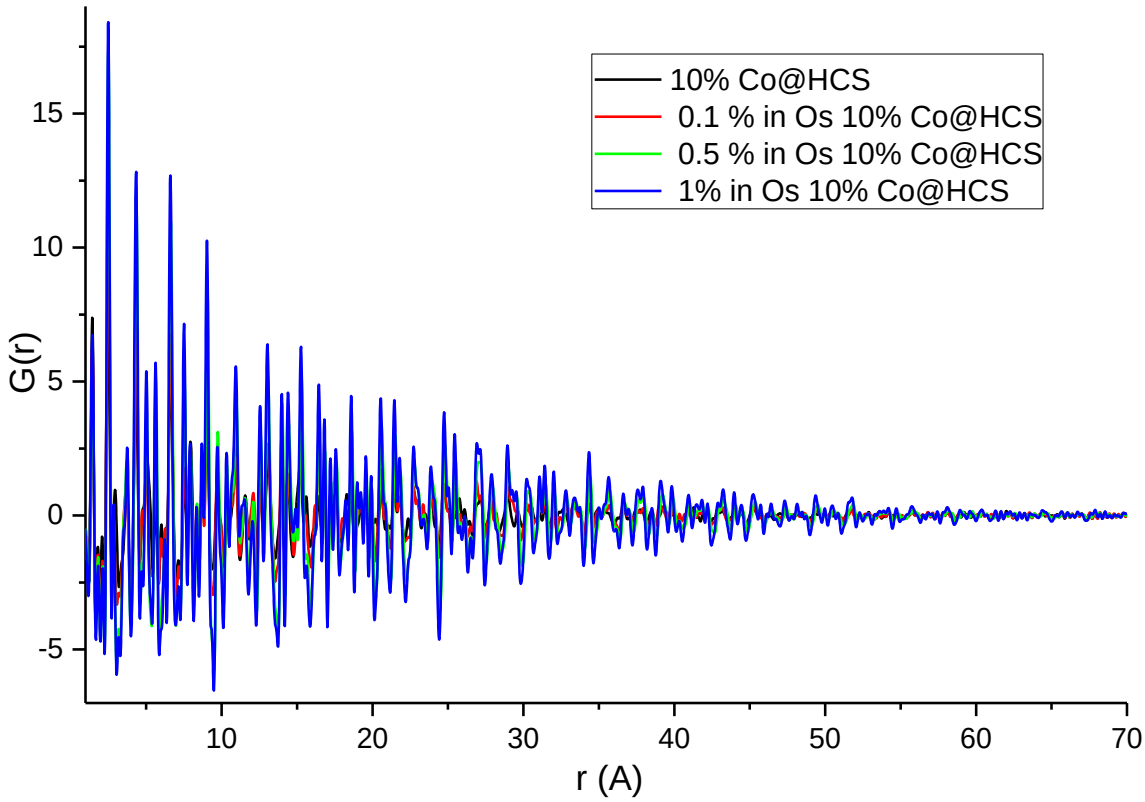

Figure S4.3. Experimental PDF of catalysts with Os supported inside the HCSs.

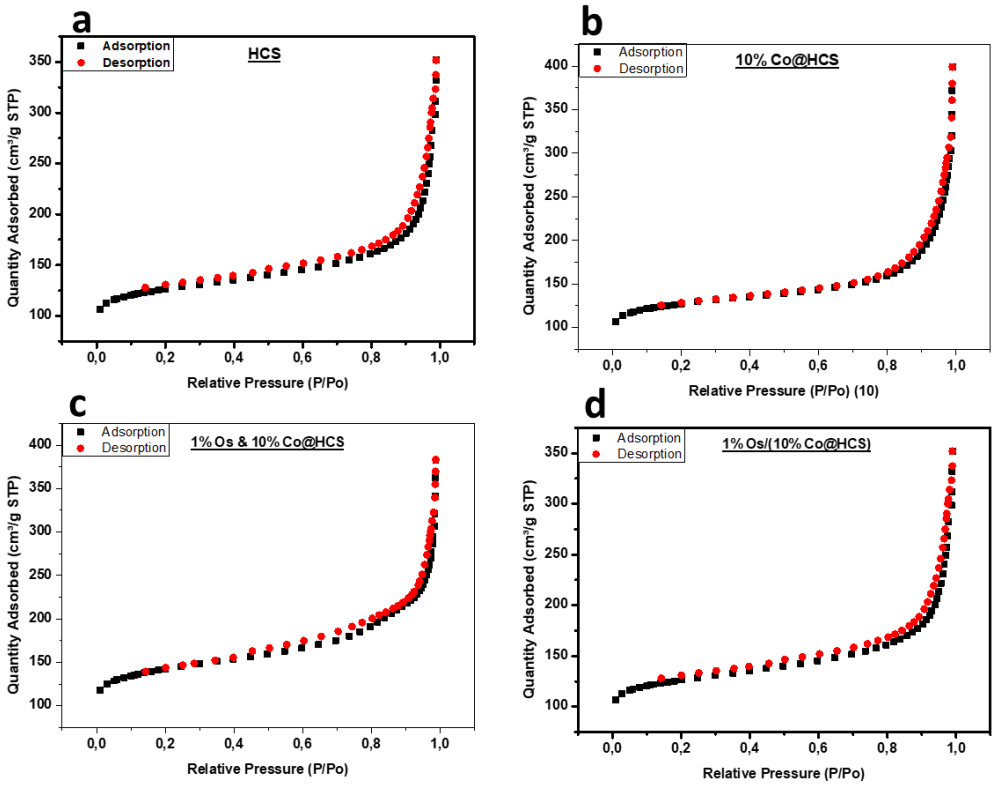

Figure S4.4: N_2 absorption-desorption curve of the a) HCS, b) 10% Co@HCS, c) 1% Os/10% Co@HCS, and d) 1% Os/(10% Co@HCS) catalysts.

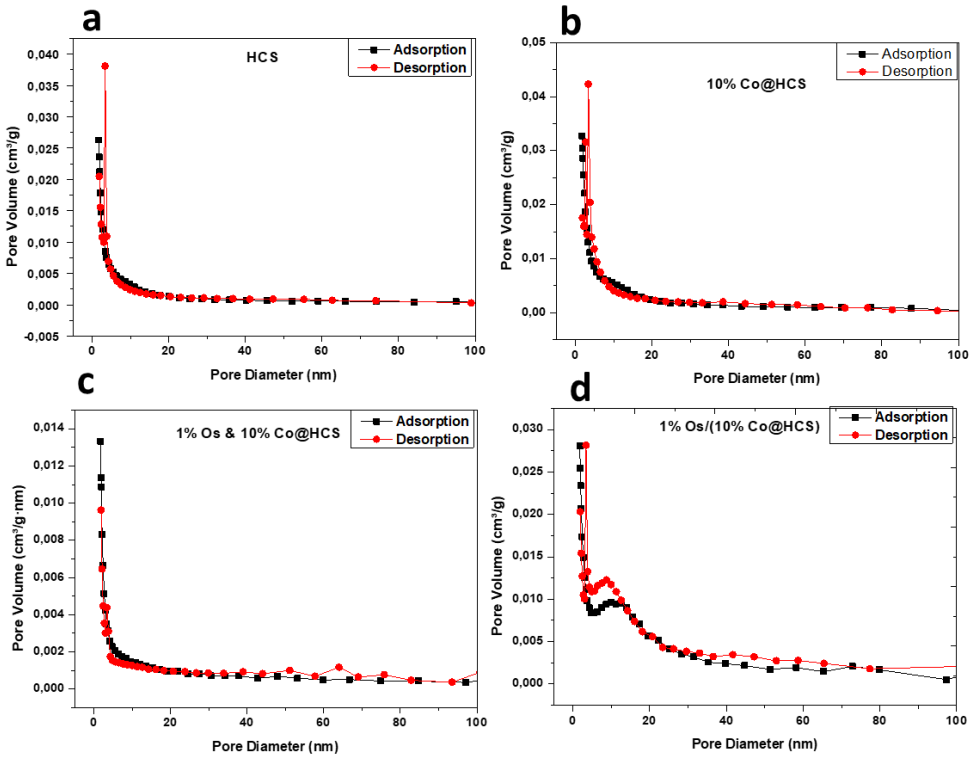

Figure S4.5: Pore size ditribution of a) HCS, b) 10% Co@HCS, c) 1%Os/10%Co@HCS, and d) 1% Os/(10%Co@HCS) catalysts.

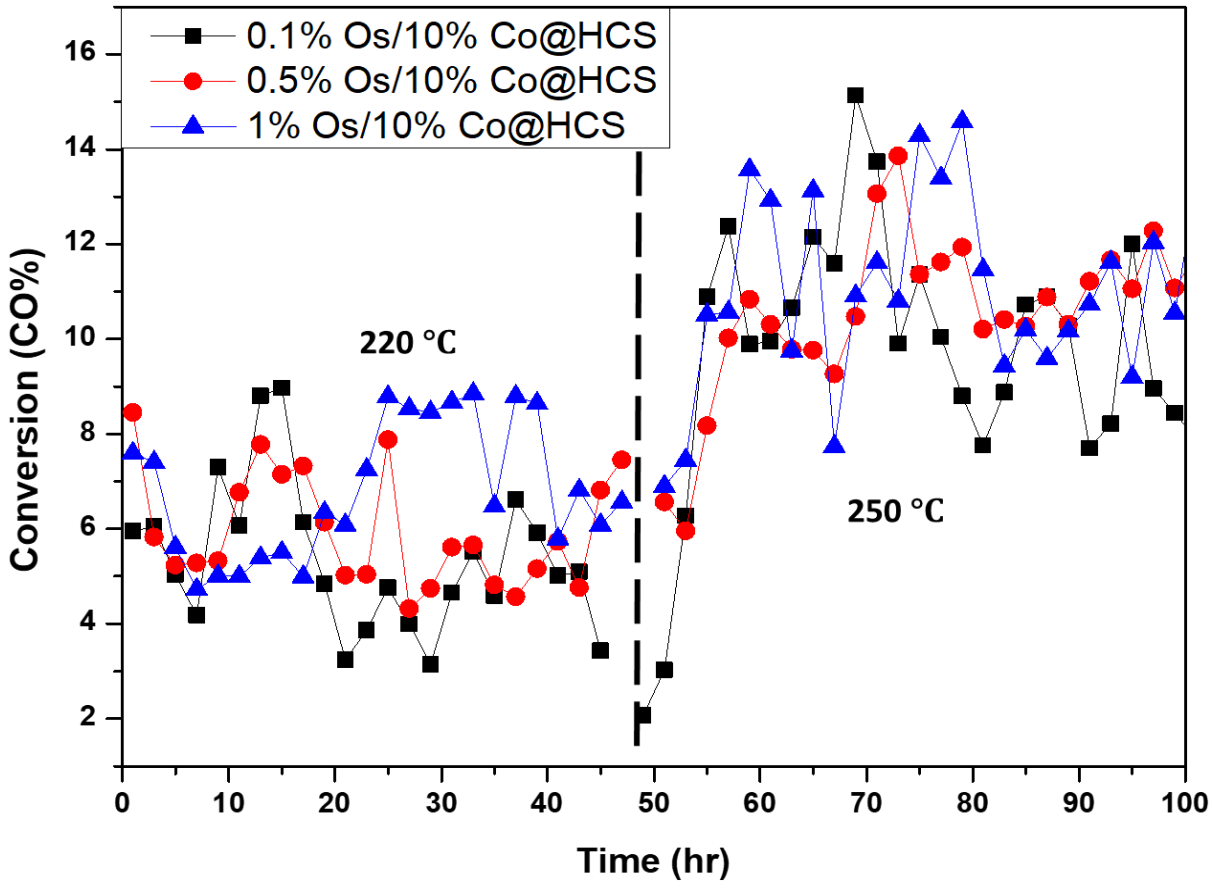

Figure S4.6. CO conversions for Os/Co@HCS catalysts over 100 hours on stream at 220 and 250 reaction temperatures.

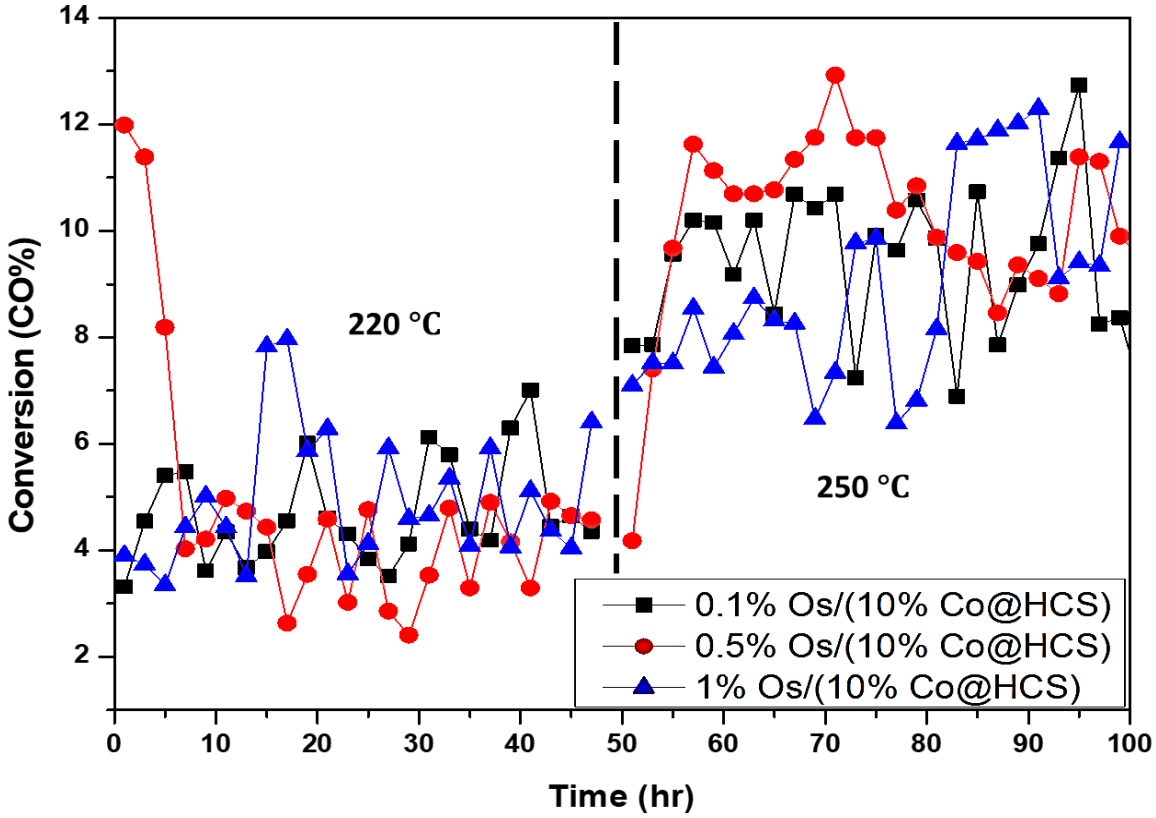

Figure S4.7. CO conversions for Os/(Co@HCS) catalysts over 100 hours on stream at 220 and 250 reaction temperatures.

Table S4.1: XRD data summary (d(°*A*), 2Theta, l fix, and hkl indices)

0.1% Os(10% Co@HCS)						
CoO						
d(Å)	2Theta (°)	I fix	h	k	l	
2.46338	42.583	729	1	1	1	
2.13335	49.579	999	2	0	0	
1.50851	72.735	517	2	0	2	
1.28646	88.104	222	3	1	1	
1.23169	93.142	143	2	2	2	
1.06668	113.98	60	4	0	0	
0.97885	132.076	87	3	1	3	
0.95406	139.289	180	4	0	2	
Co3O4						
d(Å)	2Theta (°)	I fix	h	k	l	
4.71637	21.865	93	1	1	1	
2.88818	36.083	588	2	0	2	
2.46305	42.589	999	3	1	1	
2.35819	44.582	197	2	2	2	
1.8741	57.017	10	3	1	3	
1.66749	64.881	151	4	2	2	
1.57213	69.356	240	5	1	1	
1.44409	76.546	173	4	0	4	
1.38081	80.751	2	5	3	1	
1.29163	87.66	45	6	0	2	
1.24576	91.783	64	5	3	3	
1.23152	93.158	49	6	2	2	
1.09163	110.05	43	6	4	2	
1.06351	114.506	98	7	3	1	
1.02113	122.322	21	8	0	0	
0.96273	136.595	22	8	2	2	
0.94327	142.983	55	7	5	1	
0.93705	145.329	22	6	2	6	

0.5% Os(10% Co@HCS)						
CoO						
d(Å)	2Theta (°)	I fix	h	k	l	
2.44797	42.864	733	1	1	1	
2.12	49.913	1000	2	0	0	
1.49907	73.267	515	2	0	2	
1.27841	88.804	221	3	1	1	
1.22398	93.907	142	2	2	2	
1.06	115.099	60	4	0	0	
0.97272	133.726	89	3	1	3	
0.94809	141.281	183	4	0	2	
Co3O4						
d(Å)	2Theta (°)	I fix	h	k	l	
4.71637	21.865	92	1	1	1	
2.88818	36.083	588	2	0	2	
2.46305	42.589	999	3	1	1	
2.35819	44.582	197	2	2	2	
1.8741	57.017	9	3	1	3	
1.66749	64.881	151	4	2	2	
1.57213	69.356	240	5	1	1	
1.44409	76.546	174	4	0	4	
1.38081	80.751	3	5	3	1	
1.29163	87.66	45	6	0	2	
1.24576	91.783	65	5	3	3	
1.23152	93.158	48	6	2	2	
1.09163	110.05	43	6	4	2	
1.06351	114.506	99	7	3	1	
1.02113	122.322	21	8	0	0	
0.96273	136.595	22	8	2	2	
0.94327	142.983	55	7	5	1	
0.93705	145.329	22	6	2	6	

1% Os(10% Co@HCS)						
CoO						
d(Å)	2Theta (°)	I fix	h	k	l	
2.46338	42.583	729	1	1	1	
2.13335	49.579	999	2	0	0	
1.50851	72.735	518	2	0	2	
1.28646	88.104	223	3	1	1	
1.23169	93.142	142	2	2	2	
1.06668	113.98	60	4	0	0	
0.97885	132.076	88	3	1	3	
0.95406	139.289	180	4	0	2	
Co3O4						
d(Å)	2Theta (°)	I fix	h	k	l	
4.71637	21.865	92	1	1	1	
2.88818	36.083	589	2	0	2	
2.46305	42.589	999	3	1	1	
2.35819	44.582	197	2	2	2	
1.8741	57.017	9	3	1	3	
1.66749	64.881	151	4	2	2	
1.57213	69.356	240	5	1	1	
1.44409	76.546	173	4	0	4	
1.38081	80.751	3	5	3	1	
1.29163	87.66	45	6	0	2	
1.24576	91.783	65	5	3	3	
1.23152	93.158	48	6	2	2	
1.09163	110.05	42	6	4	2	
1.06351	114.506	98	7	3	1	
1.02113	122.322	20	8	0	0	
0.96273	136.595	21	8	2	2	
0.94327	142.983	55	7	5	1	
0.93705	145.329	21	6	2	6	

0.1% Os & 10% Co@HCS

CoO

d(Å)	2Theta (°)	I fix	h	k	l
2.46124	42.622	729	1	1	1
2.1315	49.625	1000	2	0	0
1.5072	72.808	517	2	0	2
1.28534	88.2	223	3	1	1
1.23062	93.247	143	2	2	2
1.06575	114.133	61	4	0	0
0.978	132.3	88	3	1	3
0.95324	139.558	181	4	0	2

Co3O4

d(Å)	2Theta (°)	I fix	h	k	l
4.71637	21.865	93	1	1	1
2.88818	36.083	589	2	0	2
2.46305	42.589	999	3	1	1
2.35819	44.582	198	2	2	2
1.8741	57.017	10	3	1	3
1.66749	64.881	150	4	2	2
1.57213	69.356	241	5	1	1
1.44409	76.546	174	4	0	4
1.38081	80.751	3	5	3	1
1.29163	87.66	46	6	0	2
1.24576	91.783	65	5	3	3
1.23152	93.158	49	6	2	2
1.09163	110.05	43	6	4	2
1.06351	114.506	99	7	3	1
1.02113	122.322	21	8	0	0
0.96273	136.595	22	8	2	2
0.94327	142.983	56	7	5	1
0.93705	145.329	22	6	2	6

Co hcp

d(Å)	2Theta (°)	I fix	h	k	l
2.17147	48.652	258	1	0	0
2.03495	52.152	275	0	0	2
1.91584	55.665	1000	1	0	1
1.48485	74.085	124	0	1	2
1.2537	91.037	121	1	1	0
1.15055	102.054	127	0	1	3
1.08574	110.944	18	2	0	0
1.06739	113.861	129	1	1	2
1.04905	117.005	92	2	0	1
1.01748	123.073	20	0	0	4

0.5% Os & 10% Co@HCS

CoO

d(Å)	2Theta (°)	I fix	h	k	l
2.46338	42.583	730	1	1	1
2.13335	49.579	1000	2	0	0
1.50851	72.735	517	2	0	2
1.28646	88.104	223	3	1	1
1.23169	93.142	142	2	2	2
1.06668	113.98	61	4	0	0
0.97885	132.076	87	3	1	3
0.95406	139.289	181	4	0	2

Co3O4

d(Å)	2Theta (°)	I fix	h	k	l
4.71637	21.865	92	1	1	1
2.88818	36.083	588	2	0	2
2.46305	42.589	999	3	1	1
2.35819	44.582	197	2	2	2
1.8741	57.017	9	3	1	3
1.66749	64.881	150	4	2	2
1.57213	69.356	240	5	1	1
1.44409	76.546	173	4	0	4
1.38081	80.751	2	5	3	1
1.29163	87.66	45	6	0	2
1.24576	91.783	64	5	3	3
1.23152	93.158	48	6	2	2
1.09163	110.05	42	6	4	2
1.06351	114.506	98	7	3	1
1.02113	122.322	20	8	0	0
0.96273	136.595	21	8	2	2
0.94327	142.983	55	7	5	1
0.93705	145.329	21	6	2	6

Co hcp

d(Å)	2Theta (°)	I fix	h	k	l
2.17147	48.652	258	1	0	0
2.03495	52.152	275	0	0	2
1.91584	55.665	1000	1	0	1
1.48485	74.085	124	0	1	2
1.2537	91.037	121	1	1	0
1.15055	102.054	127	0	1	3
1.08574	110.944	18	2	0	0
1.06739	113.861	129	1	1	2
1.04905	117.005	92	2	0	1
1.01748	123.073	20	0	0	4

1% Os & 10% Co@HCS

CoO

d(Å)	2Theta (°)	I fix	h	k	l
2.44797	42.864	733	1	1	1
2.12	49.913	999	2	0	0
1.49907	73.267	515	2	0	2
1.27841	88.804	222	3	1	1
1.22398	93.907	142	2	2	2
1.06	115.099	61	4	0	0
0.97272	133.726	89	3	1	3
0.94809	141.281	183	4	0	2

Co3O4

d(Å)	2Theta (°)	I fix	h	k	l
4.71637	21.865	93	1	1	1
2.88818	36.083	589	2	0	2
2.46305	42.589	1000	3	1	1
2.35819	44.582	198	2	2	2
1.8741	57.017	10	3	1	3
1.66749	64.881	151	4	2	2
1.57213	69.356	240	5	1	1
1.44409	76.546	174	4	0	4
1.38081	80.751	2	5	3	1
1.29163	87.66	46	6	0	2
1.24576	91.783	64	5	3	3
1.23152	93.158	49	6	2	2
1.09163	110.05	43	6	4	2
1.06351	114.506	99	7	3	1
1.02113	122.322	21	8	0	0
0.96273	136.595	22	8	2	2
0.94327	142.983	56	7	5	1
0.93705	145.329	22	6	2	6

Co hcp

d(Å)	2Theta (°)	I fix	h	k	l
2.17121	48.658	257	1	0	0
2.0343	52.17	275	0	0	2
1.91552	55.675	1000	1	0	1
1.48451	74.105	125	0	1	2
1.25355	91.051	121	1	1	0
1.15025	102.091	127	0	1	3
1.08561	110.964	17	2	0	0
1.0672	113.892	129	1	1	2
1.04891	117.03	92	2	0	1
1.01715	123.141	20	0	0	4

10% Co@HCS

CoO

d(Å)	2Theta (°)	I fix	h	k	l
2.46124	42.622	730	1	1	1
2.1315	49.625	999	2	0	0
1.5072	72.808	517	2	0	2
1.28534	88.2	222	3	1	1
1.23062	93.247	143	2	2	2
1.06575	114.133	60	4	0	0
0.978	132.3	87	3	1	3
0.95324	139.558	181	4	0	2

Co3O4

d(Å)	2Theta (°)	I fix	h	k	l
4.71637	21.865	93	1	1	1
2.88818	36.083	588	2	0	2
2.46305	42.589	999	3	1	1
2.35819	44.582	197	2	2	2
1.8741	57.017	9	3	1	3
1.66749	64.881	151	4	2	2
1.57213	69.356	240	5	1	1
1.44409	76.546	173	4	0	4
1.38081	80.751	2	5	3	1
1.29163	87.66	45	6	0	2
1.24576	91.783	64	5	3	3
1.23152	93.158	48	6	2	2
1.09163	110.05	42	6	4	2
1.06351	114.506	98	7	3	1
1.02113	122.322	20	8	0	0
0.96273	136.595	21	8	2	2
0.94327	142.983	56	7	5	1
0.93705	145.329	21	6	2	6

Chapter 5: Fischer-Tropsch synthesis: osmium promoted Co@HCS catalysts

List of Figures

List of Tables

11,67402035 15,41851744 12,87

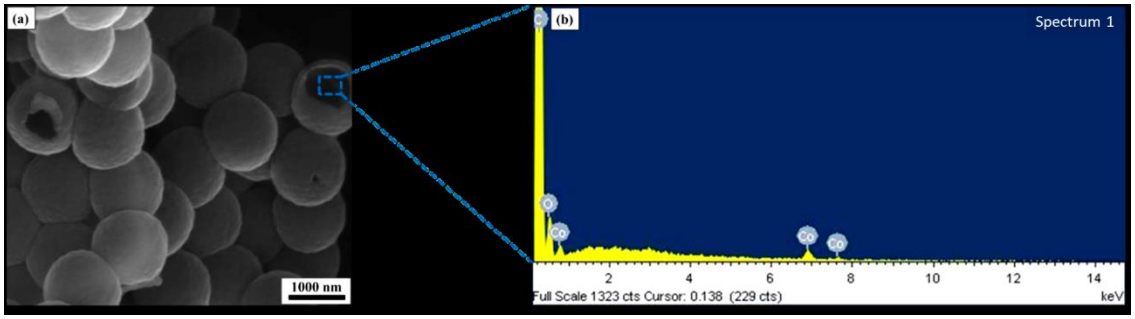

Figure S5.1: (a) SEM image and (b) EDX spectrum of 10Co@HCS.

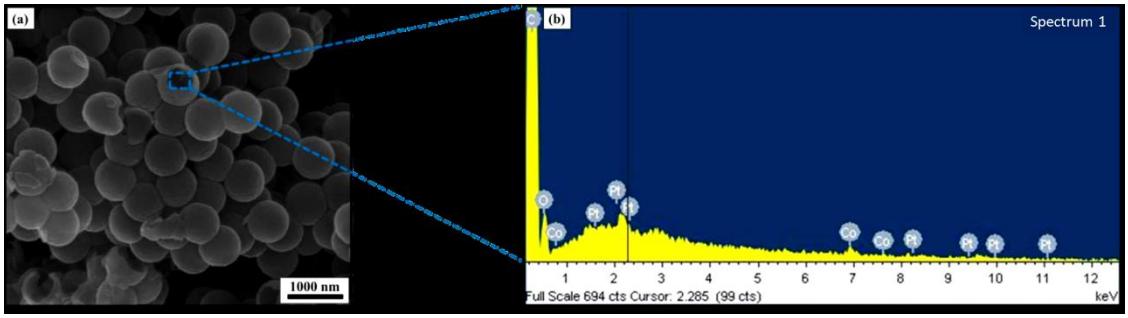

Figure S5.2: (a) SEM image and (b) EDX spectrum of 1Pt/10Co@HCS.

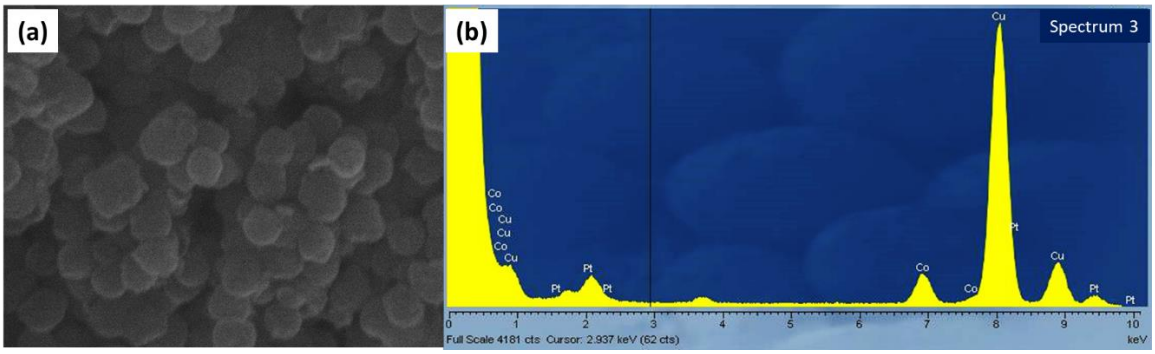

Figure S5.3: (a) SEM image and (b) TEM-EDX spectrum of 1Pt/(10Co@HCS).

(The presence of copper (Cu) was observed in the TEM-EDX due to copper grids being used as sample holder).

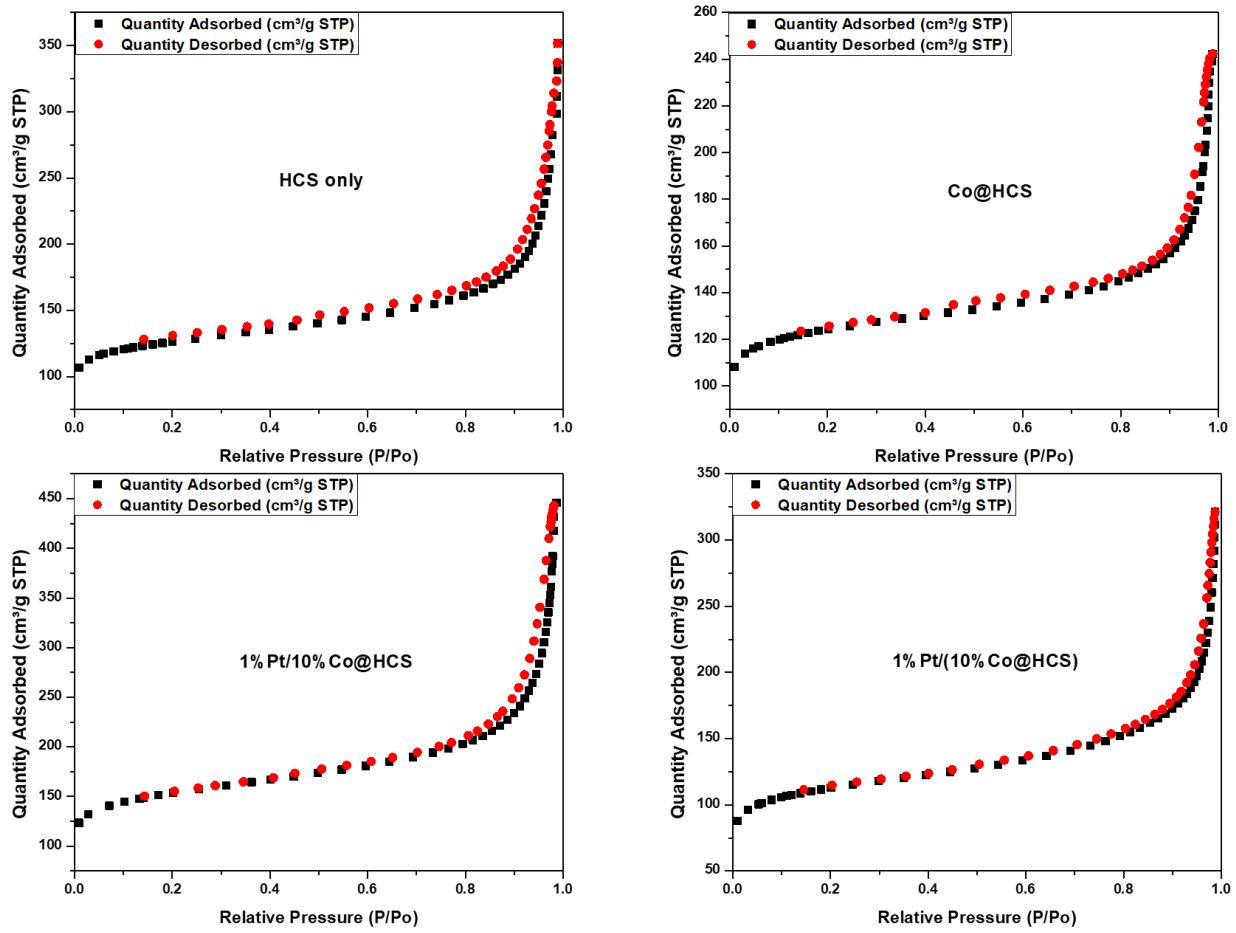

Figure S5.4: N_2 absorption-desorption isotherm curves of the HCS, Co@HCS, Pt/Co@HCS and Pt/(Co@HCS) catalysts.

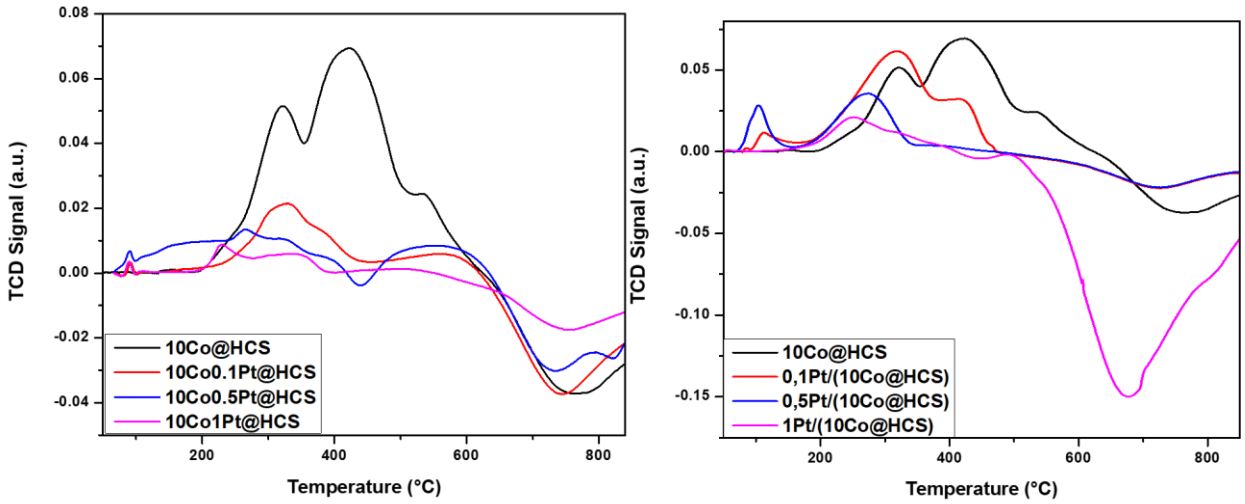

Figure S5.5: H_2-TPR profile (a) Pt/Co@HCS catalysts and Pt/(Co@HCS) catalyst (methanation peaks < 600 °C).

Table S5.1: Hydrogen consumption estimated from TPR peaks.

Sample	$Co_3O_4 + H_2 \rightarrow 3CoO$ Peak / mmol/g	$3CoO + 3H_2 \rightarrow 3Co$ Peak 2 / mmol/g	Total hydrogen consumption/ mmol/g	DOR(%)[a]
10Co@HCS	7.15	5.10	12.25	553
0.1%OsCo@HCS	4.88	1.54	6.42	297
0.5%OsCo@HCS	12.15	8.68	20.83	868
1%OsCo@HCS	6.38	6.69	13.08	666
0.1%Os/(Co@HCS)	5.46	6.76	12.22	381
0.5%Os/(Co@HCS)	5.47	2.00	7.47	472
1%Os/(Co@HCS)	3.41	0.99	4.39	318

[a]DOR > 100% due to support gasification at higher temperatures, therefore not true representative of the catalyst DOR.

Table S5.2: XRD data summary (d(°*A*), 2Theta, l fix, and hkl indices)

0.1% Os(10% Co@HCS)

CoO					
d(Å)	2Theta (°)	I fix	h	k	l
2.46338	42.583	729	1	1	1
2.13335	49.579	999	2	0	0
1.50851	72.735	517	2	0	2
1.28646	88.104	222	3	1	1
1.23169	93.142	143	2	2	2
1.06668	113.98	60	4	0	0
0.97885	132.076	87	3	1	3
0.95406	139.289	180	4	0	2

Co3O4					
d(Å)	2Theta (°)	I fix	h	k	l
4.71637	21.865	93	1	1	1
2.88818	36.083	588	2	0	2
2.46305	42.589	999	3	1	1
2.35819	44.582	197	2	2	2
1.8741	57.017	10	3	1	3
1.66749	64.881	151	4	2	2
1.57213	69.356	240	5	1	1
1.44409	76.546	173	4	0	4
1.38081	80.751	2	5	3	1
1.29163	87.66	45	6	0	2
1.24576	91.783	64	5	3	3
1.23152	93.158	49	6	2	2
1.09163	110.05	43	6	4	2
1.06351	114.506	98	7	3	1
1.02113	122.322	21	8	0	0
0.96273	136.595	22	8	2	2
0.94327	142.983	55	7	5	1
0.93705	145.329	22	6	2	6

0.5% Os(10% Co@HCS)

CoO					
d(Å)	2Theta (°)	I fix	h	k	l
2.44797	42.864	733	1	1	1
2.12	49.913	1000	2	0	0
1.49907	73.267	515	2	0	2
1.27841	88.804	221	3	1	1
1.22398	93.907	142	2	2	2
1.06	115.099	60	4	0	0
0.97272	133.726	89	3	1	3
0.94809	141.281	183	4	0	2

Co3O4					
d(Å)	2Theta (°)	I fix	h	k	l
4.71637	21.865	92	1	1	1
2.88818	36.083	588	2	0	2
2.46305	42.589	999	3	1	1
2.35819	44.582	197	2	2	2
1.8741	57.017	9	3	1	3
1.66749	64.881	151	4	2	2
1.57213	69.356	240	5	1	1
1.44409	76.546	174	4	0	4
1.38081	80.751	3	5	3	1
1.29163	87.66	45	6	0	2
1.24576	91.783	65	5	3	3
1.23152	93.158	48	6	2	2
1.09163	110.05	43	6	4	2
1.06351	114.506	99	7	3	1
1.02113	122.322	21	8	0	0
0.96273	136.595	22	8	2	2
0.94327	142.983	55	7	5	1
0.93705	145.329	22	6	2	6

1% Os(10% Co@HCS)

CoO					
d(Å)	2Theta (°)	I fix	h	k	l
2.46338	42.583	729	1	1	1
2.13335	49.579	999	2	0	0
1.50851	72.735	518	2	0	2
1.28646	88.104	223	3	1	1
1.23169	93.142	142	2	2	2
1.06668	113.98	60	4	0	0
0.97885	132.076	88	3	1	3
0.95406	139.289	180	4	0	2

Co3O4					
d(Å)	2Theta (°)	I fix	h	k	l
4.71637	21.865	92	1	1	1
2.88818	36.083	589	2	0	2
2.46305	42.589	999	3	1	1
2.35819	44.582	197	2	2	2
1.8741	57.017	9	3	1	3
1.66749	64.881	151	4	2	2
1.57213	69.356	240	5	1	1
1.44409	76.546	173	4	0	4
1.38081	80.751	3	5	3	1
1.29163	87.66	45	6	0	2
1.24576	91.783	65	5	3	3
1.23152	93.158	48	6	2	2
1.09163	110.05	42	6	4	2
1.06351	114.506	98	7	3	1
1.02113	122.322	20	8	0	0
0.96273	136.595	21	8	2	2
0.94327	142.983	55	7	5	1
0.93705	145.329	21	6	2	6

0.1% Os & 10% Co@HCS

CoO

d(Å)	2Theta (°)	I fix	h	k	l
2.46124	42.622	729	1	1	1
2.1315	49.625	1000	2	0	0
1.5072	72.808	517	2	0	2
1.28534	88.2	223	3	1	1
1.23062	93.247	143	2	2	2
1.06575	114.133	61	4	0	0
0.978	132.3	88	3	1	3
0.95324	139.558	181	4	0	2

Co3O4

d(Å)	2Theta (°)	I fix	h	k	l
4.71637	21.865	93	1	1	1
2.88818	36.083	589	2	0	2
2.46305	42.589	999	3	1	1
2.35819	44.582	198	2	2	2
1.8741	57.017	10	3	1	3
1.66749	64.881	150	4	2	2
1.57213	69.356	241	5	1	1
1.44409	76.546	174	4	0	4
1.38081	80.751	3	5	3	1
1.29163	87.66	46	6	0	2
1.24576	91.783	65	5	3	3
1.23152	93.158	49	6	2	2
1.09163	110.05	43	6	4	2
1.06351	114.506	99	7	3	1
1.02113	122.322	21	8	0	0
0.96273	136.595	22	8	2	2
0.94327	142.983	56	7	5	1
0.93705	145.329	22	6	2	6

Co hcp

d(Å)	2Theta (°)	I fix	h	k	l
2.17147	48.652	258	1	0	0
2.03495	52.152	275	0	0	2
1.91584	55.665	1000	1	0	1
1.48485	74.085	124	0	1	2
1.2537	91.037	121	1	1	0
1.15055	102.054	127	0	1	3
1.08574	110.944	18	2	0	0
1.06739	113.861	129	1	1	2
1.04905	117.005	92	2	0	1
1.01748	123.073	20	0	0	4

0.5% Os & 10% Co@HCS

CoO

d(Å)	2Theta (°)	I fix	h	k	l
2.46338	42.583	730	1	1	1
2.13335	49.579	1000	2	0	0
1.50851	72.735	517	2	0	2
1.28646	88.104	223	3	1	1
1.23169	93.142	142	2	2	2
1.06668	113.98	61	4	0	0
0.97885	132.076	87	3	1	3
0.95406	139.289	181	4	0	2

Co3O4

d(Å)	2Theta (°)	I fix	h	k	l
4.71637	21.865	92	1	1	1
2.88818	36.083	588	2	0	2
2.46305	42.589	999	3	1	1
2.35819	44.582	197	2	2	2
1.8741	57.017	9	3	1	3
1.66749	64.881	150	4	2	2
1.57213	69.356	240	5	1	1
1.44409	76.546	173	4	0	4
1.38081	80.751	2	5	3	1
1.29163	87.66	45	6	0	2
1.24576	91.783	64	5	3	3
1.23152	93.158	48	6	2	2
1.09163	110.05	42	6	4	2
1.06351	114.506	98	7	3	1
1.02113	122.322	20	8	0	0
0.96273	136.595	21	8	2	2
0.94327	142.983	55	7	5	1
0.93705	145.329	21	6	2	6

Co hcp

d(Å)	2Theta (°)	I fix	h	k	l
2.17147	48.652	258	1	0	0
2.03495	52.152	275	0	0	2
1.91584	55.665	1000	1	0	1
1.48485	74.085	124	0	1	2
1.2537	91.037	121	1	1	0
1.15055	102.054	127	0	1	3
1.08574	110.944	18	2	0	0
1.06739	113.861	129	1	1	2
1.04905	117.005	92	2	0	1
1.01748	123.073	20	0	0	4

1% Os & 10% Co@HCS

CoO

d(Å)	2Theta (°)	I fix	h	k	l
2.44797	42.864	733	1	1	1
2.12	49.913	999	2	0	0
1.49907	73.267	515	2	0	2
1.27841	88.804	222	3	1	1
1.22398	93.907	142	2	2	2
1.06	115.099	61	4	0	0
0.97272	133.726	89	3	1	3
0.94809	141.281	183	4	0	2

Co3O4

d(Å)	2Theta (°)	I fix	h	k	l
4.71637	21.865	93	1	1	1
2.88818	36.083	589	2	0	2
2.46305	42.589	1000	3	1	1
2.35819	44.582	198	2	2	2
1.8741	57.017	10	3	1	3
1.66749	64.881	151	4	2	2
1.57213	69.356	240	5	1	1
1.44409	76.546	174	4	0	4
1.38081	80.751	2	5	3	1
1.29163	87.66	46	6	0	2
1.24576	91.783	64	5	3	3
1.23152	93.158	49	6	2	2
1.09163	110.05	43	6	4	2
1.06351	114.506	99	7	3	1
1.02113	122.322	21	8	0	0
0.96273	136.595	22	8	2	2
0.94327	142.983	56	7	5	1
0.93705	145.329	22	6	2	6

Co hcp

d(Å)	2Theta (°)	I fix	h	k	l
2.17121	48.658	257	1	0	0
2.0343	52.17	275	0	0	2
1.91552	55.675	1000	1	0	1
1.48451	74.105	125	0	1	2
1.25355	91.051	121	1	1	0
1.15025	102.091	127	0	1	3
1.08561	110.964	17	2	0	0
1.0672	113.892	129	1	1	2
1.04891	117.03	92	2	0	1
1.01715	123.141	20	0	0	4

10% Co@HCS

CoO

d(Å)	2Theta (°)	I fix	h	k	l
2.46124	42.622	730	1	1	1
2.1315	49.625	999	2	0	0
1.5072	72.808	517	2	0	2
1.28534	88.2	222	3	1	1
1.23062	93.247	143	2	2	2
1.06575	114.133	60	4	0	0
0.978	132.3	87	3	1	3
0.95324	139.558	181	4	0	2

Co3O4

d(Å)	2Theta (°)	I fix	h	k	l
4.71637	21.865	93	1	1	1
2.88818	36.083	588	2	0	2
2.46305	42.589	999	3	1	1
2.35819	44.582	197	2	2	2
1.8741	57.017	9	3	1	3
1.66749	64.881	151	4	2	2
1.57213	69.356	240	5	1	1
1.44409	76.546	173	4	0	4
1.38081	80.751	2	5	3	1
1.29163	87.66	45	6	0	2
1.24576	91.783	64	5	3	3
1.23152	93.158	48	6	2	2
1.09163	110.05	42	6	4	2
1.06351	114.506	98	7	3	1
1.02113	122.322	20	8	0	0
0.96273	136.595	21	8	2	2
0.94327	142.983	56	7	5	1
0.93705	145.329	21	6	2	6

Table S5.3: Fischer-Tropsch synthesis performance of the catalysts (250 °C).

Sample	CO conversion (%)	Selectivity (C mol) (%)

		C_1	C_2-C_4	C_{5+}
10Co0.1Pt@HCS	21.8	30.1	12.8	57.1
10Co0.5Pt@HCS	23.7	32	12.1	55.9
10Co1Pt@HCS	24.5	35.6	12.8	51.6
0.1Pt/(10Co@HCS)	8.9	24.5	9.0	66.5
0.5Pt/(10Co@HCS)	10.9	25.9	9.8	64.3
1%Pt/(10%Co@HCS)	11.8	27.1	10.6	62.3

Chapter 6: The effect of shell thickness on hydrogen spillover in Os promoted Co@HCS

List of Figures

List of Tables

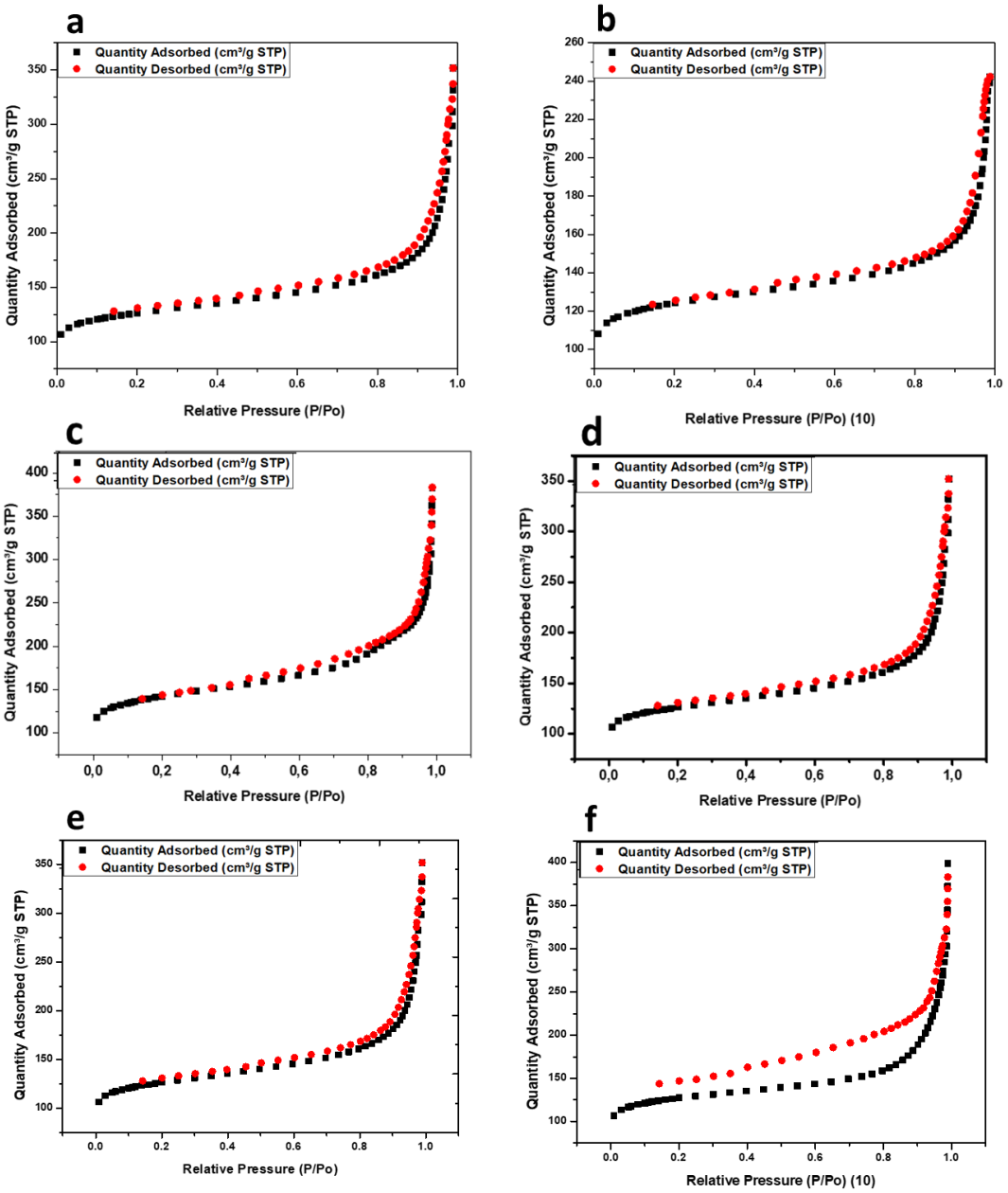

Figure S6.1: N_2 absorption-desorption isotherm curves of the a) 10%C0@HCS16nm, b) 10%Co@HCS28nm,c) 10%C0@HCS51nm, d) 1%Os/10%Co@HCS16nm, e) 1%Os/10%Co@HCS28nm and 1%Os/10%Co@HCS51nm catalysts.

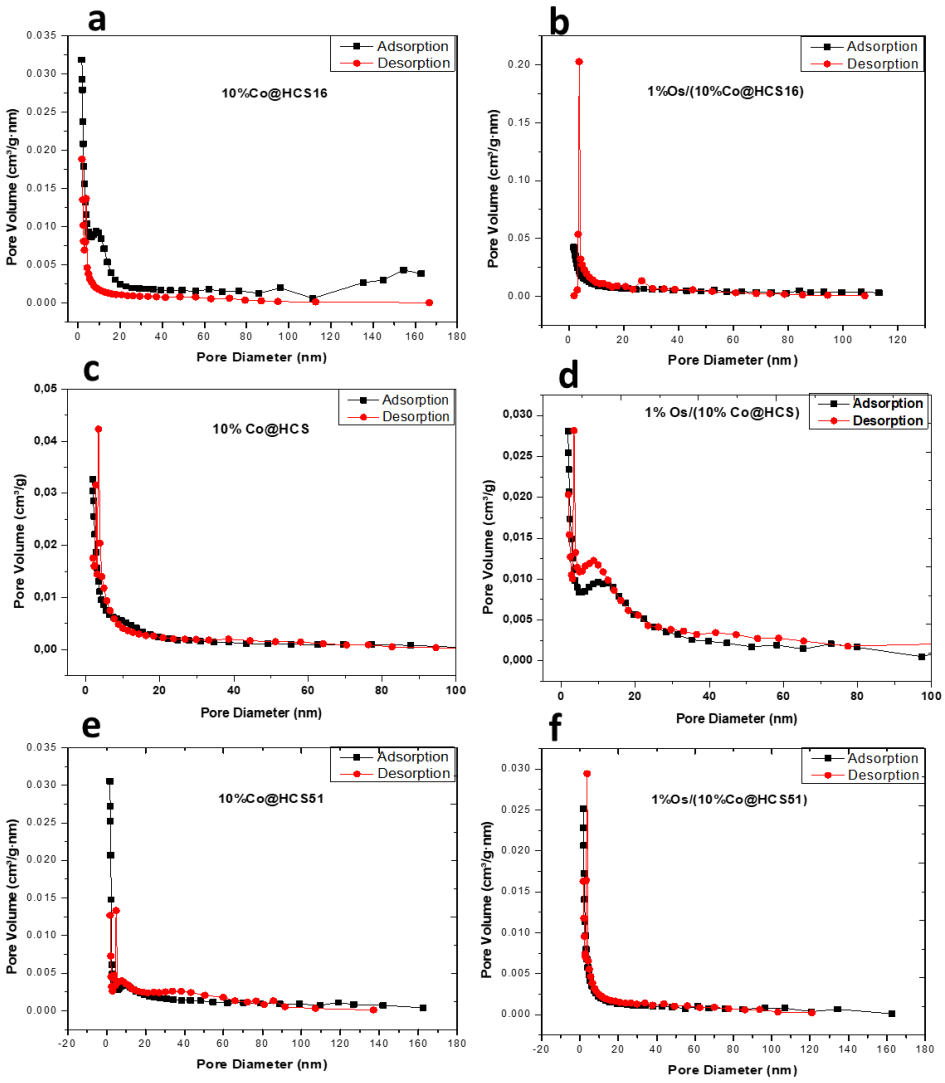

Figure S6.2: Pore size distribution a) 10%C0@HCS16nm, b) 10%Co@HCS28nm,c) 10%C0@HCS51nm, d) 1%Os/10%Co@HCS16nm, e) 1%Os/10%Co@HCS28nm and 1%Os/10%Co@HCS51nm catalysts.

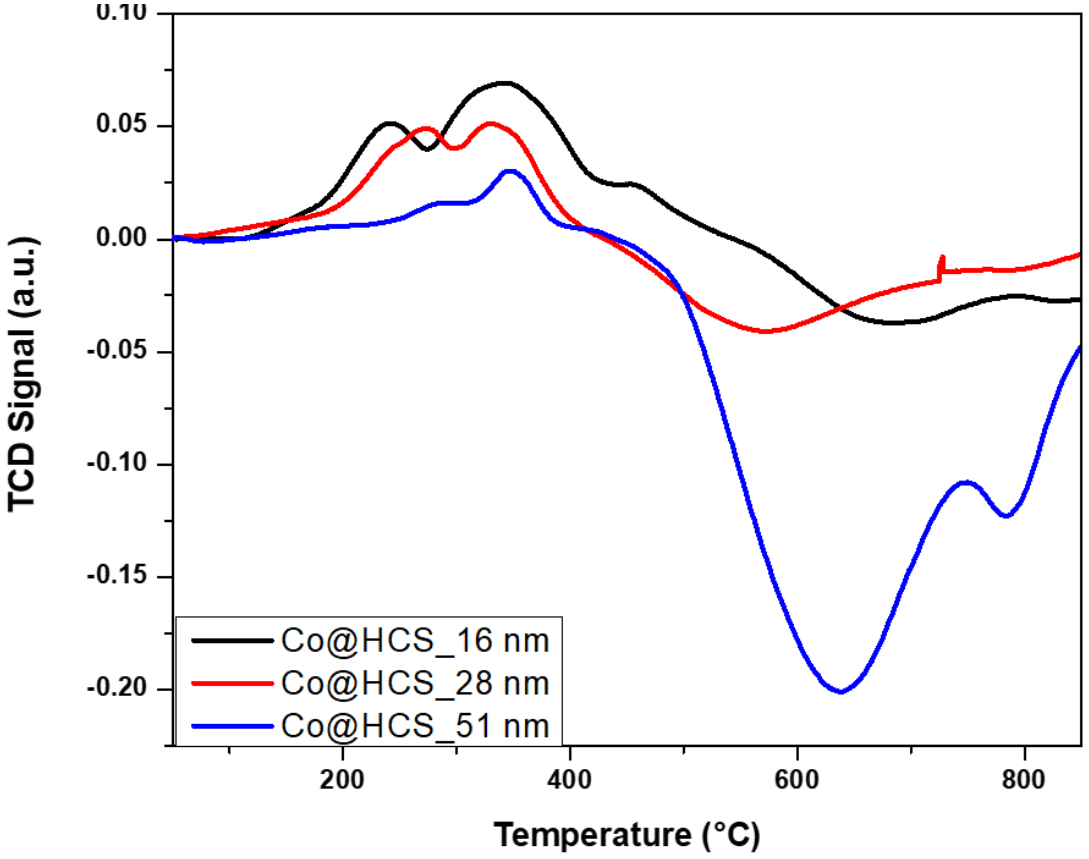

Figure S6.3. TPR profiles of Co@HCS16, Co@HCS28 and Co@HCS51

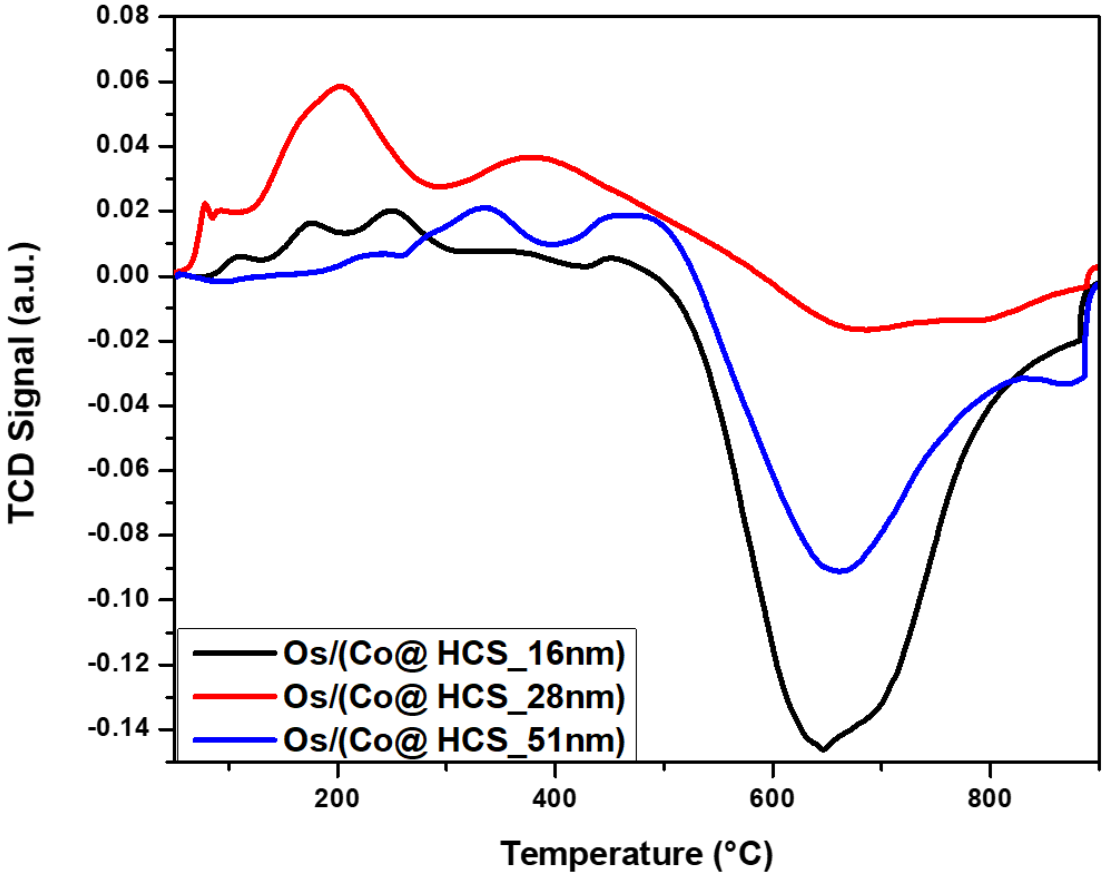

Figure S6.4: TPR profiles of Os/(Co@HCS16), Os/(Co@HCS28) and Os/(Co@HCS51)

Table S6.1: Fischer-Tropsch catalytic performance and selectivity (250 °C).

Sample Name	CO conversion (%)	Selectivity (C mol) (%)		
		C_1	C_2-C_4	C_{5+}
10%Co@HCS28	9.8	20.5	13.2	66.3
1%Os/(10%Co@HCS_16 nm)	18.0	16.6	5.8	77.6
1%Os/(10%Co@HCS_ 28 nm)	9.5	17.7	4.4	77.8
1%Os/(10%Co@HCS_51 nm)	2.8	8.2	4.2	87.5

Chapter 7: Osmium promoter effects on the hydrogen spillover and performance of nitrogen functionalized hollow carbon spheres supported cobalt Fischer-Tropsch synthesis catalysts

List of Figures

List of Tables

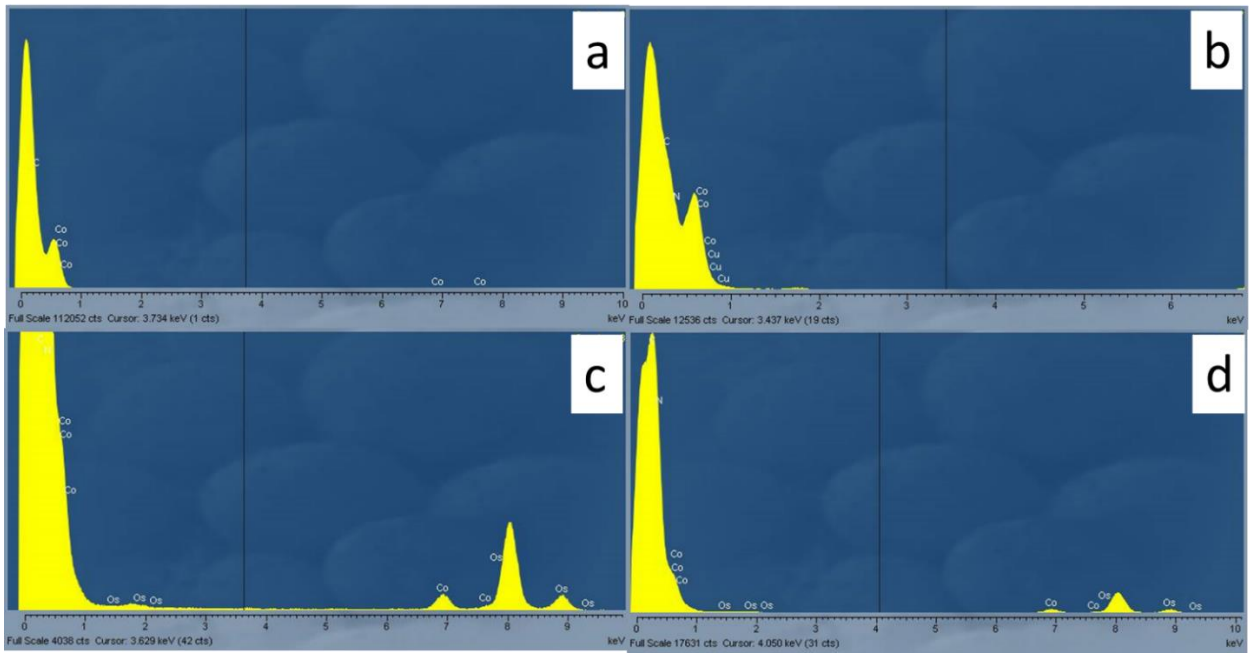

Figure S7.1: EDS spectrums of a) 10%Co@HCS, b) 10%Co@NHCS c) 1%Os/(10%Co@HCS), and d) 1%Os/(10%Co@NHCS) catalysts.

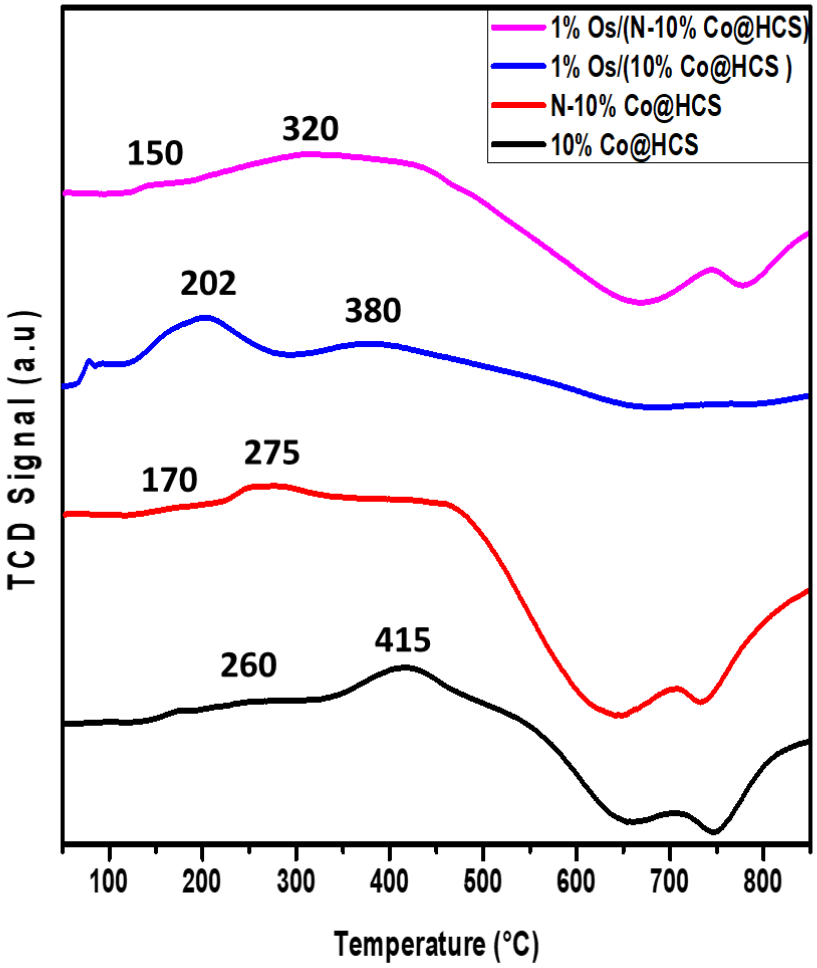

Figure S7.2: TPR profiles of 10%Co@HCS, 10%Co@NHCS, 1%Os/(10%Co@HCS), and 1%Os/(10%Co@NHCS) catalysts.

Table S7.1: XPS binding energy and atomic percentage summary

Sample Name		C 1s	O 1s	N 1s	Co 2p	Os4f7
1%Os/(10%Co@NHCS)	Peak BE	284.4	532.4	399	780.8	53.5
	Atomic %	86.8	8.4	4.3	0.3	0.2

1%Os/(10%Co@HCS)	Peak BE	284.2	531.9	399.1	780.7	53.6
	Atomic %	87.2	11.1	-	0.6	1.1
10%Co@NHCS	Peak BE	284.3	532.4	399	781.2	-
	Atomic %	87.1	8.3	4.4	0.2	-
10%Co@HCS	Peak BE	284.6	532.1	399	780.9	-
	Atomic %	86.9	12.3	-	0.8	-
NHCS	Peak BE	285	532.6	398.9	-	-
	Atomic %	74.7	8.1	17.2	-	-
HCS	Peak BE	283.9	532.2	398.7	-	-
	Atomic %	89.3	9.3	-	-	-

Table S7.2: Fischer-Tropsch synthesis performance of the catalysts (250 °C).

Sample	**CO conversion (%)**	**Selectivity (C mol) (%)**		
		C_1	C_2-C_4	C_{5+}
10%Co@HCS	8.6	27,6	17,2	63.6
10%Co@NHCS	9.1	39,8	6,3	53,9
1%Os/(10%Co@HCS)	9.5	17,7	4,4	77,8
1%Os/(10%Co@NHCS)	13,6	29,8	4,9	65,3